Imperial College London

Structural Health Monitoring of Composite Structures with distributed Fibre Optic Sensing

---

By

Yingwu Li

Thesis submitted in part fulfilment of the requirements for the degree of Doctor of Philosophy in Aeronautics of Imperial College London

Department of Aeronautics

Faculty of Engineering

Imperial College London

September 2023

Live as if you were to die tomorrow. Learn as if you were to live forever.

Declaration of Originality

I hereby declare that all the work and material presented in this thesis is composed and reported as my own. All information and data obtained from external sources are properly acknowledged and cited in text with the full list of references given in the final bibliography section.

Yingwu Li

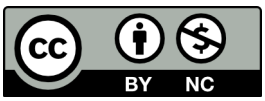
December 19, 2023

Copyright Declaration

The copyright of this thesis rests with the author. Unless otherwise indicated, its contents are licensed under a Creative Commons Attribution-Non Commercial 4.0 International Licence (CC BY-NC).

Under this licence, you may copy and redistribute the material in any medium or format. You may also create and distribute modified versions of the work. This is on the condition that: you credit the author and do not use it, or any derivative works, for a commercial purpose.

When reusing or sharing this work, ensure you make the licence terms clear to others by naming the licence and linking to the licence text. Where a work has been adapted, you should indicate that the work has been changed and describe those changes. Please seek permission from the copyright holder for uses of this work that are not included in this licence or permitted under UK Copyright Law.



Acknowledgements

I would like to express my deep appreciation to Professor Zahra Sharif-Khodaei, who is undoubtedly one of the best supervisors I have had the privilege of working with. She consistently demonstrates professionalism, patience, and a strong sense of responsibility. Personally, she is like a lighthouse, guiding me through the vast ocean of knowledge. Professor Sharif-Khodaei not only provided invaluable guidance on the specifics of my research but also emphasized the importance of considering the bigger picture throughout my PhD journey. This has enabled me to approach my research from a broader perspective. Furthermore, she granted me a significant degree of freedom and encouraged me to explore innovative approaches in my work. Additionally, she meticulously reviewed my written work, offering invaluable insights and suggestions in a highly professional manner, which has immensely contributed to my growth as a researcher. In summary, I am profoundly grateful to Professor Khodaei for her guidance during these past four years. My experience with the Structural Integrity and Health Monitoring (SIHM) Group has been one of the most valuable assets in my life.

I would also like to express my appreciation to my wife, Feifei Ren. She was the one who encouraged and accompanied me on my journey to pursue a PhD at Imperial College London. Prior to our doctoral studies, she assisted me in finding PhD opportunities, preparing for interviews, seeking scholarship opportunities, and assembling application materials, among other things. Her support and encouragement were instrumental in my decision to pursue a doctoral degree. Furthermore, owing to her exceptional performance and abilities, she herself had the opportunity to conduct doctoral research in the Structural Integrity and Health (SIHM) Monitoring Group. Her optimistic spirit and her prowess in scientific research have consistently influenced and inspired me. Simultaneously, she has offered valuable insights for my doctoral research and has provided substantial assistance with my experiments, including the manufacture of composite structures, sensor installation, and temperature experiments. It is a great honor to have Feifei by my side in this journey called life. To me, she will never age, fade, or die!

I would also like to express my appreciation to Dr. Thulasi Mylvaganam, who served as the assessor for my late-stage review. Her invaluable suggestions on my research during the late-stage review greatly contributed to the success of my PhD studies. I would like to extend my gratitude to Professor Robert Hewson and Professor Steve James for generously dedicating their time and providing valuable feedback on my thesis. Their constructive comments have

played a crucial role in refining and enhancing the quality of my work. The professional guidance received not only addressed numerous inquiries but also promises significant contributions to my future research endeavors. Additionally, I would like to extend my gratitude to several colleagues who provided me with assistance throughout my journey: Dr. Cheng Xu, who aided me in understanding mechanical theory and the OFDR system; Dr. Ilias Giannakeas, who guided me in machine learning; Dr. Sina Asadi, who assisted me in processing experimental data; Dr. Valentin Buchinger, who supported me in SMF splicing and configuration; Dr. Nan Yue, who helped me operate the temperature chamber; Dr. Llewellyn Morse, who provided valuable input for proposal revisions; Dr. Jun Li, who contributed to the selection of experimental materials; Mr. Yuhang Pan, who collaborated with me on machine learning; Mr. Haolin Li, who assisted with finite element methods; Mr. Dong Xiao, who aided in compressed sensing; Dr Zhihui Li, who helped me on single image super-resolution technique; and Mr. Francisco Rodrigues, who played a crucial role in setting up experiments. Your support and expertise were instrumental in my research journey.

As my research is primarily experimental, I dedicated a significant amount of time to various types of experiments. Therefore, I would like to extend my gratitude to Mr. Joseph Meggyesi, Mr. Keith Wolstenholme, and Dr. Stefano Del Rosso for their assistance with mechanical experiments, temperature experiments, and impact experiments, respectively. Additionally, I would like to express my appreciation to Mr. Gary Senior and Mr. Jon Cole for their help with composite specimen manufacturing and sensor installation, as well as to Mr. Franco Giammaria for his assistance with instruments. I also want to convey my thanks to Ms. Siân Haynes, Ms. Lisa Kelly, Ms. Clodagh Li, and Ms. Ela Sapinska for their support in various aspects during my PhD journey, including research management, seating arrangements, PhD administration, and finance queries.

At last, I would like to extend my heartfelt appreciation to my parents, Zhong Li and Huixiang Zhou, for their unwavering and boundless support throughout my entire PhD journey. Their love, encouragement, and sacrifices have been the cornerstone of my academic pursuit. Their belief in me, even during the most challenging times, has been a driving force behind my perseverance. I am deeply grateful for their understanding, patience, and the countless sacrifices they made to ensure my success. My accomplishments are a reflection of their dedication and love, and I owe them more than words can express.

Abstract

The utilization of Carbon fibre reinforced polymers (CFRP) in aircraft structures has increased due to their advantageous properties, including being lightweight, strong, and cost-effective. However, CFRP materials are more complex than aluminium alloys and are susceptible to damage issues such as delamination, debonding, and matrix cracking, making structural health monitoring (SHM) essential. Strain measurement is a critical SHM technique as it detects structural damage by measuring changes in strain distribution. One effective sensor for strain measurement in CFRP is the single mode fibre that can be interrogated using the optical frequency domain reflectometer technique, which provides high spatial accuracy and continuous high-precision sensing.

At present, limited research has been conducted on the analysis of measurement accuracy in the presence of complex environmental conditions, such as thermal and vibration variations. Moreover, SMFs are sensitive to both mechanical and thermal loads. Therefore, this thesis focuses on fundamental research at first, including improving the sensitivity of strain measurements, calibration of strain measurement accuracy, and consistency of strain measurement on different structures.

Upon obtaining an accurate strain distribution based on fundamental research mentioned above, the next step of this thesis focuses on damage detection and shape sensing of CFRP shells using the inverse finite element method. The detection of damage is achieved by detecting sudden changes in the strain field under loading. In addition, a widely applicable and high-accuracy shape sensing scheme based on distributed fibre optic sensing has been proposed in this thesis. This scheme combines a block-based strain acquisition method with strain extrapolation based on single image super resolution algorithms to obtain displacement fields with high accuracy and high spatial resolution.

The research objectives are geared towards enhancing the SHM of CFRP structures using distributed fibre optic sensing, which improves their performance and durability in aerospace applications.

Contents

1 Introduction **1**

1.1 Motivation 1

1.2 Objectives 8

1.3 Thesis outline 10

1.4 Publications 13

2 Background: a review of optical frequency domain reflectometry technique **14**

2.1 Distributed fiber optic sensing 14

2.2 Rayleigh-based distributed sensing 17

2.3 State of the art of the OFDR technique for aircraft structures 23

2.3.1 Spatial resolution improvement 25

2.3.2 Drawbacks of the FFT and algorithm efficiency improvement 35

2.3.3 Continuous vibration measurement and shape sensing 38

2.3.4 Challenges of embedding FOS in composite materials 45

2.3.5 Conclusions 49

3 Strain and temperature measurement based on Rayleigh backscattering **52**

3.1 Introduction 52

3.2 The sensitivity enhancement of distributed fiber optic sensors 57

3.2.1 Experimental setup 57

3.2.2 Temperature measurement sensitivity enhancement 59

3.2.3 Strain measurement sensitivity enhancement 62

3.2.4 Conclusions 63

3.3 Accuracy of distributed strain sensing in CFRP under thermal and mechanical load 66

3.3.1 Static loading experiment setup 66

3.3.2 Data analyses of static loading experiment 69

3.3.3 Conclusions 78

3.4 Accuracy of distributed strain sensing in composite laminates under fatigue loads 79

3.4.1 Fatigue experimental setup 79

3.4.2 Data analyses of fatigue experiment 80

3.4.3 Conclusions 83

3.5 Strain measurement consistency of distributed sensing 84

3.5.1 Strain-frequency shift coefficient consistency 85

3.5.2 Temperature-frequency shift coefficient consistency 90

3.5.3 Measurement uncertainty of distributed fibre optic sensors with OFDR system 94

3.5.4 Conclusions 95

4 Damage detection in composite plates based on distributed fiber optic sensing 97

4.1 Introduction 97

4.2 2D reconstruction of strain along the optical fiber axis by interpolation 101

4.2.1 Experiment Setup 102

4.2.2 Methodology 104

4.2.3 Results and discussion 110

4.2.4 Conclusions 112

4.3 A novel DI-based damage detection method 113

4.3.1 Methodology 113

4.3.2 Experiments 123

4.3.3 Results and discussion 128

4.3.4 Conclusions 133

5 Shape sensing of composite plates based on distributed fiber optic sensing 135

5.1 Introduction 135

5.2 Methodology 139

5.2.1 Inverse finite element method with drilling degrees of freedom 139

5.2.2 The strain acquisition scheme based on distributed fibre optic sensing . . 144

5.2.3 Strain extrapolation based on single image super resolution 148

5.3 Experiments 153

5.3.1 The specimens and experimental setup 153

5.4 Results and discussion 156

5.4.1 The iQS4 mesh of specimens 156

5.4.2 The shape sensing results of specimens: Specimen I (Top-left); Specimen II (Bottom-left); Specimen III (Right) 156

5.4.3 The strain extrapolation results . . . 160

5.4.4 The shape sensing result of specimen III after strain extrapolation . . . 164

5.5 Conclusions . . . 165

6 Summaries and future works **168**

6.1 Summary of background introduction . . . 168

6.2 Summary of the strain and temperature measurement research . . . 169

6.3 Summary on damage detection of CFRP structures . . . 171

6.4 Summary of shape sensing of CFRP shell structures . . . 172

6.5 Contributions and outcomes . . . 172

6.6 Future works . . . 174

A The inverse Finite Element Method **176**

A.1 The appendix of Chapter 5 . . . 176

A.2 A detailed derivation of the inverse finite element method . . . 178

A.2.1 Basic assumption . . . 178

A.2.2 iQS4 fields characterization . . . 179

A.2.3 Variational Principle . . . 189

A.2.4 Numerical integration . . . 194

A.2.5 Structure/global stiffness matrix . . . 201

A.2.6 Solution of iFEM . . . 204

References **205**

List of Figures

1.1 Distribution of composite materials in A380 [1] 2

1.2 The implementation of structural health monitoring [14, 15] 4

1.3 The structural health monitoring system based on three types of fiber optic sensors 6

2.1 Three types of intrinsic backscattering in distributed fiber optic sensing [39] . . 15

2.2 The basic sensing principle of OTDR technique 18

2.3 The schematic diagram of an OFDR system 19

2.4 The basic principle of OFDR system 20

2.5 Three ways to improve the spatial resolution of an OFDR system 25

2.6 Schematic diagram of bandwidth-division technique based on multiple BPFs . . 27

2.7 The errors induced by nonlinearity and phase noise of TLS: (a) The impact of errors introduced by the inherent nonlinearity introduced by the TLS; (b) The impact of errors introduced by the intrinsic phase noise of the TLS [88, 89] . . . 29

2.8 Signal processing steps to detect the optical frequency [91] 29

2.9 The methods adopted to address the drawbacks of FFT and improve the efficiency of algorithms 38

2.10 The two categories of methods on continuous vibration measurement with OFDR system 40

2.11 The techniques of continuous vibration measurement 44

3.1 The comparison of backscattering spectrum between sensors with and without NCF: (a) With NCF; (b) Without NCF 58

3.2 Temperature response of UV683 coating at free state: (a) Measurement data;(b) Temperature sensitivity 59

3.3 Temperature response for different coatings after surface mounting: (a) UV683 coating; (b) Polyimide coating; (c) Bare fiber optic sensor; (d) Arcylate coating . 61

3.4 The diagram of loading device and clamps: (a) The loading setup; (b) The design of clamps; (c) The clamps by 3D printing; (d) The installation of fiber optic sensors 63

3.5 The strain sensitivity of different coatings at free state: (a) Acrylate coating; (b) Bare fiber optic sensors; (c) UV683 coating 64

3.6 The strain sensitivity under different twist pre-loads at free state: (a) Without twist; (b) Twist 20; (c) Twist 30 65

3.7 Layout of sensors on specimen: (a) The sensors configuration of side 1; (b) The sensors configuration of side 2 67

3.8 Static loading experiment setup: (a) The experiment setup; (b) The side 1 of composite specimen; (c) The side 2 of composite specimen 68

3.9 Sensing segments distribution and measurement data of SMF2 in static loading experiment (under -30°C of the first test scenario): (a) The measurement data on fibre optic sensor; (b) The data after filtering and extraction 70

3.10 Data cleaning and reconstruction results of SMF2 measurements in static loading experiment: (a) The measurement data after the linear fit; (b) The measurement data after cleaning and reconstruction 72

3.11 Temperature compensation results of SMF2 in static loading experiment: (a) The temperature compensation results of distributed measurements at 6kN (375MPa) tension load; (b) The temperature compensation results along the load direction under different tension loads 73

3.12 Strain-load coefficient of Gauge2 and Strain-frequency shift coefficient of SMF2 under thermal load: (a) The Strain-load coefficient of Gauge2 under thermal load; (b) The strain-frequency shift coefficient of SMF2 under thermal load . . . 74

3.13 Strain calculation errors of SMF2 in static loading experiment: (a) The comparison of Gauge2 reference strain and the calculated strain from the SMF2 at 50°C and 80°C when the strain-frequency shift coefficient at 20°C is adopted; (b) The error for different current and baseline states combinations 76

3.14 Strain calculated from SMF2 under 10kN(625MPa) tension and 20°C 76

3.15 Numerical modelling results: (a) The model of the composite laminate; (b) The simulation result of finite element method 77

3.16 The setup of fatigue experiment: (a) The experiment setup; (b) The side 1 of specimen; (c) The side 2 of specimen 80

3.17 Measurements of SMF2 and Gauge2 in fatigue experiment (at around 54,000 cycles): (a) The measurement of SMF2; (b) The measurement of Gauge2 81

3.18 Data interpolation of single mode fibre and strain gauge measurements: (a) The interpolation result of SMF2; (b) The interpolation result of Gauge2 81

3.19 Strain-load coefficient and Gauge2 measurements in fatigue experiment: (a) The strain-load coefficient of Gauge2; (b) The strain measurement of Gauge2 82

3.20 Strain-frequency shift coefficient and calculated strain of SMF2 in fatigue experiment: (a) The Strain-frequency shift coefficient of SMF2; (The alculated strain of SMF2) 83

3.21 Null values in measurements of SMF2 in fatigue experiment: (a) The Null values in measurements of SMF2; (b) The proportion of null value with increase of fatigue cycle 83

3.22 An illustrative example of obtaining strain-frequency shift coefficients from a tensile experiment using distributed fiber optic sensing 86

3.23 The plot of strain-frequency shift coefficients under different temperatures in tensile experiment 87

3.24 The plot of strain-frequency shift coefficients under different fatigue cycles . . . 88

3.25 The plot of strain-frequency shift coefficients in three-point bending experiment 88

3.26 The K-S test results for the different test scenarios in both strain and temperature measurement: (a) The The K-S test results for strain measurement experiments; (b) The The K-S test results for temperature measurement experiments 89

3.27 The plot of temperature-frequency shift coefficients obtained from the experiments in the first group 92

3.28 The plot of temperature-frequency shift coefficients obtained from the experiments in the second group 93

3.29 The plot of temperature-frequency shift coefficients obtained from the experiments in the third group 94

3.30 The type A evaluation of standard uncertainty of all test scenarios mentioned in Section 3.5.1 and Section 3.5.2 95

4.1 The layout of fibre optical sensors: (a) The installation of fiber optic sensor; (b) The design of the layout 103

4.2 The experiment setup: (a) The specimen fixed by clamps; (b) The setup of tensile experiment 103

4.3 The raw data of fibre optical sensor: (a) The raw data before filtering; (b) The raw data after filtering 104

4.4 The strain measurements and spatial mapping. 105

4.5 Interpolation results of resampling data $f(\widetilde{s}_j^1)$ and $f(\widetilde{s}_j^5)$ (Refer Table 4.1): (a) The interpolation results of $f(\widetilde{s}_j^1)$; (b) The interpolation results of $f(\widetilde{s}_j^5)$ 110

4.6 The strain reconstruction results: (a) The true strain distribution; (b) The strain reconstruction result under $f(\widetilde{s}_j^1)$; (c) The strain reconstruction result under $f(\widetilde{s}_j^5)$112

4.7 The diagram of the proposed methodologies 114

4.8 Strain data filtering and reconstruction of distributed sensing: (a) the 1D strain measurements along the SMF; (b) the corresponding reconstructed 2D strain distribution along 1D SMF on a CFRP panel 116

4.9 Delaunay triangulation and similarity assessment: (a) The Delaunay triangulation of a neighbourhood strain set; (b) Similarity assessment of convex hulls based on Hausdorff distance and area difference 118

4.10 Damage detection schemes based on LPA coefficients: (a) Calculation of LPA coefficients based on 1D strain measurements along the SMF sensor; (b) Calculation of LPA coefficients based on 2D strain distribution of 1D SMF on CFRP panel 121

4.11 The layout of SMF sensor on the CFRP specimens 124

4.12 The low-velocity impact experiment: (a) The experiment setup; (b) The impact energy of three specimens 125

4.13 Different types of impact damage induced in CFRP specimens: (a) Damage state of three specimens after low-velocity impact experiment; (b) BVID in Specimen 2 observed by c-scan 126

4.14 The static tensile experiment: (a) The experiment setup; (b) The load response of Specimen 2 in Test 3-1 127

4.15 The LPA coefficients near Point 1,2 and 3 based on 1D strain measurements along the SMF sensor: (a) Results of Test 3-1 (reference strain: Test 1-1 under 41.7MPa); (b) Results of Test 3-1 (reference strain: Test 3-1 under 41.7MPa); (c) Results of Test 4-1 (reference strain: Test 2-1 under 10.4MPa);(d) Results of Test 4-1 (reference strain: Test 4-1 under 10.4MPa) 129

4.16 The damage index of all neighbourhood strain sets on 1D strain measurements along the SMF sensor: (a) Results of Test 3-1 (reference strain: Test 1-1 under 41.7MPa); (b) Results of Test 3-1 (reference strain: Test 3-1 under 41.7MPa); (c) Results of Test 4-1 (reference strain: Test 2-1 under 10.4MPa);(d) Results of Test 4-1 (reference strain: Test 4-1 under 10.4MPa) 130

4.17 The damage detection results based on 2D strain distribution of 1D SMF on CFRP specimens: (a) LPA coefficient of Test 3-1 (reference strain: Test 3-1 under 41.7MPa); (b) LPA coefficient of Test 4-1 (reference strain: Test 4-1 under 10.4MPa); (c) Damage index distribution of Test 3-1 (reference strain: Test 3-1 under 41.7MPa); (d) Damage index distribution of Test 4-1 (reference strain: Test 4-1 under 10.4MPa); 132

5.1 An overview of inverse Finite Element Method 140

5.2 The design and installation scheme of sensor network: Step1: basic sensing blocks design; Step2: discretization of basic sensing blocks; Step3: sensor network design; Step4: installation of sensor network 146

5.3 The schematic diagram of most prevalent and well-established SISR algorithms . 150

5.4 The experimental setup and sensor network: Specimen I (Top-left); Specimen II (Bottom-left); Specimen III (Right) 155

5.5 The iQS4 mesh of specimens 157

5.6 The shape sensing results of specimen I and specimen II: (a) The shape sensing results of specimen I; (b) The shape sensing results of specimen II 158

5.7 The deflection and deflection difference of specimen III observed by camera: (a) The deflection data obtained by camera; (b) The deflection difference of two longest edge during the compression obtained by camera 159

5.8 The shape sensing results of specimen III: (a) The displacement field of specimen III; (b) A detailed comparison between the iFEM results and the camera observations under 0.5mm load; (c) A detailed comparison between the iFEM results and the camera observations under 1mm load; (d) A detailed comparison between the iFEM results and the camera observations under 2mm load 161

5.9 The mean error of strain extrapolation: (a) The mean error of the normal strain ε_x after extrapolation on surface 1; (b) The mean error of the normal strain ε_y after extrapolation on surface 1; (c) The mean error of the shear strain γ_{xy} after extrapolation on surface 1; (d) The mean error of the normal strain ε_x after extrapolation on surface 2; (e) The mean error of the normal strain ε_y after extrapolation on surface 2; (f) The mean error of the normal strain γ_{xy} after extrapolation on surface 2 163

5.10 The maximum error of strain extrapolation: (a) The maximum error of the normal strain ε_x after extrapolation on surface 1; (b) The maximum error of the normal strain ε_y after extrapolation on surface 1; (c) The maximum error of the shear strain γ_{xy} after extrapolation on surface 1; (d) The maximum error of the normal strain ε_x after extrapolation on surface 2; (e) The maximum error of the normal strain ε_y after extrapolation on surface 2; (f) The maximum error of the normal strain γ_{xy} after extrapolation on surface 2 164

5.11 The extrapolation of strain field with BVID: (a) extrapolation result by GP; (b) extrapolation result by RBF; (c) extrapolation result by BICUBIC; (d) extrapolation result by ANR; (e) extrapolation result by APLUSE; (f) extrapolation result by NE; (g) extrapolation result by RFI; (h) extrapolation result by SCSR; (i) extrapolation result by SRCNN 165

5.12 The shape sensing results of specimen III based on different strain extrapolation algorithms: (a) GP; (b) RBF; (c) BICUBIC; (d) ANR; (e) APLUSE; (f) NE; (g) RFI; (h) SCSR; (i) SRCNN 166

A.1 The coordinate system: (a) The isoparametric coordinate system; (b) The local coordinate system 179

A.2 The isoparametric coordinate system 191

List of Tables

2.1 The distributed fiber optic sensing based on various of techniques 23

2.2 The spatial resolution obtained by different post-processing algorithms 31

3.1 Temperature sensitivity of different coating materials at the free state 60

3.2 Temperature sensitivity of different coatings after surface mounting 62

3.3 Elastic parameters of the lamina used in this subsection 66

3.4 Parameters of thermoplastic adhesive film and SMF adopted in the experiment . 78

3.5 The experiment details in strain measurement 86

3.6 The consistency assessment results of the strain-frequency shift coefficients . . . 90

3.7 The experiment details in temperature measurement 91

3.8 The consistency assessment results of the temperature-frequency shift coefficients 93

4.1 Different sensor densities 106

4.2 The results of interpolation errors in strain distribution reconstruction 111

4.3 Test scenarios in the static tensile experiment 128

5.1 The specifications of specimens adopted in this study 153

5.2 The load and basic sensing block types used for these specimens investigated in this study 154

Chapter 1

Introduction

1.1 Motivation

There is an increased interest in evaluating the health and integrity of aircraft structures continuously, largely driven by the extensive use of advanced composite materials including carbon fiber reinforced Polymer (CFRP), Glass fiber reinforced Polymer (GFRP), Quartz fiber reinforced Polymer (QFRP), and Glass reinforced aluminum laminate (GLARE) in aircraft design. For instance, the A380 incorporates composite materials in critical components such as the center wing box, wing ribs, and rear fuselage section, as depicted in Figure 1.1. The increasing adoption of composites is justified by their advantages, including their lightweight nature, superior strength, and cost-effectiveness.

However, the integration of these composite materials presents new challenges concerning durability and damage, surpassing those encountered with traditional aluminum alloys. The anisotropic properties and intricate composition of composites contribute to a heightened complexity, leading to a multitude of unpredictable damage issues. The challenges arising from this complexity encompass various aspects, including:

- **Delamination:** Delamination refers to the separation of layers within a composite material due to the varying strengths and adhesion between layers [2]. The anisotropic

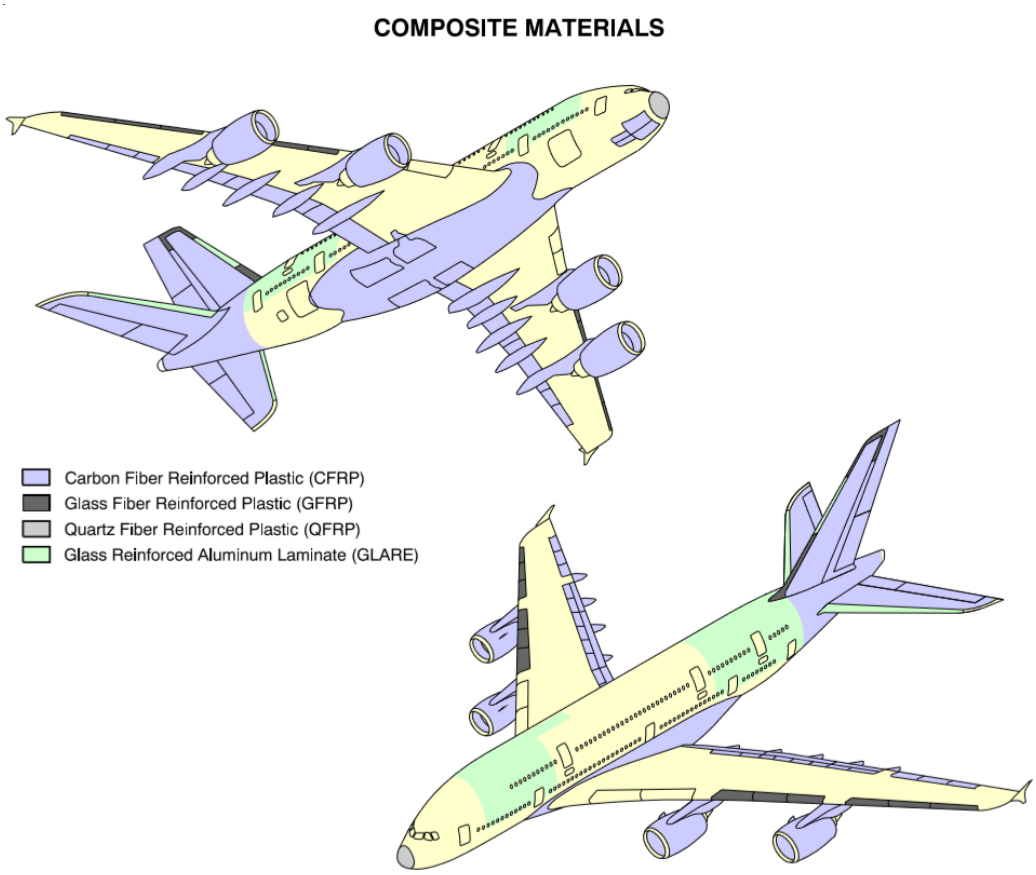


Figure 1.1: Distribution of composite materials in A380 [1]

nature of composites can result in different mechanical properties along different directions, making it challenging to predict the initiation and propagation of delamination, especially under varying loads and environmental conditions.

- **Impact damage:** When a composite material experiences an impact from foreign objects or during a collision, the anisotropic properties can cause the damage to spread in unexpected ways [3]. The intricate arrangement of fibers and matrix in composites influences the energy absorption and distribution, making the damage pattern less predictable compared to isotropic materials like metals.

- **Fatigue and crack propagation:** The anisotropic behavior of composites can lead to complex stress distributions during cyclic loading [4]. This complexity affects the initiation and propagation of cracks, making it difficult to anticipate the exact paths and rates of crack growth, especially when considering the interactions between multiple layers and interfaces.

- **Environmental degradation:** Composites can be sensitive to environmental conditions such as moisture, temperature, and chemical exposure [5]. The complex composition and anisotropic properties can create preferential pathways for environmental agents to penetrate the material, leading to unpredictable degradation and damage over time.

- **Manufacturing defects:** The complex manufacturing processes involved in creating composite materials can result in various defects such as voids, resin-rich or resin-poor areas, and fiber misalignment [6]. These defects can significantly influence the material's mechanical properties, making it challenging to predict how they will behave under different loading conditions.

- **Composite repair:** When composites sustain damage, repairing them can be more complex than repairing isotropic materials [7]. The anisotropic properties require careful consideration of fiber orientation, layer stacking sequence, and bonding techniques to restore the original structural integrity effectively.

As a result, the aerospace industry places significant emphasis on detecting and monitoring the health and integrity of composite structures. Currently, one of the most widely adopted solutions is offline maintenance, which relies on various non-destructive testing (NDT) methods to realize periodic inspections and repairs based on scheduled maintenance intervals. The commonly utilized NDT methods include visual inspection, thermography [8], and CT Scanning [9]. Additionally, shearography [10], an optical inspection technique measuring surface displacements caused by internal defects, and electromagnetic testing [11], such as eddy current and microwave testing, are also employed.

Despite the effectiveness of these methods for identifying damage, they lack the capability of real-time health and integrity monitoring of composite structures. To address this limitation, structural health monitoring (SHM) has emerged as a promising technique for achieving real-time assessment [12, 13]. SHM is a process that involves the continuous or periodic monitoring of structures to assess their health and integrity. It aims to detect and evaluate any damage, defects, or changes in the structure's condition over time, providing valuable information for

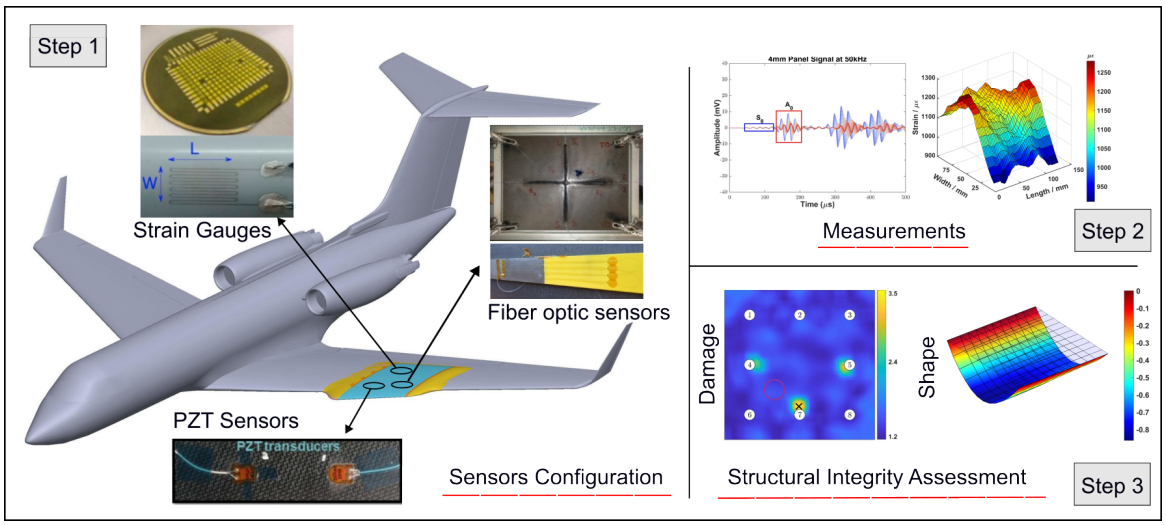


Figure 1.2: The implementation of structural health monitoring [14, 15]

maintenance and ensuring the safety and reliability of the structure. As shown in Figure 1.2, the implementation of SHM is roughly divided into three steps. The first step involves strategically installing various sensors on a structure to continuously or periodically collect data. The second step is the acquisition and pre-processing of data related to strain, vibration, temperature, and other parameters. This pre-processing mainly including data filtering, reconstruction, and storage. The collected data is then processed and analyzed in the third step using specialized algorithms to detect and evaluate any damage or anomalies within the structure. This real-time monitoring approach enables early detection of structural issues, supports informed decision-making, and facilitates timely maintenance or repairs, ensuring higher safety standards and optimizing the structural performance of critical infrastructure across various industries.

Therefore, the key advantages of SHM compared to traditional offline maintenance strategy are list as follows:

- **Early Detection of Damage:** SHM allows for the early detection of structural damage or anomalies that may not be readily visible during visual inspections. This enables timely intervention and prevents the development of serious issues that could compromise the structure's integrity.

- **Real-Time Monitoring:** SHM employs various sensors to continuously monitor the structure, providing real-time data on its condition. This real-time monitoring allows for

rapid response to any changes or damage, facilitating quick decision-making for necessary repairs or maintenance.

- **Improved Structural Performance:** By continually monitoring the structure's health, SHM helps to optimize its performance and operational lifespan. It allows for better understanding of how the structure responds to various loads and environmental conditions, which can lead to more efficient designs and improved maintenance strategies.

- **Cost-Effectiveness:** SHM can potentially lead to cost savings by reducing the need for frequent manual inspections and enabling targeted maintenance efforts. It allows maintenance activities to be performed when needed, rather than relying solely on predefined maintenance schedules.

- **Safety Assurance:** Ensuring the structural health and integrity of critical infrastructure, such as wing box, wing ribs, and fuselage section, is essential for aircraft safety. SHM provides a proactive approach to monitor these structures, reducing the risk of catastrophic failures and accidents.

Numerous studies have been conducted to develop SHM systems using various types of sensors. For instance, piezoelectric (PZT) sensors [16], fiber optic sensors (FOS) [17], acoustic emission (AE) sensors [18], strain gauges [19], temperature sensors [20], accelerometers [21], electromagnetic sensors [22], and smart multi-functional printed sensors [23]. Moreover, research on hybrid SHM systems combining different sensor types has been explored to achieve higher performance [24]. Among the mentioned sensors, fiber optical sensors hold significant importance due to their advantageous attributes such as low weight, affordability, widespread accessibility, immunity to corrosion, and resistance to electromagnetic interference. These sensors are categorized into three types based on their operating principles as shown in Figure 1.3: (1) Interferometric sensors (Mach-Zehnder sensor or Fabry-Perot sensor) [25]; (2) Grating-based sensors (fiber Bragg grating) [26]; (3) Distributed sensors [27]. While all three sensors passively measure strain or temperature, the interferometric and grating-based sensors can only detect limited points, leading to additional weight, cables, and costs in SHM systems for large structures, which is a common scenario in real-world applications. Therefore, distributed fiber optic

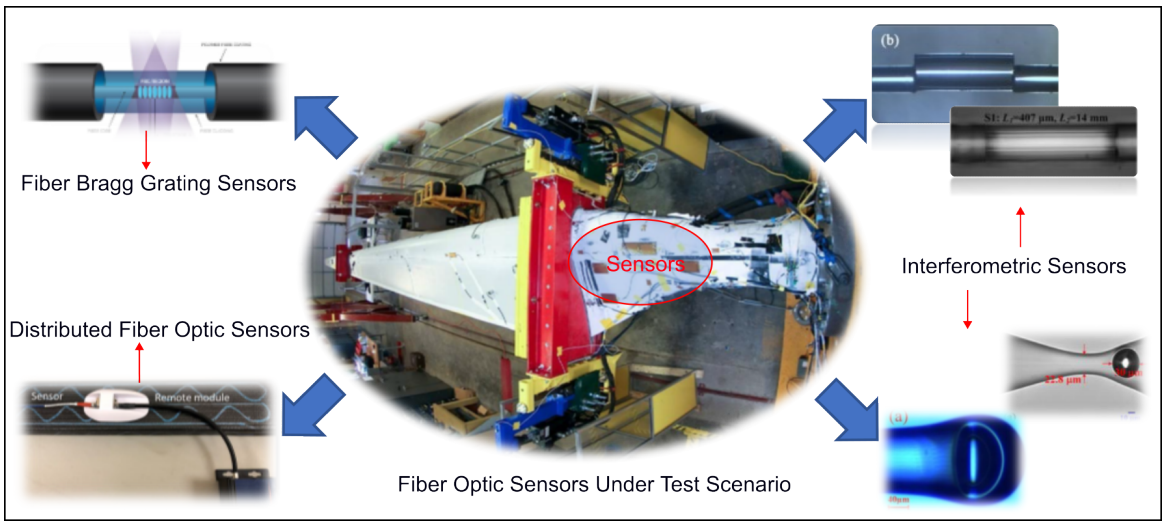


Figure 1.3: The structural health monitoring system based on three types of fiber optic sensors

sensing plays a crucial role in aircraft SHM due to its numerous advantages, such as high spatial resolution, wide measurement range, and continuous sensing capabilities along the entire length of the fiber.

The distributed fiber optic sensors can provide real-time monitoring of structural behavior and potential damage detection without the need for multiple individual sensors. This capability not only reduces the weight and complexity of the SHM system but also enhances its overall reliability and performance. Moreover, the distributed nature allows for comprehensive coverage of large aircraft structures, providing valuable data for structural health assessment and ensuring enhanced safety standards in the aerospace industry. However, despite its advantages, challenges persist in the implementation of SHM based on distributed FOS. These challenges can be summarized as follows:

- **Measurement sensitivity enhancement:** Improving the sensitivity of distributed FOS is crucial to detect smaller changes in strain or temperature accurately. Increasing sensitivity enables the detection of early-stage damage or degradation, enhancing the overall reliability of the SHM system.

- **Measurement accuracy assessment in complex environments:** Several researchers have validated the FOS for strain measurement under quasi-static loading [28, 29, 30]. However, the operational conditions of aircraft results in low frequency vibration in-service

which the SMF sensors will also be exposed to. Therefore, the accuracy of distributed strain sensing under fatigue load needs to be demonstrated. Understanding and quantifying the impact of these environmental conditions on measurement accuracy is essential to ensure precise and reliable data.

- **Measurement Consistency Assessment:** The consistency analysis of distributed FOS measurements in diverse scenarios, encompassing different structures, measurement times, and loading conditions, has received limited research attention. This can be attributed to various reasons, including the need for specialized equipment and expertise, the complexity and cost involved, limited awareness and prioritization of this aspect, and challenges related to data availability and sharing. Consequently, ensuring measurement consistency across various measurement scenarios remains a challenge for distributed FOS. It is imperative to analyze and minimize difference in measurements to guarantee uniform and reliable data, thus facilitating comprehensive SHM practices. Addressing this issue can lead to more effective and accurate SHM outcomes for critical structures.

- **Damage Detection:** Current damage detection methods that rely on fiber optic sensor strain measurements have several limitations, notably their vulnerability to environmental fluctuations and their reduced accuracy when subjected to complex loads and strain conditions. While distributed FOS offer continuous monitoring, detecting, and localizing damage accurately in complex structures remains challenging. Developing advanced algorithms and signal processing techniques to distinguish damage signatures from normal operational variations is crucial for effective damage detection.

- **Shape Sensing:** Accumulation of concealed failures has the potential to progressively reduce the lifespan of structures, leading to both economic losses and catastrophic failure of the entire structure. Consequently, it is crucial to proactively mitigate such failures and acquire precise real-time information regarding the structural safety. To attain this objective, a SHM system with the capability for three-dimensional full-field displacement, strain, and stress monitoring becomes essential [31]. Expanding the capabilities of distributed FOS to enable shape sensing of structures represents an ongoing challenge. It

contains several aspects including development of efficient and accurate shape sensing algorithms, design of standardized sensor network, and development of efficient strain extrapolation algorithms. The shape sensing would allow for monitoring and tracking structural deformations and movements, which is beneficial for ensuring optimal performance and safety.

1.2 Objectives

Considering the aforementioned challenges, this PhD project aims to address the following main tasks and research objectives, along with the proposed solutions:

- **Task 1: Measurement Sensitivity Enhancement of Single-Mode Fiber (SMF) in Distributed Sensing.** Enhancing the measurement sensitivity of SMF is crucial for achieving higher accuracy in strain and temperature measurements, especially for SHM of composites. This objective will be achieved through in-depth research on sensor configurations, including coatings and pre-loading. For instance, exploring coatings with varying thermal expansion coefficients can effectively modify the temperature measurement sensitivity of SMF.

- **Task 2: Strain Measurement Calibration.** This task involves the calibration of strain measurements for distributed sensing, with a specific focus on ensuring accuracy under challenging conditions, including temperature variations and low-frequency fatigue encountered in real-world applications. To achieve this objective, two experiments are conducted. The first experiment investigates strain measurement accuracy under varying ambient temperatures and mechanical loads, simulating thermal and mechanical stress conditions. The second experiment examines strain measurement accuracy under low-frequency fatigue, replicating real-world dynamic scenarios. Through these experiments, valuable insights are gained to ensure the reliability and precision of the distributed strain sensing system, making it suitable for practical applications in various industries where real-time and accurate strain measurements are crucial for structural health monitoring.

- **Task 3: Measurement Consistency of Distributed Fiber Optic Sensing.** This task aims to investigate the measurement consistency of distributed fiber optic sensing under various test scenarios, encompassing temperature and strain measurements across different time and space domains. It involves conducting fifty-six independent experiments, categorized into six groups, which include tensile, fatigue, three-point bending, and three sets of temperature experiments. The normality of strain-frequency shift coefficient and temperature-frequency shift coefficient of distributed fiber optic sensing, based on OFDR, are assessed through the Kolmogorov-Smirnov test. Additionally, the consistency of these coefficients is evaluated using statistical measures such as Cronbach's alpha, McDonald's omega, and Split-half reliability, all based on the confirmed normal distribution conclusion. Finally, the standard uncertainty (type A) of frequency shift measurements across the fifty-six independent test scenarios is calculated to affirm the robustness and reliability of distributed fiber optic sensing for accurate strain and temperature data acquisition in composite structures.

- **Task 4: Damage Detection of Composite Structures.** This task focuses on damage detection in composite structures using the OFDR technique, which enables real-time recording of detailed strain distribution on CFRP structures. The proposed approach presents a novel insight for damage detection based on local strain feature matching. Distributed in-plane strain measurements are utilized for plate structures under load, representing in-service applications. To achieve damage detection, a local point autocorrelation coefficient is defined based on Delaunay triangulation and Hausdorff distance. This coefficient effectively identifies discontinuities in distributed in-plate strain, allowing for accurate capturing of damage information. The damage index, defined as the integral of this coefficient, provides a robust measure for detecting damage, including Barely Visible Impact Damage (BVID) and Visible Impact Damage (VID). The efficacy of the proposed approach has been demonstrated through theoretical analysis and experimental investigations, showcasing its excellent detection results for various types of damage in composite structures. This research offers valuable insights and serves as a reference for future studies in the domain of damage detection, contributing to enhanced safety and

maintenance practices in composite structures.

- **Task 5: Shape Sensing of Composite Shell Structures.** In this task, a novel and accurate scheme is proposed for shape sensing of composite shell structures. The scheme utilizes the inverse finite element method (iFEM) with drilling degrees of freedom for shape sensing. It includes two main components: strain acquisition based on distributed fiber optic sensors and strain extrapolation using a single image super-resolution (SISR) technique. The strain acquisition process involves designing a basic sensing block capable of acquiring both normal and shear strain, implemented using fiber optic sensors. Validation of the proposed strain acquisition method is performed on three CFRP specimens with different dimensions, materials, and layouts to assess its generality and robustness under various loads. Subsequently, based on the acquired strain field, the SISR-based strain extrapolation method is proposed to obtain a displacement field with significantly higher spatial resolution using iFEM. Successful implementation of this innovative scheme will advance the field of shape sensing for composite shell structures, offering valuable insights for optimizing their design, performance, and safety in diverse engineering applications.

1.3 Thesis outline

The structure of this thesis can be summarized as follows:

- **Chapter 1:** The introduction to this chapter delves into the motivation behind this PhD research, which includes discussing the challenges surrounding the widespread use of composite materials, the benefits of SHM over traditional methods, and the obstacles in implementing SHM based on distributed fiber optic sensors. Subsequently, the research tasks and objectives of this PhD study are outlined to address the aforementioned challenges. Five tasks are proposed to tackle these issues. The remainder of this chapter provides an outline of the thesis and highlights the publications achieved during the course of the PhD study.

- **Chapter 2:** This chapter provides a comprehensive introduction to the background of distributed fiber optic sensing, with a specific focus on Rayleigh-based techniques. It introduces the principles of distributed fiber optic sensing (DFOS), including Raman, Brillouin, and Rayleigh backscattering. The significance of Rayleigh-based sensing for aircraft SHM is underscored, highlighting its principle to capture strain and temperature information. Based on this, challenges in employing the Optical Frequency-Domain Reflectometry (OFDR) technique for SHM are discussed. This chapter explores spatial resolution enhancement, algorithmic efficiency improvement, continuous vibration measurement, shape sensing, and embedding FOS in composite materials by a thorough literature review.

- **Chapter 3:**This chapter provides a comprehensive exploration of distributed fiber optic sensing, covering various critical aspects. It begins with an introduction to the significance and application of distributed fiber optic sensing, outlining challenges and objectives for subsequent sections. The discussion then delves into sensitivity enhancement techniques for distributed fiber optic sensors, including re-coating and twist pre-stress, which elevate sensor sensitivity to capture finer parameter changes. Investigation on the accuracy of distributed strain sensing in composite laminates under thermal loads is then conducted. This section addresses challenges from varying temperatures and emphasizes the need for extreme thermal load calibration to ensure precise strain measurements. In addition, this chapter further explores the accuracy of distributed strain sensing in composite laminates under fatigue loads, analyzing the impact of mechanical fatigues on strain measurements and their influence on data reliability and accuracy. Finally, this chapter examines strain measurement consistency within distributed fiber optic sensing, evaluating the sensors' reliability across diverse testing scenarios.

- **Chapter 4:** This chapter delves into two distinct techniques that harness the potential of distributed fiber optic sensing for damage detection of composite structures. The summary below encapsulates the critical aspects explored within each technique. The first technique, "2D Strain Field Reconstruction of Composite Plates Based on Distributed Fiber Optic Sensors," concentrates on meticulously reconstructing the strain

field on composite plates using distributed fiber optic sensors. This section aims to realize strain reconstruction under varying sensor densities, utilizing barycentric Lagrange and cubic spline interpolation methods. The implications of this study extend to optimizing strain measurement precision while minimizing the weight and cost of sensor network. The second technique, "A Novel Damage Detection Method for CFRP Structures Based on Distributed Strain Measurements with Fiber Optic Sensors," introduces a pioneering methodology that employs distributed strain measurements for damage detection in CFRP structures. Grounded in feature matching of local neighborhoods among distributed strain measurements, this approach addresses the complexities of damage detection under operational conditions. It capitalizes on correlations between local measurement points to differentiate between damaged and undamaged segments, offering potential solutions for challenges in damage detection in CFRP structures, including differentiating BVID and VID.

- **Chapter 5:** This chapter introduces a novel and precise approach for achieving highly accurate shape sensing of CFRP structures using the iFEM technique. The accuracy of shape sensing in practical applications is notably influenced by strain field precision, which is primarily governed by spatial measurement resolution and sensor distribution. This chapter proposes a strain acquisition method based on basic sensing blocks, utilizing distributed fiber optic sensors, resulting in a robust sensor network that enables high-accuracy shape sensing with minimal measurement data required for iFEM. The efficacy and general applicability of the proposed scheme are demonstrated through experiments on diverse CFRP samples, showcasing its feasibility, robustness, and high-precision shape sensing capabilities, even under complex loads caused by defects. In addition, to achieve a detailed displacement field distribution, the chapter introduces the SISR-based strain extrapolation technique, overcoming limitations of traditional methods. This technique is validated against multiple algorithms, highlighting its superiority in non-smooth strain fields. By integrating the proposed strain acquisition method with the SISR-based strain extension technique, this chapter outlines the potential for achieving high-fidelity shape sensing of CFRP shell structures.

- **Chapter 6:** This chapter presents a comprehensive summary of the conclusions and contributions derived from this PhD research. Furthermore, it delves into the potential avenues for future work that can be built upon the foundation laid by this study.
- **Appendix A:** This chapter includes two appendices. The first appendix corresponds to Chapter 5, while the second appendix provides a comprehensive derivation of the inverse finite element method.

1.4 Publications

1. Li, Yingwu, and Zahra Sharif-Khodaei. "Accuracy of Distributed Strain Sensing with Single-Mode Fibre in Composite Laminates under Thermal and Vibration Loads." Structural Control and Health Monitoring 2023 (2023).

2. Li, Yingwu, and Zahra Sharif-Khodaei. "A novel damage detection method for carbon fibre reinforced polymer structures based on distributed strain measurements with fibre optical sensor" Under Major revision in **Mechanical Systems and Signal Processing**

3. Li, Yingwu, and Zahra Sharif-Khodaei."The shape sensing of composite shell structures using distributed fibre optic sensing" Under review in **International Journal of Mechanical Sciences**

4. Li, Yingwu, and Zahra Sharif Khodaei. "2D strain field reconstruction of composite plates based on distributed fibre optic sensors." AIP Conference Proceedings. Vol. 2848. No. 1. AIP Publishing, 2023.

5. Li, Yingwu, and Zahra Sharif Khodaei. "The Sensitivity Enhancement of Distributed Fiber Optical Sensors." European Workshop on Structural Health Monitoring. Cham: Springer International Publishing, 2022.

6. Li, Yingwu, and Zahra Sharif-Khodaei. "Strain measurement consistency of distributed fiber optic sensors for monitoring composite structures under various loading" Published in "International Conference on Fracture, Damage and Structural Health Monitoring 2023"

Chapter 2

Background: a review of optical frequency domain reflectometry technique

2.1 Distributed fiber optic sensing

DFOS is an innovative and powerful technology that revolutionizes the way structural monitoring and measurements are conducted. Unlike traditional sensors (such as fiber Bragg gratings, strain gauges, and interferometric optic sensors) that provide point measurements, DFOS offers continuous and real-time monitoring along the entire length of an optical fiber, enabling a comprehensive understanding of the structural behavior and environmental conditions. This technology harnesses the principles of light propagation through optical fibers, taking advantage of the changes in light intensity or wavelength caused by external loads such as strain, temperature, pressure, and acoustic waves.

DFOS has found numerous applications across various industries, including civil engineering [32], oil and gas [33], telecommunication [34], medicine [35], chemistry [36] and nuclear physics [37]. In civil engineering, DFOS is used to monitor bridges, tunnels, dams, and pipelines, providing critical data on structural integrity and potential risks. In the oil and gas industry, it

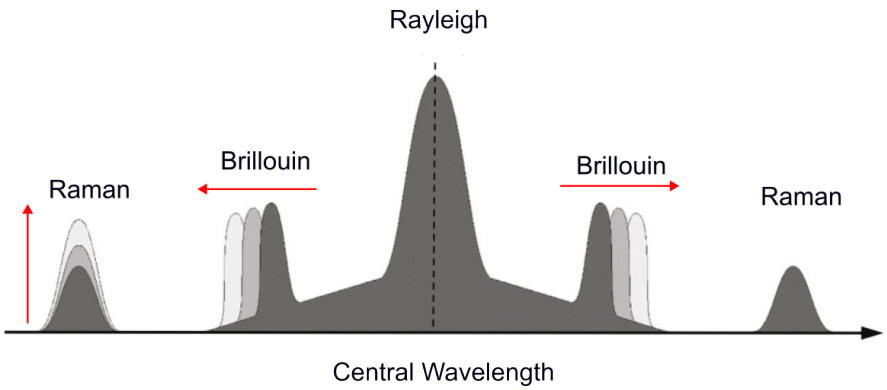


Figure 2.1: Three types of intrinsic backscattering in distributed fiber optic sensing [39]

aids in the monitoring of reservoir performance and pipeline integrity. The aerospace sector benefits from DFOS by ensuring the safety and performance of aircraft structures [27], while geotechnical engineering relies on its capabilities for monitoring soil and rock behavior [38]. As shown in Figure 2.1, distributed optical sensors commonly detect three types of intrinsic backscattering: Brillouin, Raman, and Rayleigh backscattering. Given that Brillouin and Raman backscattering involve inelastic scattering, both the central wavelength and amplitude of backscattering will be nonlinearly influenced by temperature and stress, as depicted by the red arrow in Figure 2.1.

Raman backscattering is a remarkable phenomenon in the realm of optical fiber sensing, presenting a powerful and versatile approach for distributed fiber optic sensing. Named after the Indian physicist Sir C. V. Raman, who discovered the Raman effect in 1928 [40]. This effect occurs when light interacts with the vibrational modes of molecules in an optical fiber, leading to a change in the wavelength of the backscattered light. This unique characteristic enables the measurement of temperature and strain variations along the entire length of the fiber. The fundamental principle behind Raman backscattering lies in the interaction between photons of incident light and the vibrational modes of atoms or molecules in the fiber material. When light traverses the fiber, a small fraction of the photons undergo inelastic scattering, resulting in either a shift to higher or lower energy levels. This shift in energy corresponds to a change in the wavelength of the scattered light, known as the Raman shift. The magnitude of this shift is directly related to the temperature and strain experienced by the fiber. In this type of backscattering, photons are scattered due to the vibrational and rotational transitions in the

bonds between neighboring atoms of the transmitting medium. This phenomenon enables the determination of the chemical composition and molecular structure of the medium in which it occurs.

Brillouin backscattering, named after the distinguished physicist Léon Brillouin [41], occurs due to the interaction between light waves and material waves (e.g., electrostriction and magnetostriction) within a medium, such as a fiber optic sensor. When light waves propagate through an optical fiber, some of these photons interact with material waves present in the fiber material. This interaction gives rise to the generation of new frequencies, known as Brillouin frequencies, which are shifted from the original frequency of the incident light. The extent of this frequency shift is directly correlated with the temperature and strain experienced by the fiber. By analyzing the frequency shift of the backscattered light, precise measurements of temperature and strain distribution along the fiber can be accurately obtained. Unlike Raman backscattering mentioned above, Brillouin scattering is attributed to the scattering of photons by large-scale, low-frequency phonons. This unique property makes Brillouin backscattering particularly suitable for measuring the elastic behavior and material properties of the medium in which it occurs.

Rayleigh backscattering is a fundamental optical phenomenon that plays a crucial role in distributed fiber optic sensing. Named after the British scientist Lord Rayleigh, who first described the phenomenon in the late 19th century [42]. The principle of Rayleigh backscattering is based on the interaction between light waves and microscopic density fluctuations within an optical medium, such as an optical fiber. When a beam of light propagates through the fiber, it encounters various density variations caused by random thermal motion of atoms and molecules. These fluctuations lead to small changes in the refractive index of the medium, creating tiny scattering centers within the fiber. As the incident light interacts with these scattering centers, some of the photons are scattered in various directions. A small fraction of these scattered photons, known as Rayleigh backscattered photons, travel back along the original path of the incident light. These backscattered photons carry information about the local environment in the fiber, including changes in temperature and mechanical stress. The frequency of the backscattered light is influenced by the density fluctuations in the fiber, which in turn are af-

fected by the local temperature and strain conditions. When the fiber experiences temperature changes or mechanical stress, the density fluctuations and hence the refractive index variations in the fiber also change. As a result, the frequency of the backscattered light undergoes a slight shift, known as the Rayleigh frequency shift. Different from Rama and Brillouin backscattering, the Rayleigh backscattering is elastic with no energy is lost or gained, which means the spectral component of backscattering remains the same as the incident light (when there is no temperature or mechanical load).

In recent years, distributed fiber optic sensing based on Rayleigh, Raman, and Brillouin backscattering has generated significant attention and widespread adoption, particularly in the field of SHM. Among these techniques, Rayleigh-based distributed sensing stands out due to its high spatial resolution, suitable measurement range, and cost-effectiveness, making it the preferred choice for SHM of aircraft.

2.2 Rayleigh-based distributed sensing

Rayleigh-based distributed sensing includes two techniques: Optical Time Domain Reflectometry (OTDR) and OFDR. Figure 2.2 illustrates the OTDR technique, which is employed in optical fiber sensing to determine changes in the fiber's optical properties. The process involves generating a short pulse of light that is launched into one end of the fiber. As the light propagates along the fiber, a portion of it is backscattered due to various optical phenomena. The OTDR unit continuously monitors the backscattered light signal over time, generating an OTDR trace that indicates the distribution of backscattered light intensity along the fiber's length. By analyzing the trace, events such as splices, connectors, bends, and breaks within the fiber can be identified and located. OTDR has extensive applications in telecommunications and fiber optic networks for testing and troubleshooting purposes, as well as in SHM applications to detect changes in strain, temperature, or other physical parameters using optical fiber-based sensors.

However, due to the high speed of light, achieving high spatial resolution becomes challenging,

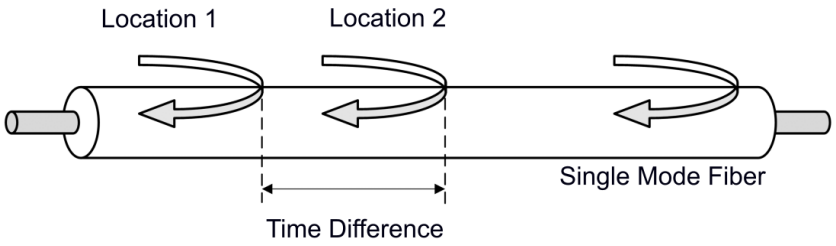


Figure 2.2: The basic sensing principle of OTDR technique

as it would require an impractically large sampling frequency, making it less suitable for aircraft applications. Fortunately, this limitation is easily overcome with the OFDR technique in the frequency domain. In OFDR, the frequency-swept light is split into two parts by optical couplers. One part illuminates the FOS, while the other acts as a local reference light, interfering with the Rayleigh backscattering light of the FOS. The resulting interference signal contains valuable strain or temperature information along the FOS, which is demodulated using Fourier transform and correlation calculations. This technique effectively addresses the sampling frequency limitation of OTDR, making it more suitable for SHM applications, particularly for aircraft structures.

Figure 2.3 illustrates the basic schematics of an OFDR system. The OFDR setup comprises of a Tunable Laser Source (TLS), Optical Coupler (OC), circulator, Photo Detector (PD), and the Fiber Under Test (FUT). The TLS emits light that is split into two beams by the OC. Both beams have the same spectral component but differ in amplitude. The beam with higher amplitude is directed towards the FUT, generating Rayleigh backscattering light. The other beam serves as a reference light. The Rayleigh backscattering light and the reference light interfere at another OC, creating a coherent field containing information along the entire FUT. This coherent field can be seen as the superposition of interferences between Rayleigh backscattering from different fiber segments and their corresponding reference light. Consequently, analyzing the interference of each fiber segment allows obtaining the coherent field, enabling the comprehensive assessment of the FUT's optical properties.

In Figure 2.3, the input light is denoted as $\widetilde{U}_{\text{in}}$, the reference light as $\widetilde{U}_{\text{out1}}$, the Rayleigh backscattering light as $\widetilde{U}_{\text{out2}}$, and the output light intensity as I_{out}, and they are represented by Equation 2.1 :

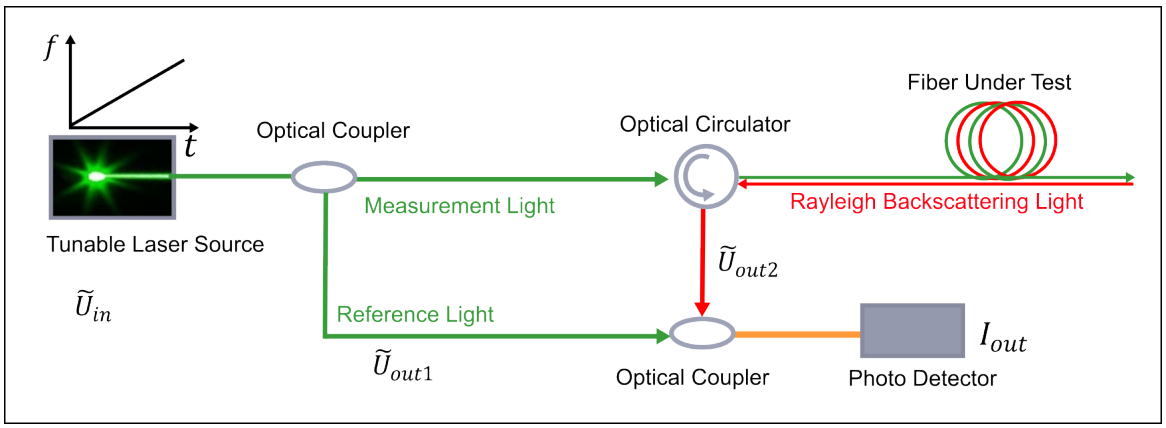


Figure 2.3: The schematic diagram of an OFDR system

$$\widetilde{U}_{\text{in}} = A_0 e^{i\omega(t)t} \tag{2.1a}$$

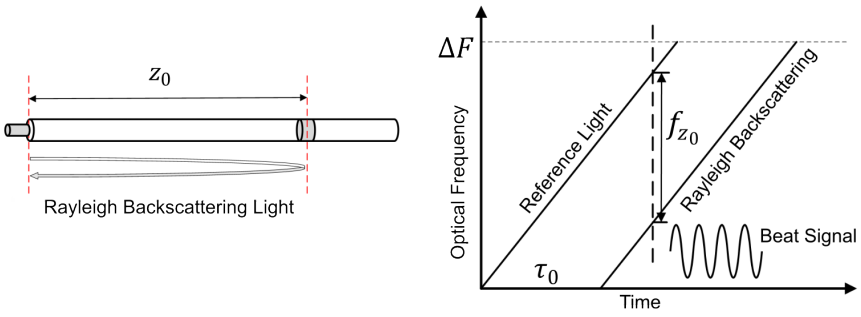
$$\widetilde{U}_{\text{out1}} = A_1 e^{i\omega(t+\tau_1)t} \tag{2.1b}$$

$$\widetilde{U}_{\text{out2}} = A_2 e^{i\omega(t+\tau_2)t} \tag{2.1c}$$

where A_0, A_1, and A_2 represent the amplitude of the input light, reference light, and Rayleigh backscattering light, respectively. $\omega(t)$, $\omega(t+\tau_1)$, and $\omega(t+\tau_2)$ correspond to the corresponding cycles of the input light, reference light, and Rayleigh backscattering light, respectively. The difference in τ_1 and τ_2 is due to the distinct optical paths of the reference light the and Rayleigh backscattering light. Therefore, the expressions of the output light detected by the photodetector after interference are expressed by Equation 2.2:

$$\widetilde{U}_{out} = A_1 e^{i\omega(t+\tau_1)t} + A_2 e^{i\omega(t+\tau_2)t} \tag{2.2}$$

Applying the Euler's formula, Equation 2.2 can be simplified to Equation 2.3:



(a) (b)

Figure 2.4: The basic principle of OFDR system

$$\tilde{U}_{out} = A_1\{\cos[\omega(t+\tau_1)t] + i\cdot\sin[\omega(t+\tau_1)t]\} + A_2\{\cos[\omega(t+\tau_2)t] + i\cdot\sin[\omega(t+\tau_2)t]\}$$

$$= \{A_1\cos[\omega(t+\tau_1)t] + A_2\cos[\omega(t+\tau_2)t]\} + i\cdot\{A_1\sin[\omega(t+\tau_1)t] + A_2\sin[\omega(t+\tau_2)t]\} \tag{2.3}$$

Therefore, the output light intensity is expressed by Equation 2.4:

$$\begin{aligned} \mathrm{I}_{out} &= \widetilde{U}_{out}\cdot\widetilde{U}^*_{out} \\ &= \{A_1\cos[\omega(t+\tau_1)t] + A_2\cos[\omega(t+\tau_2)t]\}^2 + \{A_1\sin[\omega(t+\tau_1)t] + A_2\sin[\omega(t+\tau_2)t]\}^2 \\ &= {A_1}^2 + {A_2}^2 + 2A_1A_2\cos\,\omega t(\tau_1-\tau_2) \end{aligned} \tag{2.4}$$

To illustrate the fundamental principle of the OFDR technique in detail, Figure 2.4 provides an example. In Figure 2.4(a), a fiber segment with a length of z_0 is considered, where a time delay (τ_0) exists between the Rayleigh backscattering light and its corresponding reference light, expressed by Equation 2.5:

$$\tau_0 = \frac{2z_0n_0}{c} \tag{2.5}$$

where n_0 is the refractivity at z_0 and c is the speed of light in vacuum. The light emitted by the TLS is linear in frequency, leading to the generation of a beat signal resulting from

the interference between the Rayleigh backscattering light and the reference light (as depicted in Figure 2.4(b)). The beat frequency, denoted as f_{z_0}, is expressed in Equation 2.6. In this equation, γ is the sweeping speed of the optical frequency.

$$f_{z_0} = \gamma\tau_0 = \frac{2z_0 n_0 \gamma}{c} \tag{2.6}$$

As per Equation 2.6, there is a proportionality between the location along the fiber and the beat frequency. Consequently, the location can be determined by analyzing the frequency components of the coherent field using the Fast Fourier Transform (FFT). However, due to the uncertainty principle [43], the frequency components of the coherent field undergo aliasing, affecting the achievable spatial resolution. The theoretical spatial resolution is determined by the minimum recognizable frequency interval:

$$\Delta z = \frac{c\Delta\tau}{2n} = \frac{c}{2n\Delta F} \tag{2.7}$$

where Δz is the spatial resolution; $\Delta\tau$ expresses the minimum time interval between two adjacent segments; ΔF is the optical frequency sweeping span of the TLS; n is the refractivity index.

As described earlier, the coherent field detected by photodetector is transformed into a frequency domain signal using FFT, representing the reflectivity pattern along the entire fiber. Subsequently, a rectangular window comprising of N points is applied to extract the sensing data from the frequency domain signal, corresponding to the reflectivity pattern on a specific segment. When this segment undergoes stress, the reflectivity pattern changes accordingly. The alterations in the reflectivity pattern are then determined through inverse fast Fourier transform (IFFT) to obtain the strain on that segment. Consequently, the actual spatial resolution in the OFDR system is calculated by Equation 2.8. Frequently, there exists a substantial disparity between the theoretical and measured spatial resolutions. As exemplified in [44], the theoretical spatial resolution is stated as 40 μm, yet the measured spatial resolution is only

4mm. Furthermore, while enhancing the spatial resolution of the measurement is possible by reducing the number of sampling points (N) used in the FFT, such an adjustment may also result in a reduction in the measurement's robustness.

$$\Delta z' = N\Delta z = \frac{Nc}{2n\Delta F} \tag{2.8}$$

In summary, Typical measurement parameters based on techniques are summarized in Table 2.1. According to this table, Raman-based distributed sensing is excellent in high-temperature measurements and provides higher sensitivity for temperature sensing but is generally associated with higher costs, making it particularly competitive in temperature sensing applications [45]. Meanwhile, Brillouin-based distributed sensing is well-suited for both temperature and strain measurements; however, it may have limitations in spatial resolution compared to Rayleigh-based distributed sensing, especially in applications like SHM of aircraft. Nonetheless, Brillouin-based distributed sensing finds extensive use in SHM of large structures like bridges, roads, and buildings within the civil engineering domain [46]. Each of these distributed sensing techniques offers distinct advantages, and the choice of technique depends on the specific requirements and objectives of the monitoring application.

For SHM of aircraft based on DFOS, numerous sensors with high spatial resolutions (at the millimeter level), a medium measuring range (e.g., several hundred meters), and a high sampling frequency (e.g., several hundred hertz) are essential. Considering the commercial equipment outlined in Table 2.1, Rayleigh-based distributed sensing emerges as the most promising technique for SHM of aircraft based on DFOS. However, challenges persist when adopting this technique for aircraft SHM. Consequently, a review of potential approaches to enhance the performance of OFDR in aircraft SHM is undertaken in the following subsection.

The SHM of aircrafts As shown in Table 2.1

Table 2.1: The distributed fiber optic sensing based on various of techniques

	Rayleigh	Raman	Brillouin
Typical system	OFDR	OTDR	OTDR
Sensing type	Strain/Temperature	Temperature	Strain/Temperature
Measurement range	70-100 m	20 km	10 km
Spatial resolution	5 mm	1-2 m	10 cm
Strain accuracy	$1\mu\varepsilon$	$1\mu\varepsilon$	$25\mu\varepsilon$
Suppliers	LUNA/4DSP	AP sensing/ Halliburton Co. Sensornet Ltd.	OZ Optics Omnisens SA/Neubrex

2.3 State of the art of the OFDR technique for aircraft structures

The Rayleigh backscattering based OFDR technique stands as one of the most widely adopted methods for interrogating distributed optical sensors. Its applications span across various research areas, including aeronautics [27, 47], civil engineering [32, 48, 49, 50, 38, 51, 52, 53, 54, 55], energy [56, 39, 57, 33, 58], telecommunication [34, 59], chemistry [60, 61, 62, 36, 63, 64], and nuclear engineering [65, 66, 67, 37]. Throughout these research endeavors, the advantages of OFDR have been extensively demonstrated. However, when applying this technique to SHM of aircraft, several challenges arise. Specifically, in the context of being adopted as a maintenance strategy, OFDR as a SHM technique needs to obtain a 90/95% reliability and probability of detection to meet the stringent requirements of aircraft maintenance [68].

- The first challenge lies in improving its spatial resolution. Higher spatial resolution is crucial for obtaining detailed temperature and strain distribution in SHM. However, limitations of TLS, such as the frequency sweeping span and nonlinearity, can reduce the spatial resolution of OFDR [69, 70]. Additionally, an intrinsic phase error induced by the interference between Rayleigh backscattering and reference light further degrades the spatial resolution [71].

- The second challenge is associated with the drawbacks of the FFT used in OFDR. The uncertainty principle of FFT makes it challenging to achieve both high spatial resolution

and high measurement accuracy simultaneously. Moreover, large-scale data processing using FFT adds computational complexity to the SHM system [44, 72].

- The third challenge pertains to continuous vibration measurement and shape sensing using OFDR. While OFDR can achieve high spatial resolution and measurement accuracy in static measurements, dynamic measurements encounter environmental noise and crosstalk from multiple perturbations [73, 74]. This phenomenon makes it difficult to implement high frequency distributed acoustic sensing (DAS).

- The final challenge is related to the application of FOS in composite materials. FOS can be embedded in the composite material or surface mounted. However, depending on the integration methodology, several factors need to be considered, such as temperature compensation [75], strain transfer rate [76], and the ability to measure large strains to obtain reliable results in composite structures [77].

Based on the challenges mentioned above, this section provides a comprehensive exploration of the Rayleigh backscattering based OFDR technique, specifically focusing on its applications for SHM of composite aircraft structures. The section is structured as follows:

- **Section 2.3.1:** covering techniques aimed at improving spatial resolution in OFDR systems. It discusses strategies such as extending the frequency sweeping span, compensating for frequency sweeping nonlinearity, and addressing the intrinsic phase noise.

- **Section 2.3.2:** an overview of research related to the limitations of the FFT and enhancements to algorithm efficiency is presented.

- **Section 2.3.3:** showcases existing endeavors related to continuous vibration measurement and shape sensing using OFDR.

- **Section 2.3.4:** Challenges associated with embedding FOS in composite materials are discussed. Topics covered include temperature compensation, addressing large strain, and mitigating non-uniform lateral strain. Viable solutions to these challenges are also presented.

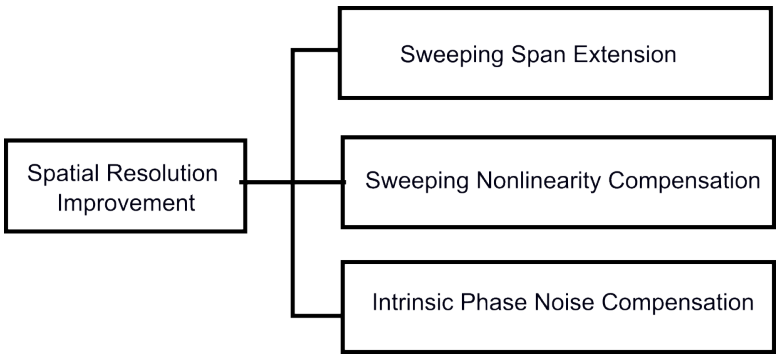


Figure 2.5: Three ways to improve the spatial resolution of an OFDR system

- **Section 2.3.5:** The section concludes by summarizing key findings and highlighting the ongoing challenges in reliably applying the Rayleigh backscattering based OFDR technique for SHM of aircraft structures.

2.3.1 Spatial resolution improvement

Achieving higher spatial resolution in the OFDR system is important for effective SHM in aircraft. As demonstrated by Equation 2.8, the spatial resolution is intrinsically linked to the frequency sweeping span of the TLS. Enhanced spatial resolution necessitates a wider frequency sweeping span, essentially translating to a higher sweeping speed. However, this higher speed introduces a larger beat frequency in the output, requiring data acquisition devices with high sampling rates. As illustrated in the literature [78], a spatial resolution of 0.97cm is attained within a measurement range of 710m. This spatial resolution corresponds to a frequency sweeping span of 10.31 GHz, implying that the sampling frequency should be at least 20 GHz in accordance with the Nyquist–Shannon sampling theorem. In addition to the frequency sweeping span, the spatial resolution is significantly influenced by the presence of frequency sweeping nonlinearity. This nonlinearity gives rise to errors during FFT computation due to the uniformity of time sampling. These errors translate to location inaccuracies, effectively compromising the overall spatial resolution. The intrinsic phase noise of TLS is another factor which deteriorates the spatial resolution drastically when a measurement range beyond the coherence length of TLS exists. Therefore, three ways to improve the spatial resolution of OFDR system are presented in Figure 2.5.

Frequency sweeping span extension

The external modulation technique stands as one of the most prevalent methodologies for extending the sweeping span of OFDR systems. In the work by [79], a significant advancement in sweeping span was achieved through the utilization of a recirculating frequency shifter (RFS) employing both 2nd-order single sideband (SSB) and 3rd-order SSB modulation. This innovative RFS exhibits great promise in optical frequency comb applications and OFDR systems, primarily due to its capacity for substantial carrier-to-carrier spacing. An application of this RFS within the OFDR framework was specifically elaborated upon in [78]. Through the application of this external modulation technique, an experimental demonstration in [78] showcased a spatial resolution of 0.97 cm across a measurement range of 710 m. In this study, a sweeping range of 882MHz was employed to achieve spatial resolution within a sweep range of 10.31GHz. In addition to SSB modulation, double sideband (DSB) modulation has also been employed to extend the frequency sweeping span, as demonstrated by [69] (Four Wave Mixing and DSB-SC Modulation). In this study, a double sideband with suppressed carrier (DSB-SC) modulation technique was combined with degenerated four wave mixing (FWM) within the OFDR system. According to the results in this study, a spatial resolution of 3.4cm was accomplished by employing a sweep range of 1GHz, representing a threefold expansion of the sweep range.

Both SSB modulation and DSB modulation offer effective means of extending frequency sweeping span. However, in conventional SSB modulation, a challenge arises from frequency overlap among adjacent high-order sidebands. This overlap complicates the extraction of these high-order sidebands using a band-pass filter (BPF). As a recent alternative [80], the injection-locking technique has been utilized to extract high-order sidebands. As the frequency sweeping span achievable through SSB modulation remains constrained, the utilization of the degenerated FWM process is further employed to expand the frequency sweeping span. In this research, a spatial resolution of 1mm was exhibited across a 2000m measurement range, equivalent to achieving a frequency sweep range of 100GHz.

As mentioned in the beginning of the subsection 2.3.1, the extension of frequency sweeping span requires high sampling rate. Numerous approaches have been devised and demonstrated

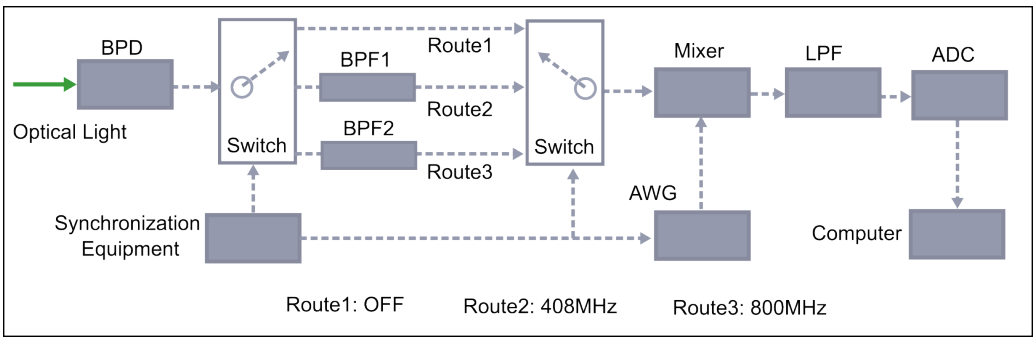


Figure 2.6: Schematic diagram of bandwidth-division technique based on multiple BPFs

to tackle the challenge of high sampling rates when extending the frequency sweeping span. A direct method to reduce sampling rate involves bandwidth-division. In 2011, a hardware-based bandwidth-division technique utilizing multiple BPF was introduced and validated [81]. The diagram in Figure 2.6 illustrates this approach which involves two electrical switches that route the signal based on synchronization equipment input. When Route 2 or Route 3 is chosen, the beat signal passes through either BPF1 or BPF2. This extraction process isolates the middle or high-frequency components. Subsequently, the extracted signal is down-converted to a lower frequency range through a mixer driven by an arbitrary waveform generator (AWG). Lastly, a low-pass filter is employed to extract the low-frequency component from either route 1, route 2, or route 3. The implementation of this technique yielded a spatial resolution of 5cm within a field trial measurement range of 39.2km.This is comparable to attaining a scanning bandwidth of 15GHz.

While the bandwidth-division technique mentioned above showcased improved performance, it tends to become expensive and less feasible when dealing with high beat frequencies. Consequently, an alternative bandwidth-division approach based on digitally enhanced interferometry has emerged [82, 83, 84]. This technique harnesses digitally enhanced interferometry [82] to segregate interferometric signals in the time domain, thereby reducing the need for high sampling rates. The digital signal processing approach based on digitally enhanced interferometry exhibits considerable promise in mitigating the need for high sampling rates within the OFDR system. Nevertheless, the incorporation of pseudorandom noise (PRN) modulation and demodulation procedures introduces substantial noise floor, which in turn limits the dynamic sensing range of the OFDR system. In 2015, a novel method known as time-gated digital optical

frequency domain reflectometry (TGD-OFDR) was introduced [85]. This innovative technique addresses the challenge of high sweeping speeds and the associated sampling rate problem while addressing the issue of a significant noise floor. More recently, another method centered around signal reconstruction has been successfully applied to the OFDR system, effectively reducing the requisite sampling rate [86].

Frequency sweeping nonlinearity compensation

The frequency sweeping signal of the TLS is typically generated using two methods [87]. One method is external modulation, wherein an external modulator is employed to drive the TLS and produce a linear frequency sweeping signal. However, this approach comes with limitations in terms of the achievable sweeping span due to the bandwidth constraints of the modulator. The other method is internal frequency sweeping, which relies on devices like Fabry-Perot or PZT to induce linear wavelength changes in the TLS, leading to linear frequency sweeping. In this case, the Fabry-Perot or PZT is controlled by voltage to modify the TLS wavelength through mechanical adjustments. However, due to the presence of mechanical components, achieving perfectly linear frequency sweeping in practical applications can be challenging. This inherent nonlinearity introduced by the TLS can result in errors during the interrogation of the OFDR system, as depicted in Figure 2.7(a). Beyond the frequency sweeping nonlinearity arising from mechanical components, the intrinsic phase noise of the TLS significantly compromises the linearity of frequency sweeping, particularly when the time delay of the Rayleigh backscattering light exceeds half of the coherent time of the TLS. The impact of errors introduced by the intrinsic phase noise of the TLS is illustrated in Figure 2.7(b).

In addressing the issue of frequency sweeping nonlinearity stemming from mechanical components within the TLS, two commonly employed methods are utilized for compensation: enhancing the laser source and employing an auxiliary interferometer. The auxiliary interferometer method is often preferred, wherein an auxiliary interferometer containing a constant delay fiber is leveraged to measure the sweeping nonlinearity of the laser source. A prevailing approach involves utilizing the output from the auxiliary interferometer as a clock signal to trigger the

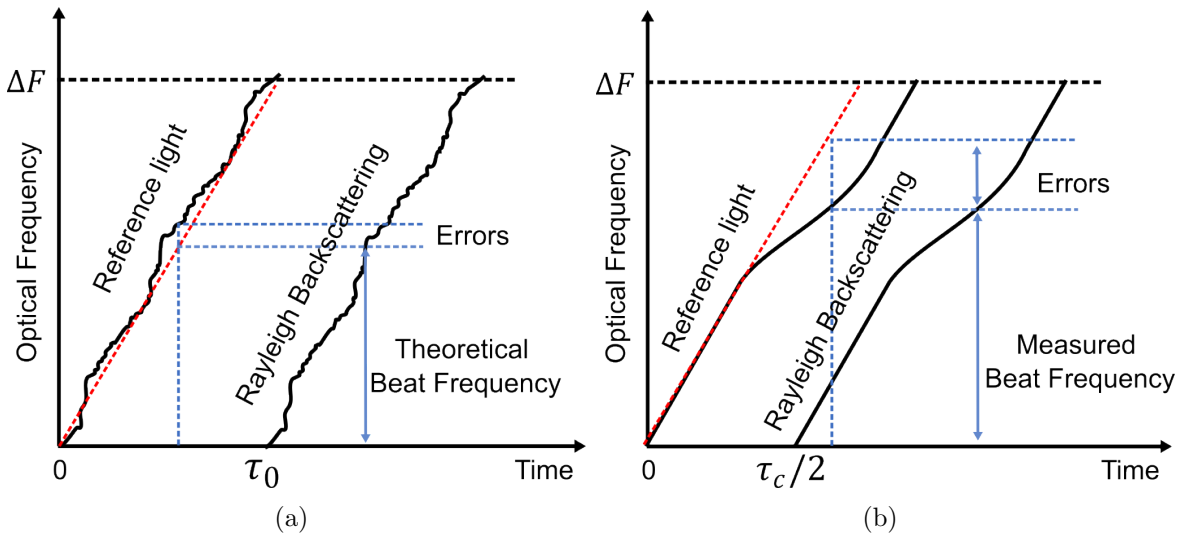


Figure 2.7: The errors induced by nonlinearity and phase noise of TLS: (a) The impact of errors introduced by the inherent nonlinearity introduced by the TLS; (b) The impact of errors introduced by the intrinsic phase noise of the TLS [88, 89]

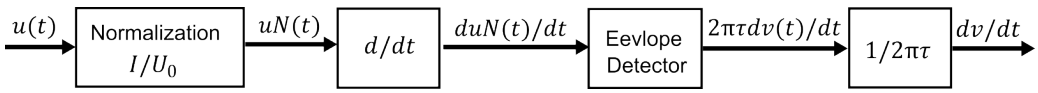


Figure 2.8: Signal processing steps to detect the optical frequency [91]

acquisition system [90, 70]. However, in practical scenarios, this signal may not consistently maintain accuracy. Therefore, the output of the auxiliary interferometer is frequently employed for calibrating sweeping nonlinearity during a subsequent post-processing phase, rather than serving as an acquisition system trigger.

In recent years, numerous post-processing algorithms have emerged. In the study by [91], an algorithm was proposed for gauging the frequency sweeping slope of lasers, outlined in Figure 2.8. Here, $u(t)$ symbolizes the alternating current (AC) component of the auxiliary interferometer output. Assuming the input of the auxiliary interferometer is denoted by $E(t) = E_0 \exp[j\phi(t)]$, where E_0 signifies the amplitude of the input optical field, and $\phi(t)$ represents the phase information of the input optical field. $\phi(t) = 2\pi \int_0^t v(u)du + \phi_0$, where $v(t)$ corresponds to the instantaneous optical frequency of the laser, and ϕ_0 indicates the initial phase of the input optical field. The expression describing the output of the auxiliary interferometer is presented by Equation 2.9.

$$I(t) = \eta|E(t) + E(t+\tau)|^2 = 2\eta|E_0|^2\{1 + \cos[\phi(t+\tau) - \phi(t)]\} \tag{2.9}$$

Where η is a coefficient that depends on the insertion loss of the couplers; τ is the delay time between the two arms of the auxiliary interferometer. When $\frac{\tau}{2v(t)}\frac{dv(t)}{dt} \ll 1$, according to Taylor expansion, the AC part of the auxiliary interferometer output is expressed by Equation 2.10.

$$u(t) = 2\eta|E_0|^2 \cos[2\pi\tau v(t)] \tag{2.10}$$

The frequency sweeping slope is acquired through the signal processing procedures illustrated in Figure 2.8. Subsequently, a resampling technique is applied to rectify the frequency sweeping nonlinearity within a measurement interferometer based on the determined frequency sweeping slope measurement outcome.

An alternative post-processing algorithm designed to counteract the frequency sweeping nonlinearity was introduced in [92], utilizing the non-uniform fast Fourier transform (NUFFT). NUFFT is known for its efficacy in non-uniform sampling applications [93, 94]. Unlike the standard FFT, NUFFT entails a convolution between a tailor-made digital window and non-uniformly sampled data, followed by the application of the FFT. In addition to NUFFT, a Deskew filter, initially employed in frequency modulated continuous wave systems, was adapted for compensating the frequency sweeping nonlinearity of OFDR in [95]. This method calculates the nonlinear phase of a TLS via an auxiliary interferometer, subsequently employing a Deskew filter to counteract the frequency sweeping nonlinearity by extrapolating the nonlinear phase throughout the spatial domain. However, as the measurement distance extends, the estimation error of the nonlinear phase grows, reducing the compensation's effectiveness for long-range applications. Hence, an enhanced Deskew filter, integrating the Cepstrum method and higher order Taylor expansion, is proposed to refine the accuracy of nonlinear phase estimation for improved compensation [96].

The interpolation technique serves as another valuable post-processing algorithm to counteract

frequency sweeping nonlinearity. In [97], a cubic spline interpolation algorithm was implemented to re-sample the raw data from the measurement interferometer. This nonlinearity is ascertained using an auxiliary interferometer. Utilizing this nonlinearity data, the raw measurements from the interferometer are recalibrated to a set of discrete points with varying time intervals. These points serve as the basis for generating a smooth curve through cubic polynomial fitting. Subsequently, this curve is subjected to interpolation to obtain resampled data with uniform time intervals. A similar approach was outlined in [98], where a time-scale factor was deduced through zero-crossing detection in the auxiliary interferometer's output. This factor was subsequently employed to recalibrate the raw measurements from the measurement interferometer, after which the cubic spline interpolation algorithm was utilized for resampling. Demonstrating efficacy both in mitigating frequency sweeping nonlinearity and accurately predicting new data points, the cubic spline interpolation algorithm is effective across the board. An alternate signal conditioning algorithm leveraging cubic spline interpolation was introduced in [99]. Differing from [97] and [98], the cubic spline interpolation is applied to auxiliary interferometer data. The spatial resolution enhancements obtained through various post-processing algorithms are summarized in Table 2.2, revealing the interpolation algorithm's superior performance in enhancing the spatial resolution of OFDR.

Table 2.2: The spatial resolution obtained by different post-processing algorithms

algorithms	reference	Spatial resolution/cm	Measurement range/m
NUFFT	[92]	5	50
Deskew filter	[95]	20	10000
Deskew filter	[96]	80	8000
Interpolation algorithm	[97]	0.03	300
Interpolation algorithm	[98]	0.017	155
Interpolation algorithm	[99]	0.036	-

The second approach to address frequency nonlinearity involves enhancing the laser source itself. For instance, a wideband phase locking technique is embraced to enhance the frequency sweeping linearity, resulting in the generation of a highly coherent linear laser in the study presented by [100]. Similarly, an approach based on the optoelectronic phase-locked loop technique is introduced to enhance the frequency sweeping linearity of laser sources [101]. Beyond these strategies, a variety of lasers are incorporated into OFDR systems to tackle the frequency

sweeping nonlinearity challenge. For instance, a sinusoidal frequency scan optical frequency domain reflectometry (SFS-OFDR) is established based on a sinusoidal frequency scan laser, proving valuable in numerous research domains [102, 103, 73, 104, 74, 105]. This laser type is adopted due to the difficulties in achieving suitably linear scans with conventional lasers. Although the frequency behavior of a sinusoidal frequency scan laser isn't linear, it can be approximated as linear through short windows at the maximum slope [103, 73]. Moreover, certain algorithms have been proposed to process raw data from SFS-OFDR, aiming to enhance accuracy and reduce processing time[104, 74, 105]. More recently, an innovative fiber laser with inherent frequency self-scanning characteristics has been integrated into OFDR systems, displaying potential for compensating frequency sweeping nonlinearity [106, 107].

Particularly, when considering OFDR systems based on an external cavity laser diode, comprehensive investigations have been conducted into the mathematical aspects of sampling errors and the creep of PZT translators. Corresponding models have been developed, forming a foundation for subsequent hardware or software modifications aimed at enhancing spatial resolution. For example, strategies such as dynamic recalibration of the PZT translator's driving signal have been devised based on these model outputs. A sampling error model for the auxiliary interferometer was elaborated upon in the work by [108]. This model discerns that the sampling error diminishes with escalating frequency sweeping speeds. Additionally, a more finely tuned sampling error model was introduced in [109]. This latter model identifies two distinct sources of sampling errors and proposes appropriate remedies. One source is attributed to the inherent error of the auxiliary interferometer, while the other arises from acquisition delays.

The frequency sweeping nonlinearity also emerges from hysteresis and creep exhibited by the PZT translator. A mathematical model was formulated to assess the nonlinearity of the external cavity laser diode in [110]. A comparable model was developed in [111] to counter the effects of hysteresis and creep in the PZT translator. In this instance, the instantaneous frequency of the interference signal is estimated through an extended Kalman filter. These estimated values are subsequently integrated to derive the interferometric phase. This integration effectively mitigates the impact of frequency sweeping nonlinearity on the phase extraction process.

Intrinsic phase noise compensation

In an OFDR system, the beat signal at z_0 (as shown in Equation 2.5 and Figure 2.4 (a)) is converted to frequency domain by FFT. The one-side spectral density of this frequency domain signal is described in [71], which shows in Equation 2.11.

$$S_I^1(f) = (1+R)^2\delta(f) + 2R\cdot exp(\frac{-2\tau_0}{\tau_c})\cdot\delta\big(f-f_{\mathbf{z}_0}\big) + \frac{2R\tau_c}{1+\pi^2{\tau_c}^2(f-f_{\mathbf{z}_0})^2}\left\{1-exp(\frac{-2\tau_0}{\tau_c})\cdot\left[cos2\pi\big(f-f_{\mathbf{z}_0}\big)\tau_0+\frac{sin2\pi\big(f-f_{\mathbf{z}_0}\big)\tau_0}{\pi\tau_c\big(f-f_{\mathbf{z}_0}\big)}\right]\right\} \tag{2.11}$$

Here, R represents the reflectivity of the FUT; δ symbolizes the unit-impulse response function; τ_0 stands for the time delay; τ_c denotes the coherent time of the TLS; and f_{z_0} represents the beat frequency at the location z_0 as defined in Equation 2.5. In accordance with Equation 2.11, the one-side spectral density is composed of three components: the direct-current term, the coherent term, and the intrinsic phase noise term. The direct-photocurrent term $(1+R)^2\delta(f)$ relies on the value of R when the frequency is zero. The coherent term,$2R\cdot exp(\frac{-2\tau_0}{\tau_c})\cdot\delta\big(f-f_{\mathbf{z}_0}\big)$, forms a unit-impulse response function at f_{z_0}. This term encapsulates details about location and optical intensity. The remaining portion of Equation 2.11 constitutes the intrinsic phase noise term. The amplitude of the coherent term amounts to $2R\cdot exp(\frac{-2\tau_0}{\tau_c})$. This amplitude diminishes rapidly as the delay time approaches half of the coherent time. Conversely, the amplitude of the intrinsic phase noise term becomes dominant when the measurement distance extends beyond half of the coherent distance. The one-side spectral density outlined in Equation 2.11 transitions into a Lorentzian Function due to the presence of the intrinsic phase noise term. Consequently, the existence of the intrinsic phase noise term exacerbates the decline in spatial resolution as the measurement range increases. This phenomenon leads to an uneven distribution of spatial resolution along the entire length of the FUT.

Numerous investigations have been dedicated to mitigating the effects of intrinsic phase noise, aiming to expand measurement range and enhance spatial resolution. Many studies have con-

centrated on addressing this phase noise through specialized data processing algorithms, leading to the development of Phase Noise Compensated OFDR systems (PNC-OFDR). One variant of PNC-OFDR, rooted in the concept of "concatenately generated phase" (CGP), has been introduced in literature [112, 113, 114]. The CGP technique employs an auxiliary interferometer for phase noise compensation. Within this approach, the FUT is segmented into distinct sections. The calculated CGPs derived from the auxiliary interferometer are utilized to offset phase noise in various segments. However, as the FUT's length increases, the spatial resolution tends to deteriorate due to residual noise. A thorough analysis of this noise source has been carried out in literature [114]. To illustrate the effectiveness of this OFDR system variant, a field trial was conducted in [115]. Furthermore, alternative algorithms grounded in concatenative reference phase [89], phase noise term measurement [116] (Long Measurement Range OFDR Beyond Laser Coherence Length), and optical power spectrum analysis [117] have all exhibited good performance in compensating for intrinsic phase noise. Using the research in Literature [117] as an example, compensation for inherent noise enabled the attainment of a spatial resolution of 30m within a measurement range of 100km.

Other investigations have directed their attention toward refining the experimental setup. One notable enhancement is Delay Shift Averaging (DSAV), grounded in the utilization of an optical frequency comb source and a tunable delay line [118]. Preceding the emergence of DSAV, a similar technique referred to as Frequency Shift Averaging (FSAV) had been employed to address intrinsic phase noise compensation. FSAV involves averaging outcomes from multiple independent reflectometry measurements conducted at distinct optical frequencies. To accommodate FSAV, a laser source with an extensive frequency variation range is required. Hence, optical frequency comb sources boasting broad frequency variation ranges are introduced to the OFDR system. The tunable delay line, integrated into the reference path, facilitates the establishment of different optical frequencies. This application of an optical frequency comb source within the FSAV framework has also been demonstrated elsewhere [88]. Beyond FSAV and DSAV, an innovative approach grounded in an optical fiber delay loop, encompassing a delay fiber and a frequency shifter, was introduced for compensating the intrinsic phase noise term [119, 71]. The delay loop, positioned along the reference path, serves to curtail the optical

path difference between the reference and measurement paths, ensuring it remains substantially smaller than the laser source's coherence length. The frequency shifter functions as a counter, diligently tracking the number of circulation loops.

In recognition of the intrinsic phase noise term's origin from the interference between Rayleigh backscattering and reference light, an innovative approach termed Incoherent Optical Frequency Domain Reflectometry (I-OFDR) has been developed [102]. This system is exclusively engineered to detect Rayleigh backscattering light emanating from the FUT. Subsequently, a comprehensive transfer function of the Rayleigh backscattering light is computed, encapsulating all the pertinent information across the entire FUT. The I-OFDR system has demonstrated commendable performance in applications such as strain measurement [120] and the interrogation of delicate Fiber Bragg Grating (FBG) arrays [121, 122].

2.3.2 Drawbacks of the FFT and algorithm efficiency improvement

The FFT holds a pivotal role in the OFDR system, facilitating the transformation of signals from the time domain to the frequency domain. Nevertheless, as elucidated in the beginning of this chapter (2), there exist numerous limitations inherent to FFT that impact the effectiveness of the OFDR system. One prominent limitation is encapsulated by the uncertainty principle, implying that heightened spatial resolution comes at the expense of compromised strain or temperature accuracy. Moreover, the complex computational nature of FFT renders it ill-suited for managing substantial data sets, leading to diminished efficiency. Consequently, the demand for a real-time processing algorithm becomes imperative to enhance the performance of the OFDR system.

Numerous approaches have emerged to counteract the limitations associated with FFT. A recent advancement involves employing the wavelet transform as a signal processing technique to mitigate the uncertainty inherent to FFT [123, 72]. Specifically, the Morlet wavelet transform has been harnessed to alleviate frequency overlap and enhance frequency details, especially at higher spatial resolutions. The synergy between wavelet parameters and sensing variables, such as temperature and strain, is demonstrated in these studies. Consequently, by judiciously

configuring wavelet parameters, spatial resolution and sensing accuracy can be simultaneously heightened. The relationship between spatial resolution and measurement accuracy is intrinsically linked to the length of a rectangular window, as defined by Equation 2.8. A shorter window equates to superior spatial resolution but diminished strain or temperature precision due to the uncertainty principle. Therefore, optimizing this rectangular window length assumes pivotal importance in achieving a balance between spatial resolution and measurement accuracy, particularly under high spatial resolutions. Recent investigations have delved into this aspect, employing a model grounded in noise variance and a defined quality factor to estimate strain measurement errors [124]. This quality factor aids in selecting the ideal rectangular window length for optimization. Beyond wavelet transforms and rectangular window analysis, a novel approach rooted in image processing has emerged to enhance measurement accuracy in scenarios with high spatial resolutions [44]. Here, original OFDR data is transformed into a 2D image encapsulating cross-correlation traces across the FUT. This image undergoes spatial filtering using techniques like mean value filtering or non-local means, followed by frequency-based wavelet denoising. Notably, the overlapped window strategy is embraced to mitigate resolution deterioration, a common challenge when employing image processing methodologies.

Although the algorithms mentioned above can effectively tackle the uncertainty issues associated with FFT, their inherent complexity places a substantial computational load on the OFDR system. Furthermore, the considerable volume of data generated by the OFDR system necessitates ample memory resources to obtain fine resolutions. Given the intricacies of these algorithms and the sheer data volume, their applicability often remains confined to controlled laboratory settings. Consequently, a rapid and efficient data processing algorithm is imperative for real-world implementation. An example of this requirement can be found in a study involving the integration of FBG sensors into the OFDR system for distributed measurements [125]. Here, a specialized group delay calculation method is employed to enhance data processing efficiency. Diverging from FFT, which furnishes the full Bragg spectral profile, this group delay calculation approach exclusively discerns Bragg peak shifts. This innovative methodology reduces processing time by a significant 92.5% compared to conventional FFT-based data processing in OFDR systems.

In addition to exploring alternatives to FFT, a strategy that combines FFT with the segmented chirp-Z transform (SCZT) has been introduced for expedited spectrum analysis [126] (Fast Spectrum Analysis for an OFDR Using the FFT and SCZT Combination Approach). This method is tailor-made for specific frequency analyses. Initially, FFT is employed to perform a broad frequency range analysis, quickly identifying zoom bands of interest. Subsequently, these bands undergo precise examination using an optimized SCZT technique, supplemented by parallel computing techniques. The integration of SCZT serves to counteract the degradation of measurement resolution arising from frequency overlap. Remarkably, the combined approach exhibits a 30% efficiency improvement compared to conventional FFT-based methods. Another innovative technique was put forth in [127] to enhance data processing efficiency when incorporating FBG sensors into an OFDR system. This methodology hinges on cross-correlation, weighted sliding windowed fast Fourier transform (W-WFFT), and logistic activation functions. The initial step entails calculating the cross-correlation between measurement and reference signals. This cross-correlation output then undergoes processing via W-WFFT to derive the distribution of Bragg peak shifts. Subsequently, a thresholding operation, facilitated by logistic activation functions, refines the measurement accuracy. Notably, the reported approach achieves speeds approximately tenfold faster than conventional FFT. Several other algorithms not only concentrate on enhancing the OFDR interrogation process but also bolster the efficiency of phase noise compensation processes [128]. One such example is the introduction of a hardware-adaptive algorithm, which obtains real-time phase noise compensation, thereby enhancing the overall efficiency of the OFDR system.

Numerous studies focusing on algorithmic efficiency improvements have yielded positive outcomes, particularly in static applications. However, dynamic scenarios necessitate even more efficient algorithms due to the substantial volume of recorded data. An illustrative case is the employment of an OFDR system for distributed acoustic sensing (DSA), where daily data accumulation can exceed 1 terabyte [129]. DSA exemplifies a prevalent dynamic application, prompting extensive investigations into augmenting the processing efficiency of OFDR systems tailored for DSA applications. For instance, a rapid processing algorithm tailored for DSA, relying on two consecutive FFT operations, was detailed in [74]. In another notable effort [129],

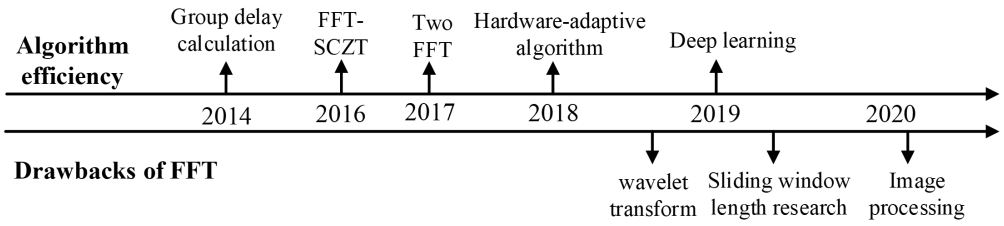


Figure 2.9: The methods adopted to address the drawbacks of FFT and improve the efficiency of algorithms

deep learning techniques were harnessed to process substantial data loads within OFDR systems employed in DSA. Here, the methodology capitalizes on generative adversarial networks (GANs) to simulate the DAS system and produce training datasets. These datasets then facilitate the training of artificial neural networks (ANNs), which subsequently process experimental data directly. A comprehensive overview of methods aimed at mitigating FFT limitations and enhancing algorithmic efficiency is presented in Figure 2.9.

2.3.3 Continuous vibration measurement and shape sensing

Shape sensing is pivotal in SHM as it facilitates the continuous monitoring of structural deformations and alterations in a structure's geometry in real-time. This technology furnishes detailed insights into the shape, position, and movement of structural elements, aiding in the detection of anomalies like deformations, displacements, or misalignments. Such anomalies can serve as indicators of potential structural damage or deterioration. Furthermore, the vibration monitoring is also important to SHM. Vibrations have the potential to contribute to fatigue and overloading of structural elements. The surveillance of vibration levels aids in recognizing patterns linked to fatigue, facilitating proactive measures to prevent structural damage and prolong the lifespan of components.

However, research efforts in the realm of OFDR have predominantly concentrated on static scenarios, with fewer studies demonstrating its aptitude for continuous vibration measurement. Several factors contribute to this prevailing trend.

- The escalating demand for heightened measurement repetition rates and the management

of substantial data volumes in dynamic applications pose formidable challenges to real-time processing capabilities.

- The issue of crosstalk arises when dealing with distinct vibration points. In this context, the modulation of measurement light at a prior vibration point engenders crosstalk when the modulated light encounters a subsequent vibration point. The severity of this crosstalk intensifies as vibration frequencies ascend.

- The constricted sweeping span characteristic of dynamic applications significantly diminishes spatial resolution, thereby rendering further exploration into facets like shape sensing in dynamic scenarios with OFDR a challenging endeavor.

Previous investigations into vibration measurement and shape sensing in aircraft SHM predominantly leaned towards FBG, primarily due to their elevated sensitivity and established interrogation systems. This section aims to elucidate the most recent advancements in continuous vibration measurement and shape sensing facilitated by the Rayleigh backscattering based OFDR technique.

Continuous vibration measurement with OFDR system

Continuous vibration measurement holds immense significance in the context of aircraft SHM. Consequently, thorough investigation into vibration measurement via the Rayleigh backscattering-based OFDR technique is imperative. Numerous of studies have been done for realizing continuous vibration measurement. In this section, these methods are roughly divided into two categories including phase extraction and other methods, as shown in Figure 2.10.

The majority of research endeavors pertaining to continuous vibration measurement have been focused on phase extraction. This emphasis stems from the direct correspondence between the phase alterations of the Rayleigh backscattering spectrum and the vibrations being measured. To obtain accurate measurement of higher vibration frequencies, diverse methods have been employed to extract phase variations induced by vibrations. For example, in a bid to achieve enhanced vibration frequency measurement, a study utilized an I-OFDR system to successfully

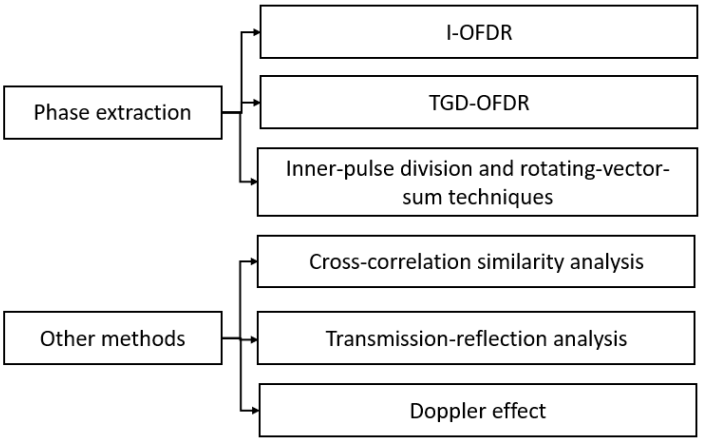


Figure 2.10: The two categories of methods on continuous vibration measurement with OFDR system

measure vibrations at a frequency of 2 kHz [130]. The paper meticulously calculates the alterations in the length of the FUT as well as the variations in optical power caused by vibration events between reflection points by extracting phase changes within the Rayleigh backscattering spectrum. Similarly, in other works [103, 73, 105], a sinusoidally swept-frequency laser was employed to drive the OFDR system. This approach not only enhances back-reflected power but also augments the Signal-to-Noise Ratio (SNR), thereby facilitating more accurate phase extraction. As a result, acoustic vibrations were effectively detected in [103] and [73] at frequencies of 1 kHz and 2.7 kHz, respectively.

In 2015, a novel approach for phase extraction was introduced, leveraging TGD-OFDR for vibration measurement [131]. This technique utilizes a 90-degree optical phase extraction process. By employing TGD-OFDR, the frequency sweeping speed is elevated, which in turn helps mitigate the impact of environmental phase noise. However, the vibration frequency that could be accurately measured was limited to 600 Hz, and only one vibration event was demonstrated experimentally. Due to the limited performance of this initial approach, an enhanced TGD-OFDR system was subsequently proposed [132], incorporating the inner-pulse frequency-division method and the rotated-vector-sum technique. This advancement extended the measurable vibration frequency to 1.25 kHz, enabling the detection of two distinct vibration events in experimental scenarios. In recent times, the TGD-OFDR-based vibration measurement technique has achieved even more remarkable performance improvements [133]. These

enhancements are attributed to several factors, including the utilization of a LiNbO3 intensity modulator with an expansive modulation bandwidth, which enhances the spatial resolution of the system. Furthermore, noise suppression is achieved through the application of a matched filter and the rotated-vector-sum method. Through these advancements, the system achieved a notable enhancement in measurable frequency, reaching 5 kHz, and successfully detecting two vibration events in experimental trials.

In addition to the vibration measurement technique relying on TGD-OFDR, an innovative data analysis algorithm was introduced by [134]. This algorithm was designed to accurately extract phase information from the Rayleigh backscattering spectrum. Notably, the algorithm compensates for various errors, including phase noise and frequency sweeping nonlinearity. A significant contribution of this algorithm is its capability to address challenges related to overlapped perturbations in multi-vibration measurements. By applying this algorithm, an impressive vibration frequency of up to 12.5 kHz can be reliably measured, and the system can detect multiple vibration events with precision using the OFDR technique. Another recent advancement in phase extraction methodology is based on the combination of inner-pulse division and rotating-vector-sum techniques [135]. This method incorporates a Hanning time window, effectively suppressing crosstalk issues that may arise between different vibration points.

The phase extraction technique has garnered considerable attention in the realm of vibration measurement and has been extensively studied in recent years. However, a significant challenge lies in balancing the SNR, spatial resolution, and measurement range, which remains a prominent bottleneck. As a result, researchers have explored alternative methods to accomplish vibration measurement. In 2012, a novel approach called cross-correlation similarity analysis (CCSA) was introduced for vibration measurement [116]. This method involves conducting two independent measurements of the FUT under different vibrational states—vibrated and non-vibrated. The resulting measurements are then subjected to correlation analysis to identify vibration events. Through the CCSA method, two vibration events along the FUT can be simultaneously detected, achieving a vibration frequency of up to 2 kHz. This CCSA method was further validated in long-range vibration measurement, demonstrating successful results with a vibration frequency of 500 Hz [136]. However, achieving multi-vibration measurement using

the CCSA method poses challenges. In pursuit of multi-vibration measurement capabilities, a novel approach based on the diverse characteristics of Rayleigh backscattering spectrum was proposed [137]. This method capitalizes on both the optical frequency shift in the frequency domain and the distinctive "V" shape in the spatial domain of the Rayleigh backscattering spectrum for vibration measurement. Nonetheless, this new method does not yet provide vibration frequency information.

In addition to the CCSA method, a novel approach based on transmission-reflection analysis (TRA) is explored in [138] using an I-OFDR system. The TRA technique involves assessing both transmitted and reflected optical power to detect vibration events along the FUT. Another research effort involves the utilization of FBG sensors within an OFDR system to measure vibrations [139]. This is achieved by employing current-modulated laser diodes for rapid frequency sweeping. By employing FFT, the different central wavelengths of the FBGs are interrogated, allowing the measurement of vibration events that influence the FBGs' central wavelengths. This method achieves a measurable frequency of 3 kHz and successfully captures three synchronous vibration events along the FUT. Although, in another study [140], FBG sensors are used for vibration measurement of a helicopter blade, the obtainable measurement frequency is only 150 Hz. In recent research, a novel algorithm based on the Doppler effect in all-fibre Michelson interferometers is proposed for vibration measurement [141]. This approach uses FFT to convert the beat signal of the OFDR system into a frequency signal, which is then segmented in the frequency domain. Taking one segment as an example, the inverse Fourier transform is applied to acquire the filtered response of this segment. By subsequently performing FFT on this response, the distribution of frequency components is obtained. The effects of frequency noise induced by vibrations in other segments are mitigated by subtracting adjacent segment data from the FFT results. This leaves behind the frequency component that corresponds to the vibration frequency of the measured segment. This innovative method demonstrates impressive performance in vibration measurement. It achieves a measurable frequency of up to 8 kHz at a spatial resolution of 15–20 cm and 30 kHz at a spatial resolution of 1.5 m. Moreover, this method enables synchronous vibration measurement across 30 segments along a FUT.

While significant progress has been made in vibration measurement research, only a limited number of studies have demonstrated continuous vibration measurement capability. This challenge mainly stems from the presence of crosstalk between different vibration points. Crosstalk complicates the distinction between adjacent vibration events, posing a barrier to accurate measurement. To address this issue, numerous studies have focused on minimizing crosstalk. In 2012, initial efforts were made to theoretically analyze crosstalk arising from multi-reflection and spectral shadowing in temperature measurement utilizing low-reflective fiber Bragg gratings [142]. Subsequently, in 2018, a crosstalk-free theory and design were proposed to effectively mitigate crosstalk between vibration points in continuous vibration measurement [143]. This innovative approach introduced a dynamic phase interrogation theory that not only eliminated crosstalk but also enabled real-time interrogation. Further developments in this area led to the proposal of a theory regarding the crosstalk between preceding and subsequent vibrations [144]. The theory demonstrated that the modulation induced by a preceding vibration, with a measurement time shorter than the vibration period, results in a frequency or wavelength shift in the Rayleigh backscattering spectrum—a phenomenon similar to the Doppler shift. Exploiting this concept, a distance tracking technique was devised. This technique estimates the frequency shift caused by the preceding vibration through cross-correlation calculation. The estimated frequency shift is subsequently utilized to counteract the crosstalk between preceding and subsequent vibrations. This approach was validated through successful multi-point vibration measurements along a fiber. In Figure 2.11, we provide an overview of the techniques employed for continuous vibration measurement.

Shape sensing with OFDR system

Shape sensing is a critical application in aircraft SHM, offering essential insights into aircraft status during testing, operations, and maintenance. However, the utilization of the Rayleigh backscattering based OFDR technique for shape sensing has been relatively scarce. In 2010, an approach leveraging I-OFDR was introduced, allowing measurement of length changes between different reflections, thus enabling structural deformation assessment with the OFDR system [145].

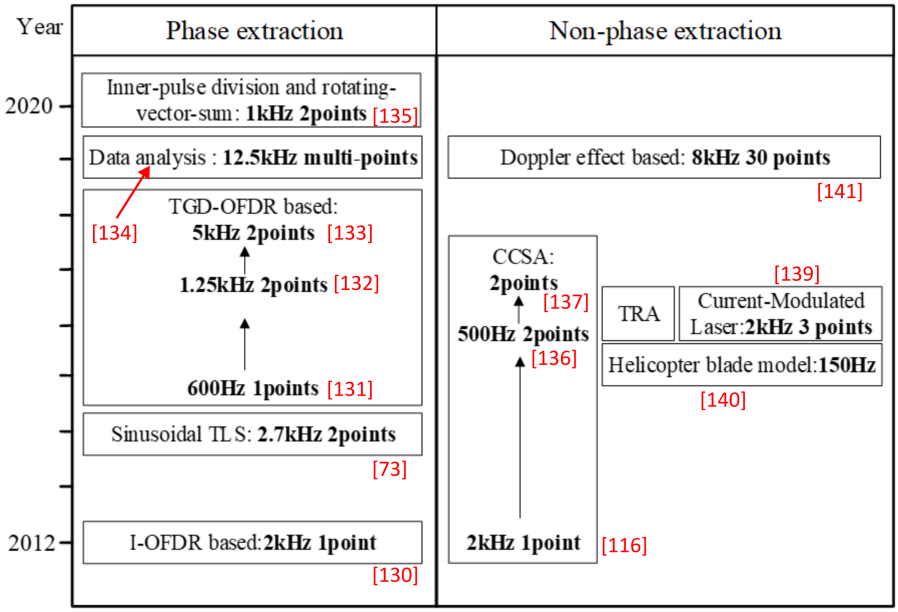


Figure 2.11: The techniques of continuous vibration measurement

Formally in 2012, the first shape sensing technique utilizing an OFDR system was proposed [146]. It employed a twisted-fiber configuration for high-resolution 3D shape sensing, demonstrated using a generalized flexible structure. More recently, a study on shape sensing using the OFDR system has emerged [147]. Employing a local spectrum matching method, researchers managed to eliminate spurious and multiple peaks during measurements. However, the method is currently restricted to 2D shape sensing, and its application is limited by the need to attach fiber optic sensors to opposing surfaces of structures.

Presently, the OFDR-based shape sensing techniques are also being developed in the medical field. Given the high resolution of the Rayleigh backscattering based OFDR technique, medical researchers are increasingly drawn to the potential of shape sensing using this method. A shape sensing approach targeting surgical needles using OFDR was introduced in [148]. Ultraviolet (UV) exposed single-mode fibers SMFs were employed to enhance Rayleigh backscattering. By combining three parallel SMFs into a fiber triplet, 3D shape sensing was achieved. A similar strategy has been effectively applied in intra-arterial image guidance [35] and minimally invasive surgery [149].

2.3.4 Challenges of embedding FOS in composite materials

Two prevalent installation approaches are employed for incorporating FOS in aircraft SHM: surface-mounted and embedded configurations. The surface-mounted method, due to the fragility of FOS, finds more relevance in controlled laboratory research. On the contrary, the embedded approach is better suited for practical application. Consequently, the trend in aircraft SHM is leaning towards embedding FOS, which offers enhanced performance under real-world conditions. However, integrating the Rayleigh backscattering based OFDR technique into the embedded setup presents numerous challenges.

- One significant barrier involves temperature compensation, owing to the FOS's susceptibility to both strain and temperature. Aircrafts undergo substantial temperature fluctuations throughout their operational cycles, intensifying the need for effective compensation.
- Another critical challenge is accurate measurement of large strains and addressing non-uniform lateral strain effects. The measurement range of strain for OFDR systems is narrower compared to other strain sensors like strain gauges and FBG sensors. The application of OFDR-based strain measurement systems capable of measuring strains exceeding $3000\mu\varepsilon$ is rarely documented.
- Moreover, embedding FOS in composite materials introduces birefringence due to non-uniform lateral strains, leading to axial strain measurement errors.

Given these challenges, the latest advancements in OFDR-based research addressing temperature compensation, large strain measurement, and non-uniform lateral strain compensation are discussed in this subsection.

Temperature compensation

Aircraft often encounter extreme conditions, such as wide temperature fluctuations and even cryogenic temperatures, during their operations. These conditions can introduce errors in strain

measurements when employing the Rayleigh backscattering based OFDR technique in aircraft SHM. While the OFDR technique has demonstrated exceptional accuracy and stability in continuous temperature or strain sensing scenarios [150, 75, 151, 152, 153], simultaneously measuring strain and temperature remains a challenge. To tackle this challenge, various temperature compensation methods have been proposed for applications utilizing the OFDR technique. Many of these studies have focused on employing polarization-maintaining fiber. This type of fiber supports two distinct polarization modes, each with its own refractive index, resulting in different sensitivities to temperature and strain. This intrinsic distinction between the two polarization modes lends itself to calculating temperature and strain simultaneously, offering a promising avenue for addressing this concern.

For example, polarization maintaining FBG sensors were introduced for temperature compensation purposes in 2011 [154]. Although successful discrimination between temperature and strain was achieved, notable discrepancies were observed in continuous measurements. In a subsequent study [155], polarization maintaining FBG sensors were employed to enable temperature compensation in a four-point bending test. This experiment demonstrated enhanced accuracy compared to the findings in [154]. Temperature and strain sensing exhibited average errors ranging from -0.9°C to 1.3°C and -31$\mu\varepsilon$ to 19$\mu\varepsilon$, respectively. However, the measurement accuracy of the OFDR system in this setup remained inferior to its counterparts like FBGs and strain gauges. To address this limitation, researchers proposed a relationship between measurement accuracy and the refractive index difference in polarization maintaining FBG sensors [156]. They introduced a numerical model for temperature compensation in continuous strain sensing using these FBG sensors. The model revealed that enhancing the measurement accuracy hinges on increasing the refractive index difference in polarization maintaining FBG sensors. However, it was noted that the rate of improvement diminishes as the refractive index difference increases. This study found a way to improve measurement accuracy when polarization maintaining FBG sensors are employed for simultaneous strain and temperature measurements. In another investigation, common polarization maintaining fiber optics were evaluated for temperature compensation [157]. This research achieved impressive outcomes, including high spatial resolution (6.5mm), minimal temperature sensing error (0.8 °C), and low

strain sensing error ($7\mu\varepsilon$).

Besides polarization maintaining fiber, alternative approaches have been investigated for temperature compensation. In one instance, a system combined both Brillouin and Rayleigh backscattering to enable simultaneous temperature and strain measurement [158]. This approach yielded a temperature accuracy of ± 1.2°C and a strain accuracy of $\pm 15\mu\varepsilon$ and. However, the incorporation of both Brillouin and Rayleigh backscattering necessitates a complex interrogation system and complex data processing algorithms, rendering this strategy impractical for real-world applications. An innovative method centered on two types of fibers, namely a standard SMF and a reduced-cladding SMF, has been proposed [159]. These two sensors are installed side by side and treated as a single sensing unit. The distinct sensitivity responses of the SMF and the reduced-cladding SMF to temperature and strain, respectively, enable simultaneous measurements. This strategy demonstrated temperature errors of 0.31°C and strain errors of $7.97\mu\varepsilon$, showcasing its efficacy.

Large strain and non-uniform lateral strain

In conventional OFDR, cross-correlation calculation is employed to determine the frequency shift between the measurement spectrum and the reference spectrum. This is feasible due to the shared characteristics between these two spectra. However, when measuring a large strain under high spatial resolution, this resemblance between the spectra diminishes considerably. This deterioration stems from the deformation of the measurement spectrum, introducing errors into the cross-correlation calculation. As a result, the applicability of the OFDR technique in applications requiring the measurement of large strains becomes limited.

Numerous studies have been dedicated to enhancing the measurement range of the Rayleigh backscattering based OFDR technique. In one such effort [160], an amplifying add-on module is introduced to extend the strain measurement range. Positioned between the OFDR system and the FUT, this module mitigates noise and compensates for optical losses. However, even with this module, the deformation of the measurement spectrum persists under large strain conditions. To tackle this issue, a solution based on local similar characteristics is proposed

[161]. Despite the reduced global similarity between the measurement and reference spectra due to deformation, certain local similar characteristics still persist. Thus, the strain calculation is achieved by matching these local characteristics and deriving the shifts between them. Recently, a combined approach of spectrum registration and spatial calibration has been introduced to maintain high spatial resolution while measuring large strains [77]. This method employs a local measurement spectrum segment technique to uphold high spatial resolution. Through this approach, strains up to $7000\mu\varepsilon$ have been successfully demodulated.

In addition to situations involving large strains, strain measurement errors can also stem from non-uniform lateral strains resulting from the embedding of FOS into composite materials or bending during installation. Consequently, compensating for non-uniform lateral strain is crucial when implementing the OFDR technique for Aircraft SHM. Two key strategies have emerged for addressing this challenge.

The first approach focuses on the development of bend loss-free FOS. Multiple techniques have been utilized to create FOS with low bending loss, including the chemical vapor deposition process [162], nano-structures techniques [163], trench management around the core [164], and photonic crystal fiber [165]. However, most of these FOS operate within the visible wavelength range or are applied in fiber-to-the-home scenarios. In 2018, a bend loss-free FOS was introduced based on Ge-doped-core photonic crystal fiber for distributed sensing using the OFDR technique [166]. This FOS managed to achieve a bend diameter of up to 2mm without experiencing bend loss. This innovation has opened up the possibility of implementing OFDR for real SHM applications in aircrafts.

The second strategy revolves around lateral strain measurement through the use of OFDR systems. Polarization calculation forms the basis of lateral strain measurement for various FOS. One such example is the Panda-type fiber, a commonly used polarization FOS [167]. This fiber exhibits two polarization modes with distinct refractive indices. While both indices alter equally when longitudinal strain is applied, lateral strain introduces disparate changes. Thus, lateral strain is calculated by separately gathering data from these two polarization modes. A similar polarization-based strategy is employed in [168], where a long-length FBG

sensor is utilized to measure lateral strain using the OFDR system. The lateral strain applied to this sensor induces birefringence, creating two polarization states and leading to FBG peak separation. The degree of peak separation is detected by the OFDR system, enabling the calculation of the lateral strain. A comprehensive numerical simulation elucidating the two polarization states of the long-length FBG sensor is discussed in [169]. Another numerical model addressing polarization-dependent loss interrogation of cascaded identical FBGs is presented in [170]. This model establishes the connection between the spectral evolution of FBGs and birefringence, underscoring the advantages of polarization-based calculations in lateral strain measurement.

Although the FBG-based techniques mentioned above exhibit promising potential for lateral strain measurement, they often struggle to achieve csontinuous sensing. Additionally, the method centered around Panda-type FOS can prove cost-prohibitive, especially for long-range applications. Consequently, a continuous lateral strain measurement method based on SMF is introduced. This method involves integrating a polarization state generator and a polarization state analyzer into the OFDR system [171].

2.3.5 Conclusions

This comprehensive review delves into the theory and applications of the Rayleigh backscattering-based OFDR technique for Aircraft SHM. The document meticulously outlines the challenges that need to be overcome to ensure the dependable application of the Rayleigh backscattering-based OFDR technique in aircraft SHM. Leveraging these challenges as a foundation, the paper proceeds to introduce noteworthy research endeavors that have advanced the Rayleigh backscattering-based OFDR technique. Ultimately, the overarching aim of this review is to propel the widespread adoption of the OFDR technique in the field of aircraft SHM.

For effective SHM in aircraft, an OFDR system with fine spatial resolution is essential to capture complex temperature and strain distributions. Presently, three key strategies have been extensively explored to enhance spatial resolution. These strategies encompass extending the frequency sweeping span, compensating for frequency sweeping nonlinearity, and addressing

intrinsic phase noise. Broadening the frequency sweeping span translates to a increase of frequency sweeping speed, consequently enhancing theoretical spatial resolution.

Regarding frequency sweeping nonlinearity compensation, the majority of methods leverage auxiliary interferometers. Through data garnered from these auxiliary interferometers, nonlinearity is typically rectified using post-processing algorithms. Among these algorithms, the interpolation algorithm excels in delivering high spatial resolution within the mid-range of measurement, aligning well with the SHM requirements for aircraft. Tackling intrinsic phase noise, which becomes prominent at distances exceeding half of the coherent distance, is complex. It's particularly crucial for long-distance measurements. Hence, incorporating a TLS with an extended coherent distance emerges as a viable solution when deploying OFDR systems in aircraft SHM. In addition to the enhancement of spatial resolution, the uncertainty principle inherent in the FFT creates a barrier to simultaneously improving spatial resolution and measurement accuracy. To address this challenge, strategies such as the Morlet wavelet transform, optimization of rectangular window, and image processing have emerged. However, the adoption of these algorithms introduces substantial computational load to OFDR systems, which is particularly concerning in the context of aircraft SHM.

As OFDR techniques are deployed in real aircraft SHM scenarios, several challenges demand attention. Continuous vibration measurement and shape sensing are pivotal components of aircraft SHM. Vibration measurement based on phase extraction stands as a classic approach, capable of detecting vibration frequencies up to 12.5 kHz. Meanwhile, a novel Doppler effect-based strategy has showcased the potential to detect up to 30 vibration events simultaneously, each with frequencies up to 8 kHz. Notwithstanding, the existing methodologies still require further refinement to meet the stringent demands of continuous vibration measurement and shape sensing in aircraft SHM.

The crucial aspect of temperature compensation predominantly hinges on polarization FOS. Typically, this approach achieves temperature measurement errors below 1°C. Clearly, considerable work remains to be done in the realm of temperature compensation when applying the OFDR technique to aircraft SHM. Furthermore, the presence of large strain situations and

non-uniform lateral strain, particularly in composite material embedding, can lead to substantial inaccuracies in strain measurement. Mitigating such issues requires strategies like relying on local similar characteristics for large strain situations and utilizing low bending loss fibers and polarization fibers to counteract the effects of non-uniform lateral strain.

Chapter 3

Strain and temperature measurement based on Rayleigh backscattering

3.1 Introduction

CFRP have been widely used in various aircraft structures [172, 173, 172, 174], due to their outstanding advantages including light weight, superior strength, and low costs. However, durability, unforeseen and complex damage scenarios are challenges that require attention. Damage types in CFRP include delamination, debonding, fibre breakage and matrix cracking, and are difficult to characterise and detect [175, 176, 17], which makes the monitoring the integrity of composite parts particularly important [177, 178, 179, 180].

To address this challenge, SHM has emerged as a solution to assess the structural integrity of CFRP components. SHM is an effective method for assessing the integrity of composite materials through continuous monitoring [181]. SHM techniques can monitor the type, size and severity of the damage in composite structures based on sensors permanently installed on the structures [182]. Active sensing and passive sensing are the two main research directions for SHM of composite structures [183, 184, 185, 186]. In passive sensing, fiber optic sensors are one of the most widely used sensors. For example, many types of fiber optical (FO)sensors including FBG, Mach-Zehnder sensor, and Fabry-Perot sensor are adopted in SMH of composites [17,

187, 188, 189] . By implementing SHM, it becomes possible to continuously monitor the health of CFRP structures during their operational life, thereby reducing maintenance expenses and enhancing overall safety [190]. SHM provides real-time data on crucial parameters, such as strain, temperature, and load, to evaluate the safety of composite structures.

Various FO sensors have been adopted in different SHM applications [191, 192, 193]. For example, buckling detection based on distributed FO sensors [194], hybrid piezoelectric-fibre optic system based on FBG [195, 196], embedded FBG sensors in SHM of complex composite structures [197] and sandwich panel [198]. In addition, the FO sensors are adopted in composites manufacturing monitoring [199, 200] and damage detection [201, 17]. For in-field applications, however, much more FBG sensors are required than distributed FO sensors to obtain sufficient measurements, which results in higher system weight and cost.

In recent years, the OFDR has emerged as a prominent method in the realm of SHM and condition monitoring due to its capacity for real-time monitoring and early detection of potential defects or damage in various structures [202, 203, 204]. This is because it can provide high accurate distributed sensing signals, which provides much more measurement data compared with single point sensors (FBG, M-Z sensor, F-P sensor). Many studies have been carried out to monitor composite structures based on the distributed fiber optical sensors[205, 206, 207]. According to the introduction in Chapter 2.2, the fundamental principle of this technique involves exploiting the interference phenomenon between Rayleigh backscattering and incident light to characterize the loading state along a SMF [208]. Rayleigh backscattering of SMFs is used to interfere with the incident light to produce a beat signal. The frequency and amplitude of this beat signal corresponds to a specific location on the SMF and the Rayleigh backscattering intensity at that location, respectively, since the light frequency of Rayleigh backscattering does not change during the above processes. Moreover, the intensity of this backscattering is related to defects introduced during the manufacturing process. The beat signal is adopted as a unique code to identify a position on the SMF [209]. When this position is subjected to an external load, the resulting strain causes a frequency shift of the beat signal which is then calculated by matching the beat signals before and after loading. The strain is finally measured using a determined strain-frequency shift coefficient. This coefficient is the ratio between the strain

shift and the corresponding frequency shift. Specifically, to detect this shift, cross-correlation analysis is performed between the reference and the loading states in the frequency domain [194]. Consequently, the measurement principle of OFDR can be mathematically expressed by Equation 3.1.

$$\Delta v = K_T \Delta T + K_\varepsilon \Delta \varepsilon \tag{3.1}$$

In this equation, the frequency shift caused by the total external load is represented by Δv, while ΔT and $\Delta \varepsilon$ signify the thermal and the mechanical load contributions, respectively. The temperature-frequency shift coefficient and strain-frequency shift coefficient are denoted by K_T and K_ε, respectively. For detailed expressions of these coefficients, readers can refer to [210]. The unique ability of OFDR to provide distributed measurements with sub-millimeter spatial resolution makes it a valuable tool for investigating a wide range of samples including composites.

SMFs interrogated by OFDR have been adopted as strain sensors in many studies for various analyses of composite structures [211]. For example, shape sensing of a beam-like composite structure [202], damage detection in composite wind turbines [39], multi-Parameter strain sensing of composites [212], hygrothermal degradation of single fibre composite [213] and health state assessment of composite laminates during manufacturing [214]. Furthermore, the small size of SMF makes it suitable for application to complex composite structures including cylinders [215], bonded lap joints [30] and CFRP plates with circular hole [216]. Nonetheless, there remain several pressing research challenges that need to be addressed when implementing distributed optical fiber sensing for composite structures through OFDR systems. These challenges are outlined below:

- Many methods have been adopted to enhance the measurement sensitivity of fiber optical sensors. For example, special metal coating [217], improvement of demodulation algorithms [218], pre-straining inducing [219], and system improvement [220]. However, few studies are paying attention to enhancing the measurement sensitivity of distributed

fiber optical sensors. The purpose of SHM is to permanently monitor the integrity of the structure during in-service condition. This means that the aircraft structure is subjected to a complex load environment including temperature and fatigue load. Therefore, the SHM system should reliably operate under the operational and environmental conditions of flight. This requires a high sensitivity to both strain and temperature, as well as robust algorithms to compensate these effects so that a reliable diagnosis can be carried out, minimizing false alarm and missed-detection rates.

- As the measurement results of SMFs are influenced by thermal loads, many studies have been conducted on temperature compensation to improve the strain measurement accuracy [28]. However, the temperature compensation cannot eliminate the strain measurement error induced by variations in the strain transfer coefficient due to temperature fluctuations [221]. The temperature fluctuations are inevitable in field applications, which induce non-negligible errors in strain measurement even with temperature compensation applied. Therefore, investigation of strain measurement accuracy under thermal loads is essential for the field applications of SMF-based distributed sensing in CFRP.

- Several researchers have validated the FO sensors for strain measurement under quasi-static loading [28, 29, 30]. However, the operational conditions of aircraft results in low frequency fatigue loads in-service which the SMF sensors will also be exposed to. For example, this will affect the adhesion and embedding quality of SMF sensors [222, 223]. Therefore, the accuracy of distributed strain sensing under fatigue load needs to be demonstrated. When measuring the strain based on distributed SMFs, the strain-frequency shift coefficient is usually obtained in a straightforward way by reading the frequency shift under a known load [224, 225, 226, 227]. This method is unable to obtain high-precision strain information in complex environment such as during flight.

- The significance of consistency assessment on OFDR measurements is of high importance, as it directly influences the reliability and validity of the recorded data [228]. However, limited consistency analysis of OFDR measurements have been conducted in various scenarios, including different structures, measurement times, and loading conditions. This

may be due to different reasons, including lack of specialized equipment and expertise, high complexity and cost, limited awareness and prioritization, and data availability and sharing.

This chapter primarily delves into the investigation of distributed fiber optic sensing using the OFDR technique. Considering the challenges discussed earlier, the focal points of this chapter are the sensitivity enhancement, accuracy assessment amid temperature variations, accuracy assessment during low-frequency fatigue loads, and consistency and uncertainty analysis. The following contents of this chapter is organized as follows:

- **Section 3.2**: the sensitivity enhancement of temperature measurement and strain measurement are investigated by researching the sensor parameters, including coating types and pre-loading. Experimental setup including SMF sensor manufacturing and UV curable material selection are presented at this subsection.

- **Section 3.3**: the strain measurement accuracy of distributed SMF under thermal loads is studied. The results show that environmental condition is one of the critical factors that needs to be considered for higher accuracy of strain sensing with distributed SMFs. It also demonstrates that at certain temperature range the strain-frequency shift coefficient can be considered constant, but outside it range it needs to be compensated.

- **Section 3.4** investigates the measurement error of SMF under fatigue loads through strain-frequency shift coefficient analyses through a fatigue experiment. The results demonstrate that the strain measurement errors of SMF-based distributed sensing under low frequency fatigue load is negligible and the fatigue loads mainly increase the ratio of null values in strain measurements.

- **Section 3.5** presents a thorough examination of the measurement consistency of OFDR, investigating their reliability, consistency and applicability under different test scenarios: different load, different temperature (surface mounted and in a free state) and uncertainty analysis to assess the uncertainty of strain and temperature measurements.

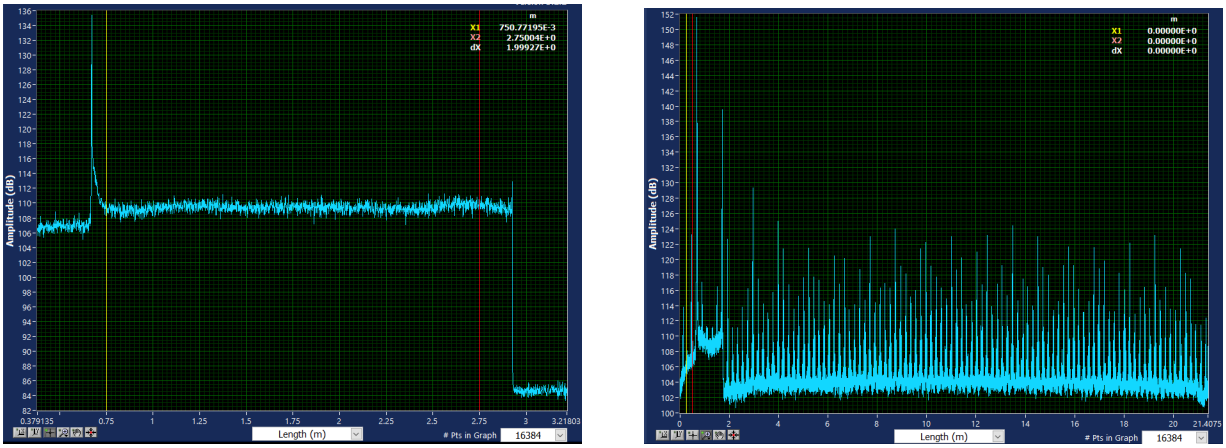
3.2 The sensitivity enhancement of distributed fiber optic sensors

Distributed sensing with FOS has many advantages for strain monitoring, shape sensing and damage detection. However there are various factors that affect the sensitivity of the sensors. In this subsection, different parameters such as types of coating and twist pre-stress are investigated to enhance the measurement sensitivity of distributed FOS used in Rayleigh-Backscattering sensing (ODiSI-B manufactured by Luna Innovations), exposed to environmental and operational conditions of aircraft. To enhance the temperature measurement sensitivity, different UV curable materials including UV683, UV639 (manufactured by Permabond Engineering Adhesives Ltd) were adopted as the FOS coating. Compared to commonly used coatings such as acrylates and polyimide, these UV-curable coatings exhibit different Poisson's ratios and hardness, leading to distinct temperature sensitivities. However, this temperature sensitivity difference decreased significantly when FOS are mounted onto the surface of composite laminates due to the adhesive. To improve the strain measurement sensitivity, different coatings and pre-stressing of fibre (in form of twisting) are induced in FOS. Experiments confirm a small enhancement of strain measurement sensitivity with different coatings. A greater sensitivity enhancement was observed when pre-stress was induced before the tensile test.

3.2.1 Experimental setup

The OFDR system adopted in this experiment is ODiSI-B optical distributed sensor interrogator manufactured by LUNA Ltd. This system can realize nearly continuously strain or temperature measurement along the SMF with high accuracy and speed. This system is based on Rayleigh backscattering interference detection, which is sensitive to Fresnel reflection. Therefore, special SMF sensors with Fresnel reflection elimination are needed for this system in real applications. This type of SMF sensors consists of three parts: LC/APC connector, SMF, and no core fiber (NCF). The SMF is used as sensing part while the NCF is used for eliminating the Fresnel

reflection at the end of the sensor. The comparison of backscattering spectrum between sensor with and without NCF is shown in Figure 3.1. This figure illustrates that the backscattering spectrum of the sensor without NCF includes noise caused by the Fresnel reflection.



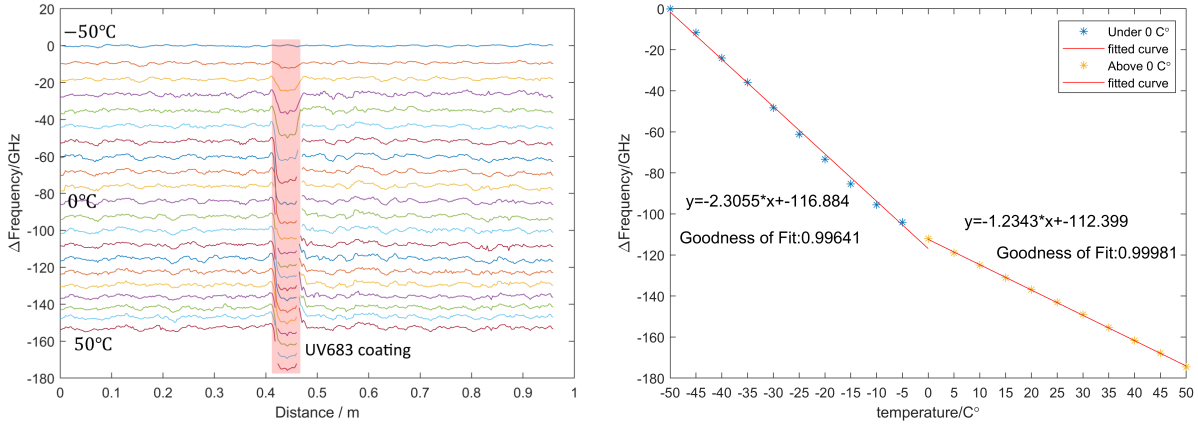
(a) (b)

Figure 3.1: The comparison of backscattering spectrum between sensors with and without NCF: (a) With NCF; (b) Without NCF

After the SMF sensor is manufactured, different coating materials are investigated for the temperature sensitivity enhancement. The recoating is realized by an optical fiber recoat device FSR-05 manufactured by Fujikura Ltd. The UV curable coating materials are required. After comparing parameters of numerous UV curable materials, UV683 and UV639 manufactured by Permabond Ltd were selected for the coating experiment since they are both suitable for FSR-05 and have different mechanical properties after curing. In addition, a thermoplastic film based on modified polyolefins (Pontacol 22.100) was adopted as adhesive to bond the SMFs to CFRP specimens. This type of thermoplastic film is employed due to its advantages of uniform and controllable pasting thickness, easy replacement, and maintenance. Thermoplastic films with similar properties can also be used to validate this work. The SMF with polyimide coating adopted in this subsection is manufactured by FIBERCORE Ltd, with a model number of SM1500 (9/125)P. The SMF with acrylate coating adopted in this subsection is manufactured by THORLAB Ltd, with a model number of 1550BHP.

3.2.2 Temperature measurement sensitivity enhancement

The measurement results of SMF change when exposed to temperature variation, due to thermal expansion. Therefore, selecting an appropriate coating can improve the temperature sensitivity of SMF. Based on this principle, temperature sensitivity of the bare fiber and four types of coating is investigated by temperature experiments. These experiments are carried out inside the Temperature Applied Sciences (TAS) conditioning chamber. The temperature range for these experiments was -50 to 50°C. The temperature information is directly obtained from the output of TAS conditioning chamber in these temperature experiments. Furthermore, these coatings were investigated under both free state and surface mounted state respectively to isolate the effect of temperate variation on sensor only and sensor surface bonded to composite with adhesive. The frequency shift of the fiber as a function of temperature is obtained which can then be used to mitigate and correct for the effect of temperature variation during in service operation.



(a) (b)

Figure 3.2: Temperature response of UV683 coating at free state: (a) Measurement data;(b) Temperature sensitivity

Figure 3.2(a) shows the measurement results of SMF sensor which contains UV683 coating. The recoated part (area covered by red shadows, which is around 0.06m) is obvious because of temperature sensitivity difference between UV683 and original coating (acrylate coating). Therefore, the temperature sensitivity of UV683 coating is calculated and plotted in Figure 3.2(b). This figure illustrates that UV683 coating shows different temperature sensitivity when

temperature is below and above 0°C. It is worth pointing out that 0 °C here is just an estimate. It is only used to roughly distinguish between the high-temperature range (small temperature sensitivity) and the low-temperature range (large temperature sensitivity). For example, in Figure 3.2(b), this value approaches -5 °C. This means that piecewise function is more suitable for describing the temperature sensitivity of these coatings.

The same temperature experiments were carried out with UV639, polyimide, and acrylate coatings. The sensitivity results for those coatings show identical characteristics with UV683 coating. However, the temperature sensitivity of UV683 and UV639 is much higher than polyimide and acrylate coatings when temperature is below 0°C. Finally, a temperature experiment of the bare fiber is conducted to compare its temperature sensitivity with different types of coating materials. The temperature sensitivity of different coating materials and bare fiber are summarized in Table 3.1. This table illustrates that the effect of the coating on temperature sensitivity is more pronounced at temperatures below 0°C. When temperature is above 0 °C, the temperature sensitivities of different coatings are similar to the bare fiber, which means that the effect of coating on temperature sensitivity is negligible. The new UV curable material adopted in this experiment (UV683 and UV639) shows much higher temperature sensitivity than commonly used acrylate and polyimide coating for temperatures below 0°C. Meanwhile, the polyimide coating shows lower degree of sensitivity difference in the whole temperature range than any other coating.

Table 3.1: Temperature sensitivity of different coating materials at the free state

Material type	Above 0°C (GHz/°C)	Below 0°C (GHz/°C)	Difference (GHz/°C)
UV683	2.31	1.23	1.08
UV639	2.15	1.29	0.86
Polyimide	1.31	1.21	0.1
Acrylate	1.70	1.38	0.32
Bare fiber	1.04	1.23	0.19

The aforementioned results are acquired when the sensor is in an unrestrained state. In this unconstrained condition, the SMF sensors are positioned directly on the surface of the specimen without any bonding. After this, another temperature experiment was conducted when

these SMF sensors are surface mounted on a composite plate. These sensors are mounted on the surface of the specimen with a thermoplastic adhesive film based on modified polyolefins manufactured by Cornelius. The specimen with SMF and thermoplastic adhesive film is placed in a vacuum heating table for around 1h under vacuum and 150°C. The SMF is mounted well on the surface of specimen after cooling down.

The temperature range of the experiment is -50 to 50 °C (Due to data loss at low temperatures, some results only show results above -30 °C or -40 °C). Since the UV683 and UV639 coatings show similar temperature sensitivity in the previous experiment (free state), only the UV683 coated fiber is investigated when surface mounted by thermoplastic adhesive film based on modified polyolefins. Therefore, the temperature sensitivity of the bare fiber and three different recoated sensors surface mounted are investigated.

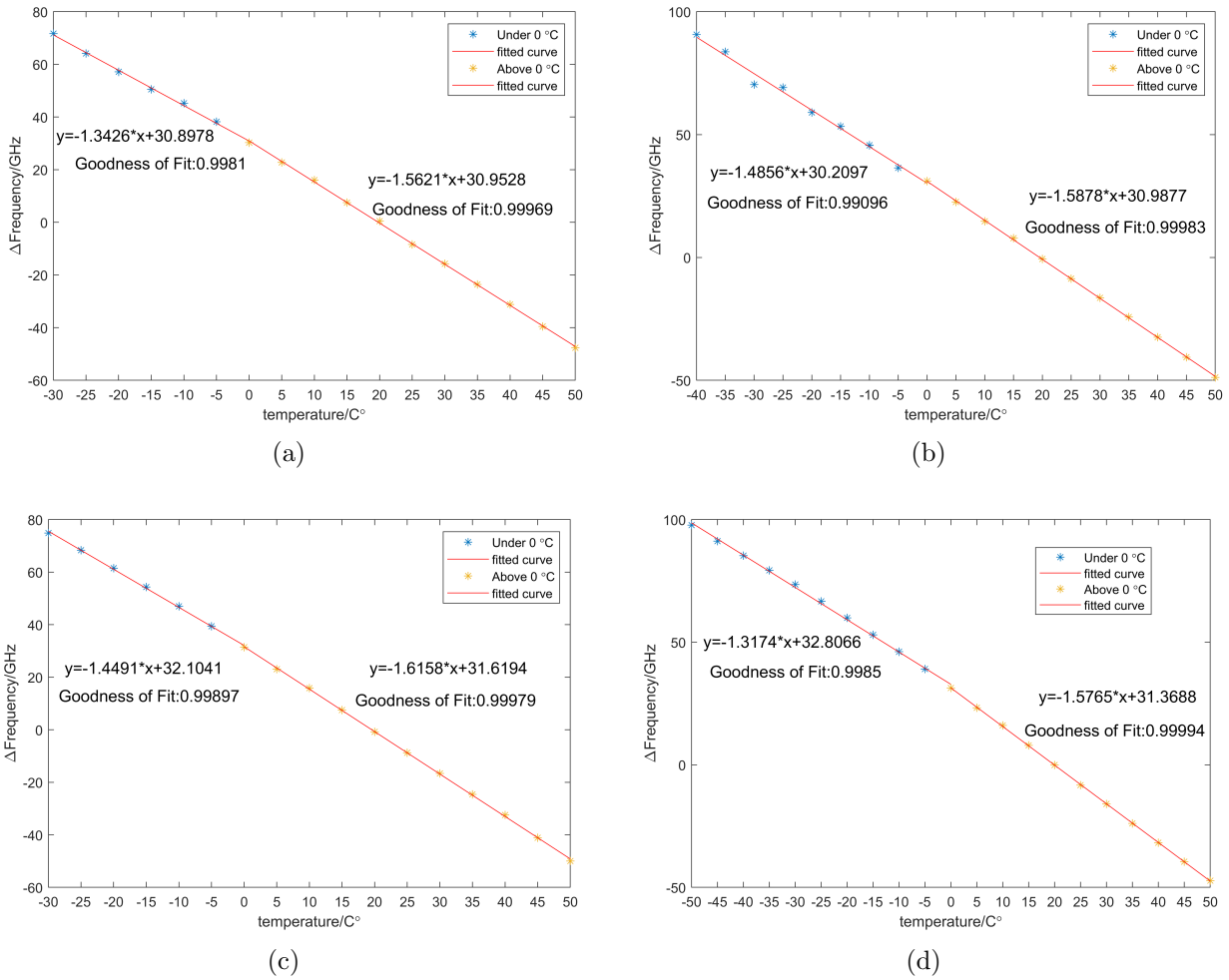


Figure 3.3: Temperature response for different coatings after surface mounting: (a) UV683 coating; (b) Polyimide coating; (c) Bare fiber optic sensor; (d) Arcylate coating

The temperature experiment results are shown in Figure 3.3. As with the free state, the specific values of different coatings are summarized in a table (table 3.2). This table illustrates that temperature sensitivity decreases significantly after surface mounting when temperature is below 0 °C. All coatings show similar temperature sensitivity in the whole temperature range. This phenomenon demonstrates that the effect of coating type on temperature sensitivity is negligible when the SMF is surface mounted on the structures. This is because the temperature sensitivity of SMF is mainly determined by the thermal response of composites and thermoplastic adhesive film after surface mounting.

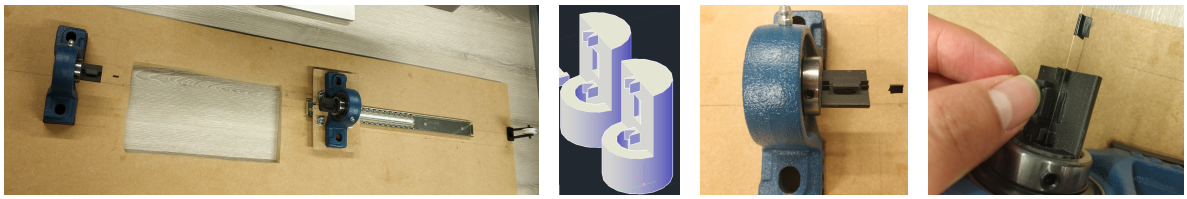
Table 3.2: Temperature sensitivity of different coatings after surface mounting

Coating material	Below 0°C (GHz/°C)	Above 0°C (GHz/°C)	Difference (GHz/°C)
Original acrylate	-1.32	-1.58	0.26
UV683	-1.34	-1.56	0.22
Bare	-1.45	-1.62	0.17
Original polyimide	-1.49	-1.59	0.10

3.2.3 Strain measurement sensitivity enhancement

Two strategies were adopted to enhance the strain sensitivity of the fiber optic sensors in this subsection. The first one is using different coating. The second one is inducing pre-stressing to the SMF sensors by twisting the fibre. The strain in these two strategies were measured by ODiSI-B system with the strain-frequency shift coefficient of 6.7$\mu\varepsilon$/GHz. A loading device was designed for this experiment to enable controlled twisting of the SMF, shown in Figure 3.4(a) and Figure 3.4(b) shows the design of the special clamps required for twisting. The installation of fiber clamps is shown in Figure 3.4(c) and Figure 3.4(d). This loading device is used to directly apply uniform twisting to SMF. When subjecting the device above to a load, the counterweight is linked to the fiber optic clamp on the right side via a thin wire and a pulley. Furthermore, with the left bearing secured, a torsional load can be induced on the fiber by rotating the right bearing.

The first strategy is conducted based on the bare fiber and two coatings including UV683



(a) (b) (c) (d)

Figure 3.4: The diagram of loading device and clamps: (a) The loading setup; (b) The design of clamps; (c) The clamps by 3D printing; (d) The installation of fiber optic sensors

coating and acrylate coating. During the experiment, 10 uniform weights were added step by step in order to apply controlled strain and monitor the response of the sensor at each strain level. All experiments were repeated ten times to ensure the reliability of the data. The mean results of these experiments are shown in Figure 3.5, where Figure 3.5(a) shows the strain sensitivity of the original acrylate coating; Figure 3.5(b) is the strain sensitivity of the bare fiber; Figure 3.5(c) is the strain sensitivity of the UV683 recoated fiber. The strain sensitivity of UV683 coating and acrylate coating are only slightly different from the bare fiber.

The second strategy is inducing pre-load before recoating. Different number of twists is induced before the uniform weights are applied. As same as as first strategy, all experiments were repeated ten times to ensure the reliability of the data. The mean results of these experiments are shown in Figure 3.6, where (a) is the strain sensitivity without pre-load (b) shows the strain sensitivity with 20 twists; (c) is the strain sensitivity with 30 twists. It is worth noting that the strain sensitivity in Figure 3.5 is different from the strain sensitivity in Figure 3.6. This is because the weights adopted in these experiments are different. The former one weighs approximately twice as much as the latter. Therefore, this diagrams illustrate that inducing the pre-load can improve the strain sensitivity of SMF sensors in distributed sensing.

3.2.4 Conclusions

The enhancement of temperature and strain measurement sensitivity in SMF based distributed sensing was investigated. Different UV curable materials including UV683 and UV639 were adopted to enhance the temperature measurement sensitivity. According to the experimental

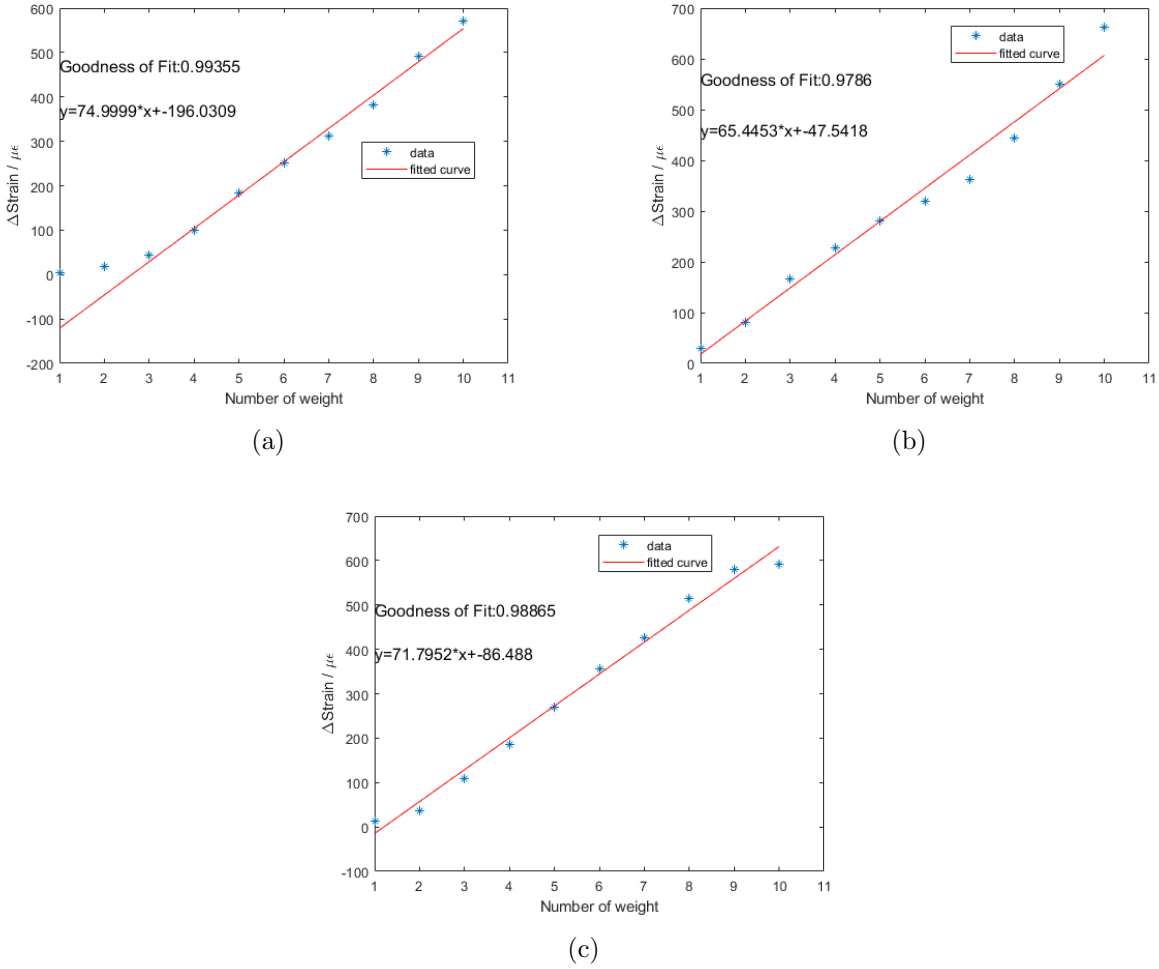


Figure 3.5: The strain sensitivity of different coatings at free state: (a) Acrylate coating; (b) Bare fiber optic sensors; (c) UV683 coating

result, UV curable coatings show different temperature sensitivity when temperature is below and above 0°C. For example, temperature sensitivity of UV683 is 2.31 GHz/°C and 1.23 GHz/°C respectively when temperature is below and above 0°C. Comparing with the commonly used coatings such as acrylates and polyimide, these UV curable coatings show higher temperature sensitivity, especially in low temperature range (-50°C to 0 °C). Several factors could contribute to this phenomenon, such as an elevated thermal strain transfer coefficient resulting from the hardening of the coating material at low temperatures, potential temperature measurement errors during the experiment, and other experimental inaccuracies. Consequently, additional experimental validation is required. In addition, the temperature sensitivity of different types of coating materials decreases significantly when SMF sensors are mounted to the surface of composite laminates. This is because the adhesive severely influences the temperature response

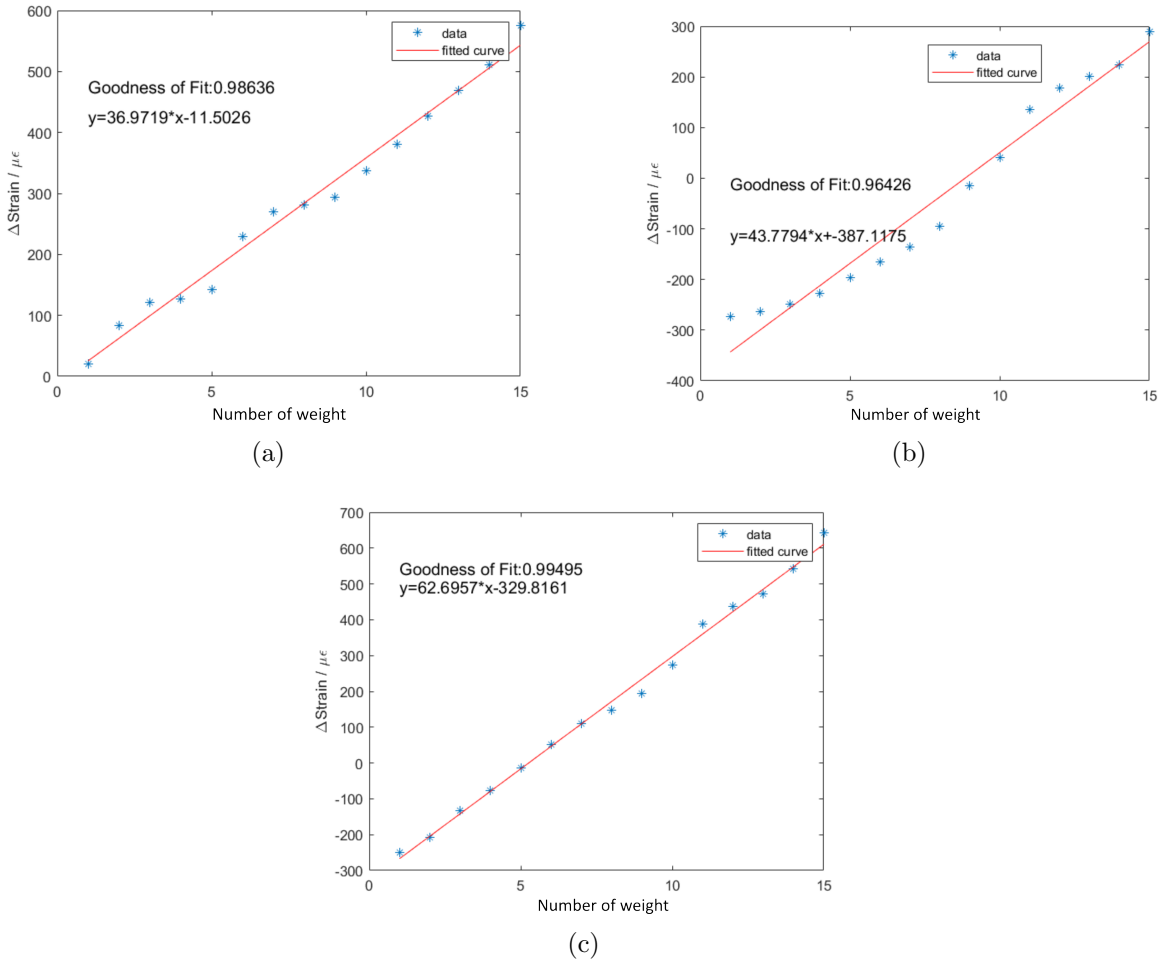


Figure 3.6: The strain sensitivity under different twist pre-loads at free state: (a) Without twist; (b) Twist 20; (c) Twist 30

of the coating when surface mounted.

To improve the strain measurement sensitivity, different coatings and pre-stress are induced in SMF sensors. Experiments confirm a small enhancement of strain measurement sensitivity with different coating. A greater sensitivity enhancement than different coatings is observed when pre-stress is induced by twisting the fiber, before tension is applied. However, it was concluded that applying pre-stress through twisting of the fiber is not a very controlled way for increasing its sensitivity. Further investigation is required to propose a strategy to control the induced pre-stress in a repeatable way and to ensure that there will not be significant relaxation in time. The higher strain sensitivity is essential for applications such as high accurate strain measurement, temperature measurement, and temperature compensation.

3.3 Accuracy of distributed strain sensing in CFRP under thermal and mechanical load

In this subsection, the strain measurement accuracy of SMF under thermal load is investigated by strain-frequency shift coefficient analyses. This research allows for the application of SMF sensors for structural health monitoring in real operational conditions. The strain measurement accuracy under combined static tension and thermal load is investigated experimentally, which demonstrated that temperature fluctuations induce non-negligible error in the strain measurement, even with temperature compensation applied. The temperature fluctuation range which can induce measurement errors is quantified as less than -20°C or higher then 55°C. Findings from experiments can be applied to improve the structural health monitoring reliability for in service application and reduce false positives.

3.3.1 Static loading experiment setup

Specimen and sensors

The size of the specimen manufactured and tested is $50 \times 100 \times 3.2$mm. This specimen is made of CYTEC non crimp fabric. The layout of this specimen is $[45/90/-45/0/45/0_2/-45]_s$. The thickness is 3.2mm and the elastic properties of the lamina is shown in table 3.3.

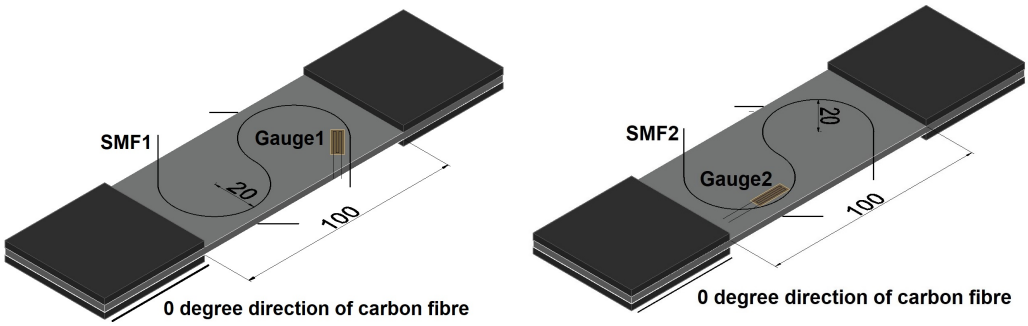
Table 3.3: Elastic parameters of the lamina used in this subsection

Parameters	Symbol	Unit	Value
Elastic modulus	E_{11}	MPa	111800
	$E_{22} = E_{33}$		7620
Poisson's ratio	v_{23}	-	0.450
	$v_{12} = v_{13}$		0.290
Shear modulus	G_{23}	MPa	2628
	$G_{12} = G_{13}$		4130

The single mode fibre (SM1500(9/125)P manufactured by FIBERCORE) and strain gauges are

both adopted in the experiment for strain measurement. The SM1500(9/125)P with polyimide coating has a variety of features such as high temperature survival and bend insensitive, which makes it very attractive for distributed strain sensing. In this work, the single mode fibres were adopted for strain measurement of composite laminates under both mechanical load and thermal load. The frequency shift of SMF can be related to a temperature or strain change. This relationship is expressed in equation3.1. In this equation, both K_T and K_ϵ are usually regarded as constant in the reported applications. For example, this equation works in a temperature range of -40°C to 220°C or in a strain range of -10000$\mu\epsilon$ to 10000$\mu\epsilon$ for ODiSI-B system manufactured by LUNA Ltd.

The SMF and strain gauges are bonded to the surface of the specimen by a thermoplastic adhesive film based on modified polyolefins (Pontacol 22.100). This type of thermoplastic adhesive film is adopted because of advantages including easy maintenance, high peel strength, and controllable thickness [201, 182, 229, 183]. As shown in Figure 3.7, two "S" shape SMF, called SMF1 and SMF2 are mounted on each sides of the specimen independently, to provide strain readings in different directions. The SMF was extended directly out from the edge of the specimen. A strain gauge is mounted on each sides of the specimen: on side 1 at $-45°$ with respect to the fibre direction, defined as Gauge1 (as shown in Figure 3.7(a)), and at 0° on side 2 (as shown in Figure 3.7(b)) defined at Gauge2. The data acquired by these two strain gauges are used as reference strain for the strain-frequency shift coefficients calculation.



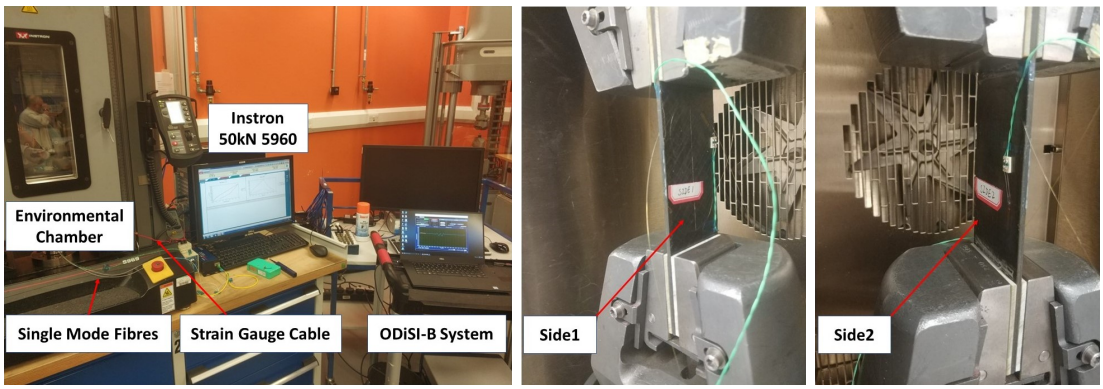
(a) (b)

Figure 3.7: Layout of sensors on specimen: (a) The sensors configuration of side 1; (b) The sensors configuration of side 2

Static loading experiment

In the static loading experiment, a simultaneous loading of temperature and tension was applied to the specimen. This load was realized by the combination of an Instron dual-column machine (Instron 50kN 5960 system) and a fitted environmental chamber(Instron 3119-600) shown in Figure 3.8(a). Figure 3.8(b) and Figure 3.8(c) show side 1 and side 2 of the specimen in the test set-up. The SMF data was acquired by ODiSI-B system manufactured by LUNA Ltd. The temperature on the surface of specimen in this experiment is measured by a wired digital thermometer (68022-2P manufactured by Gain Express Holdings Ltd.).

Two types of tests were carried out: first test scenario is measurement of frequency shift with tensile load, under different temperature. In this test scenario, the temperature changed from -30°C to 80°C in steps of 5°C. Each time when the temperature stabilised, the reference spectrum of SMF sensor was reset. A 0 to 10kN (625MPa) tensile load was then applied to the specimen and the frequency shift of SMF was acquired. Therefore, this frequency shift is only caused by tension load under different temperature. Another test scenario was to continuously measure the frequency change with tension and temperature variation. In this test, the temperature changed from -30°C to 80°C in steps of 5°C. The reference spectrum of SMF is only set once at -30°C. A 0 to 10kN (625MPa) tension load is directly applied to the specimen each time after the temperature became stable. Therefore, the measured frequency shift in this test scenario contains the combined effects of both tension and temperature variation.



(a) (b) (c)

Figure 3.8: Static loading experiment setup: (a) The experiment setup; (b) The side 1 of composite specimen; (c) The side 2 of composite specimen

3.3.2 Data analyses of static loading experiment

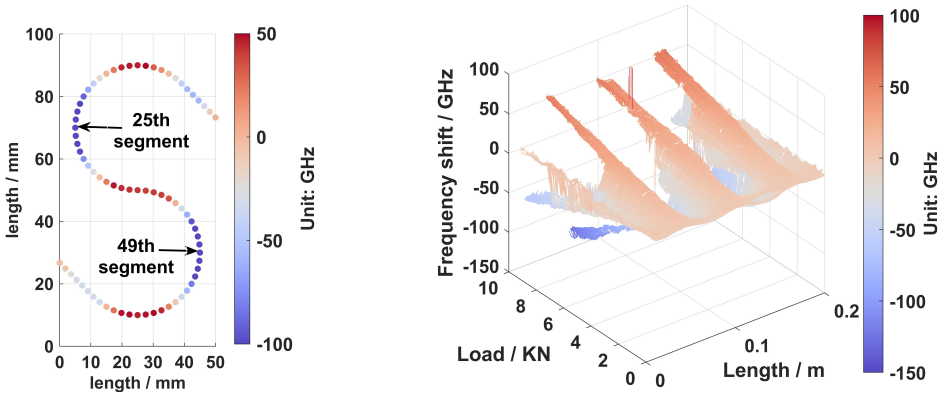
Data cleaning and reconstruction

In the static loading experiment, many outliers and null values are observed in the measurement data acquired by ODiSI-B system because of similarity degenerate between measurement and reference Rayleigh backscattering under high load, which can significantly affect the results [161, 77]. Therefore, an algorithm is developed for data cleaning and reconstruction. The data of SMF2 at -30°C in an independent test of the first test scenario, is used to illustrate the data reconstruction algorithm. The first step is outlier elimination. This is realized by local outlier factor (LOF) algorithm [230].This method is adopted becasue of the continuity of strain measurements. A constant LOF (Δv_{LOF} in equation 3.2) is sufficient to achieve the outlier elimination in this experiment since the outliers are orders of magnitude greater than other data points. Assuming that the measurements of SMF is $(x_i, \Delta v_i), (i = 1, 2, \cdots, N)$. The data after the elimination with LOF algorithm ($\Delta \widetilde{v_i}$) is shown in equation 3.2.

$$\Delta \widetilde{v_i} = \begin{cases} null & \Delta v_i' \geq \Delta v_{LOF} \\ \Delta v_i & \Delta v_i' < \Delta v_{LOF} \end{cases} \qquad i = 1, 2, 3, \cdots, N \tag{3.2}$$

After the elimination, the data of surface mounted area is extracted according to peak alignment. Since the spatial resolution of ODiSI-B system is 2.6mm, 73 sensing segments are included along the fibre length according to its layout. The peak value of measurement data indicates the sensing segment along the loading direction in the static loading experiment (around 25th and 49th sensing segment as shown in figure 3.9(a)). Therefore, the data along the fibre orientation is extracted according to the locations of the peak values. The data after filtering and extraction is shown in Figure 3.9(b). The x-axis shows the spatial distribution of the measurement segments of SMF, which range from 0 to 0.2m; the y-axis shows the static load from 0 to 10 kN ; the z-axis plots the frequency shift of ODiSI-B at each measurement segment under

each static load.



(a) (b)

Figure 3.9: Sensing segments distribution and measurement data of SMF2 in static loading experiment (under -30°C of the first test scenario): (a) The measurement data on fibre optic sensor; (b) The data after filtering and extraction

Null values are observed after outlier elimination, which implies a significant information loss. The occurrence of data drop-outs can be attributed to the potential challenges posed by large strain gradients and their impact on the performance of the correlation algorithm. In situations where substantial strain gradients are present, the correlation algorithm may face difficulties in accurately tracking and matching the pattern changes in frequency domain. Large strain gradients can lead to rapid and significant changes in the features in frequency domain after FFT, making it challenging for the algorithm to maintain a continuous and reliable correlation. Temporal-based and spatial-based reconstruction methods [231] are adopted to address this problem since the measurement data has a clear spatial and temporal pattern. In time domain, linear fit between load and frequency shift is adopted first for data reconstruction. This is because of the linear relationship between the tension load and the measurements for every measurement segments on SMF. All missing data was reconstructed after the linear fit in time domain. The results are shown in Figure 3.10(a). However, because of low signal-noise ratio and measurement errors, there still exist errors after the linear fit. These errors (discontinuous value) are clearly indicated in Figure 3.10(a). Therefore, the robust locally weighted scatter-plot smoothing (RLOWESS) algorithm is adopted to eliminate these errors and to smooth the the data in temporal and spatial domain [232]. The discrete measurements of SMF measurements after outlier elimination and linear fit reconstruction is $(x_i, \Delta\hat{v}_i), i = 1, 2, 3, \cdots, N$. The mea-

surements within a local sliding window at $[x_p, x_q], (1 \leq p < q \leq N)$ are adopted for RLOWESS algorithm. The weighted function adopted in this method is given by the symmetric tricube function shown below.

$$w_k = \left(1 - \left|\frac{x_{\lfloor (p+q)/2 \rfloor} - x_k}{d_{pq}}\right|^3\right)^3 \qquad k = p, p+1, \cdots, q-1, q \tag{3.3}$$

where w_k is the weight of the $k-th$ measurement in the linear regression; $x_{\lfloor (p+q)/2 \rfloor}$ is the centre of the local sliding window, which has the highest weight in linear regression; x_k is the measurements within the local sliding window; d_{pq} is the Euclidean length of the local sliding window. Therefore, the sum of the residual squares after weighted linear regression is expressed by Equation 3.4.

$$J(a,b) = \frac{1}{(q-p+1)} \sum_{k=p}^{q} w_k (a \cdot x_k + b - \Delta\hat{v}_k)^2 \qquad k = p, p+1, \cdots, q-1, q \tag{3.4}$$

where a and b are the estimated coefficients of weighted linear regression. Therefore, the optimal solution of a and b is obtained by minimising $J(a,b)$, as expressed in Equation3.5.

$$\begin{cases} \dfrac{\partial J(a,b)}{\partial a} = \dfrac{2}{(q-p+1)} \displaystyle\sum_{k=p}^{q} w_k \cdot x_k (a \cdot x_k + b - \Delta\hat{v}_k) = 0 \\ \dfrac{\partial J(a,b)}{\partial b} = \dfrac{2}{(q-p+1)} \displaystyle\sum_{k=p}^{q} w_k (a \cdot x_k + b - \Delta\hat{v}_k) = 0 \end{cases} \qquad k = p, p+1, \cdots, q-1, q \tag{3.5}$$

Following by the weighted linear regression mentioned above, a modified weighted function based on regression residual is adopted to enhance the robustness of this algorithm. This modified weighted function is shown in Equation 3.6

$$\widetilde{w}_k = \begin{cases} (1-(r_k/6Med)^2)^2 & r_k < 6Med \\ 0 & r_k \geq 6Med \end{cases} \qquad k = p, p+1, \cdots, q-1, q \tag{3.6}$$

where $r_k = a \cdot x_k + b - \Delta\hat{v}_k$ expresses the regression residuals; $Med = |median(r_k)|$ is the median absolute deviation of the residuals. The result after data cleaning and reconstruction is shown in Figure 3.10(b).

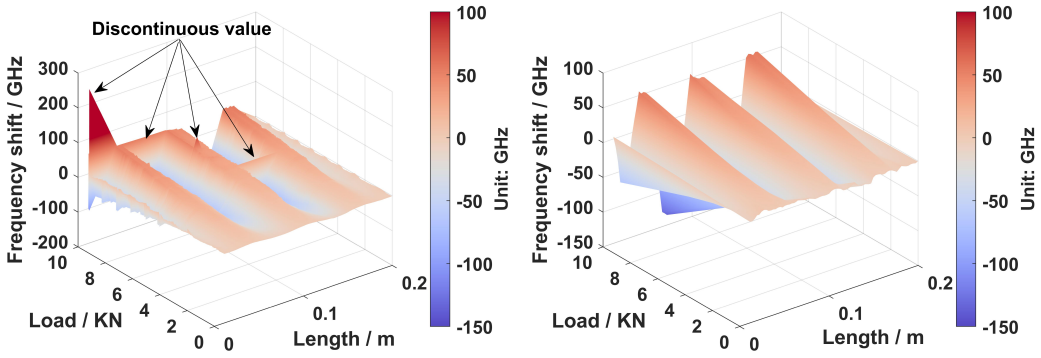


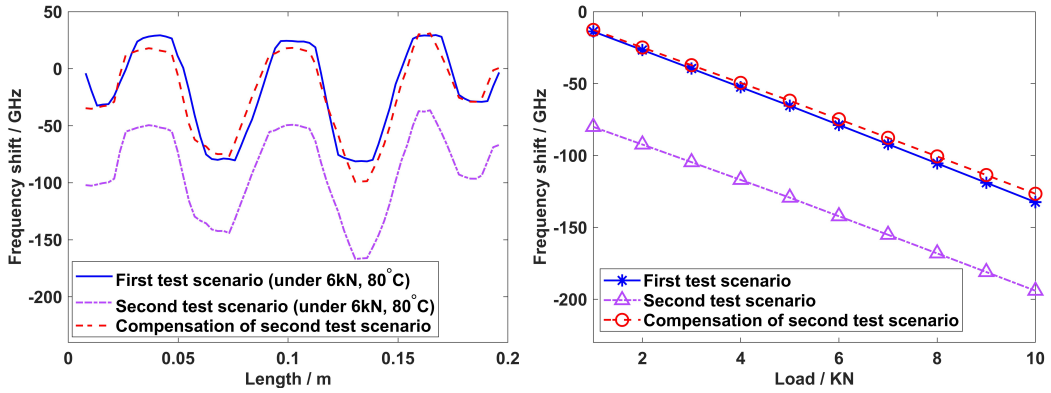
Figure 3.10: Data cleaning and reconstruction results of SMF2 measurements in static loading experiment: (a) The measurement data after the linear fit; (b) The measurement data after cleaning and reconstruction

It is worth noting that the smoothing process mentioned above is intended to restore the outliers and null values that are a result of systematic errors of ODiSI-B . However, this process may inadvertently mask crucial strain features in proximity to the damage region, thereby negatively impacting certain applications such as damage detection.

Temperature compensation

The data cleaning and reconstruction algorithm successfully restored the results in both test scenarios. As mentioned above, the recorded data in both tests are different: the continuous measurements from the second test scenario contain tension and temperature information, whereas measurements from the first test scenario are mainly influenced by tension load. To

illustrate the measurement consistency of both scenarios, a temperature compensation is applied to the continuous measurement test based on the data recorded at the part of the SMF which is only exposed to thermal load. The continuous measurements from the second test scenario are compensated and then compared with the measurements from the first test scenario. The comparison result under 80°C is shown in Figure 3.11. Where Figure 3.11(a) shows the results of distributed measurements at 6kN (375MPa) tension load. Figure 3.11(b) shows the frequency shift along the load direction, under different tension loads. Note that the data of 49th segment on SMF2 (Figure 3.9(a)) is adopted in this figure. This comparison illustrates that the compensated result of both test scenarios are highly consistent. Therefore, the measurements from first test scenario are regarded as continuous measurements with temperature compensation in the following analyses.



(a) (b)

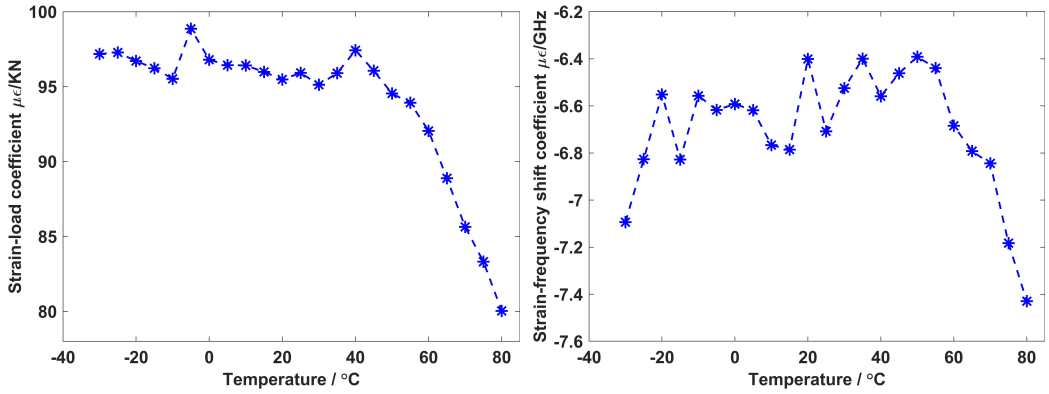
Figure 3.11: Temperature compensation results of SMF2 in static loading experiment: (a) The temperature compensation results of distributed measurements at 6kN (375MPa) tension load; (b) The temperature compensation results along the load direction under different tension loads

Strain measurement accuracy under thermal load

The measurements from the first test scenario after data cleaning and reconstruction are adopted in strain calculation based on the above analyses. Since these measurements are in the form of frequency shift of the SMF, the selection of the strain-frequency shift coefficient directly influences the strain results. Constant strain-frequency shift coefficient is usually used under different measurement states in real applications. However, the question raises that whether variability in operational conditions will also influence this coefficient. In other words, if the

strain-frequency shift is calculated at room temperature , e.g. 20°C, can this coefficient be used to convert the SFM readings recorded at a different temperature, to strain? Therefore, in this work the strain-frequency shift coefficient at different ambient temperature is investigated in detail.

The strain-frequency shift coefficient is calculated based on measurements of SMF2 and Gauge2, with Gauge2 measurements being adopted as the reference strain. Therefore, the reliability of these strain gauge measurements at different temperatures is first investigated. Under the experimental conditions in this subsection, this stability can be directly reflected by the variation in strain-load coefficient of Gauge2. This strain-load coefficient is the ratio between strain shift and the corresponding load shift. This coefficient should be stable because it is not expected to see any reduction in the CFRP modulus at -30°C to 80°C [233]. However, as shown in Figure 3.12(a), a significant decreasing trend is observed at temperatures greater than 45°C. This decrease is mainly caused by deterioration of the thermoplastic adhesive film used for bonding the sensors.



(a) (b)

Figure 3.12: Strain-load coefficient of Gauge2 and Strain-frequency shift coefficient of SMF2 under thermal load: (a) The Strain-load coefficient of Gauge2 under thermal load; (b) The strain-frequency shift coefficient of SMF2 under thermal load

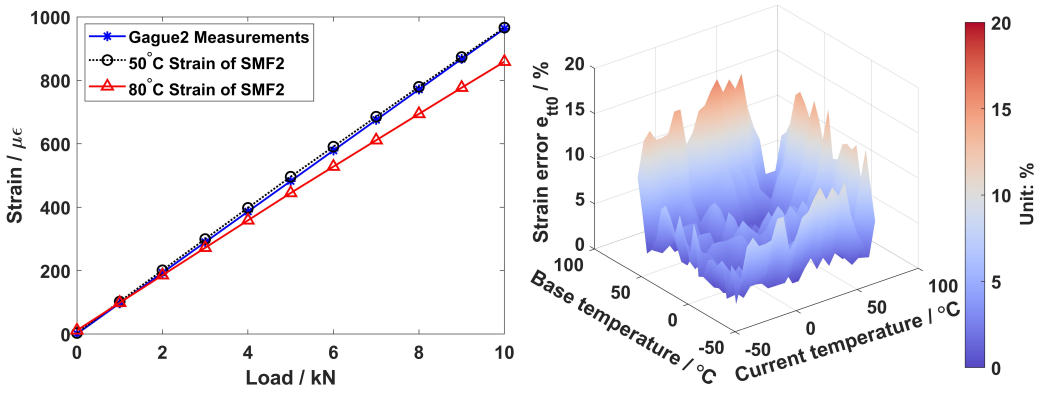
To obtain a reliable reference strain, the average value of strain-load coefficient at temperatures below 45°C is adopted to calibrate the measurement strain of Gauge2 above 45°C. With the calibrated reference strain and SMF2 measurements near Gauge2 (49th segment shown in Figure 3.9(a)), the strain-frequency shift coefficient is directly calculated and shown in Figure 3.12(b). This coefficient is stable when temperature stays between -20°C and 55°C. However, when

temperature becomes higher than 55°C or lower than -20°C, a significant decrease is observed. This decrease induces non-negligible errors in SMF strain even with temperature compensation when a constant strain-frequency coefficient is adopted. This conclusion is demonstrated by Figure 3.13(a) which shows a comparison of Gauge2 reference strain and the calculated strain from the SMF2 at 50°C and 80°C when the strain-frequency shift coefficient at 20°C is adopted. Note that the data of 49th segment on SMF2 (Figure 3.9(a)) is adopted in this figure. Based on this conclusion, a further analysis of SMF strain error is conducted. In this analysis, the frequency shift under current state and the strain-frequency shift coefficient under baseline state are adopted to calculate the SMF strain. The error between the calculated SMF strain and the reference strain is defined as e_{tt_0}:

$$e_{tt_0} = \frac{g(t_0)\Delta f - S_{gt}}{S_{gt}} \times 100\% \tag{3.7}$$

where t is temperature of the current state, t_0 is temperature of the baseline state; Δf expresses the frequency shift of the SMF under the current state; $g(t_0)$ expresses the strain-frequency coefficient for the baseline state; S_{gt} denotes the reference strain under the current state. The error for different current and baseline states combinations are shown in Figure 3.13(b). In this figure, the x-axis is the temperature of current state (the frequency shift data of SMF2 is adopted under this temperature); the y-axis shows the temperature of baseline state (the strain-frequency shift coefficient is adopted under this temperature); the z-axis express the percent error of calculated strain compared with reference strain. For comparing with reference strain, only the data of 49th segment on SMF2 (Figure 3.9(a)) is adopted in this figure. This figure illustrates that e_{tt_0} increases rapidly when temperature of the current or the baseline state is below -20°C or above 55°C. This result suggests that a constant strain-frequency shift coefficient cannot be adopted for strain measurement at all temperature conditions. However,there exists a temperature insensitive area according to 3.13(b). When the temperature of both current and baseline states are between -20°C to 55°C, e_{tt_0} is less than 2% and a constant strain-frequency shift coefficient can be adopted. Therefore, the calibration of strain-frequency shift coefficient

is only necessary when the measurement temperature is out of this range.



(a) (b)

Figure 3.13: Strain calculation errors of SMF2 in static loading experiment: (a) The comparison of Gauge2 reference strain and the calculated strain from the SMF2 at 50°C and 80°C when the strain-frequency shift coefficient at 20°C is adopted; (b) The error for different current and baseline states combinations

Numerical verification

The SMF strain is calculated and analyzed in the previous sections. For example, the calculated strain along SMF2 under different load at 20°C is shown in Figure 3.14.

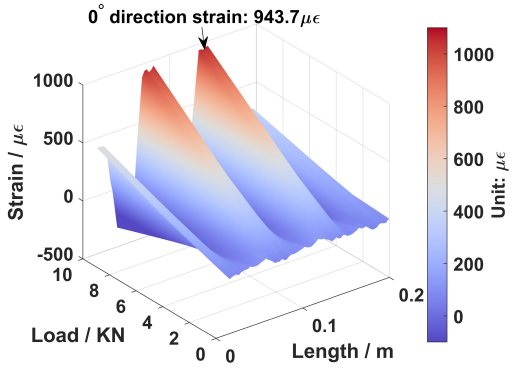
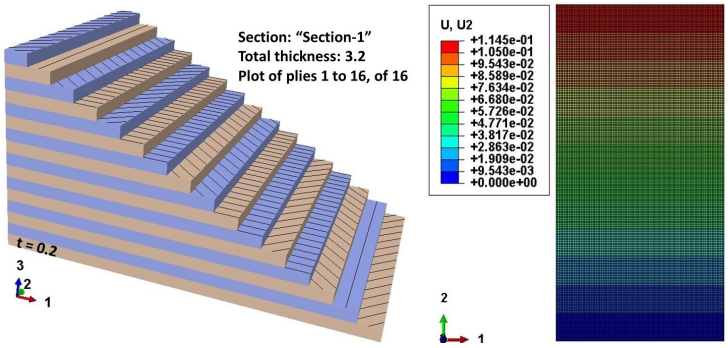


Figure 3.14: Strain calculated from SMF2 under 10kN(625MPa) tension and 20°C

To validate the reliability of the calculated strain, a numerical model is built based on the elastic parameters of the carbon fibre which is shown in table 3.3. Figure 3.15(a) shows the model of the composite laminate. A 10kN (625MPa) tension load is applied to the short edge of the composite laminate. The simulation result is shown in Figure 3.15(b). The maximum

displacement is $0.1145mm$, which means the strain of the specimen under 10KN (625MPa) tension is $1145\mu\varepsilon$.



(a) (b)

Figure 3.15: Numerical modelling results: (a) The model of the composite laminate; (b) The simulation result of finite element method

As shown in Figure 3.14, the calculated strain of SMF2 under 10kN(625MPa) tension at 0° direction is $943.7\mu\varepsilon$ ($t_0 = t = 20°C$), which is less than the numerical result. This is mainly because of the strain transfer rate between the substrate and SMF. In the work of [234], a model is built to estimate this strain transfer rate α by Equation 3.8. The expression of k in this equation is shown in Equation 3.9

$$\alpha = 1 - \frac{2sinh(0.5kL_f)}{kL_f cosh(kL)} \tag{3.8}$$

$$\frac{1}{k^2} = \frac{E_f}{G_a}\left(\frac{r_f}{2} - \frac{\pi {r_f}^2}{D}\right)\left(\frac{h}{4} - \frac{r_f}{2}\right) + \frac{h_i}{2G_m}\left[E_a\left(h - \frac{\pi {r_f}^2}{D}\right) - E_f\frac{\pi {r_f}^2}{D}\right] \tag{3.9}$$

Where α is strain transfer rate; L_f represents the sensing gauge length; r_f expresses the radius of SMF; h denotes bonding thickness; D is the bonding length; G_m is the shear modulus of composite laminate; E_f is the elastic modulus of SMF; h_i represents the influence depth of the shear stress; E_a denotes the elastic modulus of the adhesive film; G_a is the shear modulus of the adhesive film.

The parameters of the thermoplastic adhesive film and SMF adopted in this experiment are summarized in table 3.4. With these parameters, the strain transfer rate is therefore obtained

using Equation 3.8 and Equation 3.9, which was calculated to be 0.842 (set $G_m \approx G_{23}$). In this experiment, the strain transfer rate calculated from the modelling result and SMF measurement is 0.824. This result agrees fairly well with the value of the strain transfer rate calculated from the literature [234]. This result demonstrates that the calculated strain of SMF2 based on the proposed data cleaning and reconstruction, temperature compensation, strain-frequency shift coefficient calibration is highly accurate and reliable.

Table 3.4: Parameters of thermoplastic adhesive film and SMF adopted in the experiment

Parameters	Symbol	Unit	Value
Sensing gauge length	L_f	mm	10
SMF radius	r_f	mm	0.0625
Bonding thickness	h	mm	1
Influence depth	h_i	mm	1
Bonding width	D	mm	1
Bonding length	$2L$	mm	10
Shear modulus of composite laminate	$G_m \approx G_{23}$	MPa	2628
Elastic modulus of SMF	E_f	MPa	72000
Elastic modulus of film	E_a	MPa	2780
Shear modulus of film	G_a	MPa	1000

3.3.3 Conclusions

This subsection investigates the robustness of single mode fibres, as strain sensors, for in-field application where the operational and environmental conditions such as thermal fluctuations can influence the reliability of the strain distribution. Because SMF do not measure strains directly, there needs to be a conversion coefficient used for transferring the recorded frequency-shifts to strain output. In this subsection, the influence of temperature on the calculation of this conversion coefficient was investigated in detail. To this aim, the static loading experiment was conducted on a CFRP specimen under thermal and mechanical loads. The strain measurement were compared with strain gauge readings and the errors of the SMF-based distributed sensing were investigated by strain-frequency shift coefficient analyses under temperature fluctuation.

In summary, SMF-based distributed sensing own much higher spatial resolution compared to strain gauges. In addition, the findings of this study reveal that temperature fluctuations intro-

duce significant errors in strain measurement, despite employing temperature compensation. Nevertheless, a temperature-insensitive range exists, within which these errors are negligible. In the current investigation, this temperature-insensitive range was identified as -20°C to 55°C. To achieve highly accurate strain measurements during in-field applications when the measurement temperature falls outside this range, it becomes imperative to calibrate the strain-frequency shift coefficient.

3.4 Accuracy of distributed strain sensing in composite laminates under fatigue loads

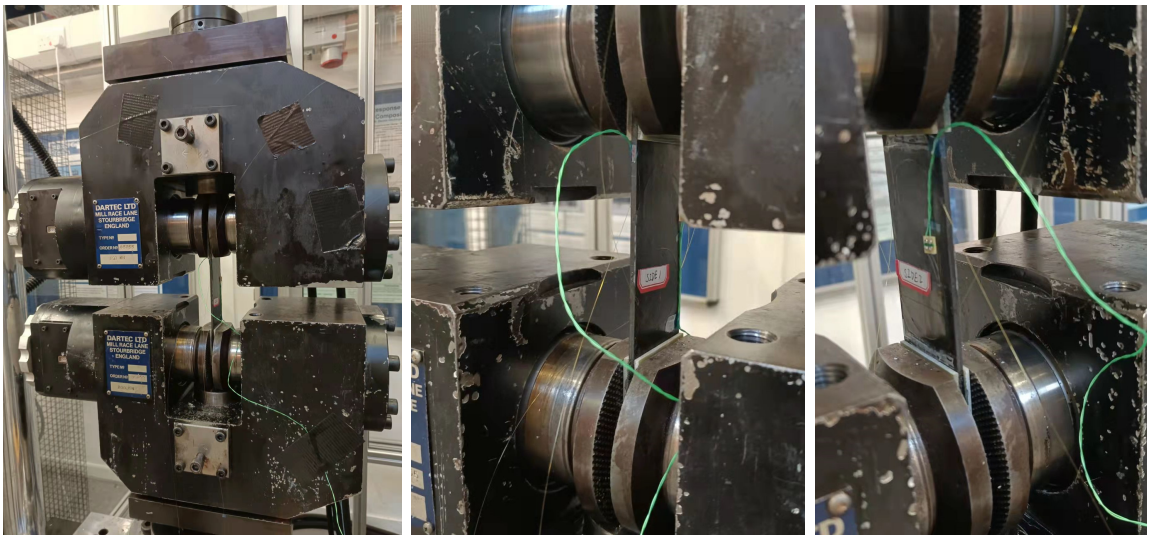
This subsection delves into the examination of strain measurement accuracy for SMF under the influence of fatigue loads using strain-frequency shift coefficient analyses. This investigation is significant for enabling the practical application of SMF sensors in real-world operational conditions for structural health monitoring. A fatigue experiment is conducted to evaluate the accuracy of strain measurements under low-frequency fatigue loads.

The outcomes of the fatigue experiment concluded that loads primarily lead to an increase in the proportion of null values in the recorded strain measurements.

3.4.1 Fatigue experimental setup

The specimen and sensors utilized in the fatigue experiment are identical to those introduced in Chapter 3.3. In the fatigue experiment, a 5 Hz sine wave signal was used. The range of this load was set between 0 and 3kN (187.5MPa). The specimen was tested in an Instron 8032 servo-hydraulic universal testing machine, as shown in 3.16(a). Side 1 and side 2 of the specimen in the test set-up are depicted in Figure 3.16(b) and Figure 3.16(c), respectively.

The fatigue experiment lasted for a whole week to reach more than 1.6 million fatigue cycles. This experiment was carried out at room temperature. The strain gauge data was measured



(a) (b) (c)

Figure 3.16: The setup of fatigue experiment: (a) The experiment setup; (b) The side 1 of specimen; (c) The side 2 of specimen

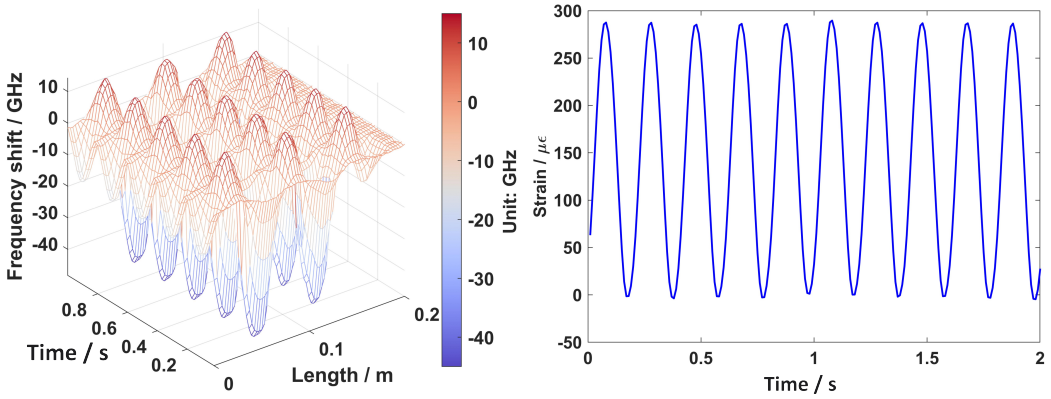
automatically every 1000 fatigue cycles. As for the SMF data, only SMF2 was measured about every hour during the day time. This is because the ODiSI-B system cannot support multiple channels during dynamic measurements. The main purpose of the fatigue experiment was to evaluate the applicability of the SMF under continuous dynamic measurement and frequency-strain coefficient stability under low frequency mechanical load.

3.4.2 Data analyses of fatigue experiment

Dynamic measurements and data re-sampling

In the fatigue experiment, the data of SMF2 and Gauge2 (shown in Figure 3.7) was measured under cyclic load with a frequency of 5Hz and an amplitude of 3kN (625MPa). The SMF2 measurements at around 54,000 cycles is shown in Figure 3.17(a). This diagram illustrates high precision continuous sensing by the SMF under low frequency tensile load. Figure 3.17(b) shows the strain data of Gauge2 at around 54,000 cycles. As with the static measurements, SMF-based distributed sensing obtains more strain information on specimen than strain gauges.

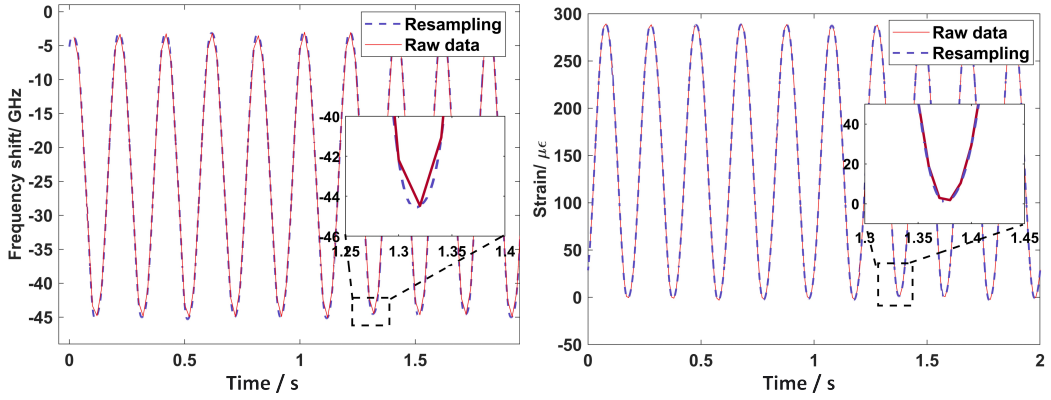
The sampling frequency of SMF2 and Gauge2 is 50Hz and 100Hz respectively. To compare the



(a) (b)

Figure 3.17: Measurements of SMF2 and Gauge2 in fatigue experiment (at around 54,000 cycles): (a) The measurement of SMF2; (b) The measurement of Gauge2

measurement results of SMF2 and Gauge2, the SMF2 measurements near Gauge2 are adopted (49th segment shown in Figure 3.9(a)). An interpolation method is then applied to unify the sampling frequency. The results of SMF2 and Gauge2 are shown in Figure 3.18(a) and Figure 3.18(b) respectively. The sampling frequency after the interpolation is 5kHz.



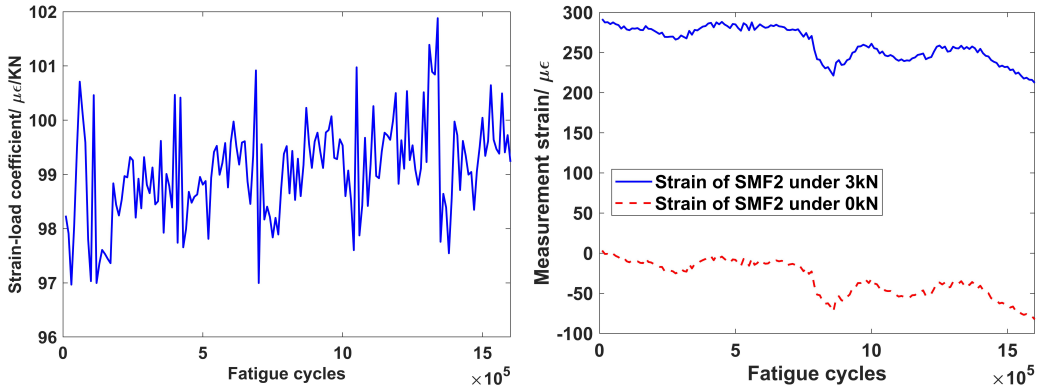
(a) (b)

Figure 3.18: Data interpolation of single mode fibre and strain gauge measurements: (a) The interpolation result of SMF2; (b) The interpolation result of Gauge2

Strain measurement error under low frequency load

As with the static analysis, the Gauge2 measurements are adopted as the reference strain in strain-frequency shift coefficient calculation of SMF2. Therefore, the reliability of Gauge2 measurements throughout the fatigue experiment is first investigated based on the analysis of strain-load coefficient. The calculation result of this coefficient is shown in Figure 3.19(a). This

figure illustrates that the ratio between the strain shift and the corresponding load shift is stable during the whole fatigue experiment. In addition, the value of this coefficient is consistent with the result in the static loading experiment shown in Figure 3.12(a). However, the reading of Gauge2 creeps with the increase of the fatigue cycle, even though the strain-load coefficient stays stable. This creep behaviour is illustrated in 3.19(b) which shows the reading at 0kN and 3kN (187.5MPa). In this figure, the reading of Gauge2 at 0kN gradually creeps from $0\mu\varepsilon$ to $-100\mu\varepsilon$ throughout the whole fatigue experiment. Because of the long duration of the fatigue test, it is highly probable that this phenomenon is a result of errors in the strain measurement instrument. Therefore, the Gauge2 reading at the beginning of the fatigue experiment was adopted as the reference strain during the whole fatigue experiment to avoid this creep effect.

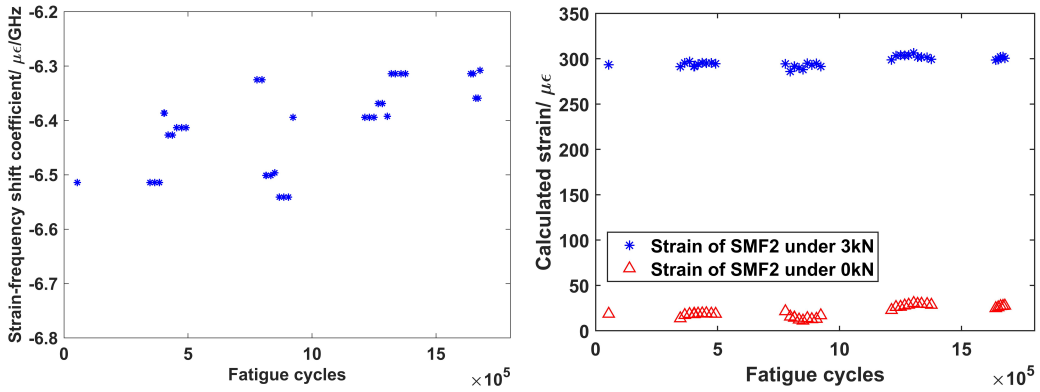


(a) (b)

Figure 3.19: Strain-load coefficient and Gauge2 measurements in fatigue experiment: (a) The strain-load coefficient of Gauge2; (b) The strain measurement of Gauge2

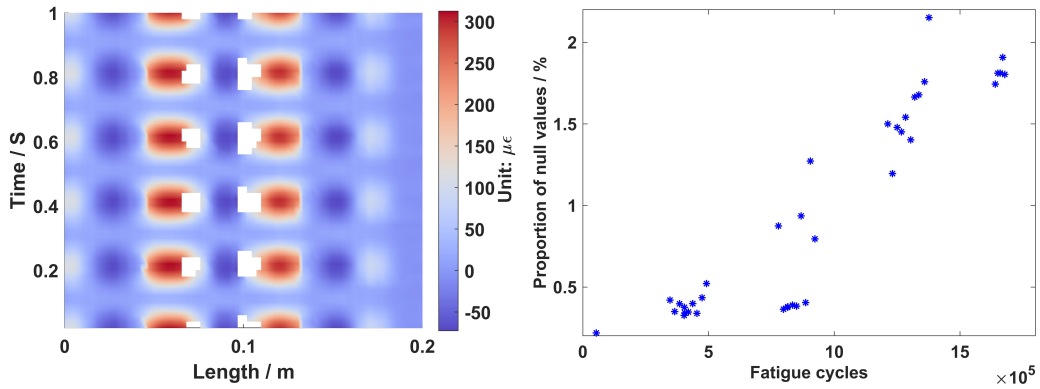
The strain-frequency coefficient is then obtained based on reference strain and reading of 49th segment on SMF2 (Figure 3.9(a)) at 3kN(187.5MPa). The result of this coefficient is shown in Figure 3.20(a). The strain-frequency coefficient stays stable and is consistent with the result in static loading experiment shown in Figure 3.12(b) during the whole fatigue experiment. Therefore, the strain under 0 to 3kN (0 to 187.5MPa) during fatigue experiment measured by SMF2 is calculated based on the frequency shift of SMF2 and the strain-frequency coefficient. The peak values of the calculated strains are shown in Figure 3.20(b). A constant load is induced during the fatigue experiment because the reference spectrum of the SMF is set before the experiment, which is the reason for non-zero values in Figure 3.20(b) when the tension load is 0kN. These two diagrams demonstrate that strain measurement errors of the SMF-

based distributed sensing under low frequency fatigue load is negligible when a constant strain-frequency shift coefficient is adopted. Although the fatigue experiments do not show significant influence on the strain-frequency shift coefficient, there is a clear tendency that the proportion of null values in the SMF2 measurements increases with the increase of fatigue cycles. These null values in strain measurements are shown as white area in Figure 3.21(a). The proportion of null value with increase of fatigue cycle is shown in Figure 3.21(b).



(a) (b)

Figure 3.20: Strain-frequency shift coefficient and calculated strain of SMF2 in fatigue experiment: (a) The Strain-frequency shift coefficient of SMF2; (The alculated strain of SMF2)



(a) (b)

Figure 3.21: Null values in measurements of SMF2 in fatigue experiment: (a) The Null values in measurements of SMF2; (b) The proportion of null value with increase of fatigue cycle

3.4.3 Conclusions

This subsection explores the robustness of SMF as strain sensors for in-field applications, where operational and environmental conditions such as mechanical load can impact the reliability of

strain distribution measurements. The key conclusions can be summarized as follows:

- A reading creep of Gauge2 is observed even though the strain-load coefficient is stable during the entirety of the fatigue experiment. In contrast, the calculated strain and strain-frequency coefficient of SMF2 remained stable during the whole fatigue experiment, which means that strain measurement errors of SMF-based distributed sensing under low frequency load is negligible. This conclusion illustrates the advantage of SMF for accurate distributed sensing in low-frequency load compared to strain gauges.

- Although the fatigue experiments do not show significant influence on SMF2 measurement values, there is a clear tendency that the number of null values in SMF measurements will increase as the fatigue cycles increase. Therefore, data reconstruction algorithms are required for recovering the strain information when SMF is adopted for strain measurement of composite laminate under low frequency fatigue load. It is worth noting that excessive data reconstruction may lead to the suppression of important features in the strain field, which can have adverse effects on various applications, including damage detection. Specifically, while the primary goal of the smoothing process is to restore the null values arising under low frequency tensile load, it can also unintentionally dampen critical strain features near the damage region, thereby hampering potential uses such as damage detection.

3.5 Strain measurement consistency of distributed sensing

So far, it has been demonstrated that the resolution, consistency and reliability of strain sensing with distributed FOS, is subject to variability under various conditions (static load, dynamic load, temperature, etc.) Therefore, it is essential to test the accuracy of the strain sensing under various operational and environmental conditions which can be represented by different test cases. Therefore, this subsection presents a comprehensive investigation into the measurement

consistency of distributed sensing in composite structures under a diverse test matrix. The study encompasses fifty-six independent experiments, categorized into six groups, comprising of tensile, fatigue, three-point bending, and three sets of temperature experiments. The strain-frequency shift coefficient and temperature-frequency shift coefficient of distributed fiber optic sensing based on OFDR in different test scenarios are visually represented by plots obtained from ESTIMATION STATISTICS BETA [235], and their normality is rigorously assessed utilizing the Kolmogorov-Smirnov test [236]. Furthermore, the coefficients' consistency is evaluated through Cronbach's alpha [237], McDonald's omega [238], and Split-half reliability[239], predicated on the confirmed normal distribution conclusion.

3.5.1 Strain-frequency shift coefficient consistency

The strain-frequency shift coefficient in various experiments

Since the measurement of OFDR is presented with frequency shift, the strain is obtained by a strain-frequency shift coefficient according to Equation 3.1. In this research, the reading of strain gauge is adopted as the reference strain, which is adopted to calculate the strain-frequency shift coefficient. Therefore, the strain-frequency shift coefficient under different test scenarios is obtained. An illustrative example of obtaining strain-frequency shift coefficients from a tensile experiment using distributed fiber optic sensing is demonstrated in Figure 3.22. In the depicted subfigure at the bottom-right of Figure 3.22, 1000 measurement values of strain gauge and SMF sensor (GHz) during the tensile experiment are presented. The blue line in the subfigure represents the strain gauge measurement in units of $\mu\varepsilon$, while the red line represents the SMF sensor measurement in units of GHz. From these measurements, points between 601 to 900 are selected to calculate the strain-frequency shift coefficients, which are depicted in the top-right subfigure. Similar procedure is applied to calculate the temperature-frequency shift coefficient in temperature experiments. In this case, the reference temperature is readily obtained from the environmental chamber, eliminating the need for additional temperature sensors.

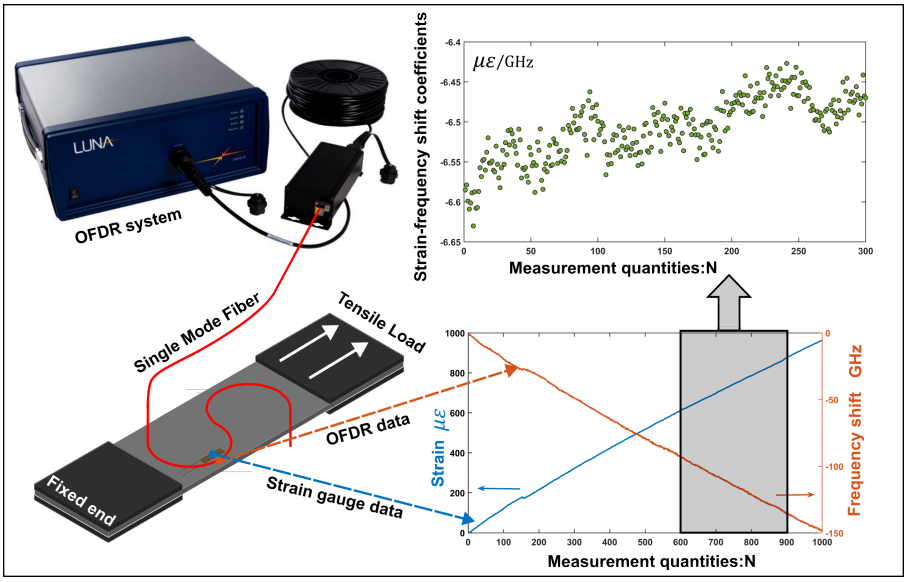


Figure 3.22: An illustrative example of obtaining strain-frequency shift coefficients from a tensile experiment using distributed fiber optic sensing

In this subsection, the results of this coefficient obtained from a tensile test, a fatigue test, and a three-point bending test are utilized. Detailed experimental information can be found in Table 3.5. The specimens used in these experiments are composed of the same composite material, namely TENAX$^{@}$ − E IMS65 E23 24K, and have a consistent layout of $[45/90/-45/0/45/0_2/-45]_s$. And the SMF sensors coated with polyimide were model SM1500(9/125)P, manufactured by FIBERCORE are adopted in these experiments. The polyimide coating has notable features, such as high temperature survival and bend insensitivity, making it highly desirable for distributed strain sensing applications. All distributed sensing data were obtained using the ODiSI-B system, manufactured by LUNA Ltd. In addition, a thermoplastic film based on modified polyolefins (Pontacol 22.100) was adopted as adhesive to bond the SMFs to CFRP specimens in these experiments.

Table 3.5: The experiment details in strain measurement

Test scenarios	Dimensions / mm	Load configuration	Temperature °C	Test quantities
Tension	200 × 50 × 3.2	0-10 kN	-30∼70	12
Fatigue	200 × 50 × 3.2	0-3 kN / 5 Hz 1677700 cycles	Room	13
Three-point bending	300 × 225 × 3.2	0-90 N	Room	9

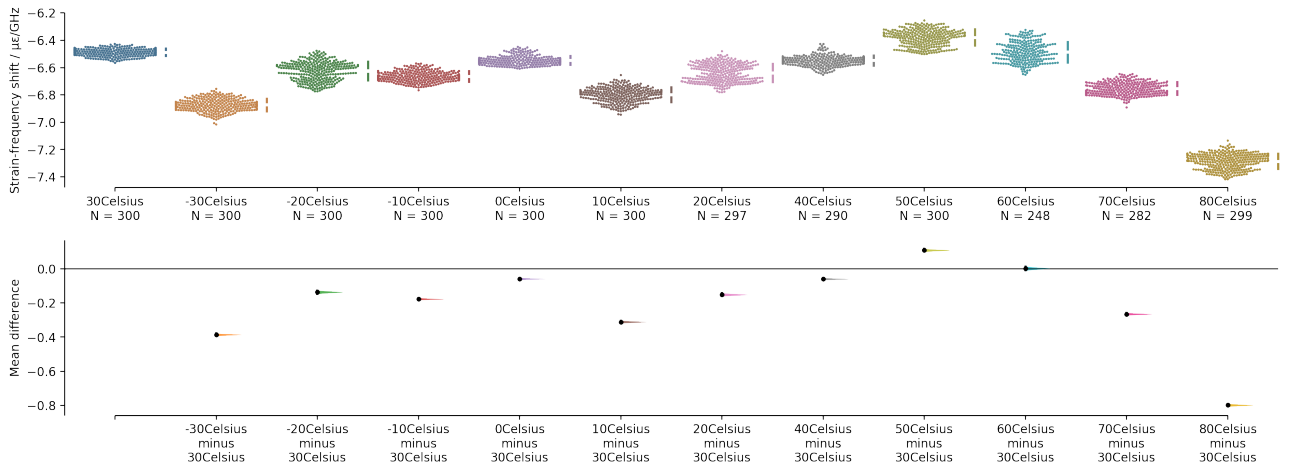


Figure 3.23: The plot of strain-frequency shift coefficients under different temperatures in tensile experiment

The tensile experiment was conducted at various ambient temperatures, ranging from -30 to 70°C with a 5°C step. The plot of strain-frequency shift coefficients under different temperatures is depicted in Figure 3.23. The x-axis represents different tests conducted under different temperatures, while the y-axis indicates the corresponding strain-frequency shift coefficients. The results obtained at 30°C (room temperature) serve as the reference for calculating the differences between different tests, and these differences are shown at the bottom of Figure 3.23. Observations reveal that the strain-frequency shift exhibits slight variations with changes in ambient temperature, particularly when the ambient temperature falls below −20°C or exceeds 70°C.

The fatigue experiment involved continuous testing for 1,677,700 cycles at room temperatures. The plot of strain-frequency shift coefficients under different fatigue cycles is presented in Figure 3.24. The x-axis of the plot represents different fatigue cycles, while the y-axis indicates the corresponding strain-frequency shift coefficients. It is evident from the results that this coefficient does not exhibit significant variation with an increase in fatigue cycles. Furthermore, the maximum mean difference between test 1 at cycle 53,600 and other tests (less than 0.4 $\mu\varepsilon$/GHz) is lower compared to that observed in the tensile experiment under different ambient temperatures (less than 0.8 $\mu\varepsilon$/GHz).

The strain-frequency shift coefficients from nine tests conducted under room temperature in

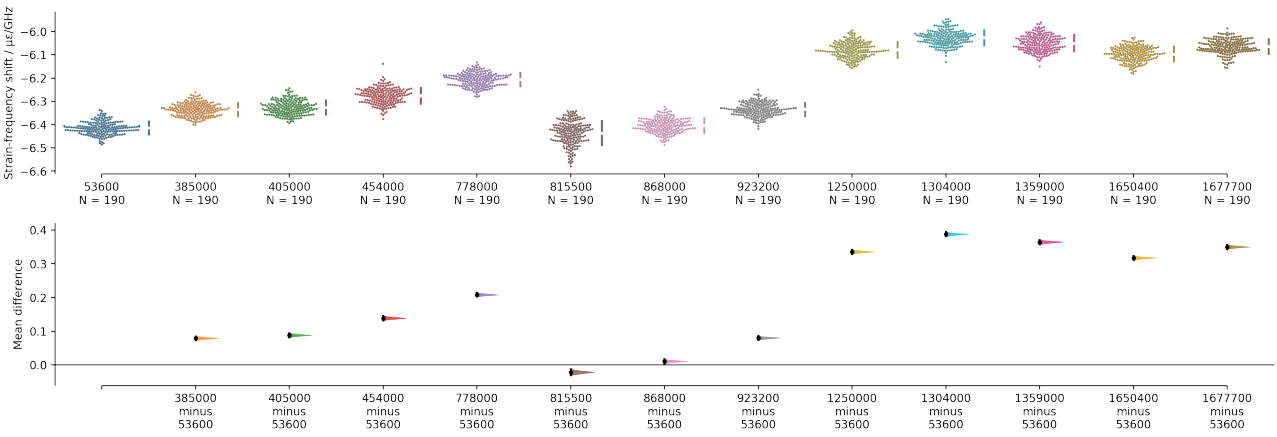


Figure 3.24: The plot of strain-frequency shift coefficients under different fatigue cycles

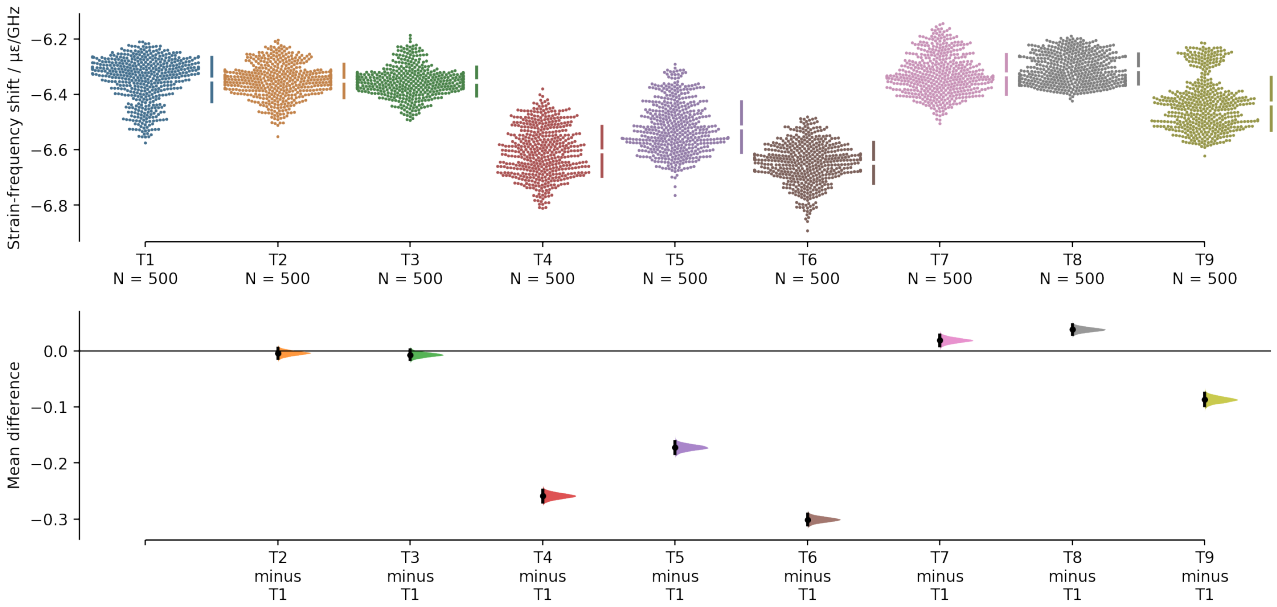
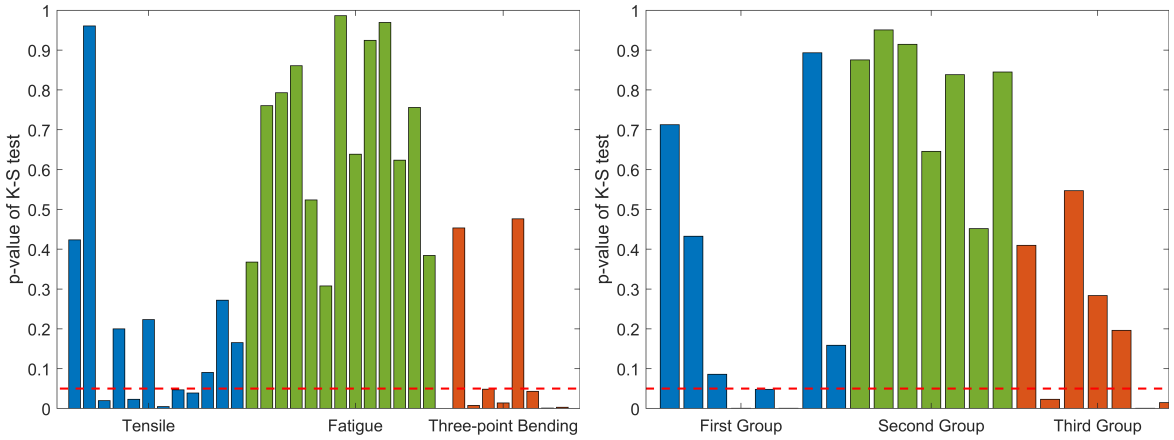


Figure 3.25: The plot of strain-frequency shift coefficients in three-point bending experiment

the three-point bending experiment are depicted in Figure 3.25. The x-axis represents T1 to T9, corresponding to test 1 to test 9, while the y-axis represents the strain-frequency shift coefficients. Similar to the observations in the fatigue experiment, the strain-frequency shift coefficients in the three-point bending experiment exhibit a comparable level of stability, as the mean difference between test 1 and other tests is less than 0.4 $\mu\epsilon$/GHz.



(a) (b)

Figure 3.26: The K-S test results for the different test scenarios in both strain and temperature measurement: (a) The The K-S test results for strain measurement experiments; (b) The The K-S test results for temperature measurement experiments

Consistency assessment of strain-frequency shift coefficient

In this subsection, the normality of the measurement of strain-frequency shift coefficients presented in subsection 3.5.1 is assessed firstly using the Kolmogorov-Smirnov (K-S) test. Widely recognized for testing the normality of measurements, additional information on the K-S test can be found in [236]. The test results for the different test scenarios are displayed in Figure 3.26(a). In this histogram, the x-axis representing various test scenarios, while the y-axis shows the p-value of the K-S test (ranging from 0 to 1). The p-value means the probability of observing a test statistic as extreme as, or more extreme than, the observed value under the hypothesis of normal distribution. The p-values for test scenarios in the tensile experiment are indicated by blue bars, for the fatigue experiment by green bars, and for the three-point bending experiment by red bars. The red dashed line represents the significance level of the hypothesis test, conventionally set at 0.05. Based on the figure, it can be inferred that the measured strain-frequency shift coefficients under most test scenarios conform to the normal distribution.

The measurement errors in different test scenarios are clearly independent, and all the measurements in these tests exhibit the same relationship with the underlying construct, as indicated by Equation 3.1 (tau-equivalent). Leveraging the normal distribution conclusion obtained from

the K-S test, various coefficients, such as Cronbach's alpha (α), McDonald's omega (ω), and Split-half reliability coefficient, can be employed to assess the internal consistency of the strain-frequency shift coefficients measured in different test scenarios [240, 241]. The results of the consistency assessment of the strain-frequency shift coefficients presented in subsection 3.5.1 are summarized in Table 3.6. Based on the results presented in this table, the strain-frequency shift coefficients demonstrate high consistency across different test scenarios, including temperature variations , fatigue, and three-point bending experiments.

Table 3.6: The consistency assessment results of the strain-frequency shift coefficients

Test scenarios	Cronbach's alpha (α)	McDonald's omega (ω)	Split-half reliability coefficient
Tension	0.991	0.998	0.993
Fatigue	0.997	0.999	0.991
Three-point bending	0.992	0.997	0.992
All three types	0.997	0.999	0.997

3.5.2 Temperature-frequency shift coefficient consistency

The temperature-frequency shift coefficient in different experiments

In this subsection, a comprehensive analysis of the temperature-frequency shift coefficient derived from data collected during twenty-two independent temperature experiments was conducted. These experiments were organized into three distinct groups. The first group encompassed temperature measurements of SMF sensors (acrylate coating) in their free state, consisting of eight independent experiments. The temperature configuration in this group is -50 °C to 50 °C with a step of 5 °C. The second group encompassed temperature measurements of SMF sensors (acrylate coating) in their mounted state, consisting of seven independent experiments. The temperature configuration in this group is -50 °C to 50 °C with a step of 5 °C. The third group encompassed temperature measurements of SMF sensors (polyimide coating) in their free state, consisting of seven independent experiments. The temperature configuration in this group is -30 °C to 80 °C with a step of 5 °C. The details of these three groups of

experiments are summarized in Table 3.7.

The SMF sensors with acrylate coating were model 1550BHP from THORLABS, while the SMF sensors coated with polyimide were model SM1500(9/125)P, manufactured by FIBERCORE. All distributed temperature sensing data were obtained using the ODiSI-B system, manufactured by LUNA Ltd. In addition, a thermoplastic film based on modified polyolefins (Pontacol 22.100) was adopted as adhesive to bond the SMFs to CFRP specimens in these experiments.

Table 3.7: The experiment details in temperature measurement

Test scenarios	Temperature range °C	Temperature step °C	Coating material	Sensor state	Test quantities
First Group	-50∼50	5	Acrylate	Free	8
Second Grou	-50∼50	5	Acrylate	Surface mounted	7
Third Group	-30∼80	5	polyimide	Free	7

The temperature-frequency shift coefficients obtained from the experiments in the first group are visualized using a plot in Figure 3.27. The x-axis represents Test 1 (T1) to Test 8 (T8), while the y-axis denotes the values of the temperature-frequency shift coefficient (denoted by 'T-frequency shift coefficient'). The difference between T1 and the rest of the experiments is presented at the bottom of this figure, indicating that the mean difference is less than 0.07 °C / GHz.

The installation of SMF sensors (acrylate coating) on the surface of composite panels significantly affects the temperature-frequency shift coefficient compared to their free state counterparts. Based on the temperature-frequency shift coefficients obtained in the experiments of the second group, the value of this coefficient decreases from -1.55 °C / GHz (free state) to -1.04 °C / GHz (surface mounted). The detailed measurement data is presented in Figure 3.28. Notably, the maximum mean difference after installation decreased to 0.03 °C / GHz compared to the free state situation (0.07 °C / GHz) in the first group shown in Figure 3.27. This observation indicates that the installation of SMF sensors improves the measurement stability of temperature.

In the third group of experiments, all SMF sensors were coated with polyimide, resulting in

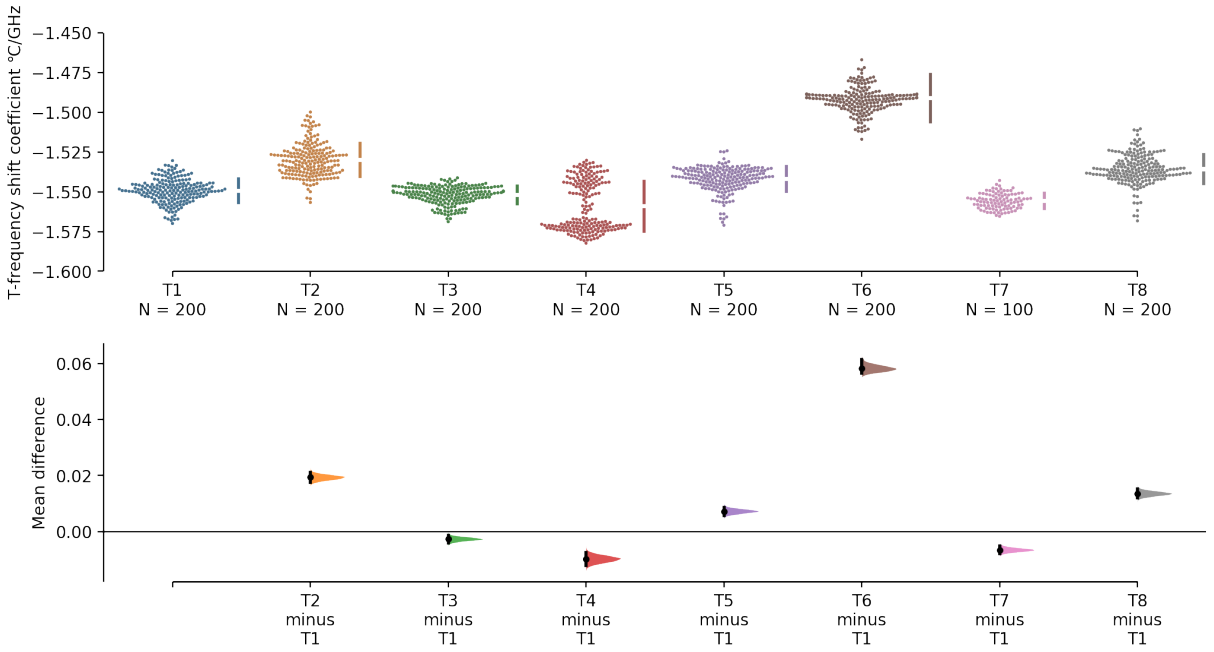


Figure 3.27: The plot of temperature-frequency shift coefficients obtained from the experiments in the first group

a different temperature-frequency shift coefficient compared to the previous two groups. The detailed results of experiments in this group are presented in Figure 3.29. According to the figure, the temperature-frequency shift coefficient of SMF sensors coated with polyimide is approximately -1.28 °C / GHz. This value is slightly smaller than that observed for SMF sensors coated with acrylate (-1.55 °C / GHz). However, it is worth noting that the maximum mean difference in Figure 3.29 is less than 0.03 °C / GHz, which is equivalent to the surface mounted sensors in the second group. This indicates that the SMF sensors with polyimide coating exhibit higher stability in temperature measurement compared to those with acrylate coating.

Temperature-frequency shift coefficient consistency assessment

In this subsection, we employed the same procedures as in Section 3.5.1 to assess the consistency of the temperature-frequency shift coefficient across various experiments. Due to the different coefficient values observed in the three groups, the consistency assessment was carried out independently within each temperature experiment group. The results of the K-S tests for the three

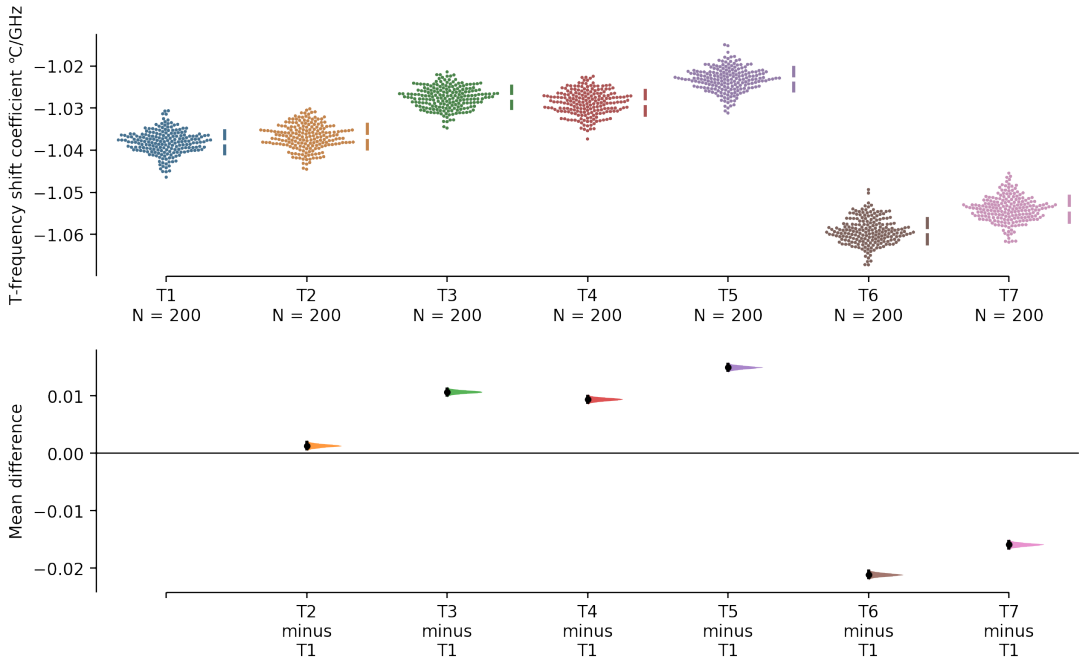


Figure 3.28: The plot of temperature-frequency shift coefficients obtained from the experiments in the second group

experimental groups are presented in Figure 3.26(b). The p-value, indicated by the red dashed line, was set at 0.05 for characterizing the normality of measured temperature-frequency shift coefficient in different experiments. It can be observed that nearly all tests exhibit conformity to the normal distribution, especially in the surface mounted situation within the second group. As a consequence, the consistency assessment of the temperature-frequency shift coefficient was represented by Cronbach's alpha, McDonald's omega, and Split-half reliability coefficient, which are summarized in Table 3.8. The results presented in this table provide compelling evidence for the high temperature measurement consistency of distributed fibre optic sensors in composite structures under various test scenarios.

Table 3.8: The consistency assessment results of the temperature-frequency shift coefficients

Test scenarios	Cronbach's alpha (α)	McDonald's omega (ω)	Split-half reliability coefficient
First Group	0.988	0.993	0.979
Second Group	0.999	0.999	0.984
Third Group	0.941	0.977	0.955

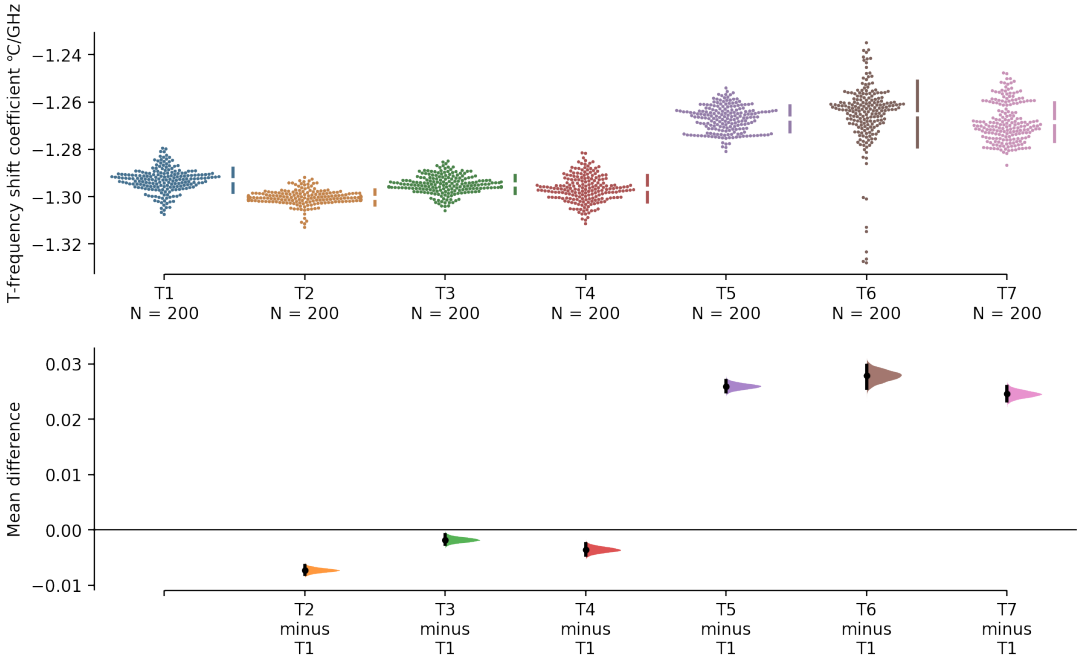


Figure 3.29: The plot of temperature-frequency shift coefficients obtained from the experiments in the third group

3.5.3 Measurement uncertainty of distributed fibre optic sensors with OFDR system

According to the type A evaluation of standard uncertainty, as defined in the "Guide to the Expression of Uncertainty in Measurement" (GUM) [242] published by the Joint Committee for Guides in Metrology (JCGM), the uncertainty of measurement can be mathematically expressed in Equation 3.10.

$$s(\bar{q}) = \sqrt{\frac{\sum_{i=1}^{n}(q_i - \bar{q})^2}{n(n-1)}} \tag{3.10}$$

In this equation, the type A evaluation of standard uncertainty is determined based on the mean value ($\bar{q}$) of the measurement data, the quantity of data points (n), and the individual measurement points (q_i). Utilizing this definition, the uncertainty degree of measurements in all test scenarios mentioned in Section 3.5.1 and Section 3.5.2 is calculated and visualized in Figure 3.30. The x-axis of the histogram represents different test scenarios, with labels mentioned in Section 3.5.1 and Section 3.5.2(same as Figure 3.26, Table 3.5, and Table 3.7), comprising a total of fifty-six experiments (corresponding to fifty-six bars). The y-axis displays the values of

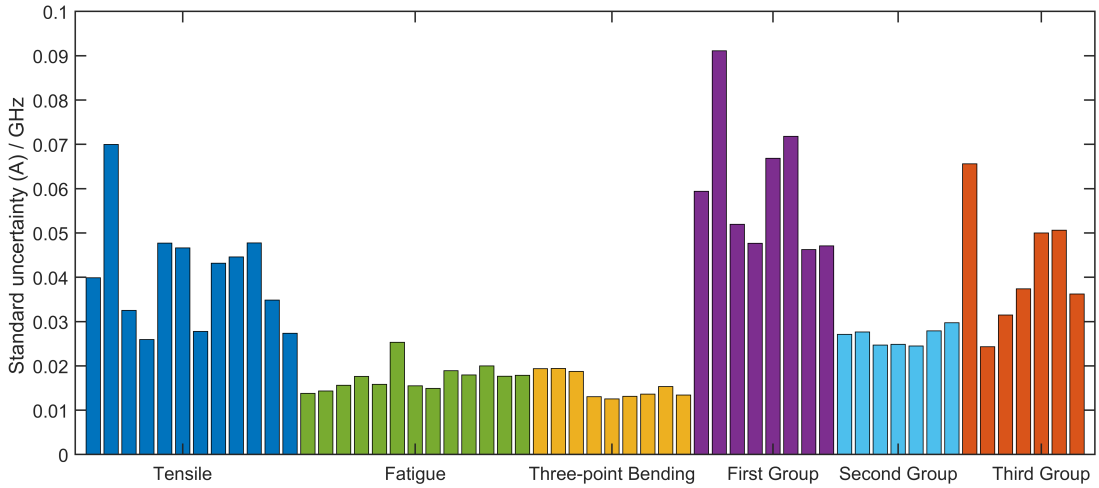


Figure 3.30: The type A evaluation of standard uncertainty of all test scenarios mentioned in Section 3.5.1 and Section 3.5.2

the type A evaluation of standard uncertainty. The results in this figure are obtained from 200 measurement points in each test scenario. According to the findings depicted in Figure 3.30, the type A evaluation of standard uncertainty in various test scenarios is consistently less than 0.1 GHz (n=200). This suggests that the uncertainty degree of measurement is low and remains stable when distributed fiber optic sensors are employed to obtain strain or temperature data in composite structures.

3.5.4 Conclusions

This subsection was focused on assessing the measurement consistency of distributed fiber optic sensing under various test scenarios. The measurement data from fifty-six independent test scenarios were categorized into six groups, including tensile experiments (thirteen tests), fatigue experiments (twelve tests), three-point bending experiments (nine tests), and three groups of temperature experiments (twenty-two tests). The normality of these coefficients was determined using the Kolmogorov-Smirnov (K-S) test, and their consistency was further assessed through Cronbach's alpha, McDonald's omega, and Split-half reliability based on the normal distribution conclusion. In addition, the standard uncertainty (type A) of frequency shift measurement in these fifty-six independent test scenarios are calculated and presented in this research. The main findings of this study are as follows:

- The strain-frequency shift coefficient in different tests consistently measured around -6.4 $\mu\varepsilon$/GHz. However, the stability of this coefficient was influenced by changes in ambient temperature, especially when the ambient temperature falls below $-20°$C or exceeds 70°C. Despite the variation, the measurement of this coefficient demonstrated high consistency across different test scenarios.

- The value of the temperature-frequency shift coefficient was affected by factors such as the coating material of SMF sensors and their installation state. The coefficients obtained from three groups of temperature experiments were -1.55 °C / GHz (acrylate coating in a free state), -1.04 °C / GHz (acrylate coating after surface mounting), and -1.28 °C / GHz (polyimide coating in a free state), respectively. The coefficient showed higher stability when SMF sensors with polyimide coating were used or when the SMF sensors were installed. Additionally, the measurement of this coefficient also exhibited high consistency across different test scenarios.

- The standard uncertainty (type A) of frequency shift measurements in the fifty-six independent test scenarios was found to be less than 0.1 GHz (when 200 measurement points were used in the calculation). This indicates that the degree of uncertainty of measurement remains stable when employing distributed fiber optic sensors to obtain strain or temperature in composite structures.

Chapter 4

Damage detection in composite plates based on distributed fiber optic sensing

4.1 Introduction

In the realm of damage detection in CFRP, FOS hold significant importance due to their advantageous attributes such as low weight, affordability, widespread accessibility, immunity to corrosion, and resistance to electromagnetic interference. A considerable number of cutting-edge studies on the detection of CFRP damage are based on various FOSs, including FBG [243, 244, 245], distributed SMF [246], and fiber optical interferometer [247, 248, 24]. These studies can be broadly divided into three categories: acoustic emission, vibration-based modal identification, and strain field analysis.

In acoustic emission, FBGs or fibre optical interferometers are utilized as transducers to capture the guided wave signal generated by actuators (typically piezoelectric sensors) after it has propagated through the CFRP structures [249, 250, 251, 252, 253]. The integrity of the CFRP structures is assessed by comparing the baseline signal (when there is no damage) with the current signal (when the state is unknown). This method partially alleviates the limitations of traditional acoustic emission systems, which are solely based on piezoelectric sensors, by reducing the use of cables and increasing embedded performance [254, 255, 256, 257]. However,

it remains susceptible to errors, common in all baseline-based approaches, due to operational deviations, variations in bonding quality, or temperature fluctuations. There is also a practical disadvantage for embedding the FOS, which can introduce strength reduction to the composite based on their location, and more importantly if they are broken or damaged, there is no option to repair them which means the whole part has to be replaced, which is not acceptable for industrial application of this method to large scale composite structures [258].

In vibration-based modal identification method, FBGs or distributed SMFs are utilized as transducers to acquire discrete or distributed dynamic strain [259, 260]. This dynamic strain is then utilized to perform computational modal analysis, which results in the calculation of the strain frequency response function of structures. Complex mode indicator function,[261] random decrement and mode shape extraction [244], and Hankel matrix with single value decomposition [262] are among the methods used in computational modal analysis. Despite the substantial progress that has been made in the non-destructive testing of structures through modal analysis, few studies have been conducted utilizing FOSs. The main reason for this is the limitations in measurement accuracy and frequency range of FOS, particularly distributed SMFs, compared to their counterparts such as scanning Laser Doppler Vibrometers and accelerometers [263, 264, 265]. Furthermore, since regular vibration input is required for modal analysis, this technology is more suited for non-destructive testing of structures in laboratory environments rather than in-service applications.

Therefore, for in-service applications, damage detection through the analysis of the strain field is considered to be the most promising approach [266, 267]. Fibre optical sensors, including FBGs and distributed SMFs, are frequently utilized to gather robust strain data from structures due to their high strain sensitivity. This data is then utilized to assess the integrity of CFRP structures. The fundamental principle behind this approach is that the strain field near damage area, such as splitting, delamination, or fibre breakage, experiences changes after the damage occurs [268, 269, 270, 271, 272, 273]. In addition, residual strain or strength after damage is also considered to be a crucial index for assessing structural integrity [274, 275, 276, 277, 278]. Based on this, the most straightforward approach is to identify discontinuities in the measured strain as damages [279, 280, 281, 282, 283], as supported by recent experimental studies in

[284] and [285]. Furthermore, in place of strain measurement, more basic and detailed spectral parameters of FOS (shape, intensity, polarization state, etc.) can be employed to indicate the damage state of structures, as demonstrated in [286, 287, 288, 289, 290, 291, 292]. It is evident that this straightforward method only proves to be effective when the external load is substantial or when the structures have reached a failure state. This, however, is not suitable for the early detection of damage, particularly for BVID. This conclusion is supported by the experimental results presented in [284] and [285]. In addition, huge amounts of sensors are required in real composite structures to obtain accurate strain filed even with distributed sensing based on single mode fiber. This means high cost and weight of the SHM system. Few research has paid attention to critically investigating reducing cost and weight of SHM system based on distributed strain sensing by identifying the minimum required sensor density.

In an effort to improve the accuracy, reliability, and timeliness of damage detection in CFRP structures, various methods have been proposed to effectively capture discontinuities in the strain field. For example, the use of machine learning techniques, such as principal component analysis [39, 293, 294, 295], artificial neural networks [296, 297, 298], and deep learning [299], has been extensively researched in strain field-based damage detection. The results of these studies have demonstrated the feasibility and advantages of using machine learning for this purpose. However, there are some limitations to using these techniques for in-service structural health monitoring, such as the need for large amounts of training data, high computational costs, low interpretability, and a tendency towards overfitting. An alternative approach is to establish a damage index (DI) based on extracted features from the strain field. The features extracted for the DI include Pearson correlation coefficient [17], standard deviation [204, 300, 301], and first or second order derivatives [302, 194]. This DI-based approach is shown to be highly sensitive to damage (especially for BVID) in CFRP structures. Additionally, it has high interpretability and requires lower computational costs, making it a potential solution for in-service applications. Despite the promise of the DI-based damage detection approach, there are still limitations and challenges to be addressed. One issue is the limited detection points allowed by the use of FBGs. Additionally, the deviation or derivatives of strain measurement are prone to uncertainties due to variying operational and environmental conditions of structures in service, such as those

caused by complex strain distribution and temperature variation.

Based on the challenges mentioned above, two research objectives are presented in this chapter:

- **2D reconstruction of strain along the optical fiber axis by interpolation:** In this objective, the strain reconstruction under different sensor densities is studied based on barycentric Lagrange and cubic spline interpolation methods. The fibre optical sensors were mounted on the surface of a composite laminate. The distance between the SMF sensing part is 5mm. The measurements under 5mm were adopted as true strain distribution, which correspond to high-fidelity data. The measurements under larger sensor distance (10,15,20,25,30mm) are identified as the low-fidelity data and were interpolated to 5mm as reconstructed strain. This reconstructed strain was then compared with the true strain distribution. The errors of strain reconstruction under different sensor densities were studied in this subsection. The results obtained in this research are meaningful for both increasing strain measurement accurate and decreasing weight and cost of SHM system.

- **A novel DI-based damage detection method:** this subsection proposes a novel approach based on feature matching of local neighborhoods among distributed strain measurements. This approach utilizes the correlation between local measurement points to differentiate between damaged and undamaged parts, offering new insights and potential solutions to the challenges faced in damage detection of CFRP structures under operational conditions. The primary contributions of this study include: (1) The feasibility of utilizing distributed strain measurements, in conjunction with image processing techniques, for the purpose of detecting damage in CFRP structures has been demonstrated through theoretical analysis and experimentation. (2) The local point autocorrelation based on Delaunay triangulation and Hausdorff distance is defined and proved to be an effective criterion for identifying those measurement points located near the damage site in CFRP structures. (3) The prior knowledge of the non-damaged strain distribution is not required in proposed approach. Furthermore, the effectiveness of the approach in detecting a variety of damage types, including BVID and VID, in CFRP structures has

been demonstrated.

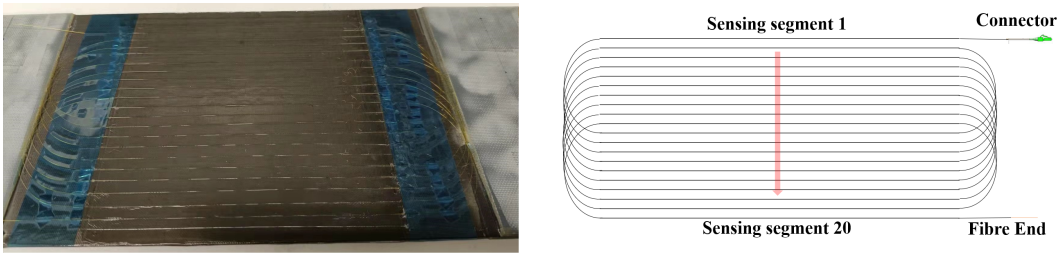
In this subsection, the organization is summarized as follows: 4.3.1 introduces the methodology, which includes the OFDR technique, strain measurements filtering and reconstruction, local point autocorrelation, and damage detection schemes. 4.3.2 details the implementation of the low-velocity impact experiment and the static tensile experiment. 4.3.3 presents the analysis of the strain measurements obtained from the experiments and the resulting damage detection outcomes. Finally, 4.3.4 offers the main conclusions, inferences, limitations, and suggestions for future research.

4.2 2D reconstruction of strain along the optical fiber axis by interpolation

In this subsection, the strain reconstruction with interpolation methods was investigated based on measurements of distributed fibre optical sensors. It should be noted that all strains mentioned in this subsection represent strains along the optical fiber axis. The strain measurements under different sensor densities $(5, 10, 15, \cdots, 30mm)$ were adopted in this investigation. The measurements under 5mm distance were adopted as true strain distribution (high-fidelity data). The other measurements were interpolated to 5mm by barycentric Lagrange and cubic spline methods. These interpolated results were adopted as the low-fidelity data and to compare with the true strain distribution. The results show that the accuracy of strain reconstruction decreases with the increase of sensors distance. Specifically, the local patterns of strain distribution are lost after the reconstruction when the sensor distance of measurement data is much larger ($\geq$6 times) than the sensor distance of reconstruction data. However, the main trends of the reconstructed strain distribution is consistent with the true strain distribution. In addition, the barycentric Lagrange interpolation shows better stability than the cubic spline interpolation, especially for measurements with large sensor distance.

4.2.1 Experiment Setup

In the experiment, a quasi-isotropic composite laminate made of M21 T800 material with a size of $230 \times 118 \times 2mm$ was adopted. The length of End-Tab is 50mm. The distributed sensing system adopted in this experiment is ODiSI-B optical distributed sensor interrogator manufactured by LUNA Ltd.The spatial resolution of this system is 2.6mm. The SM1500(9/125)P manufactured by FIBERCORE was adopted in the experiment for strain measurement. This kind of fibre with polyimide coating has a variety of advantages such as high temperature survival, bend insensitive and enhanced photo sensitivity, which makes it very attractive for distributed strain sensing. The fibre optical sensor was mounted on the surface of composite laminate with a kind of epoxy potting compound (sourced from RS Components with Stock number 199-1468). This epoxy potting compound can provide strong adhesion quality in various harsh conditions without significant lateral strain on fibre optical sensors, which makes it much easier for long distance distributed sensing with OFDR system. Therefore, any room temperature-curing epoxy resin with strong adhesive ability can be used as a substitute to verify the work of this subsection. The layout of fibre optical sensors is shown in Figure 4.1. As shown in this figure, a wraparound layout was adopted in manufacturing. This scheme was adopted because it realizes both high density and large bend radius of fibre optical sensors. The distance between two adjacent sensing segments on composite laminate is 5mm. The signal transmission loss in fibre optical sensors is decreased because of large bend radius, which increases the measurement accuracy and stability. In this experiment, a continuous tension load (0-10 KN) is applied to composite specimen by Instron 5980 Series Dual Column Floor Frames (250KN). The tensile load was applied along the longer side of the specimen. The experiment setup is shown as Figure 4.2.



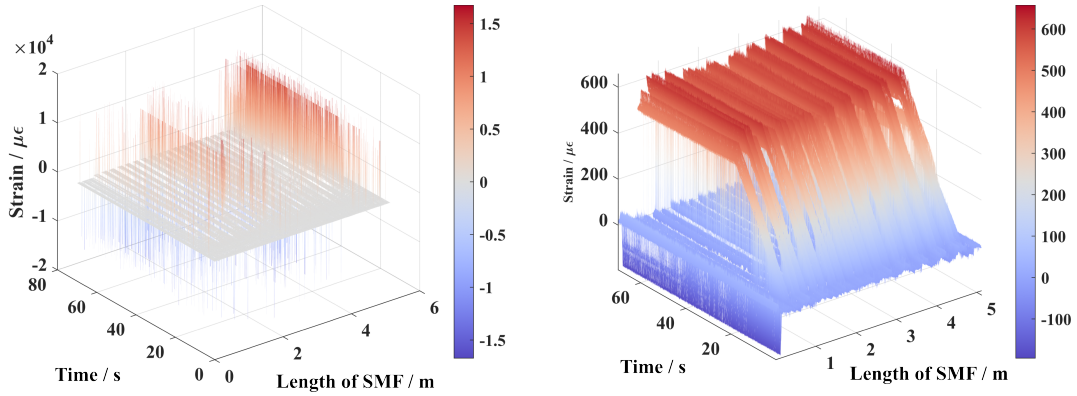
(a) (b)

Figure 4.1: The layout of fibre optical sensors: (a) The installation of fiber optic sensor; (b) The design of the layout



(a) (b)

Figure 4.2: The experiment setup: (a) The specimen fixed by clamps; (b) The setup of tensile experiment



(a) (b)

Figure 4.3: The raw data of fibre optical sensor: (a) The raw data before filtering; (b) The raw data after filtering

4.2.2 Methodology

Measurement results

The measurement data of fibre optical sensor is shown in Figure 4.3. The raw data is shown in the left picture of Figure 4.3, noise is observed in this figure. This is mainly caused by mismatch of reference and Rayleigh back scattering spectrum[161, 77]. This kind of noise is filtered by a constant threshold because that the noise is usually much larger than normal data. The measurements after filtering is shown in the right picture of Figure 4.3.

After filtering, the measurements of fibre optical sensor were converted to strain by a constant strain-frequency shift coefficient (The default value of the ODiSI-B system at room temperature: $-6.7\mu\epsilon/GHz$). The strain data obtained from fibre optical measurements is shown in Figure 4.4(a). According to the layout of fibre optical sensor mentioned in chapter 2, there exists a mapping between measurements and real spatial location. This mapping is shown in Figure 4.4. In this figure, $s_1, s_2, s_3, \cdots, s_{20}$ means sensing segments arranged sequentially along the fibre optical sensor. $f(s_1), f(s_2), f(s_3), \cdots, f(s_{20})$ means the sensing segments assigned in Figure 4.1.

The measurements of fibre optical sensor are expressed as $a_1, a_2, a_3, \cdots, a_n$. The sensing segments arranged sequentially along the fibre optical sensor are expressed as $s_1, s_2, s_3, \cdots, s_{20}$.

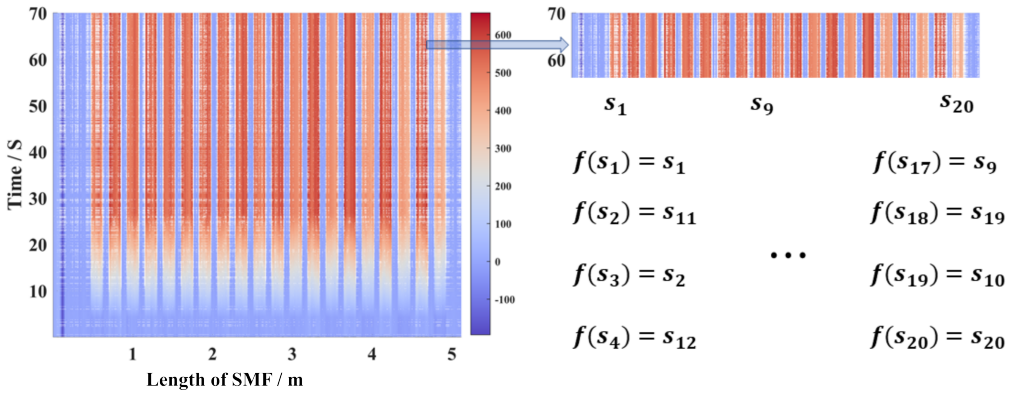


Figure 4.4: The strain measurements and spatial mapping.

There exists a relationship as follows:

$$s_i = [a_{k_i}, a_{k_i+1}, a_{k_i+2}, \cdots, a_{k_i+p-1}] \quad i = 1, 2, \cdots, 20 \quad 1 \leq k_i \leq 20 \tag{4.1}$$

where k_i is the beginning of s_i. p express the length of sensing segments. Therefore, the strain matrix of composite laminate under load is obtained with the spatial mapping.

$$s' = f([s_1, s_2, \cdots, s_{20}]^T) = f([\widetilde{s}_1, \widetilde{s}_2, \cdots, \widetilde{s}_p]) = [f(\widetilde{s}_1), f(\widetilde{s}_2), \cdots, f(\widetilde{s}_p)] \tag{4.2}$$

$$\widetilde{s}_j = [a_{k_1+j-1}, a_{k_2+j-1}, \cdots, a_{k_{20}+j-1}]^T \quad j = 1, 2, \cdots, p \tag{4.3}$$

In this subsection, the strain reconstruction under different sensor densities is studied. Therefore, $f(\widetilde{s}_j)$ is adopted as true strain distribution in interpolation research. Different sensor densities were simulated by resampling $f(\widetilde{s}_j)$. The resampling results is $f(\widetilde{s}_j^q)$, as shown in Table 4.1. The interpolation of $f(\widetilde{s}_j^q)$ is adopted to compare with $f(\widetilde{s}_j)$ to assess the strain reconstruction accuracy.

Table 4.1: Different sensor densities

	Sensor Distance/mm	Measurements	Total points(m)
$f(\widetilde{s}_j^1)$	2×5	$f([a_{k_1+j-1}, a_{k_3+j-1}, \cdots, a_{k_{19}+j-1}]^T)$	10
$f(\widetilde{s}_j^2)$	3×5	$f([a_{k_1+j-1}, a_{k_4+j-1}, \cdots, a_{k_{19}+j-1}]^T)$	7
$f(\widetilde{s}_j^3)$	4×5	$f([a_{k_1+j-1}, a_{k_5+j-1}, \cdots, a_{k_{17}+j-1}]^T)$	5
$f(\widetilde{s}_j^4)$	5×5	$f([a_{k_1+j-1}, a_{k_6+j-1}, \cdots, a_{k_{16}+j-1}]^T)$	4
$f(\widetilde{s}_j^5)$	6×5	$f([a_{k_1+j-1}, a_{k_7+j-1}, \cdots, a_{k_{19}+j-1}]^T)$	4

Barycentric Lagrange interpolation

Barycentric Lagrange interpolation is an efficient method to realize data reconstruction [303]. In this subsection, the data of $f(\widetilde{s}_j^q)$ is set as $[y_1, y_2, y_3, \cdots, y_m]$. The corresponding position coordinates are $[x_1, x_2, x_3, \cdots, x_m]$. The Lagrange polynomial is therefore written as

$$p(x) = \sum_{j=1 \ j\neq k}^{m} \frac{(x-x_1)(x-x_2)\cdots(x-x_k)\cdots(x-x_m)}{(x_j-x_1)(x_j-x_2)\cdots(x_j-x_k)\cdots(x_j-x_m)} y_j \tag{4.4}$$

The barycentric weights is defined by

$$\omega_j = \frac{1}{\prod_{k=1 \ k\neq j}^{m}(x_j - x_k)} \tag{4.5}$$

Therefore, the Lagrange polynomial is written as

$$p(x) = \prod_{k=1}^{m}(x-x_k) \sum_{j=1}^{m} \frac{\omega_j}{x-x_j} \tag{4.6}$$

The barycentric Lagrange polynomial is defined as follows

$$P(x) = \frac{p(x)|_{y_i}}{p(x)|_{y_i \equiv 1}} = \frac{\sum_{j=1}^{m} \frac{\omega_j}{x - x_j} y_i}{\sum_{j=1}^{m} \frac{\omega_j}{x - x_j}} \tag{4.7}$$

Considering the measurement point is uniformly distributed in length range $x_j \in [a, b]$, $x_j = a + \frac{b-a}{m-1}(j-1)$. Therefore, the barycentric weights is calculated as:

$$\omega_j = (-1)^j C_{m-1}^j \frac{(-1)^{m-1}}{(\frac{b-a}{m-1})^{m-1}(m-1)!} \tag{4.8}$$

However, when m is large, the barycentric weights change fast because of $C_{(m-1)}^j$, which leads unacceptable errors near the two ends of the length range $[a, b]$. This is known as Runge phenomenon. One efficient way to avoid this phenomenon is interpolation based on Chebyshev points. The first kind Chebyshev points and corresponding barycentric weights are calculated as ($x_j \in [-1, 1]$):

$$x_j^c = cos\frac{(2j+1)}{(2m+2)}\pi \tag{4.9}$$

$$\omega_j^c = (-1)^j sin\frac{2j+1}{2m+2}\pi \tag{4.10}$$

The second kind Chebyshev points and corresponding barycentric weights are calculated as ($x_j \in [-1, 1]$):

$$x_j^c = cos\frac{j}{m}\pi \tag{4.11}$$

$$\omega_j^c = (-1)^j \begin{cases} \frac{1}{2} & j = 1 \ or \ j = m \\ 1 & 1 < j < m \end{cases} \tag{4.12}$$

Since the measurement data $[y_1, y_2, y_3, \cdots, y_m]$ is uniformly distributed, the data at Chebyshev points are obtained by linear estimation.

$$y_j^c = y_k + \frac{y_{k+1} - y_k}{x_{k+1} - x_k}(x_j^c - x_k) \quad x_j^c \in [x_k, x_{k+1}] \quad k = 1, 2, \cdots, (m-1) \tag{4.13}$$

Cubic spline interpolation

The cubic spline interpolation is another efficient method to realize data reconstruction [304]. The essential principle is piecewise function fitting for the measurement data. The piecewise function can be written as follows.

$$S(x) = \begin{cases} s_1(x) & x \in [x_1, x_2] \\ s_2(x) & x \in [x_2, x_3] \\ \cdots & \\ s_{m-1}(x) & x \in [x_{m-1}, x_m] \end{cases} \tag{4.14}$$

where the piecewise functions shown in Equation (4.14) are defined as cubic polynomial

$$s_j(x) = a_j(x - x_j)^3 + b_j(x - x_j)^2 + c_j(x - x_j) + y_j \qquad j = 1, 2, \cdots, (m-1) \tag{4.15}$$

Some conditions at measurement points are proposed to grantee the smoothness of $S(x)$. Specifically, the adjacent functions ($s_j(x)$ and $s_{j+1}(x)$) have the same zero to two derivative values at their intersection $x_j (j = 1, 2, 3, \cdots, (m-2))$

$$\begin{cases} s_j(x_{j+1}) = s_{j+1}(x_{j+1})) \\ s_j^{'}(x_{j+1}) = s_{j+1}^{'}(x_{j+1}) \\ s_j^{''}(x_{j+1}) = s_{j+1}^{''}(x_{j+1}) \end{cases} \tag{4.16}$$

Based on Equation (4.15) and Equation (4.16) mentioned above, the undetermined coefficients a_j and c_j in $s_j(x)$ can be expressed by b_j and b_{j+1} as follows ($j = 1, 2, 3, \cdots, (m-2)$).

$$\begin{cases} a_j = \dfrac{b_{j+1} - b_j}{3(x_{j+1} - x_j)} \\ c_j = \dfrac{y_{j+1} - y_i}{x_{j+1} - x_j} - \dfrac{b_{j+1} + 2b_j}{3(x_j + 1 - x_j)} \end{cases} \tag{4.17}$$

This relationship is expressed by a matrix in Equation (4.18).

$$\begin{bmatrix} 1 & 4 & 1 & & 0 & 0 & 0 \\ 0 & 1 & 4 & \cdots & 0 & 0 & 0 \\ 0 & 0 & 1 & & 0 & 0 & 0 \\ & \vdots & & \ddots & & \vdots & \\ 0 & 0 & 0 & & 1 & 0 & 0 \\ 0 & 0 & 0 & \cdots & 4 & 1 & 0 \\ 0 & 0 & 0 & & 1 & 4 & 1 \end{bmatrix} \begin{bmatrix} b_1 \\ b_2 \\ b_3 \\ \vdots \\ b_{m-1} \\ b_m \end{bmatrix} = \frac{3}{(x_{j+1} - x_j)^2} \begin{bmatrix} y_1 - 2y_2 + y_3 \\ y_2 - 2y_3 + y_4 \\ y_3 - 2y_4 + y_5 \\ \vdots \\ y_{m-3} - 2y_{m-2} + y_{m-1} \\ y_{m-2} - 2y_{m-1} + y_m \end{bmatrix} \tag{4.18}$$

where $[b_1, b_1, \cdots, b_m]^T$ is undetermined coefficients. However, only $(m-2)$ independent equations are built according to the recurrence relation. Therefore, two other conditions need to be induced to calculate above matrix. These lead to different types of cubic spline interpolation methods. Such as natural splines ($b_1 = b_m = 0$), parabolic runout spline ($b_1 = b_2, b_{m-1} = b_m$), and cubic runout spline ($b_1 = 2b_2 - b_3, b_m = 2b_m - b_{m-1}$).

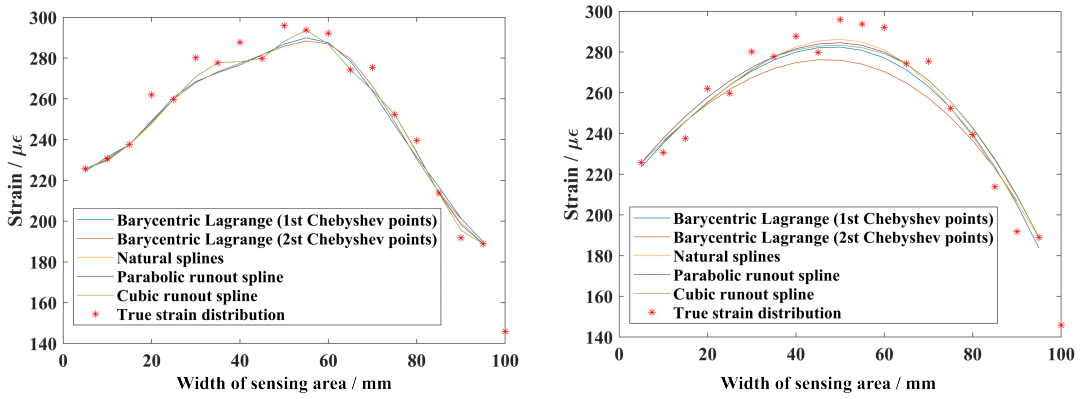


Figure 4.5: Interpolation results of resampling data $f(\widetilde{s}_j^1)$ and $f(\widetilde{s}_j^5)$ (Refer Table 4.1): (a) The interpolation results of $f(\widetilde{s}_j^1)$; (b) The interpolation results of $f(\widetilde{s}_j^5)$

4.2.3 Results and discussion

Based on the interpolation methods mentioned above, all $f(\widetilde{s}_j^q)$ in Table 4.1 were interpolated and compared with true strain distribution $f(\widetilde{s}_j)$. The interpolation results for $f(\widetilde{s}_j^1)$ and $f(\widetilde{s}_j^5)$ under 5KN tension load with different methods are shown in Figure 4.5. As shown in this figure, the true strain distribution at different location is different even under one-axis tension load. This is mainly because of different mechanical parameters and strain transfer rate in different location. This difference on strain distribution generate relatively fixed local pattern in true strain distribution. The comparison between these two interpolation results shows that the accuracy of strain reconstruction decreases with the increase of sensors distance. This means that local patterns of strain distribution are lost after the reconstruction.

The strain reconstruction results based on different sensor layout distance $f(\widetilde{s}_j^q)$ is defined as $\hat{s}$. Therefore, the average error of reconstructed strain compared with true strain distribution is shown as follows.

$$\overline{e} = \frac{1}{20p} \sum_{x=1}^{p} \sum_{y=1}^{20} \frac{|s^{'}(x,y) - \hat{s}(x,y)}{s^{'}(x,y)} \times 100\% \tag{4.19}$$

The results of interpolation errors in strain distribution reconstruction are shown in Table

4.2. This table demonstrates the relation between the accuracy of strain reconstruction and sensor distance. Specifically, the average error of reconstructed strain compared with true strain distribution increase with increase of sensor distance. The average errors of barycentric Lagrange interpolation methods are slightly larger than cubic spline interpolation methods. This is because that the adopted linear estimation in data estimation at Chebyshev points induces extra errors. However, the barycentric Lagrange interpolation methods show much better stability than cubic spline interpolation methods with the increase of sensor distance. For example, the average error under $f(\widetilde{s}_j^5)$ increases by 103.31% compared with $f(\widetilde{s}_j^1)$ when cubic runout spline is adopted. However, this value is 47.46% when barycentric Lagrange based on 1st Chebyshev method is adopted.

Table 4.2: The results of interpolation errors in strain distribution reconstruction

	$f(\widetilde{s}_j^1)$	$f(\widetilde{s}_j^2)$	$f(\widetilde{s}_j^3)$	$f(\widetilde{s}_j^4)$	$f(\widetilde{s}_j^5)$
Barycentric Lagrange based on 1st Chebyshev	1.58%	2.20%	2.04%	2.13%	2.33%
Barycentric Lagrange based on 2st Chebyshev	1.74%	2.41%	2.32%	2.48%	2.78%
Natural splines	1.15%	1.71%	1.74%	1.96%	2.03%
Parabolic runout spline	1.17%	1.74%	1.75%	1.99%	2.25%
Cubic runout spline	1.21%	1.85%	1.86%	2.03%	2.46%

The strain reconstruction results based on barycentric Lagrange interpolation under different sensor distance are shown in Figure 4.6.From left to right, the first figure is true strain distribution.The second figure express the strain reconstruction result under $f(\widetilde{s}_j^1)$, in which the sensor distance of measurement data is twice than the sensor distance of reconstruction data. The third figure shows the strain reconstruction result under $f(\widetilde{s}_j^5)$. The comparison between these three figures also demonstrates that local patterns of strain distribution are lost after the reconstruction when the sensor distance of measurement data is much larger ($\geq$ 6 times) than the sensor distance of reconstruction data. However, the main trends of reconstructed strain distribution consistent with the true strain distribution.

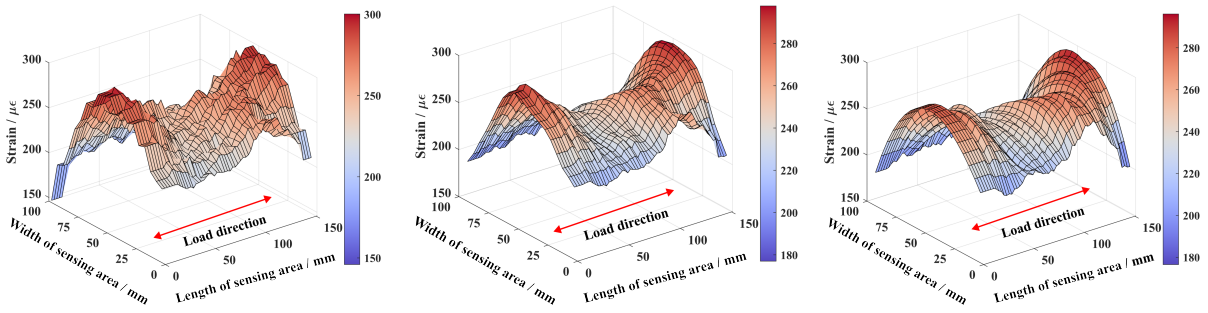


Figure 4.6: The strain reconstruction results: (a) The true strain distribution; (b) The strain reconstruction result under $f(\widetilde{s}_j^1)$; (c) The strain reconstruction result under $f(\widetilde{s}_j^5)$

4.2.4 Conclusions

The research on strain reconstruction with interpolation methods based on distributed fibre optical sensor measurements is conducted in this subsection. The main conclusions are summaries as follows.

- The accuracy of strain reconstruction decreases with the increase of sensors distance, which means that the average error of reconstructed strain compared with the true strain distribution increases with the increase of sensor distance. For example, the average error of cubic runout spline method increased from 1.21% to 2.46% when the sensor distance increased from 10mm to 30mm.

- The average errors of barycentric Lagrange interpolation methods are slightly larger than cubic spline interpolation methods. This is mainly because of the linear estimation of data at Chebyshev points.

- The barycentric Lagrange interpolation methods show much better stability than cubic spline interpolation methods with the increase of sensor distance.

- Local patterns of strain distribution are lost after the reconstruction when the sensor distance of measurement data is much larger ($\geq$6 times) than the sensor distance of reconstructed data. However, the main trends of reconstructed strain distribution consistent with the true strain distribution.

Based on these conclusion, future work on damage detection with reconstructed strain field will be conducted. In addition, More complex methods can be adopted to decrease the errors induced by data estimation when barycentric Lagrange interpolation methods are adopted. For example, calculating the data at Chebyshev points with polynomial function [305].

4.3 A novel DI-based damage detection method

This subsection presents a novel DI-based approach for damage detection in CFRP structures based on local strain feature matching. The proposed approach utilizes distributed in-plane strain measurements (obtained by OFDR technique) for plate structures under load to define a local point autocorrelation coefficient based on Delaunay triangulation [306] and Hausdorff distance [307]. This coefficient effectively identifies the discontinuities in distributed in-plate strain, enabling accurate capture of damage information through the damage index which is defined as the integral of this coefficient. Notably, the proposed approach requires no prior knowledge of the non-damaged strain distribution and yields excellent detection results for both BVID and VID. Leveraging the advantages of distributed strain sensing, coupled with image processing technology for the purpose of in-service damage detection of CFRP structures, the proposed novel method is a promising technology. The efficacy of this technology has been demonstrated in this subsection through theoretical analysis and experimental investigations, offering valuable insights and reference for future research in this domain.

4.3.1 Methodology

In practical applications, two challenges associated with distributed strain measurement based on OFDR are encountered. The first challenge pertains to the existence of outliers in raw data, which has been discussed in previous studies [161, 77]. The second challenge is the limitation of acquiring only one-dimensional strain, which is unable to represent the spatial distribution of strain on 2D CFRP plate structures. Therefore, filtering and reconstruction of raw strain data is proposed to obtain reliable strain distribution. Subsequently, the development of a

damage detection scheme is presented, which is used to detect discontinuities in the distributed in-plate strain during loading. The proposed methodology includes: obtaining neighbourhood strain sets, sparse representation of the neighbourhood strain set by convex hull representation (obtained by Delaunay Triangulation), similarity assessment of convex hull during loading, and calculation of damage index based on sparse representation and similarity assessment. The diagram of the proposed methodology is illustrated in Figure 4.7. The proposed methodology is then verified and validated with three CFRP plates, impacted with with low velocity impacts of different energy to cause different damage severity. The specimens are subjected to static load after impact, and the strain data within the SMFs were collected and 2D strain distribution along 1D SMF was reconstructed to demonstrated the capabilities of the developed methodology.

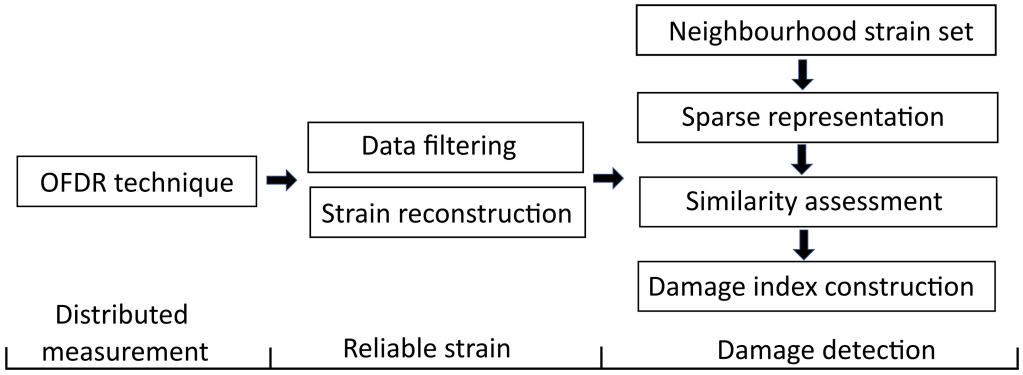


Figure 4.7: The diagram of the proposed methodologies

Strain measurements filtering and reconstruction

Data filtering and reconstruction are critical steps in the data processing workflow and can significantly impact the accuracy and effectiveness of subsequent analyses and models. Filtering and reconstruction of raw strain data recorded by FOS (along the fibre axis) is necessary to obtain reliable in-plane strain distribution map. The steps for achieving data filtering and reconstruction are listed below.

1. Outliers in measurements are eliminated by applying the local outlier factor (LOF) approach, which is a widely adopted method for outlier detection [230]. An example of

outliers in real strain measurements is presented in Figure 4.8(a). LOF evaluates the deviation of the target data from its local neighbours. Assuming a is an object in the strain measurement set $A(a \in A)$, the LOF of a is expressed as:

$$LOF_k(a) = \frac{1}{|N_k(a)|} \sum_{b \in N_k(a)} \frac{lrd_k(b)}{lrd_k(a)} \tag{4.20}$$

where $N_k(a)$ is a set of k-nearest neighbors around a; b denotes any object in $N_k(a)$; $lrd_k(a)$ and $lrd_k(b)$ defined as local reachable density of a and b, respectively. They have same definition, which shown as:

$$lrd_k(a) = \frac{|N_k(a)|}{\sum_{b \in N_k(a)} max\{d_k(b), d(a,b)\}} \tag{4.21}$$

where $d_k(b)$ is the Euclidean distance between b and its k-th nearest neighbor, $d(a,b)$ express the Euclidean distance between a and b. Outliers in the data are identified by LOFs much greater than 1. The LOF threshold should be carefully selected to distinguish true outliers from discontinuous data induced by damage in the strain field, as the latter is crucial for the identification of damage.

2. Data reconstruction here refers to the process of converting one-dimensional (1D) strain measurements of a SMF to a two-dimensional (2D) strain distribution based on the structure's shape and layout of SMF. The specific implementation involves locating the effective sensing segment on the SMF according to the layout, removing redundant non-sensing segment measurements, defining a matrix with location information based on the structure's shape, and arranging the data of the effective sensing segments into this matrix.

   Figure 4.8(a) presents an example in the follow-up experimental verification of this work, which measures the strain field of a rectangular CFRP panel in a certain load state using a SMF sensor. This figure depicts all the strain data measured along the SMF, providing no information about the structure. In contrast, Figure 4.8(b) shows the data after reconstruction under the same load state, where the x-axis and y-axis indicate the panel's length and width, respectively, and the z-axis represents the strain data corresponding

to each location on this panel. This processing enhances the data's interpretability and plays a vital role in subsequent damage detection, particularly for complex structures. The experimental procedure and findings are presented in detail in the experimental subsection of this article.

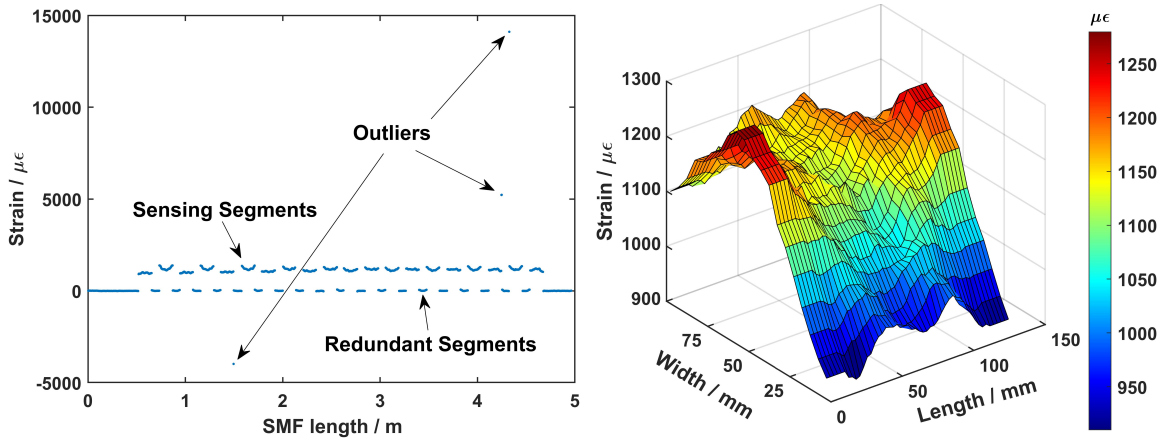


Figure 4.8: Strain data filtering and reconstruction of distributed sensing: (a) the 1D strain measurements along the SMF; (b) the corresponding reconstructed 2D strain distribution along 1D SMF on a CFRP panel

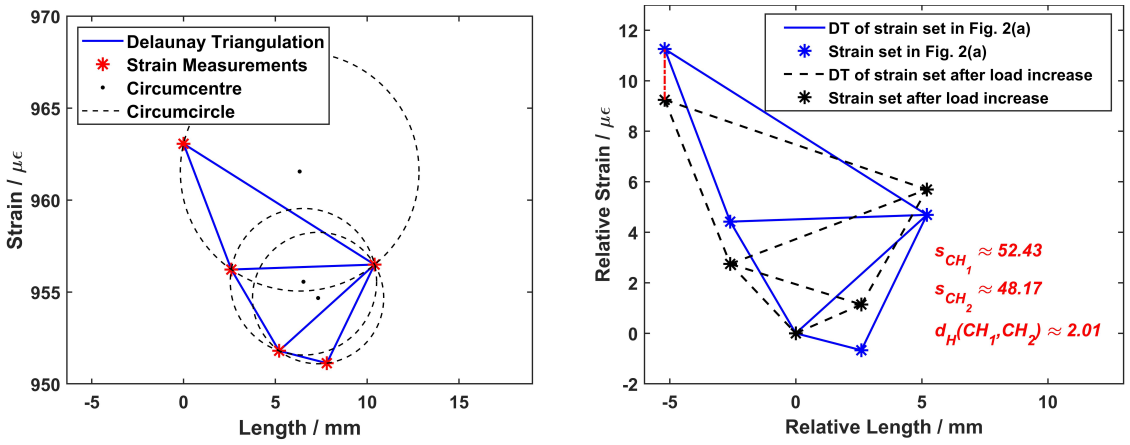
The sparse representation and similarity assessment of neighbourhood strain set

The strain data obtained from distributed fibre optic sensors is divided into multiple collections of measurement points containing adjacent spatial locations, referred to as neighbourhood strain sets. Identification of discontinuities in the strain field is performed through analysis of these neighbourhood strain sets, including sparse representation and similarity assessment. Sparse representation involves the adoption of image processing techniques to extract features for representing the neighbourhood strain set. The Delaunay triangulation is adopted to partition the neighbourhood strain set in the spatial distribution figure of strain, obtaining a unique convex hull that contains all the strain measurements in the set. This convex hull is defined as the sparse representation of the neighbourhood strain set. Consequently, detection of discontinuities in the strain field can be transformed into the evaluation of similarity changes of the convex hull during loading. If the similarity (autocorrelation) of the convex hull significantly deteriorates during loading, it indicates discontinuity in the strain field.

As mentioned in the beginning of Chapter 4.3.1, the sparse representation of neighbourhood strain set is realized by the Delaunay triangulation (DT) method [306], which has been widely employed in various research for feature matching, such as ship collision [308], image matching [309, 310], atmospheric remote sensing [311], fingerprints and palmprint recognition [312], and motion detection [313] due to its robustness and effectiveness. The Delaunay triangulation is based on the Delaunay condition, which mandates that all circumcircles of generated triangles have empty interiors. This condition ensures that the generated triangles have the largest minimum angle and represent the relationship between the scattered points as sparsely as possible. After the Delaunay triangulation, the neighbourhood strain set is represented by a unique convex hull (under no degeneracies), enabling the sparse representation of neighbourhood strain set with good structure and minimal redundancy. This unique convex hull considers the constraints of all objects within the neighbourhood strain set, imparting a strong capacity for describing the neighbourhood strain set. Furthermore, many well-established methods, such as the divide-and-conquer algorithm [314] and incremental insertion algorithm [315], have been utilized to expedite the acquisition of Delaunay triangulation.

Figure 4.9(a) presents the Delaunay triangulation of a neighbourhood strain set comprising of five adjacent points which were selected from the FOS measurements shown in Figure 4.8(a). The x-axis and y-axis represent the measurement points' locations and corresponding strain values, respectively. The locations of the points depicted in this illustration are relative to the first point rather than the actual locations on the SMF. The red asterisks indicate the strain measurements, while the Delaunay triangulation is represented by solid blue line. The circumcircles of triangles and their corresponding circumcentres are represented by black dotted lines and black dots, respectively. Notably, the Delaunay condition is satisfied, as there are no points within the circumcircles.

The similarity assessment of the convex hull, acquired through Delaunay triangulation under distinct loads, is a suitable approach for discontinuity detection in strain field. This phenomenon is attributed to the fact that strain discontinuity is observed in the event of damage, leading to a reduction in the similarity of convex hulls. Assuming that the strain measurements in neighbourhood strain set presented in Figure 4.9(a) is expressed as $S = \{(l_i, \epsilon_i) \quad i = 1, 2, 3, 4, 5\}$,



(a) (b)

Figure 4.9: Delaunay triangulation and similarity assessment: (a) The Delaunay triangulation of a neighbourhood strain set; (b) Similarity assessment of convex hulls based on Hausdorff distance and area difference

where l_i is the location of i-th point, ϵ_i express the strain measurement of i-th point. With the increase of load, this set changes to $S^{'} = \{(l_i, \epsilon_i^{'}) \quad i = 1, 2, 3, 4, 5\}$. Since the similarity of the convex hulls is our concern, these two sets are transformed into $\hat{S} = \{(l_i - l_3, \epsilon_i - \epsilon_3) \quad i = 1, 2, 3, 4, 5\}$ and $\hat{S}' = \{(l_i - l_3, \epsilon_i^{'} - \epsilon_3^{'}) \quad i = 1, 2, 3, 4, 5\}$. Figure 4.9(b) depicts the Delaunay triangulation of $\hat{S}$ and $\hat{S}'$, where the x-axis and y-axis denote the location and strain relative to the middle point (the third point) in the neighbourhood strain set, respectively. A good similarity between these two convex hulls is observed, which signifies that no strain discontinuity is observed within the neighbourhood strain set after loading.

In order to mathematically evaluate the similarity of the convex hulls mentioned above, the Hausdorff distance and the area of the convex hulls are employed in this work. The Hausdorff distance is defined as the distance between two discrete point sets, and is commonly used for evaluating the similarity of polygons. This method has been successfully applied in various fields, including medical image segmentation [316], three-dimensional (3D) objects retrieval [317, 318], graph matching[319], and multi-objective optimization [320]. The Hausdorff distance between the convex hulls in Figure 4.9(b) can be calculated as Equation 4.22:

$$d_H(CH_1, CH_2) = max\{h(CH_1, CH_2), h(CH_2, CH_1)\} \tag{4.22}$$

where CH_1 and CH_2 express the vertices of these two convex hulls, we have $CH_1 = \hat{S}$ and $CH_2 = \hat{S}'$ in this example. $h(CH_1, CH_2)$ and $h(CH_2, CH_1)$ are defined as Equation 4.23 and Equation 4.24:

$$h(CH_1, CH_2) = max\{min\{d_E(ch_i, ch_j)\}\} \quad ch_i \in CH_1, ch_j \in CH_2 \tag{4.23}$$

$$h(CH_2, CH_1) = max\{min\{d_E(ch_i, ch_j)\}\} \quad ch_i \in CH_2, ch_j \in CH_1 \tag{4.24}$$

where $d_E(ch_i, ch_j)$ denotes the Euler distance between ch_i and ch_j, and $i, j = 1, 2, 3, 4, 5$. The Hausdorff distance between these two convex hulls in Figure 4.9(b) is labelled and marked with dash-dotted red line. In this study, we have defined the local point autocorrelation (LPA) coefficient of the neighbourhood strain set as the product of the area difference between these two convex hulls and their Hausdorff distance.

$$LPA = |S_{CH_1} - S_{CH_2}| \cdot d_H(CH_1, CH_2) \tag{4.25}$$

where S_{CH_1} and S_{CH_2} represents the area of the two convex hulls mentioned above, and are depicted in Figure 4.9(b). In addition to using the Hausdorff distance for the assessment of convex hulls' similarity, this autocorrelation incorporates the difference in the areas of the convex hulls obtained through Delaunay triangulation. Because significant changes in the area of convex hull obtained from the same set of measurement points under different loads indicate possible damage. Therefore, a large LPA in value means high probability of damage. In addition, the proposed LPA coefficient in this study improves the robustness and reduces false positives in damage detection by incorporating the area difference.

Damage detection based on one-dimensional strain measurements

Based on the relationship between LPA coefficient and potential damage, this investigation proposes a damage detection framework for CFRP structures. By using the 1D distributed measurements taken under continuous loading, damage data can be gathered by computing

and analysing the LPA coefficients of all neighbourhood strain sets spanning the entire SMF. The implementation approach is outlined below.

1. The distributed strain measurements are processed by performing data filtering and reconstruction, as outlined in Chapter 4.3.1.

2. During the loading process, a reference strain is selected for calculating the LPA coefficients.

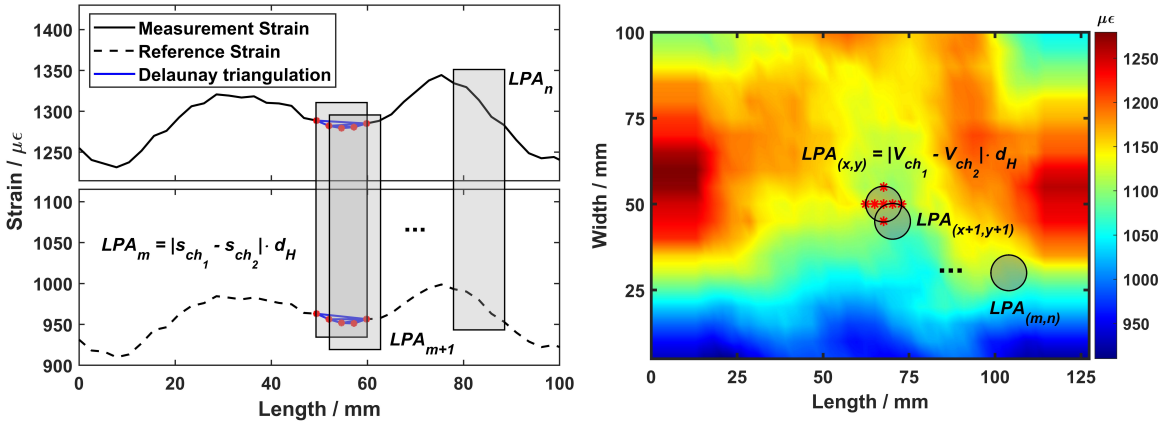
3. The LPA coefficients are calculated based on the reference strain selected during the loading process according to Equation 4.25. Figure 4.10(a) demonstrates the implementation of this step using the example from Figure 4.9(b). The x-axis represents the location of the measurement points, and the y-axis shows the measured strain. The black dash line represents the reference strain, and the black solid line represents the measured strain. The Delaunay triangulation results from Figure 4.9(b) are represented by the solid blue line here. The grey sliding rectangle in Figure 4.10(a) is used to define the neighbourhood strain set to calculate the LPA coefficient array. The LPA coefficients of all neighbourhood strain sets along the SMF during the entire loading process can be stored in a 2D matrix, as shown in Equation 4.26.where $u(u \in N^*)$ denotes the total number of neighbourhood strain sets and $w(w \in N^*)$ represents the number of loading states obtained during the loading process. It is important to note that dynamic damage detection can be achieved by interpolating the LPA coefficient array to this 2D matrix in real-time.

$$X_{u,w} = \begin{bmatrix} LPA_{1,1} & \cdots & LPA_{1,w} \\ \cdots & LPA_{x,z} & \cdots \\ LPA_{u,1} & \cdots & LPA_{u,w} \end{bmatrix} \quad x \in [1,u] \quad z \in [1,w] \tag{4.26}$$

4. The calculation of the DI is predicated by the matrix $X_{u,w}$. As shown in Equation 4.27, the damage index is computed as the integral of the LPA coefficient over the entire loading process, which effectively mitigates the influence of random noise and enhances the

robustness of damage detection. Matrix $DI_{u,w}$ denotes the possibility of damage occurring near the neighbourhood strain set. The emergence of damage incites a substantially larger damage index in the neighbourhood strain sets near the affected area in comparison to the non-affected sets. Thus, high damage index values relative to other neighbourhood strain sets indicate a higher probability of damage.

$$\begin{aligned} DI_{u,w} &= \int_{load} [LPA_{1,z}, LPA_{2,z}, \cdots, LPA_{u,z}]^T \\ &= \sum_{z=1}^{w} [X_{u,w}(1,z), X_{u,w}(2,z), \cdots, X_{u,w}(u,z)]^T \end{aligned} \tag{4.27}$$



(a) (b)

Figure 4.10: Damage detection schemes based on LPA coefficients: (a) Calculation of LPA coefficients based on 1D strain measurements along the SMF sensor; (b) Calculation of LPA coefficients based on 2D strain distribution of 1D SMF on CFRP panel

Damage detection based on two-dimensional strain measurements

The damage detection scheme for CFRP structures based on fibre optic sensors relies directly on the 1D strain measurements obtained from SMF sensor. However, for complex plate structures, it may be more desirable to acquire the full in-plane strain field and damage information related to the actual CFRP structures, as shown in Figure 4.8(b). Therefore, in this subsection, we propose a damage detection scheme based on the 2D strain distribution of 1D SMF on the surface of the CFRP structure. The procedure of this scheme is similar to the one mentioned in Chapter 4.3.1, with the difference being discussed below.

The calculation of LPA coefficients is modified in the proposed damage detection scheme based on the 2D strain distribution of 1D SMF on the surface of the CFRP structures. The key difference is in the selection of neighbourhood strain set, which now changes from 1D to 2D. To address this, a 3D Delaunay triangulation is required for the strain set on the 2D surface. Similar to 2D Delaunay triangulation, the 3D Delaunay triangulation condition ensures that the circumscribed sphere of all tetrahedra have empty interiors and maximize the minimum angle of tetrahedra. Further information on 3D Delaunay triangulation can be found in [321, 322, 323]. As a result, the local point autocorrelation coefficient is revised as Equation 4.28:

$$LPA = |V_{CH_1} - V_{CH_2}| \cdot d_H(CH_1, CH_2) \tag{4.28}$$

Where V_{CH_1} and V_{CH_2} express the volume of two convex hulls (CH_1 and CH_2) obtained by the 3D Delaunay triangulation. $d_H(CH_1, CH_2)$ is the Hausdorff distance between these two convex hulls.

In this study, the 2D strain distribution of 1D SMF presented in Figure 4.8(b) serves as an exemplary case to explain the calculation process of LPA coefficients based on 3D Delaunay triangulation, as demonstrated in Figure 4.10(b). The x-axis and y-axis represent the sensing area along the length and width of the CFRP panel, respectively, while the strain is represented by different colours, with the colour bar on the right indicating the corresponding values. The neighbourhood strain set is defined using a series of circles, with the red asterisks representing all measurement points. $LPA_{(x,y)}$ denotes the LPA coefficient of neighbourhood strain set (x, y). Assuming that the strain field contains $u \times v (u, v \in N^*)$ neighbourhood strain sets, and the strain in these sets is recorded under $w (w \in N^*)$ different loading states, the LPA coefficients of all points in the 2D strain distribution of 1D SMF throughout the loading process can be stored in a 3D matrix as shown in equation 4.29. Subsequently, the damage index is transformed into a 2D matrix using equation 4.30.

$$X_{u,v,w} = \begin{bmatrix} LPA_{(1,1),z} & \cdots & LPA_{(1,v),z} \\ \cdots & LPA_{(x,y),z} & \cdots \\ LPA_{(u,1),z} & \cdots & LPA_{(u,v),z} \end{bmatrix} \quad x \in [1,u], y \in [1,v], z \in [1,w] \tag{4.29}$$

$$DI_{u,v,w} = \sum_{z=1}^{w} \begin{bmatrix} X_{u,v,w}(1,1,z) & \cdots & X_{u,v,w}(1,v,z) \\ \cdots & X_{u,v,w}(x,y,z) & \cdots \\ X_{u,v,w}(u,1,z) & \cdots & X_{u,v,w}(u,v,z) \end{bmatrix} \tag{4.30}$$

4.3.2 Experiments

Specimen and layout

Experimental verification of the proposed damage detection algorithm was conducted on three rectangular specimens made of M21 T800 material, each measuring $280 \times 120 \times 2$ mm. These three specimens were extracted from a single large CFRP panel. For each specimen, the SMF sensors are installed on the surface using epoxy (Stock number 199-1468) sourced from RS Components. The epoxy was adopted in this experiment because it is able to cure under room conditions, offering convenience in mounting a complex sensor network.Therefore, any room temperature-curing epoxy resin with strong adhesive ability can be used as a substitute to verify the work of this subsection. The sensor layout for all three specimens is identical, as shown in Figure 4.11. This layout permits a sensing separation of 5 mm between adjacent segments with low bending losses. To implement the above-mentioned laying scheme, start by securing the two ends of the optical fiber sensor with instant adhesive (eg. super glue). Once the optical fiber sensor network is fixed using this method, immerse the entire surface with epoxy resin glue. Finally, let it stand for at least 24 hours to allow for curing. This method of laying the sensor network aims to maintain parallelism between the optical fiber sensors as much as possible. The shaded area in Figure 4.11 represents the distributed sensing area of

130×100 mm. This layout facilitates the straightforward identification of specific segments on the CFRP specimen, as substantiated by the results presented in Figure 4.8(a). Additionally, the size of the END-TABs is 50×120mm. It is worth noting that the sensors are exclusively installed on one surface of the specimens. The damage is induced by impacting the opposite surface, which lacks SMF sensors.

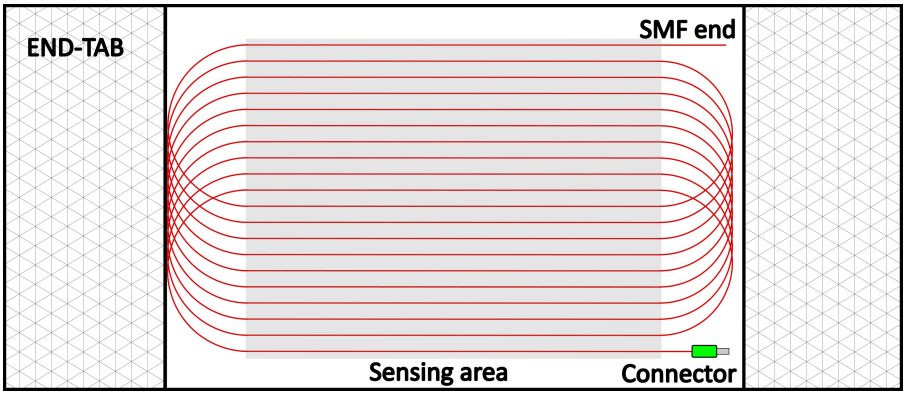
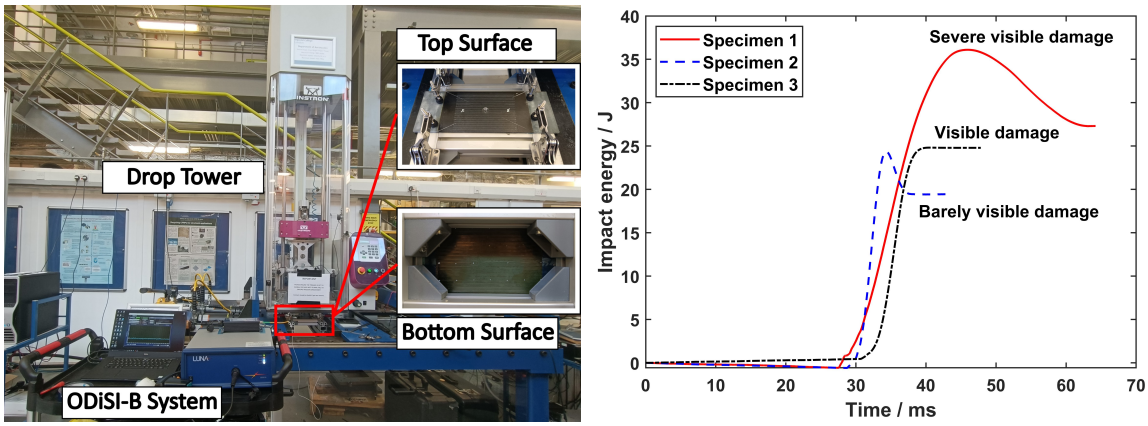


Figure 4.11: The layout of SMF sensor on the CFRP specimens

Low-velocity impact experiment

Damage was induced in the deep surface of specimens by an experiment with low-velocity impact utilizing a CEAST 9350 drop tower system, as illustrated in Figure 4.12(a). This system is able to comprehensively record the profiles of the entire impact event through a dedicated data acquisition system (CEAST DAS 16000), including force, energy, displacement, and velocity data with time. The impacting tup employed in the experiment featured a 10mm diameter.This low-velocity impact experiment was conducted to simulate scenarios that are typically encountered in aircraft maintenance and operation. These scenarios encompass instances of improper maintenance practices, such as the application of force near a jack pad or unintended impacts involving tools or ground-support equipment (tow vehicles), inadvertent dropping of tools. It is worth to note that such impact events pose significant threats to the composite industry. This is due to their propensity to induce intricate failure mechanisms and internal damage, especially the BVID. The consequences of these damages are substantial and manifest as a substantial reduction in the structural properties of composite materials[324, 325, 326].

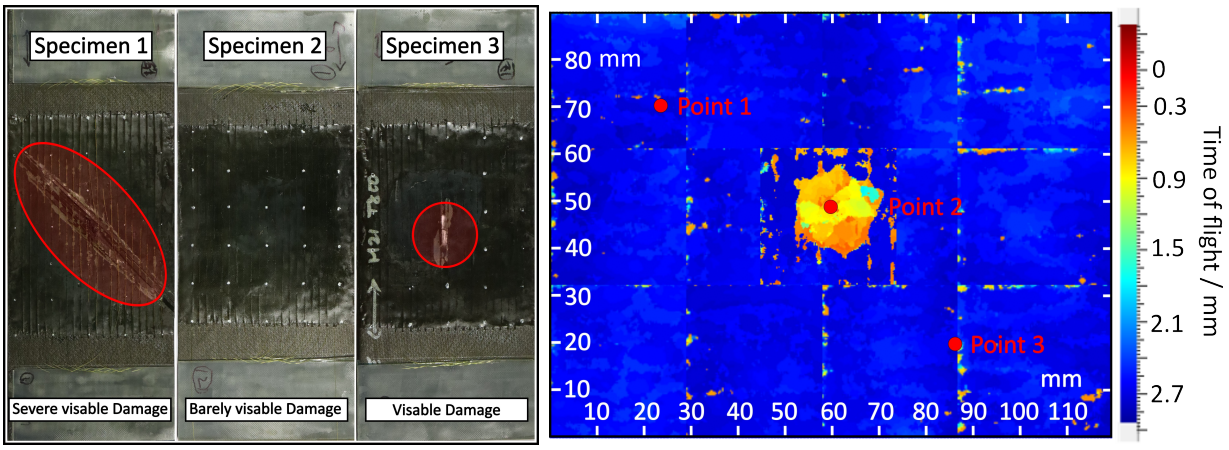
The impact energy of the three experiments is presented in Figure 4.12(b), where the x-axis



(a) (b)

Figure 4.12: The low-velocity impact experiment: (a) The experiment setup; (b) The impact energy of three specimens

denotes the time during the impact and the y-axis denotes the impact energy. It can be observed that specimen 1 absorbed the largest impact energy, followed by specimen 3, while specimen 2 absorbed the least impact energy. Accordingly, visible impact damage was observed for specimen 1 and 3 after impact. However, only barely visible impact damage was observed for specimen 2 through c-scan, as shown in Figure 4.13(b), where the size of the c-scan area was 120 × 90mm, which is slightly smaller than the sensing area of the SMF sensor. Despite setting the impact energy at the same level for specimen 2 and specimen 3, it was observed that specimen 2 absorbed marginally less energy compared to specimen 3. This discrepancy can be attributed to minor variations in the impact location and discrepancies in manufacturing quality. Figure 4.13(a) shows the three specimens after the low-velocity impact experiment. It should be noted that the SMF sensor on the surface of specimen 1 was also broken and could not be used for strain measurement in subsequent experiments. To enhance the interpretability of the subsequent damage detection results, three locations on the specimen are marked as Point 1, Point 2, and Point 3 in Figure 4.13(b) with red dot and text description, and the strain measurement results of Specimen 2 and Specimen 3 at these locations will be discussed in detail in the subsequent section to illustrate the performance of the proposed damage detection algorithm.



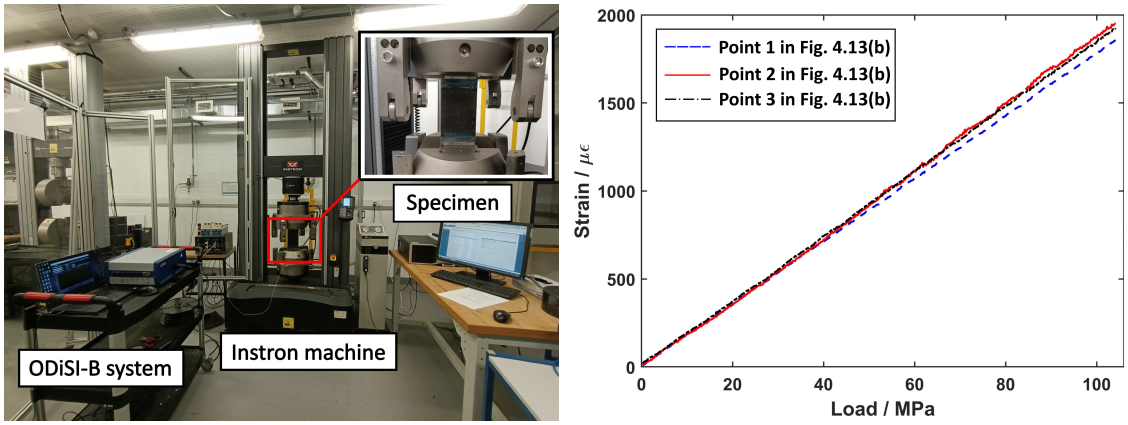
(a) (b)

Figure 4.13: Different types of impact damage induced in CFRP specimens: (a) Damage state of three specimens after low-velocity impact experiment; (b) BVID in Specimen 2 observed by c-scan

Static tensile experiment

This section focuses on specimens 2 and 3 since the SMF sensor on specimen 1 was damaged during the impact experiment, as previously mentioned. Prior to and after the low-velocity impact experiment, static tensile experiments were conducted on specimens 2 and 3 using a 250 kN tensile machine from Instron (Instron 5980 Series Dual Column Floor Frames (250KN)). More specifically, the experimental procedure begins with a static tensile test to collect strain data in an undamaged state. Subsequently, a C-scan is conducted to confirm the absence of damage in the specimens. Following the verification by C-scan, damage is intentionally introduced to the specimens through low-velocity impact experiments. After the damage is induced, another C-scan is performed to assess the extent of BVID in specimen 2. Finally, static tensile tests are conducted once more on both specimen 2 and specimen 3 to collect strain data in a damaged condition. This entire process simulates the data collection scenarios that SMF sensors would encounter during real-world damage events in composite structures. The proposed methodology relies on measuring local strain changes in the damaged area of the composite plates, to indicate damage and therefore the structure has to be subjected to load while recording the response with SMF. Figure 4.14(a) illustrates the experimental setup of static tensile experiment, which involved using the ODiSI-B system to obtain distributed strain

data throughout the loading process. A zoomed view of the CFRP specimen is also provided on the right side of the figure.



(a) (b)

Figure 4.14: The static tensile experiment: (a) The experiment setup; (b) The load response of Specimen 2 in Test 3-1

Table 4.3 depicts all the test scenarios for the static tensile experiment. These scenarios involved conducting tensile tests with and without damage for specimens 2 and 3. As indicated in this table, the tensile loads applied in these test scenarios are significantly lower than the failure load of CFRP structures. This implies that during the experiments, specimen 2 and 3 experience controlled tensile loads without reaching structural failure. Five controlled tensile tests were conducted for each test scenario to ensure the reliability of strain data and simulate the typical working conditions of damaged structures. The reference signal of the OFDR system is reset, and the tensile load is completely released after each tensile test to prevent the influence of residual strain in the specimens. The tensile load for each test is presented in Table 4.3. For instance, in Test 1-1, Specimen 2 underwent a loading process from 0 MPa to 41.7 MPa, followed by an unloading process from 41.7 MPa to 0 MPa. The load for specimen 2 with BVID was set higher than the other scenarios to amplify changes in the local strain field caused by presence of damage. The strain response of Point 1, 2 and 3 (marked in Figure 4.13(b)) in Test 3-1 is presented in Figure 4.14(b). It is observed that the strains at these locations increase linearly with the load increase, indicating that obtaining damage information directly from the strain response is challenging when BVID is present in CFRP structures.

Table 4.3: Test scenarios in the static tensile experiment

Test scenario	Specimen	Test Number	Load / MPa	Damage State
1	2	1-1	0-41.7	Without Damage
		1-2	0-44.2	
		1-3	0-44.6	
		1-4	0-44.2	
		1-5	0-44.6	
2	3	2-1	0-43.8	Without Damage
		2-2	0-44.2	
		2-3	0-44.6	
		2-4	0-44.2	
		2-5	0-44.6	
3	2	3-1	0-104.2	With BVID
		3-2	0-138.7	
		3-3	0-168.1	
		3-4	0-180.4	
		3-5	0-172.7	
4	3	4-1	0-41.7	With VID
		4-2	0-43.3	
		4-3	0-43.5	
		4-4	0-43.0	
		4-5	0-43.3	

4.3.3 Results and discussion

Damage detection result based on one-dimensional strain measurements

In the static tensile experiments, the stability of multiple repetitions of each test scenario was observed to be good. Consequently, for the purpose of realizing damage detection using the algorithm proposed in this chapter, the strain measurements in Test 3-1 and Test 4-1 were used to represent the strain data under two typical damage states, namely BVID and VID, respectively. Figure 4.15 depicts the LPA coefficients of neighbourhood strain sets near Point 1, 2 and 3 (as marked in Figure 4.13(b)) in Test 3-1 and Test 4-1. It is worth mentioning that the unit of the LPA coefficient and damage index is not marked in the figures presented in this chapter. This is because that the employed image processing method makes the unit complex and lacks practical meaning. Instead, the damage is evaluated based on its magnitude.

The LPA coefficients in Test 3-1 are presented in Figure4.15(a) and 4.15(b). As per step 2 in subsection 4.3.1, the strain measurements obtained in Test 1-1 (without damage) and those obtained in Test 3-1 (with damage) are utilized as reference strain for Figure 4.15(a) and 4.15(b), respectively. In both figures, the LPA coefficients close to the damage (Point 2) exhibit significantly different characteristics than the other points (Point 1 and 3). Although the utilization of pristine state strain (form Test 1-1) as a reference has been observed to yield superior outcomes, it is noteworthy that the reference strain selected in the presence of damage (form Test 3-1) can also determine the damaged state. Therefore, the proposed LPA coefficient can identify the measurement points close to the damage without relying on the pristine state reference strain, indicating its potential in damage identification of CFRP structures.

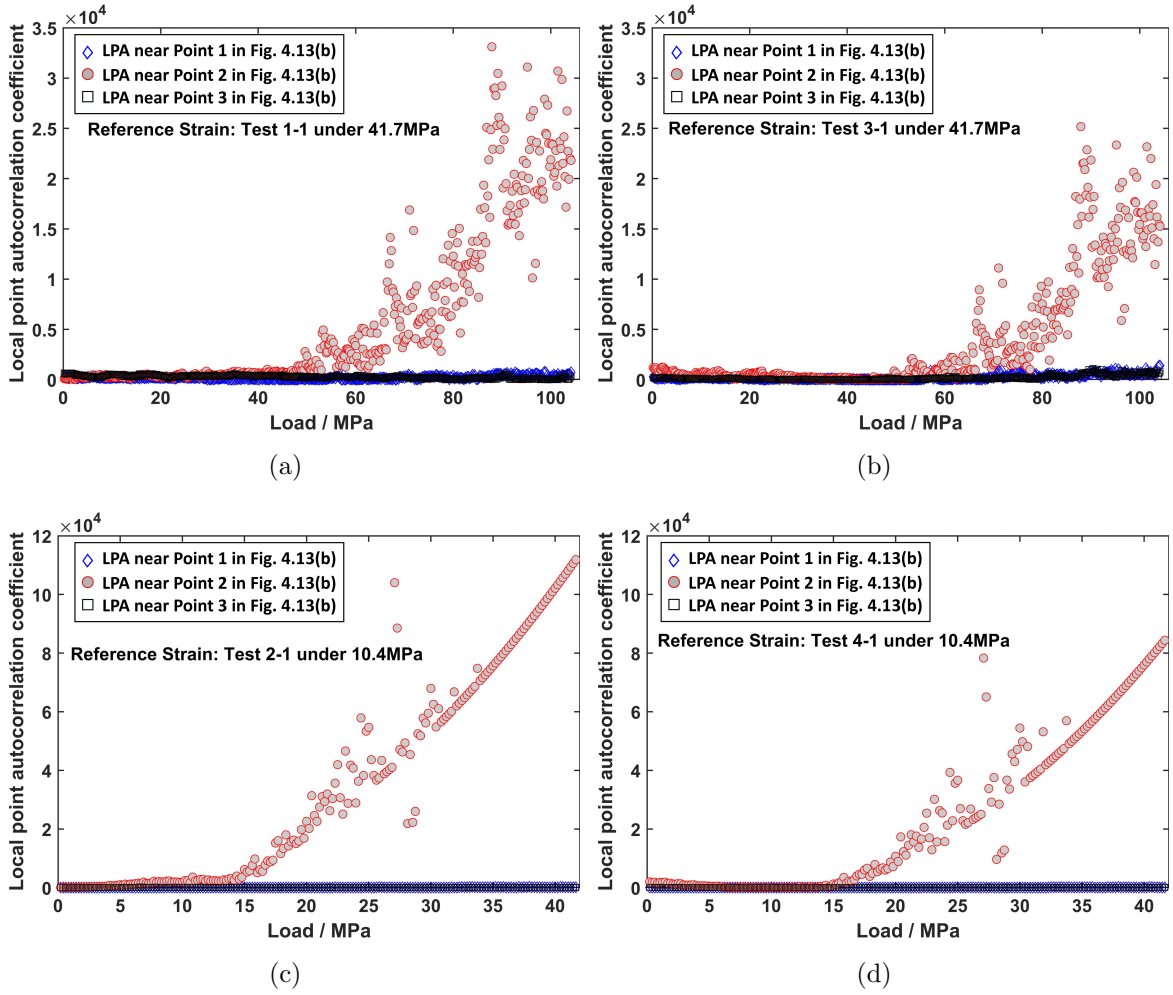


Figure 4.15: The LPA coefficients near Point 1,2 and 3 based on 1D strain measurements along the SMF sensor: (a) Results of Test 3-1 (reference strain: Test 1-1 under 41.7MPa); (b) Results of Test 3-1 (reference strain: Test 3-1 under 41.7MPa); (c) Results of Test 4-1 (reference strain: Test 2-1 under 10.4MPa);(d) Results of Test 4-1 (reference strain: Test 4-1 under 10.4MPa)

The LPA coefficients near Point 1, 2 and 3 (as marked in Figure 4.13(b)) in Test 4-1 are depicted in Figures 4.15(c) and 4.15(d). Similar to Test 3-1, Figure 4.15(c) and 4.15(d) illustrate the results obtained under reference strain with and without damage. Comparable conclusions regarding damage identification can be inferred from both figures, as stated in the analysis of Test 3-1. It is noteworthy that the VID in Test 4-1 can be detected at a significantly lower load than the BVID in Test 3-1. Moreover, the magnitude of the LPA coefficients in Test 4-1 is much higher than that in Test 3-1. This is due to the fact that the BVID has a smaller impact on the strain field than the VID under the same load.

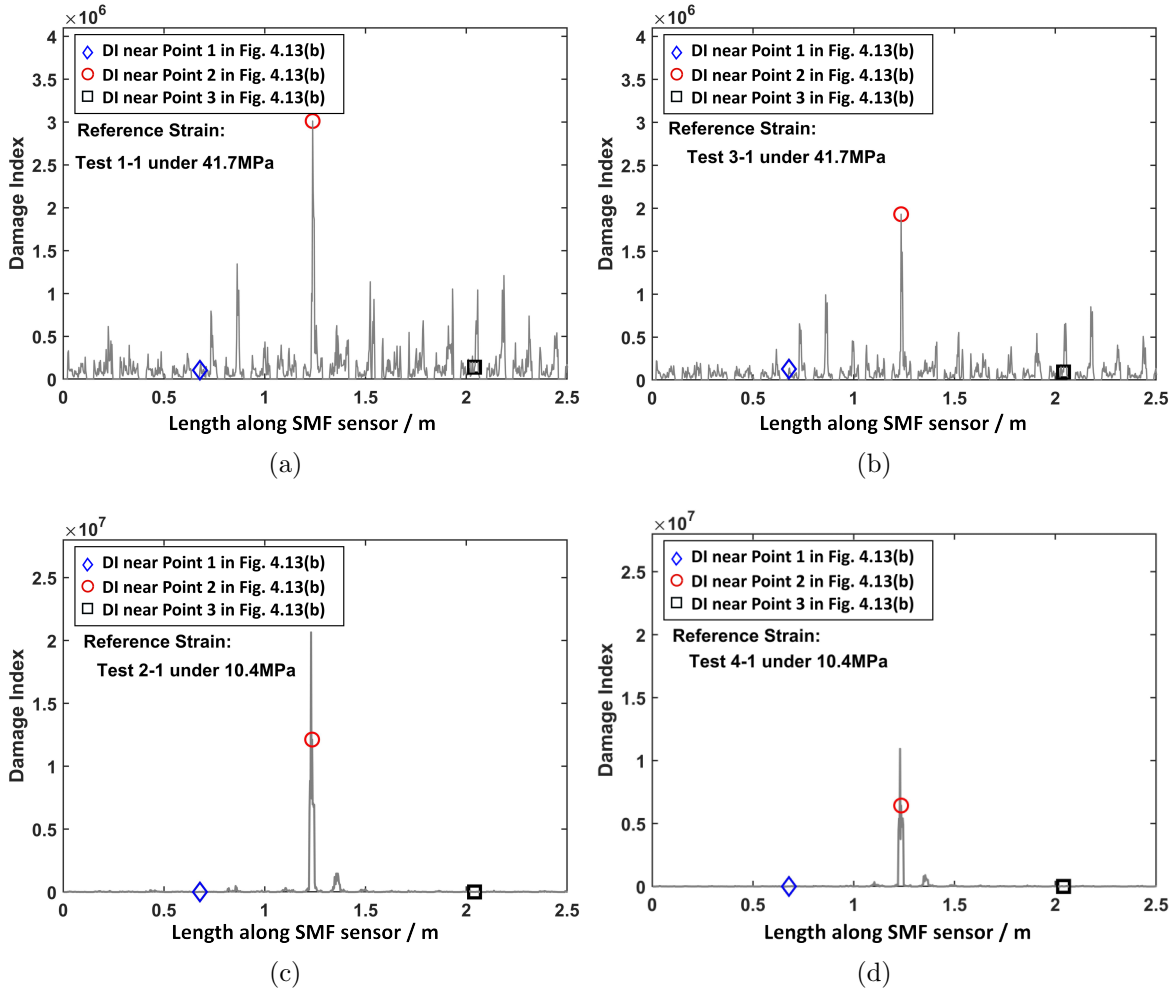


Figure 4.16: The damage index of all neighbourhood strain sets on 1D strain measurements along the SMF sensor: (a) Results of Test 3-1 (reference strain: Test 1-1 under 41.7MPa); (b) Results of Test 3-1 (reference strain: Test 3-1 under 41.7MPa); (c) Results of Test 4-1 (reference strain: Test 2-1 under 10.4MPa);(d) Results of Test 4-1 (reference strain: Test 4-1 under 10.4MPa)

The damage index based on the strain measurements of Test 3-1 and Test 4-1 is depicted in

Figure 4.16, wherein the x-axis illustrates the length along the SMF sensor (as illustrated in Figure 4.8(a)), and the y-axis represents the magnitude of the damage index. Figure 4.16(a) and 4.16(b) represent the result of Test 3-1 under different reference strain, while Figure 4.16(c) and 4.16(d) illustrate the outcome of Test 4-1 under different reference strain. These figures depict the positions of points 1, 2 and 3 on the SMF sensor by blue diamond, black circle and red square marks, respectively. These figures reveal a notably higher amplitude of the damage index at position 2 compared to positions 1 and 3. This suggests that position 2 is likely in close proximity to the damage site. Therefore, the damage index results presented in these figures demonstrate the efficiency of the proposed technique in detecting the measurement points proximate to the BVID and VID, regardless of whether the reference strain is selected in the presence or absence of damage, which shows the potential of this method to be applied to in-service damage detection of CFRP structure. Moreover, the damage identification outcomes align with the damage location observed in specimen 2 and specimen 3.

Damage detection result based on two-dimensional strain measurements

This subsection presents the results of damage detection based on 2D strain distribution of 1D SMF obtained from Test 3-1 and Test 4-1. The proposed algorithm for damage detection has demonstrated validity under different reference strains; thus, this subsection presents only the results based on the reference strain selected in the presence of damage. Figure 4.17(a) and 4.17(b) depict the LPA coefficients near Point 1, 2, and 3 (marked in Figure 4.13(b)). Meanwhile, Figure 4.17(c) and 4.17(d) show the distribution of the damage index on the surface of the CFRP specimens. The x-axis and y-axis in Figure 4.17(c) and 4.17(d) indicate the length and width of the sensing area on the CFRP specimens, respectively. The colour bar on the right indicates the corresponding values of damage index. The LPA coefficients obtained by Equation 4.28 based on 3D Delaunay triangulation also demonstrate excellent performance in identifying the measurement points near the damaged location, as shown in Figure 4.17(a) and 4.17(b). Using the outcomes depicted in Figure 4.17(a) as an illustration, the LPA amplitudes at Point 1, Point 2, and Point 3 exhibit negligible differences under light loads. However, as the load intensifies and surpasses 60MPa, the rate of increase in the LPA value at point 2 significantly

outpaces that of points 1 and 3. This observation suggests the existence of damage near Point 2. Furthermore, the damage index distribution aligns with the damage location observed in specimen 2 and specimen 3, indicating excellent performance in both BVID and VID, when considering the shape of CFRP structures. Notably, this damage index can be updated in real-time based on the calculation of the LPA coefficient under the current strain measurement, suggesting the possibility of in-service damage detection of CFRP structures without prior information about non-damaged strain distribution.

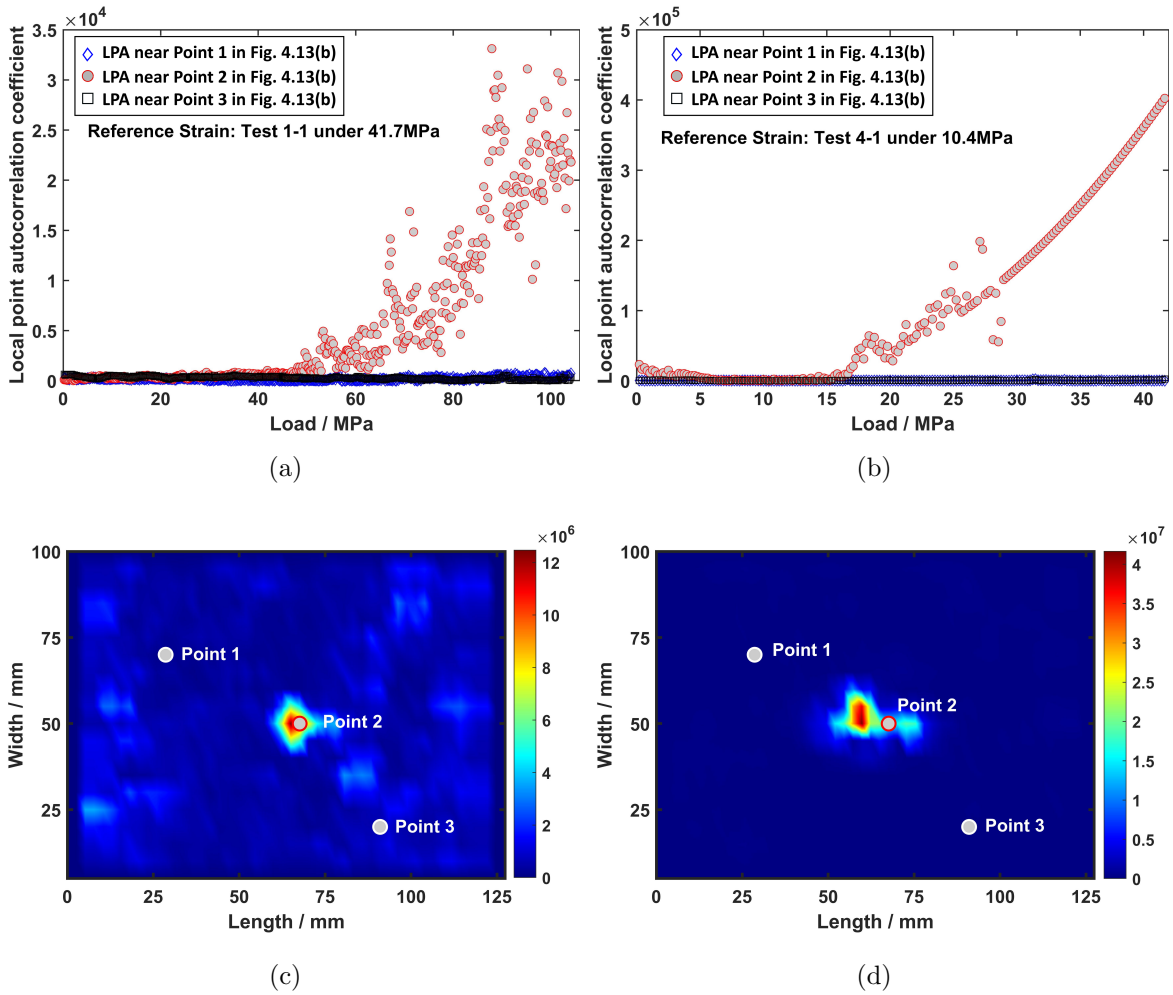


Figure 4.17: The damage detection results based on 2D strain distribution of 1D SMF on CFRP specimens: (a) LPA coefficient of Test 3-1 (reference strain: Test 3-1 under 41.7MPa); (b) LPA coefficient of Test 4-1 (reference strain: Test 4-1 under 10.4MPa); (c) Damage index distribution of Test 3-1 (reference strain: Test 3-1 under 41.7MPa); (d) Damage index distribution of Test 4-1 (reference strain: Test 4-1 under 10.4MPa);

4.3.4 Conclusions

The OFDR technique has enabled real-time recording of detailed strain distribution on CFRP structures, facilitating damage detection based on image feature matching. this chapter proposes a LPA coefficient as a key feature for damage detection in CFRP structures in service (under variable load). The LPA coefficient is defined as the area difference and Hausdorff distance between two convex hulls, generated by Delaunay triangulation of two neighbourhood strain sets under distinct loads. One set is selected from reference strain measurements, while the other is selected from current strain measurements. The variation of the LPA coefficient during the loading process indicates the discontinuities in the strain field, directly related to damage in the CFRP structures. The damage index is defined as the integral of the LPA coefficient within the entire loading process to increase the robustness of damage detection. The damage index near the damage location increases much faster than those far away from damage during load variation. The proosed methodology was validated with three composite specimens, surface mounted with SMFs and impacted with low velocity impact to cause both VID and BVID in the composite. Based on the experiments and analysis presented in this chapter, the following conclusions can be drawn.

- The LPA coefficient exhibits excellent performance in identifying the measurement points located near the damage site in CFRP structures.
- The damage detection results, based on the proposed algorithm using damage index, match well with the actual damage observed in the CFRP specimens.
- In the proposed algorithm for damage detection, no prior knowledge about the strain distribution in the pristine specimen is required, allowing the reference strain to be selected at any time, even in the presence of damage.
- The proposed algorithm demonstrates effective detection of both BVID and VID.
- The magnitude of the damage index can be used to characterize the severity of damage. For example, the damage index of VID in Specimen 3 is significantly larger than the

damage index of BVID in Specimen 2.

- Real-time damage monitoring can be achieved by updating the damage index with the LPA coefficients of current strain measurements.

Moreover, based on the principle of proposed algorithm in this chapter, the following inferences can be drawn.

- The proposed damage detection approach in this chapter integrates the LPA coefficient over the entire loading process to obtain the damage index. As the integral interval expands, the difference between the damage index near damaged and non-damaged measurement points becomes more apparent. Thus, this approach is suitable for long-term damage detection of CFRP structures.
- The feature matching-based approach proposed in this chapter identifies local areas with significant strain variations. This approach is not sensitive to changes in ambient temperature since temperature changes result in uniform strain variations. Therefore, this method can be considered robust in complex environments.
- The selection of neighbourhood strain set is crucial in this approach. A large neighbourhood strain set leads to a broad local strain distribution, resulting in decreased sensitivity to small-sized damage. Conversely, a small neighbourhood strain set may reduce the robustness of damage detection.

There are some limitations in the present scenario of damage detection of CFRP structures using distributed strain sensing. These limitations include the inferior dynamic performance of distributed strain measurements (no more than 100Hz for ODiSI-B system), susceptibility to the influence of complex loading conditions, and the restricted lateral sensing range of the SMF sensor. Therefore, subsequent works will be conducted to test the efficacy of the proposed algorithm under challenging structural conditions, intricate loading conditions, and diverse sensor configurations.

Chapter 5

Shape sensing of composite plates based on distributed fiber optic sensing

5.1 Introduction

The shape sensing technique of CFRP structures is of great significance in SHM and has witnessed rapid development in recent years. This technique aims to reconstruct a high-fidelity displacement field from limited strain measurements on CFRP structures [202]. The shape sensing technique is broadly classified into three categories, namely, numerical integration-based approach (such as Ko's displacement theory) [327, 31], approximation approach based on basis functions (such as the modal method) [328], and iFEM based on the least square method [329, 330]. A comprehensive study comparing these algorithms has been conducted in the latest review and research articles [331, 332]. Among these schemes, iFEM is considered one of the most promising techniques due to its ability to accurately reconstruct a displacement field with limited strain measurements [333].

The iFEM was initially proposed by Alexander Tessler and Jan L. Spangler in [334] for shape sensing of shell structures, utilizing the first-order shear deformation theory. The iFEM method employs the finite element discretization and the least squares variational principle to solve

the inverse problem, which involves reconstructing a high-fidelity displacement field from limited strain measurements [335]. Based on this principle, several iFEM algorithms have been developed, employing different kinematic assumptions and validated theoretically and experimentally on various materials and structures. One category of extensively developed iFEM is for shape sensing of isotropic shell structures, including the three-node inverse shell element (iMIN3) [336], the four-node quadrilateral inverse-shell (iQS4) [337], and the eight-node curved inverse-shell element (iCS8) [338], which have been validated in several structures, including chemical tankers [339], bulk carriers [340], offshore wind turbine towers [341], and machine columns [342]. For anisotropic and quasi-isotropic shell structures, such as composite laminate and sandwich structures, a more complex algorithm based on the refined zigzag theory (RZT), namely iRZT, has been developed to enhance the precision of displacement field reconstruction [343, 344, 345, 346]. Another category of iFEM has been developed for shape sensing of isotropic beams based on Timoshenko's kinematic assumptions [347, 348, 349, 350, 351] and Euler-Bernoulli beam assumption [352, 353, 354]. Recently, the RZT theory has been applied in sandwich beams to improve the precision of displacement field reconstruction [355]. These iFEM algorithms for beams have been validated in applications such as tunnel monitoring [356], subsea pipelines [357, 358], and soil deformation monitoring [359]. Moreover, the above-mentioned iFEM algorithms have also been utilized for structural damage detection and integrity assessment with promising potential [360, 361, 362, 363, 364, 365]. Notably, some of the latest studies have employed boundary element [366, 367], inverse-plate quadrilateral area coordinates method [368], fuzzy networks[369], the isogeometric analysis [370] and other techniques to further enhance the performance of the iFEM algorithms.

The iFEM shows strong correlation with strain measurements in practical applications. In current research, strain gauges [347], FBG [340], and distributed fibre optic sensors [371] have emerged as the most commonly used sensors for strain measurement. Strain gauges provide normal and shear strain with ease. However, for larger structures, a huge number of cables are required [335, 372]. FBG sensors partly solve this issue as multiple sensing points can be integrated onto a single sensor, thereby reducing the cable requirement. Nonetheless, obtaining

the complete strain field, including all strain components, remains difficult with FBG sensors. Consequently, distributed fibre optic sensing is considered one of the most promising solutions due to its high directional flexibility and spatial precision. These features make it possible to acquire the normal and shear strain with high spatial precision. However, a universally applicable scheme for strain field acquisition has not been proposed in any of the existing experiments or application examples. As a result, the selection of sensors and installation schemes needs to be tailored independently for different structures and applications, which has limited the widespread adoption of iFEM.

In addition, obtaining a large amount of strain data is often infeasible due to cost limitations in practical applications. Therefore, strain extrapolation techniques have adopted as a promising solution to reduce cost and improve spatial resolution of displacement field. This technique utilizes sparse measurements to predict high-fidelity strain fields, which can effectively increase the mesh density of iFEM and improve the spatial resolution of displacement field [373]. The cubic spline interpolation is a classical method, but it tends to lose many details of the strain field. Smoothing element analysis (SEA) is another classical method proposed by Alexander Tessler and first utilized in finite element method (FEM) [374]. Recently, the effectiveness of SEA in strain extrapolation for iFEM has been demonstrated by Adnan Kefa et al [372, 375]. Furthermore, new strain extrapolation techniques based on Gaussian process (GP) [376], radial basis function (RBF) [377], polynomial [378, 379], and physics [380] have been proposed. However, these methods tend to produce smooth strain fields and lose high-frequency features in the actual strain distribution. These high-frequency features are important for both shape sensing and damage detection. Furthermore, the GP-based extrapolation technique requires substantial work in selecting kernel functions and hyperparameter settings, as well as significant computing performance when processing large amounts of data.

To address the aforementioned challenges, this research introduces a precise and block-based solution for shape sensing with distributed fibre optic sensing. The proposed scheme geometrically represents the sensor network by combination of basic sensing blocks, making it universally

applicable for different structures. The adoption of basic sensing blocks simplifies the design of sensor networks for different structures and enhances the standardization and robustness of sensor networks. The strain distribution is then obtained by combining the mesh information of iFEM with the geometric representation of the sensor network. Furthermore, to achieve high-fidelity strain fields and refine the mesh of iFEM, a novel strain extrapolation method based on single image super resolution (SISR) technique is proposed [381]. The SISR technique is originally developed for high-resolution reconstruction of images in computer vision and is well-suited to solving ill-posed problems like strain extrapolation. The proposed strain extrapolation method can effectively preserve high-frequency features of the strain field, overcoming the limitations of existing strain extrapolation techniques. The contributions of this study can be summarized as follows:

- A block-based strain field acquisition scheme based on distributed fibre optic sensing is proposed, and it was validated in three experiments with different shell structures.

- A novel strain extrapolation scheme is introduced that employs image super resolution techniques to preserve high-frequency features in the strain field. The strain extrapolation results are compared with those of existing techniques, highlighting the advantages of the proposed approach.

This chapter is structured as follows: subsection 5.2 presents the theories employed in this study, encompassing iFEM with drilling degrees of freedom, strain acquisition scheme, and SISR-based strain extrapolation technique. The details of the specimens and experiments carried out in this research are illustrated in subsection 5.3. The outcomes and discussions are presented in subsection 5.4, which include shape sensing and strain extrapolation results. Finally, the concluding remarks and summary of this chapter are presented in the last subsection.

5.2 Methodology

This subsection begins with a comprehensive overview of iFEM with drilling degrees of freedom is provided. Following this, a robust and standardized strain acquisition scheme for iFEM, based on distributed optic sensing, is introduced. Lastly, the SISR-based strain extrapolation method is proposed as a method to achieve strain field with high spatial resolution, thereby enabling the high-fidelity determination of displacement field using iFEM.

5.2.1 Inverse finite element method with drilling degrees of freedom

The iQS4 element with drilling degrees of freedom was initially introduced in [329] to enhance the robustness of iFEM when simulating curved shell structures. An overview of iFEM is illustrated in Figure 5.1. The fundamental principle of iFEM involves minimizing the difference between virtual strain, represented by a virtual displacement field, and experimental strain using the weighted least-squares formulation Φ^e.The process of obtaining virtual strain is depicted at the bottom of Figure 5.1. An isoparametric coordinate system (ξ, η) is constructed for the iQS4 element to express the interpolation of the virtual displacement field. The real iQS4 element is defined by a local coordinate system (x, y, z) located at its centroid. The unique mapping between isoparametric and local coordinate is given by bilinear isoparametric shape functions (summarized in Appendix A.1) and expressed in Equation 5.1.

$$x(\xi, \eta) = \sum_{i=1}^{4} N(\xi, \eta)_i x_i \tag{5.1a}$$

$$y(\xi, \eta) = \sum_{i=1}^{4} N(\xi, \eta)_i y_i \tag{5.1b}$$

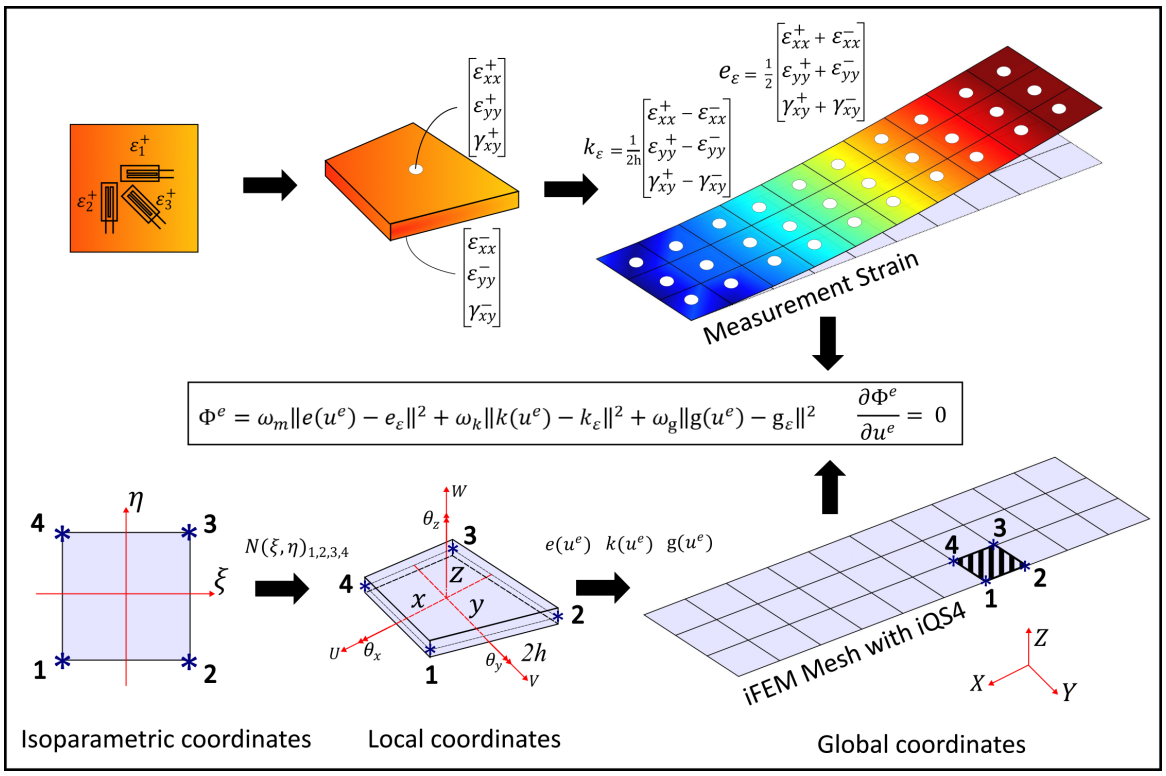


Figure 5.1: An overview of inverse Finite Element Method

In the local coordinate system, the thickness of the iQS4 element is assumed to be $2h$, such that the z coordinate is given by $z \in [-h, h]$. Similar to the Mindlin plate theory, the nodal degrees of freedom (DOFs) are defined as $U, V, W, \theta_x, \theta_y, \theta_z$. The kinematic assumption is expressed mathematically in Equation 5.2.

$$U_x = U + z\theta_y \tag{5.2a}$$

$$U_y = V + z\theta_x \tag{5.2b}$$

$$U_z = W \tag{5.2c}$$

where U_x, U_y, U_z are nodal displacement along x, y, z direction in local coordinate, respectively. Since the drilling degree of freedom is induced in this model, the distribution of kinematic vari-

ables in Equation 5.2 is expressed by interpolation based on nodal displacements in isoparametric coordinate and shown in Equation 5.3. The detailed expressions of shape functions including $L(\xi,\eta)_i$ and $M(\xi,\eta)_i$ are summarized in Appendix A.1). The detailed derivation of these results can be found in [382, 383].

$$U = \sum_{i=1}^{4} N(\xi,\eta)_i U_i + \sum_{i=1}^{4} L(\xi,\eta)_i \theta_{zi} \tag{5.3a}$$

$$V = \sum_{i=1}^{4} N(\xi,\eta)_i V_i + \sum_{i=1}^{4} M(\xi,\eta)_i \theta_{zi} \tag{5.3b}$$

$$W = \sum_{i=1}^{4} N(\xi,\eta)_i W_i - \sum_{i=1}^{4} L(\xi,\eta)_i \theta_{xi} - \sum_{i=1}^{4} M(\xi,\eta)_i \theta_{yi} \tag{5.3c}$$

$$\theta_x = \sum_{i=1}^{4} N(\xi,\eta)_i \theta_{xi} \tag{5.3d}$$

$$\theta_y = \sum_{i=1}^{4} N(\xi,\eta)_i \theta_{yi} \tag{5.3e}$$

By combining the strain-displacement relations in linear elasticity with Equation 5.2 and 5.3, the virtual strain of iQS4 element is expressed through interpolations based on nodal displacements u^e described in isoparametric coordinate system as follows:

$$\begin{bmatrix} \varepsilon_{xx} & \varepsilon_{yy} & \gamma_{xy} \end{bmatrix}^T = e(u^e) + zk(u^e) \tag{5.4a}$$

$$\begin{bmatrix} \gamma_{xz} & \gamma_{yz} \end{bmatrix}^T = \mathrm{g}(u^e) \tag{5.4b}$$

where $e(u^e)$ is the membrane strain; $k(u^e)$ expresses bending curvature; $g(u^e)$ is the transverse shear strain. The detailed expressions of u^e , $e(u^e)$, $k(u^e)$, and $g(u^e)$ are summarized in Appendix A.1). Experimental strain is typically measured using strain rosettes, FBG, or distributed fibre optic sensors. Take the strain rosette depicted in the upper left of Figure 5.1 for example, the complete strain distribution is obtained according to Equation 5.5. In this equation, $\varepsilon_{xx}^{+,-}$, $\varepsilon_{yy}^{+,-}$, and $\gamma_{xy}^{+,-}$ represent the normal and shear strain on the top (+) and bottom (−) surface of iQS4 element in the local coordinate.The $\varepsilon_{1,2,3}^{+,-}$ express the reading of strain rosettes on the top (+) and bottom (−) surface of iQS4 element, respectively. The directions of the strain rosettes are denoted by $\theta_1, \theta_2, \theta_3$.

$$\begin{bmatrix} \varepsilon_1^{+,-} \\ \varepsilon_2^{+,-} \\ \varepsilon_3^{+,-} \end{bmatrix} = \begin{bmatrix} (cos\theta_1)^2 & (sin\theta_1)^2 & sin\theta_1 cos\theta_1 \\ (cos\theta_2)^2 & (sin\theta_2)^2 & sin\theta_2 cos\theta_2 \\ (cos\theta_3)^2 & (sin\theta_3)^2 & sin\theta_3 cos\theta_3 \end{bmatrix} \begin{bmatrix} \varepsilon_{xx}^{+,-} \\ \varepsilon_{yy}^{+,-} \\ \gamma_{xy}^{+,-} \end{bmatrix} \tag{5.5}$$

Based on Equation 5.4 and 5.5, the membrane strain (e_ε) and bending curvature (k_ε) under experimental conditions can be mathematically represented by Equation 5.6. It should be noted that it is impossible to directly measure the transverse shear strain (g_ε) under experimental conditions using the strain measurements provided by Equation 5.5. Nevertheless, the deformation of shell structures is mainly governed by the membrane strain and bending curvature, and the contribution of transverse shear strain can be neglected. Therefore, it is reasonable to assume that the transverse shear strain under experimental conditions is equal to zero ($g_\varepsilon = 0$).

$$e_\varepsilon = \frac{1}{2}\begin{bmatrix} (\varepsilon_{xx}^{+} + \varepsilon_{xx}^{-}) & (\varepsilon_{yy}^{+} + \varepsilon_{yy}^{-}) & (\gamma_{xy}^{+} + \gamma_{xy}^{-}) \end{bmatrix}^T \tag{5.6a}$$

$$k_\varepsilon = \frac{1}{2h}\begin{bmatrix} (\varepsilon_{xx}^{+} - \varepsilon_{xx}^{-}) & (\varepsilon_{yy}^{+} - \varepsilon_{yy}^{-}) & (\gamma_{xy}^{+} - \gamma_{xy}^{-}) \end{bmatrix}^T \tag{5.6b}$$

In the actual deformation of an iQS4 element, the membrane strain, bending curvature, and transverse shear strain under virtual and experimental conditions should be well-matched. This implies that the actual deformation field of the iQS4 element minimizes the following weighted least-squares functional:

$$\Phi^e = \omega_m \|e(u^e) - e_\varepsilon\|^2 + \omega_k \|k(u^e) - k_\varepsilon\|^2 + \omega_\mathrm{g} \|\mathrm{g}(u^e)\|^2 \tag{5.7}$$

The functional presented in Equation 5.7 introduces the weights ω_m, ω_k, and ω_g to adjust the contributions of the membrane strain, bending curvature, and transverse shear strain, respectively. Due to practical limitations, it may not be possible to obtain strain measurements for all iQS4 elements among the whole structure. Consequently, only the weights of the iQS4 elements with measured strain are set to one, while the weights of the other elements are set to a much smaller value ($\leq 10^{-4}$) to reduce errors. The normalized Euclidean norms in Equation 5.7 are mathematically represented by Equation 5.8 in isoparametric coordinate system, where A^e is the area of the iQS4 element in the mid-plane and $|J|$ represents the determinant of the Jacobian matrix.

$$\|e(u^e) - e_\varepsilon\|^2 = \frac{1}{A^e} \iint_{A^e} [e(u^e) - e_\varepsilon]^2 \, |J| d_\xi \, d_\eta \tag{5.8a}$$

$$\|e(u^e) - e_\varepsilon\|^2 = \frac{(2h)^2}{A^e} \iint_{A^e} [k(u^e) - k_\varepsilon]^2 \, |J| d_\xi \, d_\eta \tag{5.8b}$$

$$\|\mathrm{g}(u^e)|^2 = \frac{1}{A^e} \iint_{A^e} [\mathrm{g}(u^e)]^2 \, |J| d_\xi \, d_\eta \tag{5.8c}$$

Therefore, the weighted least-squares functional in Equation 5.7 can be minimized to obtain the solutions for the real deformation field. This solution is expressed as Equation 5.9, where ε^e denotes a vector of iQS4 element containing the experimental membrane strain, bending curvature, and transverse shear strain. The k^e and f^e are the coefficient matrix of nodal displacement vector and experimental strain vector, respectively. The detailed mathematical expressions for ε^e, k^e, and f^e can be found in Appendix A.1).

$$\frac{\partial \Phi^e}{\partial u^e} = k^e u^e - f^e \varepsilon^e = 0 \tag{5.9}$$

It is noteworthy that the aforementioned conclusions are derived based on the local coordinate system (x, y, z). Therefore, Equation 5.9 is expanded to Equation 5.10 for the entire structure in the global coordinate system (X, Y, Z), where T_θ represents the transformation matrix between the local and global coordinate systems. The total number of iQS4 elements in the entire structure is denoted by n. The displacement field of the structure is then obtained by combining Equation 5.10 with the displacement boundary conditions.

$$\sum_{e=1}^{n} (T_\theta)^T k^e T_\theta \sum_{e=1}^{n} (T_\theta)^T u^e - \sum_{e=1}^{n} (T_\theta)^T f^e \varepsilon^e = 0 \tag{5.10}$$

5.2.2 The strain acquisition scheme based on distributed fibre optic sensing

In accordance with the fundamental principle of the iFEM methodology discussed in Chapter 5.2.1, experimental strain measurements have a direct impact on the calculated displacement field. Weights such as ω_m, ω_k, and ω_g (as in Equation 5.7) are introduced to reduce

errors from iQS4 elements without experimental measurements. However, the analyses in [384, 378, 379, 371] show that inaccurate displacement outcomes occur when the proportion of iQS4 elements with measured strain is low or their distribution is unreasonable. Based on the conclusions in former research, a reliable sensor network must meet specific conditions when prior knowledge about the possible strain distribution is unavailable.

- The sensor network should furnish comprehensive and adequate strain information, which includes measurements for a higher number of iQS4 elements as well as complete strain information, comprising normal and shear strains.
- For a robust sensor network, the iQS4 elements with strain measurements should be distributed as uniformly as possible to cover the entire surface of the structure. Moreover, efforts should be made to ensure symmetrical distribution of iQS4 elements with strain measurements.

Therefore, this subsection presents a strain acquisition scheme utilizing distributed fibre optic sensors, which is designed to enhance the accuracy of iFEM by satisfying the aforementioned conditions. The proposed scheme utilizes the combination of basic sensing blocks to geometrically represent the sensor network of a structure, making this approach applicable to various of structures. By adopting basic sensing blocks, the scheme simplifies the design of sensor networks for different structures, and promotes standardization and robustness of sensor networks.

Figure 5.2 illustrates the four steps involved in the design and installation of sensor networks based on distributed fibre optic sensors. The first step is to design basic sensing blocks, similar to strain rosettes, containing various measurement directions to obtain both normal and shear strain distribution on the surface. In addition, considering the geometric characteristics of fibre optic sensors, the track of SMF obtained by connecting basic sensing blocks should be C^1-continuous. A feasible Ω-type basic sensing block is presented in the top-left of Figure 5.2, which contains all directional components from $-\pi/3$ to $\pi/3$ and has a bending radius of 12.5mm to avoid bending loss. A detailed analysis of this design is expressed in [385].

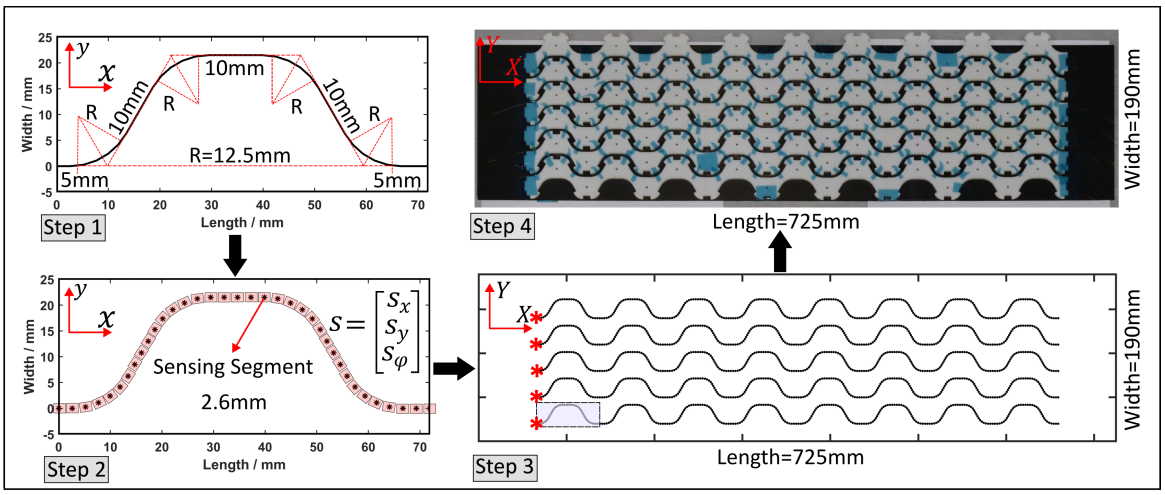


Figure 5.2: The design and installation scheme of sensor network: Step1: basic sensing blocks design; Step2: discretization of basic sensing blocks; Step3: sensor network design; Step4: installation of sensor network

The second step involves the discretization of basic sensing blocks in local coordinate system (x,y). Since the distributed sensing based on fibre optic sensors measures the discrete strain information along the sensor with high spatial resolution, all the discrete sensing segments in the Ω-type basic sensing block are mathematically expressed in Equation 5.11. In this equation, $s_x = [s_{x1}, s_{x2}, \cdots, s_{xn}]$ represents the x-coordinates of sensing segments, $s_y = [s_{y1}, s_{y2}, \cdots, s_{yn}]$ represents the y-coordinates of sensing segments, and $s_\varphi = [s_{\varphi 1}, s_{\varphi 2}, \cdots, s_{\varphi n}]$ expresses the directions of these sensing segments. It is noteworthy that the quantity of sensing segments (n) present within the basic sensing block is decided by the configuration of the shape in the first step and the spatial resolution of the distributed sensing. For instance, the spatial resolution of the commercial OFDR system (ODiSI-B) utilized in this work is 2.6mm, implying that the Euclidean distance between adjacent sensing segments in s^Ω is 2.6mm.

$$s^\Omega = \begin{bmatrix} S_x \\ S_y \\ S_\varphi \end{bmatrix} \tag{5.11}$$

The third step involves designing the sensor network in global coordinate (X, Y) based on the

basic sensing block mentioned above. In the bottom-right of Figure 5.2, a rectangular shell (725×190mm) has been used to illustrate this step using m basic sensing blocks (s^{Ω}), and the resulting sensor network is mathematically expressed in Equation 5.11. The x-coordinate of the i-th basic sensing block in the sensor network is denoted by ψ_{xi}, and the y-coordinate is represented by ψ_{yi}. The transformation matrix between the local and global coordinate systems is denoted by T_θ, where θ is the angle between the local coordinate system and the global coordinate system.

$$S = T_\theta \begin{bmatrix} s_x + \psi_{x1} & s_x + \psi_{x2} & \cdots & s_x + \psi_{xm} \\ s_y + \psi_{y1} & s_x + \psi_{y2} & \cdots & s_x + \psi_{ym} \\ s_\varphi + \theta & s_\varphi + \theta & \cdots & s_\varphi + \theta \end{bmatrix} \tag{5.12}$$

The fourth step involves the installation of the sensor network, which is based on the design obtained from step three. The sensor network obtained from the basic sensing blocks satisfies the requirements for a robust network mentioned in the beginning of this subsection, including comprehensive and sufficient strain information, uniform distribution, and a well-organized symmetric layout. Moreover, owing to its simple and highly regular design, the installation of this sensor network is straightforward. One potential approach is to employ reusable and modular moulds to facilitate the installation of the designed sensor network, as depicted in the upper right corner of Figure 5.2.

Once the geometric distribution and corresponding measurement direction of all sensing segments in the sensor network have been obtained, the strain distribution of iQS4 elements are calculated based on the iFEM mesh information. The implementation scheme is consistent with Equation 5.5, where three sensing segments with different angles are selected from a pool of k ($k \geq 3$) sensing segments within an iQS4 element to calculate normal and shear strain. To reduce calculation errors, the angular difference between the selected sensing segments should be maximized. The membrane strain and bending curvature in experiment are then obtained using Equation 5.6. In conclusion, a robust sensor network based on basic sensing blocks can be

readily assembled for various shell structures, thereby yielding a sound experimental strain field for iFEM and improving the accuracy of shape sensing. Moreover, the simplicity and regularity of such a network facilitates the installation of sensors, particularly for larger structures.

5.2.3 Strain extrapolation based on single image super resolution

In shape sensing based on iFEM, strain extrapolation is adopted to address sensor limitations and achieve high resolution displacement fields. It aims to predict surface strain in areas where no strain measurements are available with limited strain measurements. This is an underdetermined inverse problem, as the inferred high-fidelity strain distribution is not unique. The most widely used technique is the SEA, which generates a smoothed strain field for iFEM. Although this approach provides a certain level of noise suppression, it also suppresses high-frequency components that may exist in the actual strain field, which are often caused by structural complexity (such as the presence of holes) or potential damage (such as cracks or delamination). Retaining these high-frequency components in strain extrapolation is not only beneficial for improving the accuracy of shape sensing, but also important for damage detection based on iFEM.

The SISR technique, which originated in the field of computer vision, is employed to reconstruct a high-resolution (HR) image from a low-resolution image (LR). This technique also faces an underdetermined inverse problem as same as strain extrapolation. SISR is specifically designed to upscale a LR image while preserving its sharpness. In other words, it aims to retain all frequency components after the upscaling process [381]. The mathematical formulation of the SISR problem is expressed in Equation 5.13.

$$Y = DBX + v \tag{5.13}$$

In Equation 5.13, X represents the HR image, while Y denotes the corresponding LR image degraded by v, which represents additive noise. D and B represent the down-sampling and blurring operator used to acquire Y. It should be emphasized that this relationship can also be applied to describe the strain extrapolation problem, where X represents the high-fidelity strain field obtained after extrapolation and Y denotes the strain field measured by the sensor network. Therefore, the SISR technique presents itself as a promising solution for the realization of strain extrapolation.

To enable strain extrapolation using the SISR technique, the strain distribution obtained in subsection 5.2.2 is initially transformed into RGB colour space. This conversion process involves linearly mapping the strain information of each iQS4 element to a corresponding pixel. Specifically, if the strain of the i-th iQS4 element is denoted as $(\varepsilon_{xx}^i, \varepsilon_{yy}^i, \gamma_{xy}^i)$, then the corresponding colour information (R^i, G^i, B^i) is expressed by Equation 5.14. In this equation, α is a conversion coefficient used to regulate the range of high-fidelity strain results after extrapolation. When α is set to zero, the range of the strain field after strain extrapolation is equal to the range of the measured strain field, which may not be desirable in practical applications. Therefore, α is appropriately adjusted to a value greater than zero to obtain a more accurate high-fidelity strain field. In this this work, the α is set to 0.2.

$$\left[R^i, G^i, B^i\right] = \frac{1}{(\mathcal{E}_{max} - \mathcal{E}_{min})}\left[\varepsilon_{xx}^i - \mathcal{E}_{min}, \quad \varepsilon_{yy}^i - \mathcal{E}_{min}, \quad \gamma_{xy}^i - \mathcal{E}_{min}\right] \tag{5.14a}$$

$$\varepsilon_{max} = (1 + \frac{\alpha}{2}) \cdot \max\left(\varepsilon_{xx}^i, \varepsilon_{yy}^i, \gamma_{xy}^i\right) - \frac{\alpha}{2} \cdot \min\left(\varepsilon_{xx}^i, \varepsilon_{yy}^i, \gamma_{xy}^i\right) \quad i = 1, 2, 3, \cdots, k \tag{5.14b}$$

$$\varepsilon_{min} = (1 + \frac{\alpha}{2}) \cdot \min\left(\varepsilon_{xx}^i, \varepsilon_{yy}^i, \gamma_{xy}^i\right) - \frac{\alpha}{2} \cdot \max\left(\varepsilon_{xx}^i, \varepsilon_{yy}^i, \gamma_{xy}^i\right) \quad i = 1, 2, 3, \cdots, k \tag{5.14c}$$

In practical scenarios, the outcome of the aforementioned transformation is regarded as a LR image. This image is subsequently scaled up using the SISR technique to achieve strain extrap-

olation. Presently, the most prevalent and well-established SISR algorithms are those based on interpolation, dictionary training, and deep learning. The schematic diagram of these algorithms is presented in Figure 5.3. It is important to note that the images presented in this figure are solely utilized for illustrating the fundamental principles of the respective approaches. In addition, readers are advised to consult the relevant literature for a more detailed description of these algorithms.

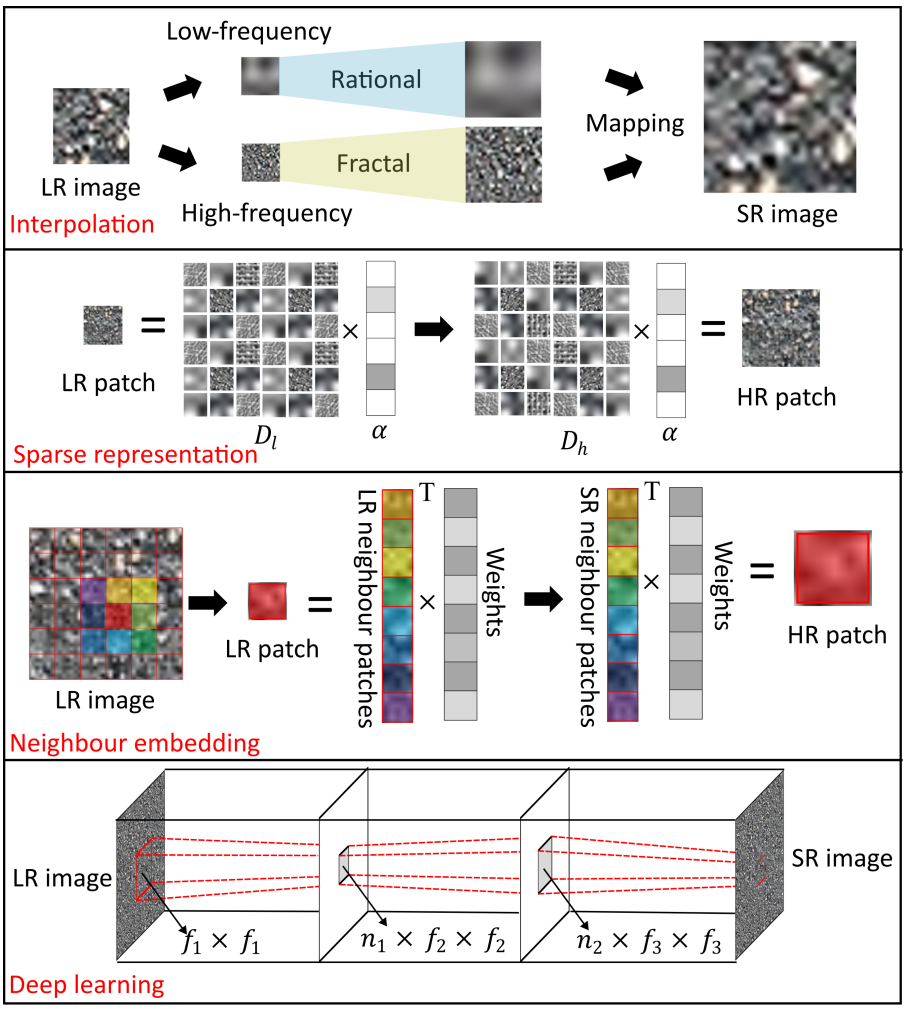


Figure 5.3: The schematic diagram of most prevalent and well-established SISR algorithms

Interpolation-based algorithms have been widely adopted in image processing for several decades, with bicubic interpolation being the most well-known techniques for SISR. However, these approaches are based on smoothness priors and tend to lose high-frequency components after upscaling. To address this issue, a rational fractal interpolation model has been proposed in [386]. As depicted in top of Figure 5.3, this model divides the image into low-frequency and

high-frequency components, which are then interpolated separately. The low-frequency component is smoother and is interpolated using rational interpolation, while the high-frequency component is upscaled using fractal interpolation. The HR image is then obtained through pixel mapping of these two interpolation results. This method effectively enhances the quality of the upscaled image by maintaining the high-frequency components, such as texture details, that are present in the original image.

The SISR approach based on dictionary learning is a widely studied method, which adopts local patches of images to learn the relationship between LR and HR images and construct dictionary pairs. The LR image is partitioned into overlapping patches to form a Markov random field, where the overlapping patches are represented by an LR dictionary. Consequently, the HR image is reconstructed using the relationship between the LR and HR dictionaries. To reduce computational costs, two solutions have been proposed based on this principle.

The first solution involves sparse representation inspired by compressive sensing. As shown in the second part of Figure 5.3, the LR patch y obtained from LR image Y (as shown in Equation 5.13) can be represented sparsely by D_l, which means $y = D_l\alpha$, where α is a sparse vector with most of its elements being zero. The sparse coding $\hat{\alpha}$ can be obtained by solving the optimization problem in Equation 5.15, where λ is the regularization weight for the l_1-norm $\|\alpha\|_1$. The corresponding HR patch x is then calculated as $x = D_h\hat{\alpha}$, where D_h is the compact dictionary for HR image X. This sparse representation solution has been shown to be a promising algorithm in SISR [387].

$$\hat{\alpha} = \arg\min_{\alpha}\{\|D_l\alpha - y\|_2^2 + \lambda\|\alpha\|_1\} \tag{5.15}$$

The second solution is the neighbour embedding algorithm (NE) [388], which is based on the

assumption that the LR and HR patches generate low-dimensional nonlinear manifolds with similar local geometry. As presented in the third part of Figure 5.3, this approach approximates the LR patch as a weighted linear combination of its K-nearest neighbour patches in Euclidean space. The HR patch is then constructed using the optimal weights obtained in LR patches. In addition, algorithms based on both sparse representation and neighbour embedding, including anchored neighbourhood regression (ANR) [389] and adjusted anchored neighbourhood regression (A^+) [390], have also been proposed and widely validated.

The final category of widely utilized SISR algorithm employs deep learning techniques. Numerous studies have been conducted to develop a variety of networks for SISR. This article highlights a typical example based on deep convolutional network [391], and readers are encouraged to refer to a comprehensive review paper for further details [381]. In this typical example, the LR image is first upsampled using bicubic interpolation to match the size of the HR image. A three-layer network is then constructed to learn an end-to-end mapping between the upsampled LR image and HR images, as shown in the bottom of Figure 5.3. The first layer employs n_1 filters with a size of $f_1 \times f_1$ to represent the upsampled LR image. The second layer non-linearly maps the outputs of the first layer to an n_2-dimensional space using n_2 filters with a size of $n_1 \times f_2 \times f_2$. The last layer linearly reconstructs the HR image using a filter with a size of $n_2 \times f_3 \times f_3$. Following training, the optimal network has parameters $f_1 = 9, f_2 = 3, f_3 = 5, n_1 = 32, n_2 = 64$, which are also adopted for the strain extrapolation in this study.

5.3 Experiments

5.3.1 The specimens and experimental setup

In order to validate the efficacy of the proposed strain acquisition scheme, three CFRP specimens with different dimensions, materials, and layouts were utilized in the experimental investigations. The detailed specifications of these specimens are summarized in Table 5.1. It is worth highlighting that in this study, the iFEM method with drilling degrees of freedom is employed instead of the iRZT theory, which is specifically designed for CFRP and sandwich structures. This choice is based on the fact that the span-to-thickness ratio of the CFRP specimens used in this study is sufficiently large. As per the findings reported in the literature [372], the results from normal iFEM and iRZT theory are almost identical when the span-to-thickness ratio exceeds 40.

Table 5.1: The specifications of specimens adopted in this study

Specimen	Dimensions / mm	Material	Layout	Span-to-thickness ratio
I	$200 \times 50 \times 3.2$	TENAX$^{@}$ – E IMS65 E23 24K	$[45/90/-45/0/45/0_2/-45]_s$	62
II	$300 \times 225 \times 3.2$	TENAX$^{@}$ – E IMS65 E23 24K	$[45/90/-45/0/45/0_2/-45]_s$	93
III	$780 \times 190 \times 1.6$	Hexply 914C-TS-5	$[0/45/-45/90]_{2s}$	458

The sensor network design and installation follows the procedure outlined in subsection 5.2.2. Two different basic sensing blocks are utilized in the sensor network design for the three specimens: the Ω-type basic sensing block, as detailed in subsection 5.2.2, and the S-type basic sensing block, which has a 20mm radius (as shown in Figure 5.5). The sensor network for specimens I and II is illustrated in Figure 5.4, while the sensor network for specimen III has been presented in Figure 5.2. In installing specimens I and II, efforts are made to enhance alignment by allowing natural bending of the SMF. Initially, the 0-degree and 90-degree points on the

SMF network are bonded with glue, maintaining the natural bending state of the remaining sensing segments. Subsequently, thermoplastic film or epoxy resin is employed to cover the entire sensor network and bond the SMF onto the specimens. Sample 3 utilizes a specialized mold to optimize sensor bonding quality and minimize measurement errors. Furthermore, Figure 5.4 also displays the experimental setup of these three specimens, with specimen I subjected to a tensile test in the top-left, specimen II employed for a three-point bending experiment in the bottom-left, and the largest specimen used in a compression experiment on the right. The specimen I and II were installed by a thermoplastic film based on modified polyolefins (Pontacol 22.100), while specimen III was installed by a kind of epoxy potting compound sourced from RS Components with Stock number 199-1468. Regarding the selection of bonding materials, Specimen I and II are smaller in dimension. The thermoplastic film with high peel strength, controllable thickness, and easy maintenance was adopted to install SMF sensor. Sample III is larger in dimension. The epoxy resin with high bonding strength and minimal pre-stress after bonding was adopted to install the SMF sensor. Table 5.2 summarizes the load and basic sensing block types used for these specimens investigated in this study.

Table 5.2: The load and basic sensing block types used for these specimens investigated in this study

Specimen	Experiment	Load	Basic sensing block type
I	Tensile Test	0-10kN	S-type
II	Three-point bending	0-90N	S-type
III	Compression Test	0-2mm	Ω-type

In the aspect of implementation, the static tensile experiment, three-point bending experiment, and compression experiment were performed using an Instron dual-column machine (Instron 50 kN 5969 system). The distributed strain was acquired by employing a commercial OFDR system (ODiSI-B) manufactured by LUNA. The experiments were conducted at room temperature, and the strain-frequency shift coefficient was set to a constant value of 6.7 $\mu\varepsilon$/GHz based on the conclusions reported in [392]. The single mode fibre utilized in these experiments was manufactured by FIBRECORE, with a model number of SM1500 (9/125)P. As specimen

I and specimen II were subjected to pure tension and pure bending, respectively, only the strain on one surface was measured. The measured data exhibits apparent periodicity due to the designed network's composition of basic blocks. Exploiting this characteristic allows for the straightforward determination of the measuring segment's position on specimens. The experiments were repeated more than three times to minimize experimental errors and ensure stable results.

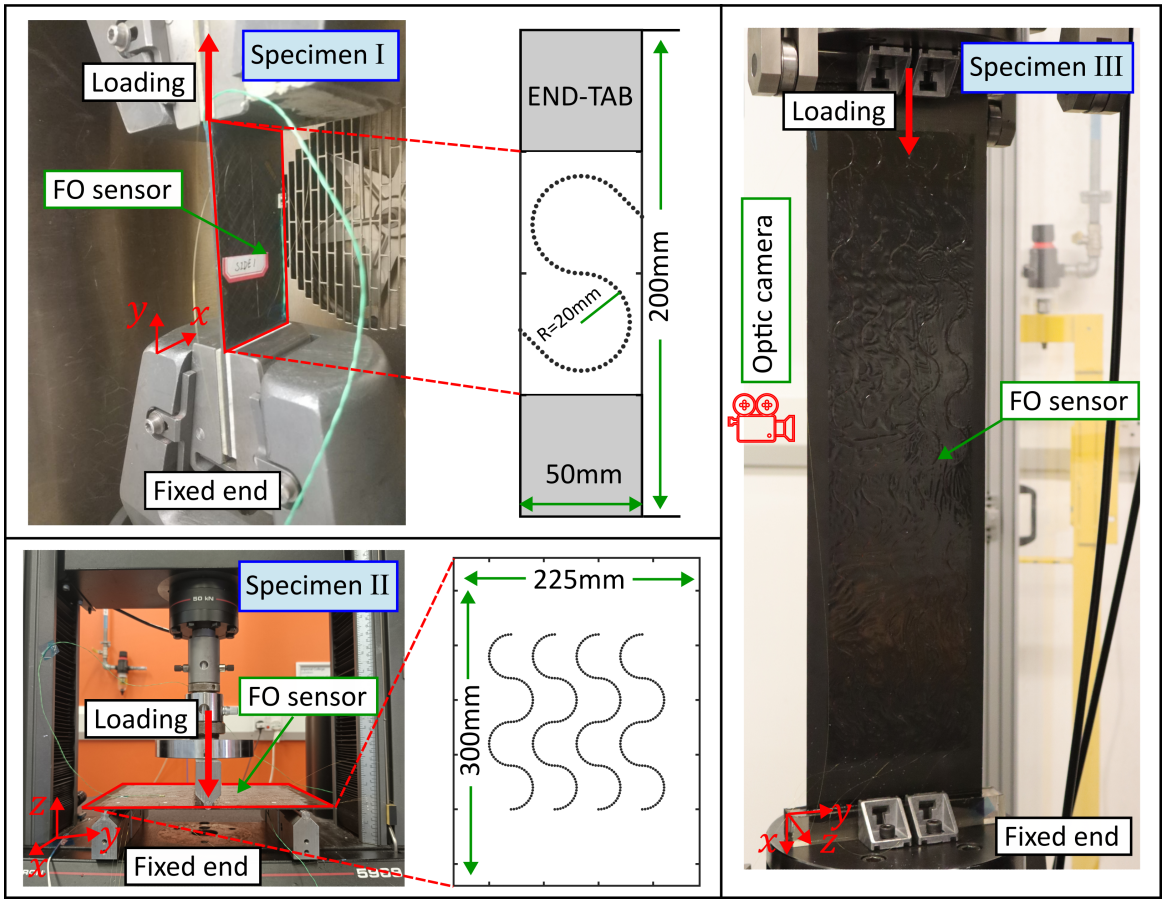


Figure 5.4: The experimental setup and sensor network: Specimen I (Top-left); Specimen II (Bottom-left); Specimen III (Right)

It is noteworthy that the displacement of clamps serves as a representative of the deformation of specimen I and specimen II, which can be easily obtained from the Instron dual-column machine during the experiment in real-time. However, in the case of the compression experiment involving specimen III, the displacement of clamps becomes boundary conditions, and is inadequate in representing the deflection of the specimen. Hence, to determine the deflection of specimen III during the compression experiment, a Canon EOS 250D digital single-lens reflex camera was employed to record the deflection of the longest side of the specimen in real-time,

with a sampling frequency of 24 Hz and a resolution of 1080×1920. The position of the optic camera is depicted in Figure 5.4.

5.4 Results and discussion

5.4.1 The iQS4 mesh of specimens

The present study describes the sensor network for three specimens, as shown in Figure 5.4 and Figure 5.2, which exhibit a gradual increase in complexity. Specimen I and specimen II are composed of one and eight S-type basic sensing blocks, respectively, whereas specimen III contains forty Ω-type basic sensing blocks. Considering the sensor network and dimensions, these three specimens were meshed with iQS4 elements as illustrated in Figure 5.5, where the light-blue area represents elements with measured strain. Therefore, the proportions of elements with measured strain in specimens I, II, and III are 50%, 27%, and 57%, respectively (This ratio represents the elements with measured values relative to the total number of elements). The designed sensor network fulfils the conditions of a robust sensor network, as discussed in the first paragraph of subsection 5.2.2. The loading direction of specimens I and III are indicated by a red arrow in this figure, while the loading of specimen II is marked by ⊙, indicating that the load direction is vertically outward. As mentioned in subsection 5.2.2, the strain distribution (including normal and shear strain) of these specimens can be obtained using the geometric representation of the sensor network and mesh information.

5.4.2 The shape sensing results of specimens: Specimen I (Top-left); Specimen II (Bottom-left); Specimen III (Right)

The outcome of the shape sensing analysis for specimen I is illustrated in Figure 5.6(a). This figure showcases the load-displacement curve obtained from both the Instron machine (Ecx-

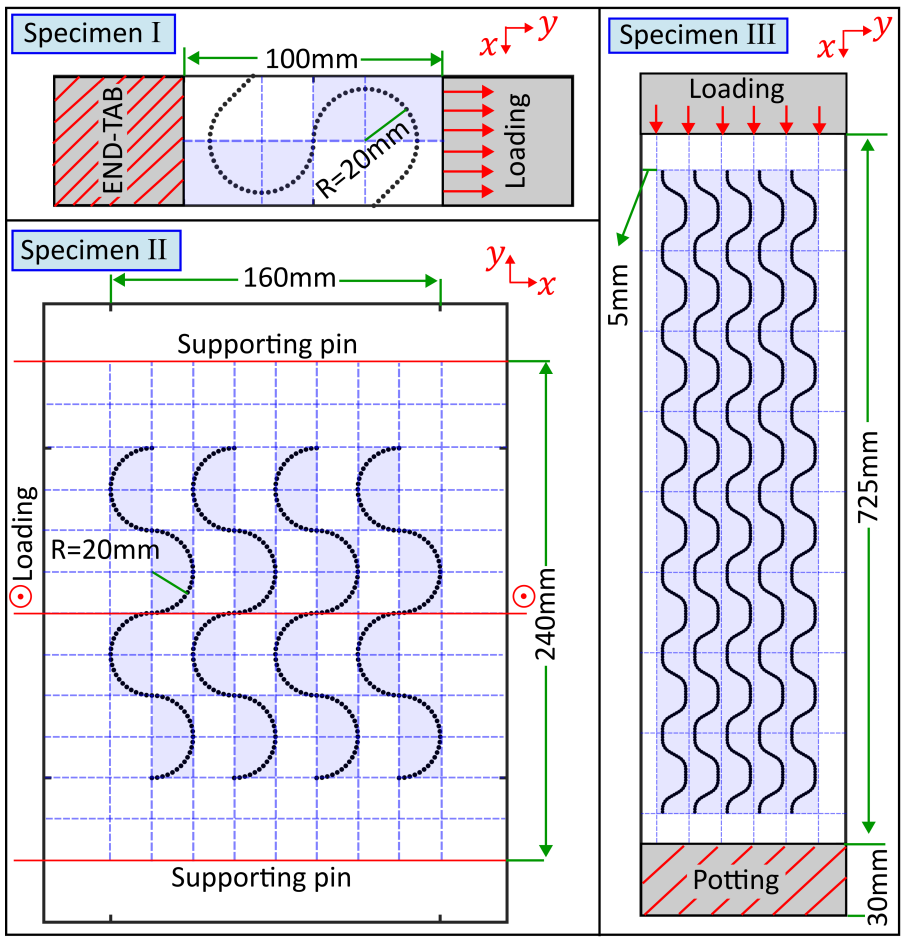


Figure 5.5: The iQS4 mesh of specimens

periment) and the iFEM calculation. The result calculated by iFEM is found to be in good agreement with the experimental value. However, minor differences between the iFEM result and experimental value can be attributed to factors such as clamp sliding and strain transfer rate between specimen I and fibre optic sensor. Furthermore, the detailed distribution of the displacement field calculated by iFEM under different loads, namely 3kN, 6kN, and 10kN, are also presented in this figure by pseudo-colour images. As specimen I comprises a single S-type basic sensing block in the tensile experiment, it serves as a simple example that effectively demonstrates the proficiency of the proposed strain acquisition scheme for shape sensing based on iFEM.

The present study investigates the generality of the proposed strain acquisition scheme by adopting specimen II and specimen III which differ in dimension, layout, material, and loading

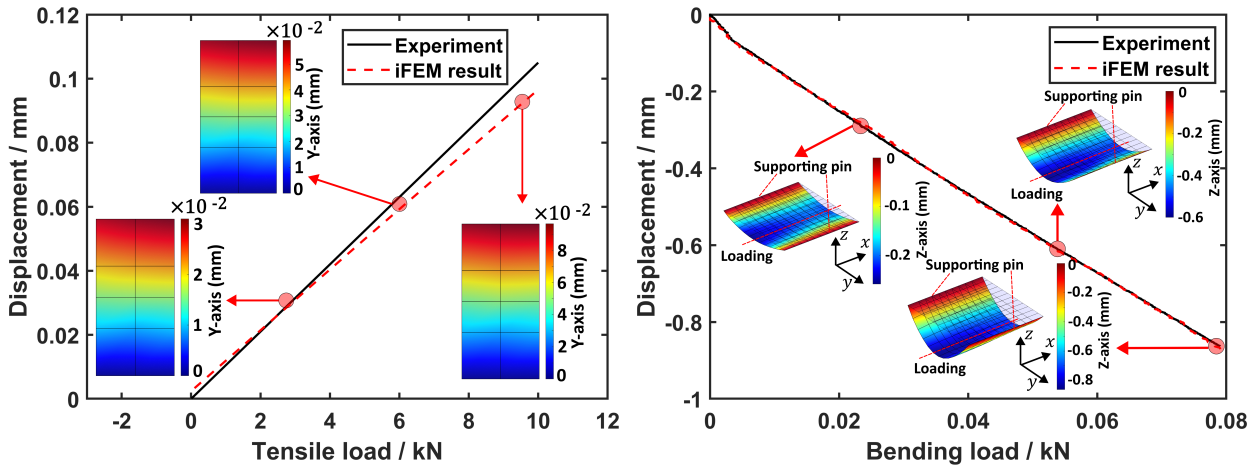
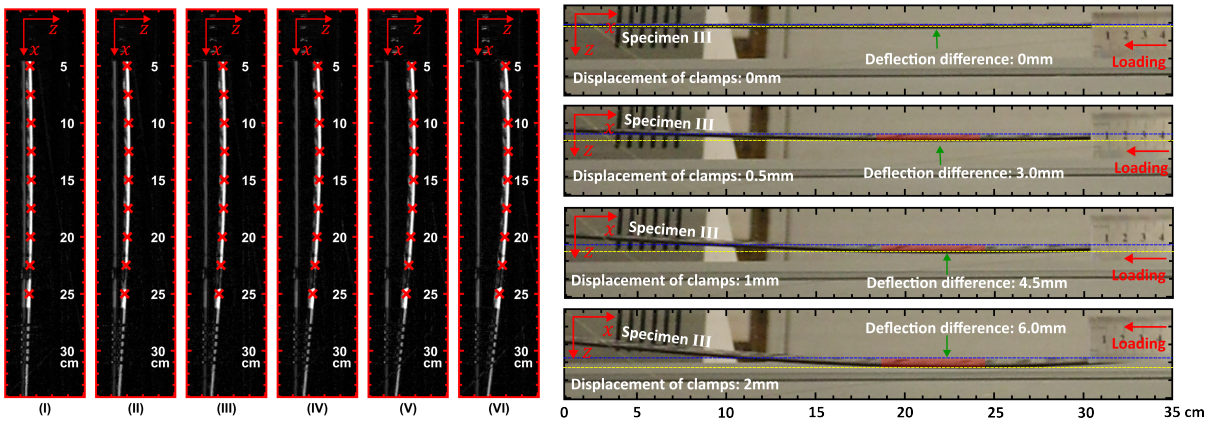


Figure 5.6: The shape sensing results of specimen I and specimen II: (a) The shape sensing results of specimen I; (b) The shape sensing results of specimen II

type. The shape sensing result of specimen II is depicted in Figure 5.6(b), which presents the load-displacement curve obtained from both the Instron machine (Experiment) and iFEM calculation. In contrast to specimen I, the displacement is along the z-axis due to bending. The figure reveals that the deflection calculated by iFEM is highly consistent with the experimental results, even though the proportion of elements with measured strain is merely 27%. This finding further confirms the robustness of the design scheme of sensor network presented in subsection 5.2.2. It can be concluded that highly accurate shape sensing can be achieved with a robust sensor network consisting of few effective iQS4 elements (those elements with measured strain). Although the proportion of effective elements is limited in specimen II, it should be noted that the dimension of the iQS4 element is only 20×20mm, which is a challenge for strain gauges or FBGs. This advantage is primarily due to the high spatial resolution of distributed sensing and good sensor network design.

As detailed in subsection 5.3.1, a camera was used to record the deflection of specimen III for comparing with the iFEM result. Figure 5.7(a) displays the deflection of specimen III at the observation edge, which refers to the edge of the specimen close to the camera, as shown in Figure 5.4. The deflection at six different compression loads of the upper clamp, namely 0.3mm, 0.6mm, 0.9mm, 1.2mm, 1.5mm, and 1.8mm, are represented in sub-figures (I) to (VI),

respectively. The white line with red marks in these figures represents the deflection captured by camera, while the light white line denotes the initial state of specimen III before loading. The deflection data presented in Figure 5.7(a) serves as a crucial criterion to evaluate the accuracy of the iFEM result for specimen III.



(a) (b)

Figure 5.7: The deflection and deflection difference of specimen III observed by camera: (a) The deflection data obtained by camera; (b) The deflection difference of two longest edge during the compression obtained by camera

A further criterion to assess the accuracy of the iFEM result for specimen III is the maximum deflection discrepancy between the observation edge and its opposite edge. During the compression experiment, a slight torsion occurred in the specimen due to the defect of potting-end induced during the manufacturing process, leading to a discrepancy in the deflection of the two longest edge (the observation edge and the opposite edge) of specimen III. This phenomenon was captured by the camera, as shown in Figure 5.7(b). This figure depicts the deflection difference measured under four conditions when the upper clamp displacement was 0mm, 0.5mm, 1mm, and 2mm, respectively. The corresponding deflection discrepancies are indicated in the figure, namely 0mm, 3.0mm, 4.5mm, and 6.0mm.

Based on the mesh structure detailed in Figure 5.5 and the experimental strain field, the displacement field of specimen III are obtained and illustrated in Figure 5.8(a). The x-axis in this figure represents the displacement of clamps during the experiment, while the y-axis represents

the compressive load during the experiment. The abrupt alteration in this curve is caused by the manufacturing defect in the potting-end. The detailed iFEM outcomes are presented by pseudo-colour images when the displacement of the upper clamp is 0.5mm, 1mm, and 2mm. Consistent with the camera observations, the iFEM results demonstrate discrepancies in deflection between the observation and opposite edges. A detailed comparison between the iFEM results and the camera observations is presented in Figure 5.8(b), 5.8(c), and 5.8(d), respectively, when the displacement of the upper clamp is 0.5mm, 1mm, and 2mm. The deflection discrepancy between the observation edge and its opposite edge depicted in these figures is consistent with the results presented in Figure 5.7(b). Based on the experimental outcomes of the aforementioned three specimens, we conclude that iFEM exhibits promising accuracy in shape sensing based on the proposed strain acquisition scheme.

5.4.3 The strain extrapolation results

The experimental strain of specimen III subjected to 1mm compression load is utilized to investigate the performance of SISR-based strain extrapolation technique. First, the measured strain distribution is downsampled by a factor of two to obtain a low-density strain field. Next, this low-density strain field is extrapolated by a factor of two to obtain a predicted strain field with the same size as the original measurements. The difference between the predicted strain field and the measured strain distribution is then employed to evaluate the performance of different strain extrapolation techniques. In this study, various SISR algorithms, including rational fractal interpolation (RFI) [386], sparse coding (SCSR) [387], neighbor embedding algorithm (NE) [388], anchored neighborhood regression (ANR) [389], adjusted anchored neighborhood regression (APLUSE) [390], and deep convolutional networks (SRCNN) [391], which are the most prevalent and well-established methods, are adopted to investigate strain extrapolation. In addition, cutting edge strain extrapolation methods such as GP [376], RBF [377], and bicubic interpolation are used as reference in this research.

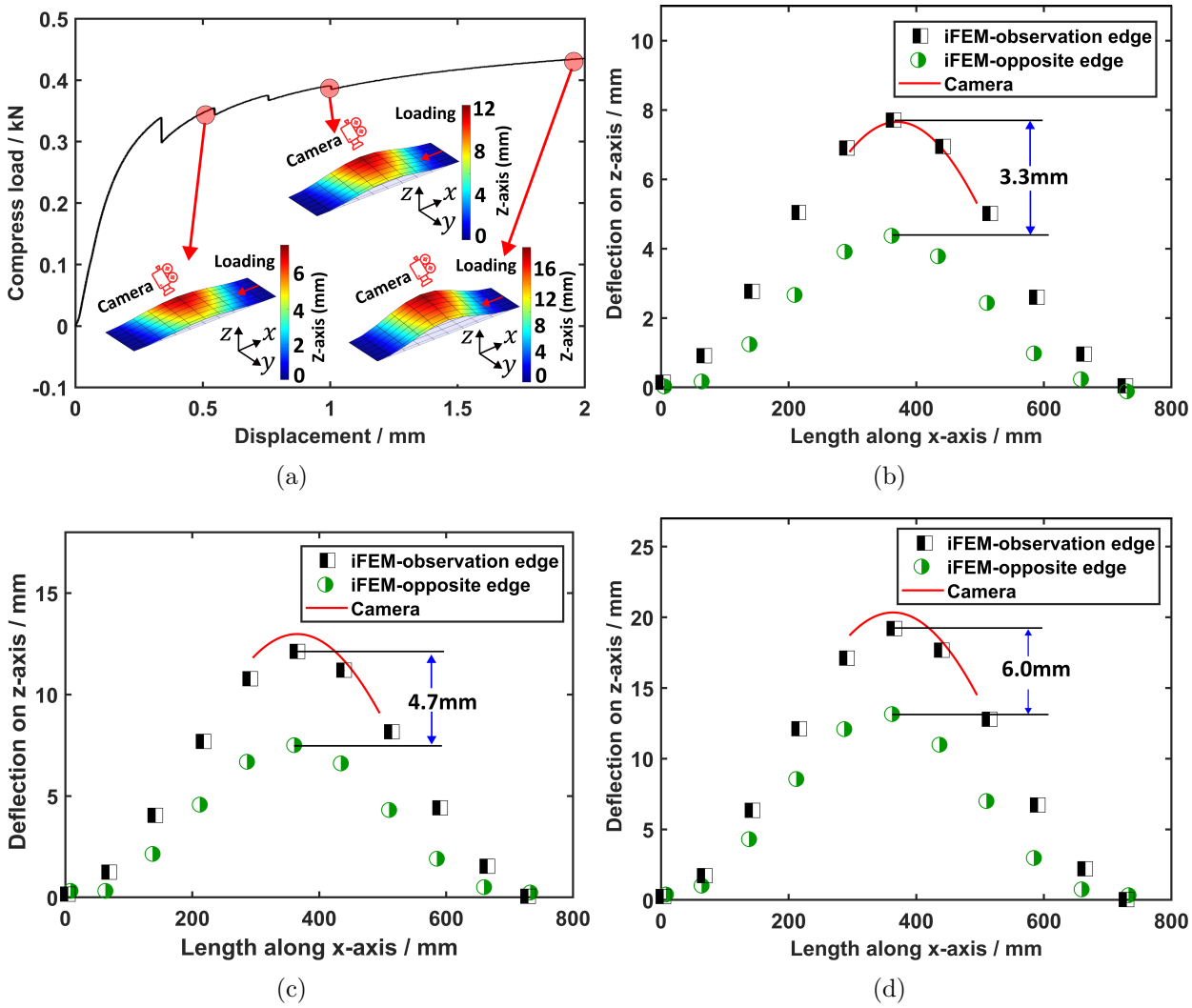


Figure 5.8: The shape sensing results of specimen III: (a) The displacement field of specimen III; (b) A detailed comparison between the iFEM results and the camera observations under 0.5mm load; (c) A detailed comparison between the iFEM results and the camera observations under 1mm load; (d) A detailed comparison between the iFEM results and the camera observations under 2mm load

The evaluation of the performance of the strain extrapolation techniques is based on the mean ($\kappa_1^{(x,y,xy)}$) and maximum errors ($\kappa_2^{(x,y,xy)}$) between the predicted and measured strain distributions. These evaluation indices are defined in Equations 5.16(a) and 5.16(b), respectively. Here, N represents the number of measurement points, and $\Delta\varepsilon$ denotes the maximum strain difference among the measured strain distribution. The measured strain and predicted strain are represented by $\varepsilon_m^{(x,y,xy)}$ and $\varepsilon_p^{(x,y,xy)}$, respectively.

$$\kappa_1^{(x,y,xy)} = \frac{100\%}{N\Delta\varepsilon}\sum_{i=1}^{N}\left|\varepsilon_{mi}^{(x,y,xy)} - \varepsilon_{pi}^{(x,y,xy)}\right| \tag{5.16a}$$

$$\kappa_2^{(x,y,xy)} = \frac{100\%}{\Delta\varepsilon} max\left(\left|\varepsilon_{m}^{(x,y,xy)} - \varepsilon_{p}^{(x,y,xy)}\right|\right) \tag{5.16b}$$

This subsection presents the results of strain extrapolation using the algorithms mentioned earlier. The mean error of the extrapolation is shown in Figure 5.9. Sub-figures (a), (b), and (c) exhibit the mean error of normal strain ε_x, normal strain ε_y, and shear strain γ_{xy} on surface one, respectively. Conversely, sub-figures (d), (e), and (f) demonstrate the mean error of normal strain ε_x, normal strain ε_y, and shear strain γ_{xy} on surface two, respectively. The mean error values resulting from the strain extrapolation techniques based on SISR algorithms are indicated by black bars, while the results obtained using the reference algorithms (GP,RBF,and BICUBIC) are represented by gray bars. The outcomes reveal that the mean error of the normal strain ε_x is comparatively higher than that of ε_y and γ_{xy}.

The maximum error of the strain extrapolation utilizing the aforementioned algorithms is illustrated in Figure 5.10, where sub-figures (a), (b), and (c) demonstrate the outcomes of ε_x, ε_y, and γ_{xy} on surface one, while sub-figures (d), (e), and (f) present the corresponding results on surface two. As with the mean error, the maximum error of ε_x has a greater impact on the overall error. Based on the results of both the mean and maximum error, we can safely conclude that SISR-based strain extrapolation yields a similar performance to the cutting edge strain extrapolation methods, including GP and RBF interpolation.

It is worth noting that the strain field of specimen III is inherently smooth due to the absence of damage or complex features like holes, resulting in minimal differences between SISR-based and traditional strain extrapolation methods. To assess the ability to preserve high-frequency components (damage features) in the strain field, experimental data from a prior study on dam-

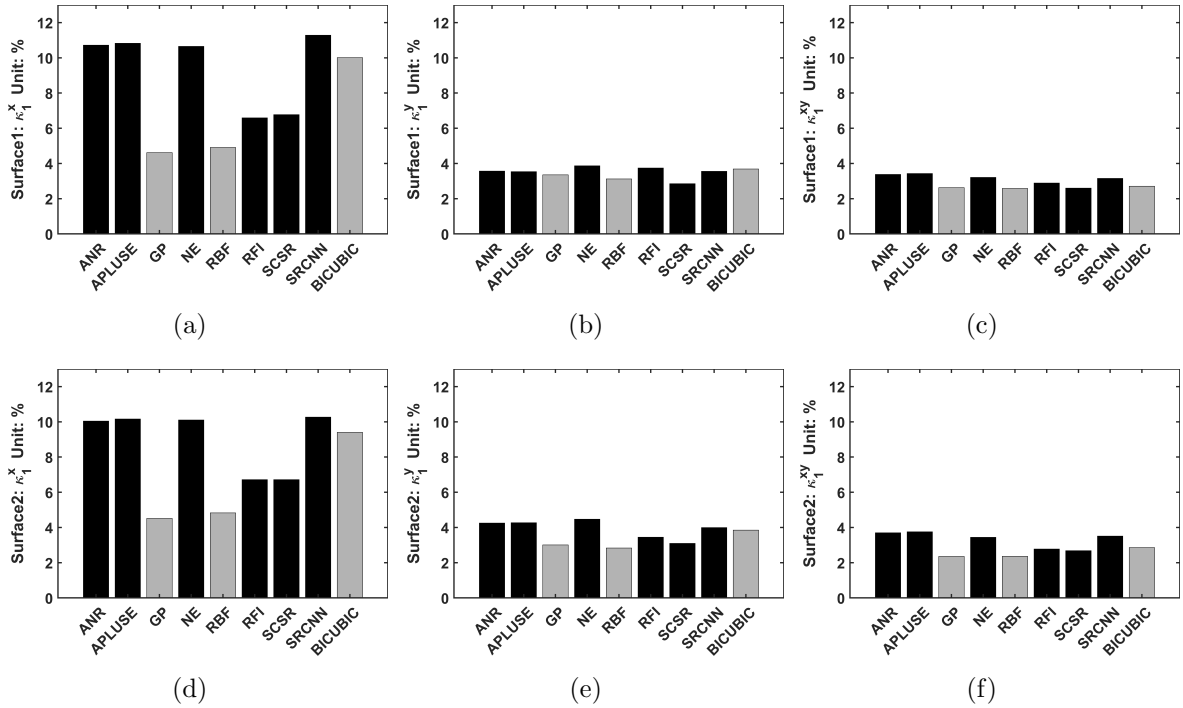


Figure 5.9: The mean error of strain extrapolation: (a) The mean error of the normal strain ε_x after extrapolation on surface 1; (b) The mean error of the normal strain ε_y after extrapolation on surface 1; (c) The mean error of the shear strain γ_{xy} after extrapolation on surface 1; (d) The mean error of the normal strain ε_x after extrapolation on surface 2; (e) The mean error of the normal strain ε_y after extrapolation on surface 2; (f) The mean error of the normal strain γ_{xy} after extrapolation on surface 2

age detection of CFRP specimens was utilized. The same procedures used for specimen III were applied to the experimental data with damage. In contrast to specimen III, the CFRP specimens with BVID show distinctive features in the strain field when subjected to tension load, usually characterized by discontinuities in the strain field, as depicted in the shaded region of Figure 5.11. The solid red line in this figure shows the strain extrapolation results obtained using various algorithms, while the dotted black line represents the experimental measurements of the CFRP specimen with BVID. The results presented in Figure 5.11 reveal that strain extrapolation algorithms based on smoothness prior (GP, RBF, BICUBIC) suppress damage-related features in the strain field to some extent. However, most of the SISR-based strain extrapolation algorithms do not suppress damage-related features. Further more, some SISR algorithms, including ANR, APLUSE, NE, and SRCNN, highlight damage-related features to some extent. Therefore, SISR-based strain extrapolation exhibits potential for application in CFRP structures with complex components (such as holes) or potential damages.

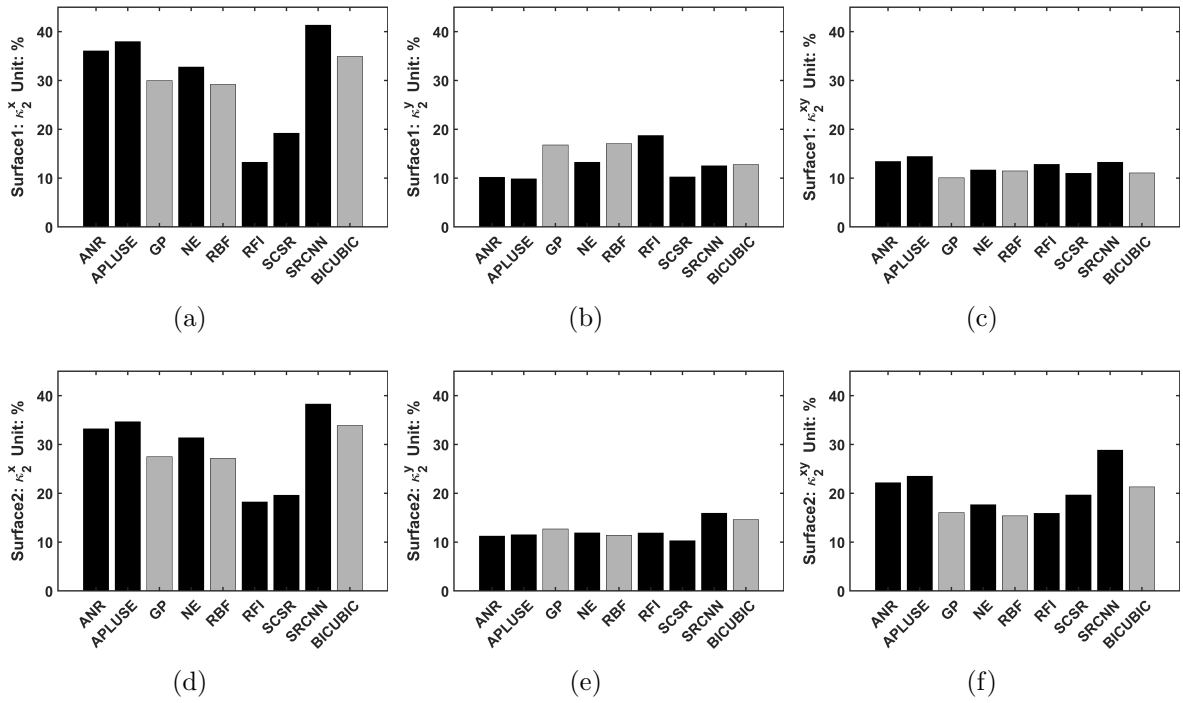


Figure 5.10: The maximum error of strain extrapolation: (a) The maximum error of the normal strain ε_x after extrapolation on surface 1; (b) The maximum error of the normal strain ε_y after extrapolation on surface 1; (c) The maximum error of the shear strain γ_{xy} after extrapolation on surface 1; (d) The maximum error of the normal strain ε_x after extrapolation on surface 2; (e) The maximum error of the normal strain ε_y after extrapolation on surface 2; (f) The maximum error of the normal strain γ_{xy} after extrapolation on surface 2

5.4.4 The shape sensing result of specimen III after strain extrapolation

The density of the iQS4 mesh can be increased based on the results of strain extrapolation to achieve a more detailed displacement field based on iFEM. The strain field of specimen III under 1mm compression is extrapolated by a factor of three to obtain a detailed strain distribution. The resulting strain distribution is then used as input for iFEM to calculate the detailed displacement field. The weight of the extrapolated strain is set to one in iFEM. Figure 5.12 presents the shape sensing results based on different strain extrapolation algorithms. The detailed distribution of the displacement field is depicted through pseudo-colour images, accompanied by a corresponding colour bar on the right side to indicate the respective val-

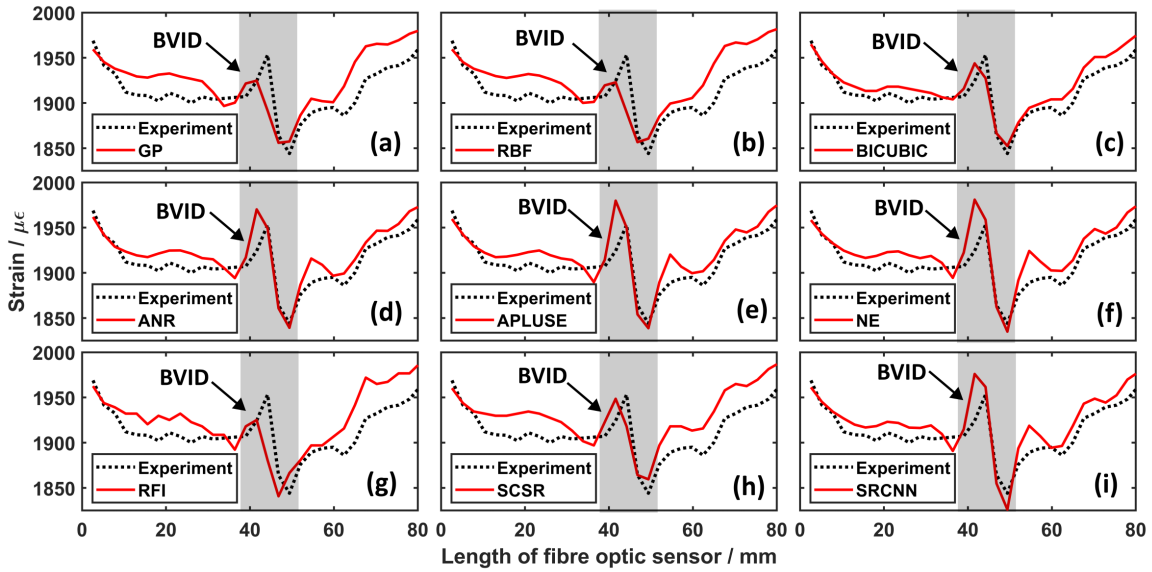


Figure 5.11: The extrapolation of strain field with BVID: (a) extrapolation result by GP; (b) extrapolation result by RBF; (c) extrapolation result by BICUBIC; (d) extrapolation result by ANR; (e) extrapolation result by APLUSE; (f) extrapolation result by NE; (g) extrapolation result by RFI; (h) extrapolation result by SCSR; (i) extrapolation result by SRCNN

ues. The results show that the displacement field obtained by iFEM based on extrapolated strain offers promising accuracy. The black dots in the figure represent the deflection result on the observation edge calculated directly from experimental measurements (as same as Figure 5.7(c)). The dashed blue line shows the deflection result on the observation edge obtained from extrapolated strain field. The deflection obtained under experimental strain and extrapolated strain match well with each other. However, the error of the GP algorithm is larger than that of other algorithms because the strain field extrapolated by GP is much smoother than that of other algorithms.

5.5 Conclusions

This chapter presents a novel and precise scheme for achieving high-accuracy shape sensing of CFRP structures based on iFEM. In practical applications, the accuracy of shape sensing is significantly influenced by the precision of strain field, which is primarily determined by the spatial resolution of the measurement and the distribution of sensors. Therefore, based

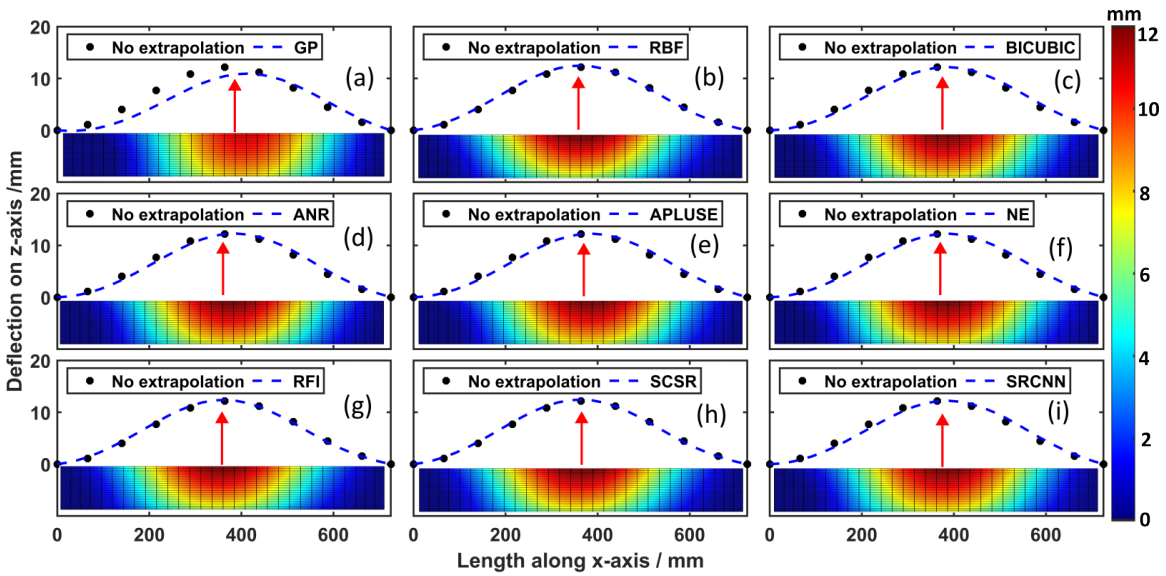


Figure 5.12: The shape sensing results of specimen III based on different strain extrapolation algorithms: (a) GP; (b) RBF; (c) BICUBIC; (d) ANR; (e) APLUSE; (f) NE; (g) RFI; (h) SCSR; (i) SRCNN

on existing research, this chapter proposes a strain acquisition method based on basic sensing blocks, utilizing distributed fibre optic sensors. The proposed method results in a robust sensor network, requiring only a limited amount of measurement data for high accuracy shape sensing using iFEM.

The efficacy and general applicability of the proposed scheme were demonstrated by conducting experiments on three different CFRP samples, varying in dimensions, materials, and layout types. The feasibility of the proposed scheme was established by conducting a tensile test on Sample I. The robustness of the sensor network designed using the proposed scheme was confirmed by a three-point bending experiment conducted on Sample II, which achieving high-precision shape sensing using only 27% of the effective iQS4 elements. Furthermore, compression experiments conducted on Sample III validated the ability of the proposed scheme to achieve high-precision shape sensing under complex loads, caused by potting-end defects.

To obtain a more detailed distribution of the displacement field, the strain extrapolation technique is employed to interpolate the strain field obtained through the proposed strain acquisition

method. However, the traditional strain extrapolation technique is limited by the smoothness assumption and not suitable for non-smooth strain fields, which are primarily caused by potential damage or special components, such as holes, in the structure. To overcome this challenge, this chapter proposes the SISR-based strain extrapolation technique. After linearly mapping the strain field to the RGB colour space, the resulting image is then extrapolated using the SISR technique. The proposed SISR-based extrapolation is superior to the traditional strain extrapolation technique as it retains the high-frequency components in the image that correspond to non-smooth regions in the strain field. The study validates several well-established SISR algorithms, including ANR, APLUS, NE, RFI, SCSR, and SRCNN, and compares their performance against cutting edge strain extrapolation algorithms, including GP, RBF, and bicubic. Experimental results show that the SISR-based extrapolation technique achieves comparable performance with GP, RBF, and bicubic in a smooth strain field, but outperforms them in a strain field with BVID, indicating that the SISR-based technique is more promising for extrapolation of non-smooth strain fields. By combining the proposed strain acquisition method and the SISR-based strain extension technique, high-fidelity shape sensing of CFRP shell structures can be achieved.

It should be mentioned that this study did not conduct any work related to the training of dictionaries or deep learning models. The dictionaries and deep convolutional networks utilized in this study were directly adopted from related original studies. It is expected that training dictionaries or deep convolutional networks with real strain fields will further enhance the accuracy of strain extrapolation. This area of research warrants further investigation in the future.

Chapter 6

Summaries and future works

This doctoral research effectively tackled numerous challenges in SHM of CFRP structures using distributed fiber optic sensing. These challenges include enhancement of measurement sensitivity (strain and temperature), measurement accuracy evaluation, assessment of measurement consistency, damage detection, and shape sensing. Therefore, research objectives corresponding to these challenges are proposed in subsection 1.2. By addressing these research objectives, this doctoral research provides a comprehensive perspective on SHM of CFRP structures using distributed fiber optic sensing. It serves as a valuable reference for related research.

6.1 Summary of background introduction

Chapter 2 serves as a comprehensive overview of distributed fiber optic sensing, with a specific focus on Rayleigh-based distributed sensing techniques. The subsequent sections concisely summarize the chapter's core content:

Introduction to Distributed Fiber Optic Sensing:

The initial segment introduces the concept and significance of DFOS. It elaborates on three distinct distributed sensing techniques, namely Raman backscattering, Brillouin backscattering, and Rayleigh backscattering. The discussion underscores the diverse applicability of DFOS across various fields and emphasizes its crucial role in SHM within aircraft structures.

Introduction of Rayleigh-Based Distributed Sensing

This portion is dedicated to introducing Rayleigh-based distributed sensing, a prominent and pivotal technique within the realm of DFOS. The elucidation revolves around the selection of Rayleigh backscattering as the prime choice for SHM in aircrafts. The working principle is detailed, underscoring its adeptness in capturing strain and temperature information along the fiber.

Challenges of the OFDR Technique in SHM of Aircrafts and Literature Review:

The central theme of this section revolves around the challenges encountered while implementing the OFDR technique for aircraft structural health monitoring. It comprehensively explores key challenges, encompassing spatial resolution enhancement, algorithm efficiency augmentation, continuous vibration measurement, shape sensing, and embedding FOS. The section is fortified with a comprehensive literature review that delves into the challenges' scope and potential remedial approaches.

In summary, Chapter 2 provides an insightful journey into the realm of distributed fiber optic sensing, spotlighting the efficacy of Rayleigh-based methodologies. It presents an exhaustive analysis of challenges inherent to employing the OFDR technique for SHM in aircraft structures, encapsulating spatial resolution advancement, algorithmic efficiency refinement, continuous vibration measurement, shape sensing, and the intricacies of integrating FOS within composite materials. The chapter's detailed examination of existing literature and exploration of potential solutions substantially enriches the comprehension and application of distributed sensing within the aviation domain.

6.2 Summary of the strain and temperature measurement research

Chapter 3 presents a comprehensive exploration of various parametric study related to distributed fiber optic sensing, as outlined in the following sections:

The Sensitivity Enhancement of Distributed Fiber Optical Sensors:

This subsection focuses on the enhancement of sensitivity in distributed fiber optic sensors. It delves into methodologies including re-coating and twist pre-stress to amplify the sensing capability of these sensors, enabling them to capture finer changes in the measured parameters.

Accuracy of Distributed Strain Sensing in Composite Laminates under Thermal and Mechanical Loads:

This subsection explores the accuracy of distributed strain sensing in the context of composite laminates subjected to both thermal and and Mechanical loads. It delves into the challenges posed by varying ambient temperatures and proposes the demands for calibration under extreme thermal load to ensure precise strain measurements.

Accuracy of Distributed Strain Sensing in Composite Laminates under fatigue Loads:

This subsection delves into the accuracy of distributed strain sensing within composite laminates under fatigue loads. It examines the impact of mechanical fatigue loads on strain measurements and analyzes how these fatigue loads influence the reliability and accuracy of the acquired data.

Strain Measurement Consistency of Distributed Fiber Optic Sensing:

The last subsection addresses the issue of strain measurement consistency in distributed fiber optic sensing. It scrutinizes the reliability of these sensors over various test scenarios.

In summary, Chapter 3 provides a comprehensive exploration of distributed fiber optic sensing, encompassing sensitivity enhancement, accuracy under thermal and fatigue loads, and the measurement consistency. By delving into these critical aspects, the research outcomes contribute to advancing the understanding and application of distributed fiber optic sensors for structural health monitoring and related applications.

6.3 Summary on damage detection of CFRP structures

Chapter 4 studies on two distinct techniques that enhance the potential of distributed fiber optic sensing for SHM of composite structures. The comprehensive summary below encapsulates the pivotal aspects explored within each technique:

Two-dimensional Strain Field Reconstruction of Composite Plates Based on Distributed Fiber Optic Sensors:

This subsection concentrates on the reconstruction of the strain field within composite plates, leveraging the capabilities of distributed fiber optic sensors. The study's objective centers on understanding strain reconstruction under varying sensor densities, facilitated by barycentric Lagrange and cubic spline interpolation methods. This study's outcomes carry profound implications for optimizing strain measurement precision, concurrently minimizing the weight and cost of SHM systems.

A Novel DI-based Damage Detection Method for Carbon Fiber Reinforced Polymer Structures Based on Distributed Strain Measurements with Fiber Optic Sensors:

This subsection introduces a novel methodology that capitalizes on distributed strain measurements for the detection of damage in CFRP structures. The approach, grounded in feature matching of local neighborhoods among distributed strain measurements, addresses the complexities of damage detection under operational conditions. The methodology capitalizes on correlations between local measurement points to differentiate between damaged and undamaged segments, offering a fresh perspective and potential solutions for the challenges inherent to damage detection in CFRP structures. Furthermore, the study underscores the technique's efficacy in detecting diverse damage types, encompassing BVID and VID in CFRP structures.

In summary, Chapter 4 shows the remarkable potential of distributed fiber optic sensing in enhancing structural health monitoring. Through meticulous strain reconstruction and innovative damage detection methodologies, the chapter demonstrates how these techniques hold the promise of revolutionizing the field, ushering in increased accuracy, efficiency, and cost-

effectiveness.

6.4 Summary of shape sensing of CFRP shell structures

Chapter 5 introduces an innovative approach aimed at achieving precise shape sensing of CFRP shell structures using the iFEM. In practical applications, the accuracy of shape sensing relies heavily on the precision of the strain field. This precision, in turn, depends on factors such as the spatial resolution of measurements and the sensor distribution. Consequently, Chapter 5 proposes a strain data acquisition method built upon fundamental sensing blocks, employing distributed fiber optic sensors.

To further refine the distribution of displacement fields, the strain extrapolation technique based on SISR technique is proposed to interpolate the strain data acquired through the proposed block-based method. This is because that the traditional strain extrapolation approach is constrained by its reliance on smoothness assumptions and may not be suitable for non-smooth strain fields, typically arising from structural damage or unique components like holes. Notably, the proposed SISR-based extrapolation method surpasses traditional strain extrapolation techniques. It preserves high-frequency components within the image, indicative of non-smooth regions in the strain field.

6.5 Contributions and outcomes

According to the summaries of this doctoral research mentioned above, all objectives in subsection 1.2 have been studied in detail. In addition, the main contributions and outcomes of this doctoral research were outlined as follows:

- The first contributions includes the research on strain and temperature measurement based on distributed fiber optic sensing. Firstly, the potential strategies for enhancing sensor measurement sensitivity, specifically through modifications in coating materials

and the application of pre-stress were proposed. The related outcomes were published in "European Workshop on Structural Health Monitoring 2022" with title "The Sensitivity Enhancement of Distributed Fiber Optical Sensors". Simultaneously, an investigation into the accuracy of distributed fiber optic measurements under temperature fluctuations and low-frequency vibrations has been conducted, revealing the significant error introduced by temperature fluctuations in strain measurements, even when employing temperature compensation techniques. The related outcomes were published as a journal paper with title "Accuracy of Distributed Strain Sensing with Single-Mode Fibre in Composite Laminates under Thermal and Vibration Loads". Lastly, employing statistical methodologies, the measurement consistency and uncertainty of distributed fiber optic sensing have been comprehensively assessed across various measurement scenarios. The related outcomes were published in "International Conference on Fracture, Damage and Structural Health Monitoring 2023" with title "Strain measurement consistency of distributed fiber optic sensors for monitoring composite structures under various loading".

- The second contribution focuses on damage detection in CFRP structures utilizing distributed fiber optic sensing. Firstly, the strain reconstruction with interpolation methods based on measurements from distributed fiber optic sensors was proposed, which benefits the optimization of the efficiency and cost-effectiveness of sensor networks. The related outcomes were published in "International Conference on Fracture, Damage and Structural Health Monitoring 2022" with title "2D Strain Field Reconstruction of Composite Plates Based on Distributed Fibre Optic Sensors". Secondly, a novel damage detection method based on distributed fiber optic sensing for CFRP structures was proposed combining with image processing techniques. Notably, the proposed approach operates independently of prior knowledge regarding non-damaged strain distribution. The related outcomes were published as a journal paper titled: "A novel damage detection method for carbon fibre reinforced polymer structures based on distributed strain measurements with fibre optical sensor".

- The final contribution pertains to shape sensing in CFRP shell structures utilizing distributed fiber optic sensing. Initially, a block-based strain field acquisition methodology

based on distributed fiber optic sensing is introduced and subsequently validated across three distinct experiments involving varying shell structures. Furthermore, an innovative strain extrapolation approach is presented, employing image super-resolution techniques to retain high-frequency characteristics within the strain field. Comparative analysis against existing techniques underscores the merits of the proposed approach in strain extrapolation. The related outcomes were summarized as a journal paper titled: "The shape sensing of composite shell structures using distributed fibre optic sensing" (under review).

6.6 Future works

Building upon the findings of this PhD research, the future research directions for employing distributed fiber optic sensing in SHM of CFRP structures can be outlined as follows:

- The research on the efficacy of the proposed damage detection algorithm under complex built up aeronautical structures such as beams, wing box, wing ribs, and fuselage section.
- The performance of proposed damage detection algorithm under complex loading conditions (under thermal, fatigue, mechanical loads and impact events), and different sensor configurations (under different density, layout, and intallation method) are worth researching. For example, ensuring accurate damage detection under diverse sensor densities and complex loads that replicate aircraft operations.
- Expanding the scope of shape sensing using distributed fiber optic sensing is valuable, encompassing a range of structural configurations beyond thin plates. This includes beams, built up structures, sandwich structures, and three-dimensional solid structures.
- Conducting research on fiber optic sensor layout optimization is imperative. Particularly in shape sensing applications involving intricate structures, the refinement of sensor placement is vital to attain both high resolution and quality strain data while minimizing

unnecessary sensing points, thereby reducing costs and computational demands. Achieving this could involve employing multi-objective optimization strategies that consider factors like sensor quantity, layout symmetry, and shape sensing precision. Approaches such as Pareto front learning, strength Pareto evolutionary algorithms, or particle swarm optimization offer promising avenues for optimizing sensor layouts.

- Although iFEM has demonstrated its potential in simple structures, its applicability becomes constrained in complex structures due to the heightened demands on measurement precision. For instance, for thick structures where the shear deformation is not negligible, the strain readings from both sides are needed. Hence, enhancing the iFEM algorithm is imperative to address these challenges effectively.

- The dictionaries and deep convolutional networks employed in this research for strain extrapolation were directly sourced from relevant original studies which pay attention on image super resolution. Therefore, the potential improvement lies in training dictionaries or deep convolutional networks with real strain field data, which has the potential to significantly enhance the precision of strain extrapolation.

- Exploring real-time shape sensing for complex structures (such as wing box) holds substantial value. The demands of numerous measurement points in large and complex structures lead to the accumulation of extensive data. The real-time acquisition, storage, and processing of this data can present considerable challenges.

Appendix A

The inverse Finite Element Method

A.1 The appendix of Chapter 5

$$N_1 = \frac{1}{4}(1-\xi)(1-\eta) \quad N_2 = \frac{1}{4}(1+\xi)(1-\eta) \tag{A.1a}$$

$$N_3 = \frac{1}{4}(1+\xi)(1+\eta) \quad N_4 = \frac{1}{4}(1-\xi)(1+\eta) \tag{A.1b}$$

$$N_5 = \frac{1}{16}\left(1-\xi^2\right)(1-\eta) \quad N_6 = \frac{1}{16}(1+\xi)\left(1-\eta^2\right) \tag{A.1c}$$

$$N_7 = \frac{1}{16}\left(1-\xi^2\right)(1+\eta) \quad N_8 = \frac{1}{16}(1-\xi)\left(1-\eta^2\right) \tag{A.1d}$$

$$L_1 = (y_1 - y_4)N_8 - (y_2 - y_1)N_5 \quad L_2 = (y_2 - y_1)N_5 - (y_3 - y_2)N_6 \tag{A.2a}$$

$$L_3 = (y_3 - y_2)N_6 - (y_4 - y_3)N_7 \quad L_4 = (y_4 - y_3)N_7 - (y_1 - y_4)N_8 \tag{A.2b}$$

$$M_1 = (x_4 - x_1)N_8 - (x_1 - x_2)N_5 \quad M_2 = (x_1 - x_2)N_5 - (x_2 - x_3)N_6 \tag{A.2c}$$

$$M_3 = (x_2 - x_3)N_6 - (x_3 - x_4)N_7 \quad M_4 = (x_3 - x_4)N_7 - (x_4 - x_1)N_8 \tag{A.2d}$$

$$u^e = \begin{bmatrix} U_i & V_i & W_i & \theta_{xi} & \theta_{yi} & \theta_{zi} \end{bmatrix}^T \quad i = 1, 2, 3, 4 \tag{A.3a}$$

$$B_i^m = \begin{bmatrix} \dfrac{\partial N_i}{\partial x} & 0 & 0 & 0 & 0 & \dfrac{\partial L_i}{\partial x} \\ 0 & \dfrac{\partial N_i}{\partial y} & 0 & 0 & 0 & \dfrac{\partial M_i}{\partial y} \\ \dfrac{\partial M_i}{\partial y} & \dfrac{\partial N_i}{\partial x} & 0 & 0 & 0 & \dfrac{\partial L_i}{\partial y} + \dfrac{\partial M_i}{\partial x} \end{bmatrix} \quad i = 1, 2, 3, 4 \tag{A.4a}$$

$$e(u^e) = [B_1^m, \quad B_2^m, \quad B_3^m, \quad B_4^m]\, u^e = B^m \cdot u^e \tag{A.4b}$$

$$B_i^b = \begin{bmatrix} 0 & 0 & 0 & 0 & \dfrac{\partial N_i}{\partial x} & 0 \\ 0 & 0 & 0 & -\dfrac{\partial N_i}{\partial y} & 0 & 0 \\ 0 & 0 & 0 & -\dfrac{\partial N_i}{\partial x} & \dfrac{\partial N_i}{\partial y} & 0 \end{bmatrix} \quad i = 1, 2, 3, 4 \tag{A.5a}$$

$$k(u^e) = \left[B_1^b, \quad B_2^b, \quad B_3^b, \quad B_4^b\right] u^e = B^b \cdot u^e \tag{A.5b}$$

$$B_i^s = \begin{bmatrix} 0 & 0 & \dfrac{\partial N_i}{\partial x} & -\dfrac{\partial L_i}{\partial x} & -\dfrac{\partial M_i}{\partial x} + N_1 & 0 \\ 0 & 0 & \dfrac{\partial N_i}{\partial y} & -\dfrac{\partial L_i}{\partial y} - N_1 & -\dfrac{\partial M_i}{\partial y} & 0 \end{bmatrix} \quad i = 1, 2, 3, 4 \tag{A.6a}$$

$$\mathrm{g}(u^e) = [B_1^s, \quad B_2^s, \quad B_3^s, \quad B_4^s]\, u^e = B^s \cdot u^e \tag{A.6b}$$

$$\varepsilon^e = [e_\varepsilon, k_\varepsilon, \mathrm{g}_\varepsilon]^T \tag{A.7a}$$

$$K^e = \int_{Ae} \left[\omega_m (B^m)^T B^m + \omega_b (2h)^2 (B^b)^T B^b + \omega_s (B^s)^T B^s\right] dA^e \tag{A.7b}$$

$$f^e = \left[\int_{A^e} [\omega_m (B^m)^T] dA^e \quad \int_{A^e} [\omega_b (2h)^2 (B^b)^T] dA^e \quad \int_{A^e} [\omega_s (B^s)^T] dA^e\right] \tag{A.7c}$$

A.2 A detailed derivation of the inverse finite element method

A.2.1 Basic assumption

The isometric coordinate system of iQS4 element is shown in Figure A.1(a).

As shown in Figure A.1(b), the displacement mode includes: U,V,W,θ_x,θ_y,θ_z.

The continuous displacement field within the iQS4 is as same as Mindlin plate, shown as:

$$U_x = U + z\theta_y \tag{A.8a}$$

$$U_y = V - z\theta_x \tag{A.8b}$$

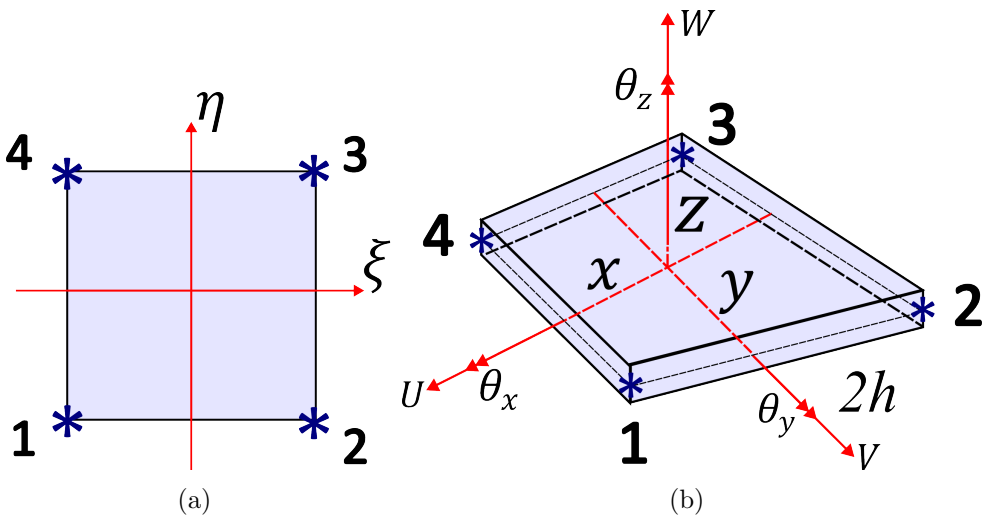


Figure A.1: The coordinate system: (a) The isoparametric coordinate system; (b) The local coordinate system

$$U_z = W \tag{A.8c}$$

A.2.2 iQS4 fields characterization

Membrane Part

Nodes' displacement:

$$q_m^e = \begin{bmatrix} U_1 & V_1 & \theta_{z1} & U_2 & V_2 & \theta_{z2} & U_3 & V_3 & \theta_{z3} & U_4 & V_4 & \theta_{z4} \end{bmatrix}^T \tag{A.9}$$

The membrane displacement field is:

$$U_m = U(\xi,\eta) = \sum_{i=1}^{4} N_i U_i + \sum_{i=1}^{4} L_i \theta_{zi} \tag{A.10a}$$

$$V_m = V(\xi,\eta) = \sum_{i=1}^{4} N_i V_i + \sum_{i=1}^{4} M_i \theta_{zi} \tag{A.10b}$$

The detailed derive is shown in literature as follows:

An improved treatment of transverse shear in the mindlin-type four-node quadrilateral element

Four-node 'flat' shell element: Drilling degrees of freedom, membrane-bending coupling, warped geometry, and behaviour

According to papers list above, the expression of N_i , L_i , M_i is expressed in Equation A.1 and A.2.

Therefore, for membrane displacement field, the discretized expression is:

$$\begin{bmatrix} U_m(\xi,\eta) \\ V_m(\xi,\eta) \end{bmatrix} = \begin{bmatrix} N_1 & 0 & L_1 & \cdots & N_4 & 0 & L_4 \\ 0 & N_1 & M_1 & \cdots & 0 & N_4 & M_4 \end{bmatrix} q_m^e \tag{A.11}$$

According to geometric equation (2D):

$$\begin{bmatrix} \varepsilon_{xm} \\ \varepsilon_{ym} \\ \gamma_{xym} \end{bmatrix} = \begin{bmatrix} \partial/\partial x & 0 \\ 0 & \partial/\partial y \\ \partial/\partial y & \partial/\partial x \end{bmatrix} \begin{bmatrix} U(\xi,\eta) \\ V(\xi,\eta) \end{bmatrix} \tag{A.12}$$

The strain field can be expressed as:

$$\begin{bmatrix} \varepsilon_{xm} \\ \varepsilon_{ym} \\ \gamma_{xym} \end{bmatrix} = \begin{bmatrix} \partial/\partial x & 0 \\ 0 & \partial/\partial y \\ \partial/\partial y & \partial/\partial x \end{bmatrix} \begin{bmatrix} N_1 & 0 & L_1 & \cdots & N_4 & 0 & L_4 \\ 0 & N_1 & M_1 & \cdots & 0 & N_4 & M_4 \end{bmatrix} q_m^e \tag{A.13}$$

This can be expressed as:

$$\begin{bmatrix} \varepsilon_{xm} \\ \varepsilon_{ym} \\ \gamma_{xym} \end{bmatrix} = \begin{bmatrix} \frac{\partial N_1}{\partial x} & 0 & \frac{\partial L_1}{\partial x} & & & \\ 0 & \frac{\partial N_1}{\partial y} & \frac{\partial M_1}{\partial y} & B_{m2} & B_{m3} & B_{m4} \\ \frac{\partial N_1}{\partial y} & \frac{\partial N_1}{\partial x} & \frac{\partial L_1}{\partial y} + \frac{\partial M_1}{\partial x} & & & \end{bmatrix} q_m^e = \begin{bmatrix} B_{m1} & B_{m2} & B_{m3} & B_{m4} \end{bmatrix} q_m^e = B_m q_m^e \tag{A.14}$$

Bending curvatures

Nodes' displacement

$$q_b^e = \begin{bmatrix} \theta_{x1} & \theta_{y1} & \theta_{x2} & \theta_{y2} & \theta_{x3} & \theta_{y3} & \theta_{x4} & \theta_{y4} \end{bmatrix}^T \tag{A.15}$$

The bending displacement field is:

$$U_b = z\theta_y(\xi,\eta) = z\sum_{i=1}^{4} N_i\theta_{yi} \tag{A.16a}$$

$$V_b = -z\theta_x(\xi,\eta) = -z\sum_{i=1}^{4} N_i\theta_{xi} \tag{A.16b}$$

Assumed continuous displacement field function:

$$\begin{bmatrix} U_b \\ V_b \end{bmatrix} = \begin{bmatrix} z\theta_y(\xi,\eta) \\ -z\theta_x(\xi,\eta) \end{bmatrix} \tag{A.17}$$

$$\begin{aligned} \theta_x(\xi,\eta) &= a_0 + a_1\xi + a_2\eta + a_3\xi\eta \\ \theta_y(\xi,\eta) &= b_0 + b_1\xi + b_2\eta + b_3\xi\eta \end{aligned} \tag{A.18}$$

Therefore:

$$\begin{aligned} a_0 + a_1\xi_1 + a_2\eta_1 + a_3\xi_1\eta_1 &= \theta_{x1} \\ a_0 + a_1\xi_2 + a_2\eta_2 + a_3\xi_2\eta_2 &= \theta_{x2} \\ a_0 + a_1\xi_3 + a_2\eta_3 + a_3\xi_3\eta_3 &= \theta_{x3} \\ a_0 + a_1\xi_4 + a_2\eta_4 + a_3\xi_4\eta_4 &= \theta_{x4} \end{aligned} \tag{A.19}$$

which is:

$$\begin{bmatrix} \theta_{x1} \\ \theta_{x2} \\ \theta_{x3} \\ \theta_{x4} \end{bmatrix} = \begin{bmatrix} 1 & \xi_1 & \eta_1 & \xi_1\eta_1 \\ 1 & \xi_2 & \eta_2 & \xi_2\eta_2 \\ 1 & \xi_3 & \eta_3 & \xi_3\eta_3 \\ 1 & \xi_4 & \eta_4 & \xi_4\eta_4 \end{bmatrix} \begin{bmatrix} a_0 \\ a_1 \\ a_2 \\ a_3 \end{bmatrix} \tag{A.20}$$

set:

$$A = \begin{bmatrix} 1 & -1 & -1 & 1 \\ 1 & 1 & -1 & -1 \\ 1 & 1 & 1 & 1 \\ 1 & -1 & 1 & -1 \end{bmatrix} \tag{A.21}$$

Therefore:

$$\begin{bmatrix} a_0 \\ a_1 \\ a_2 \\ a_3 \end{bmatrix} = A^{-1} = \frac{1}{4} \begin{bmatrix} 1 & 1 & 1 & 1 \\ -1 & 1 & 1 & -1 \\ -1 & -1 & 1 & 1 \\ 1 & -1 & 1 & -1 \end{bmatrix} \begin{bmatrix} \theta_{x1} \\ \theta_{x2} \\ \theta_{x3} \\ \theta_{x4} \end{bmatrix} \tag{A.22}$$

Therefore:

$$\begin{aligned} \theta_x(\xi,\eta) &= a_0 + a_1\xi + a_2\eta + a_3\xi\eta \\ &= \frac{1}{4}\{(\theta_{x1} + \theta_{x2} + \theta_{x3} + \theta_{x4}) + (-\theta_{x1} + \theta_{x2} + \theta_{x3} - \theta_{x4})\xi + (-\theta_{x1} - \theta_{x2} + \theta_{x3} + \theta_{x4})\eta \\ &\quad + (\theta_{x1} - \theta_{x2} + \theta_{x3} - \theta_{x4})\xi\eta] \\ &= \frac{1}{4}\{(1 - \xi - \eta + \eta\xi)\theta_{x1} + (1 + \xi - \eta - \eta\xi)\theta_{x2} + (1 + \xi + \eta\xi)\theta_{x3} + (1 - \xi + \eta - \eta\xi)\theta_{x4}] \\ &= \frac{1}{4}\{(1 - \xi)(1 - \eta)\theta_{x1} + (1 + \xi)(1 - \eta)\theta_{x2} + (1 + \xi)(1 + \eta)\theta_{x3} + (1 - \xi)(1 + \eta)\theta_{x4}\} \end{aligned} \tag{A.23}$$

That is:

$$\begin{aligned}\theta_x(\xi,\eta) &= [(1-\xi)(1-\eta),(1+\xi)(1-\eta),(1+\xi)(1+\eta),(1-\xi)(1+\eta)]\begin{bmatrix}\theta_{x1}\\ \theta_{x2}\\ \theta_{x3}\\ \theta_{x4}\end{bmatrix}\\ &= [N_1,N_2,N_3,N_4]\begin{bmatrix}\theta_{x1}\\ \theta_{x2}\\ \theta_{x3}\\ \theta_{x4}\end{bmatrix}\end{aligned} \tag{A.24}$$

Therefore, the shape function here is expressed as (This result matches well with Equation A.1):

$$\begin{aligned}N_1 &= \frac{1}{4}(1-\xi)(1-\eta) \qquad N_2 = \frac{1}{4}(1+\xi)(1-\eta)\\ N_3 &= \frac{1}{4}(1+\xi)(1+\eta) \qquad N_4 = \frac{1}{4}(1-\xi)(1+\eta)\end{aligned} \tag{A.25}$$

Same reason:

$$\theta_y(\xi,\eta) = [N_1,N_2,N_3,N_4]\begin{bmatrix}\theta_{y1} & \theta_{y2} & \theta_{y3} & \theta_{y4}\end{bmatrix}^T \tag{A.26}$$

So, interpolation result of displacement:

$$\begin{bmatrix}U_b\\ V_b\end{bmatrix} = \begin{bmatrix}z\theta_y(\xi,\eta)\\ -z\theta_x(\xi,\eta)\end{bmatrix} = \mathbf{z}\begin{bmatrix}0 & N_1 & 0 & N_2 & 0 & N_3 & 0 & N_4\\ -N_1 & 0 & -N_2 & 0 & -N_3 & 0 & -N_4 & 0\end{bmatrix} q_b^e \tag{A.27}$$

According to the geometric equation (2D) presented in Equation A.12, the strain field can be expressed as:

$$\begin{bmatrix}\varepsilon_{xb}\\ \varepsilon_{yb}\\ \gamma_{xyb}\end{bmatrix} = z\begin{bmatrix}\partial/\partial x & 0\\ 0 & \partial/\partial y\\ \partial/\partial y & \partial/\partial x\end{bmatrix}\begin{bmatrix}0 & N_1 & 0 & N_2 & 0 & N_3 & 0 & N_4\\ -N_1 & 0 & -N_2 & 0 & -N_3 & 0 & -N_4 & 0\end{bmatrix} q_b^e \tag{A.28}$$

This can be expressed as:

$$\begin{bmatrix} \varepsilon_{xb} \\ \varepsilon_{yb} \\ \gamma_{xyb} \end{bmatrix} = z \begin{bmatrix} 0 & \frac{\partial N_1}{\partial x} & & & \\ -\frac{\partial N_1}{\partial y} & 0 & B_{b2} & B_{b3} & B_{b4} \\ -\frac{\partial N_1}{\partial x} & \frac{\partial N_1}{\partial y} & & & \end{bmatrix} q_b^e = z[B_{b1} \quad B_{b2} \quad B_{b3} \quad B_{b4}] = zB_b q_b^e \tag{A.29}$$

Transverse part

The displacement mode of transverse part is expressed in Equation A.8. Therefore, the shear strain caused by transverse load is calculated by:

$$\gamma_{xz} = \frac{\partial U_x}{\partial z} + \frac{\partial W}{x} = \frac{\partial U}{\partial z} + \theta_y + \frac{\partial W}{x} \tag{A.30a}$$

$$\gamma_{yz} = \frac{\partial U_y}{\partial z} + \frac{\partial W}{y} = \frac{\partial V}{\partial z} - \theta_x + \frac{\partial W}{y} \tag{A.30b}$$

In this equation, $\frac{\partial U}{\partial z} = \frac{\partial V}{\partial z} = 0$, because in the Mindlin assusption, $U = U(x, y)$, $V = V(x, y)$. So, only θ_x,θ_y, W are included in the transverse part. Note that $\varepsilon_z = \frac{\partial W}{\partial z}$ is considered as a infinitesimal amount compared with other strain components. Therefore, the nodes' displacement in transverse part is:

$$q_m^e = \begin{bmatrix} W_1 & \theta_{x1} & \theta_{y1} & W_2 & \theta_{x2} & \theta_{y2} & W_3 & \theta_{x3} & \theta_{y3} & W_4 & \theta_{x4} & \theta_{y4} \end{bmatrix}^T \tag{A.31}$$

The transverse displacement field is:

$$U_s = z\theta_y(\xi, \eta) = z \sum_{i=1}^{4} N_i \theta_{yi} \tag{A.32a}$$

$$V_s = -z\theta_x(\xi, \eta) = -z \sum_{i=1}^{4} N_i \theta_{xi} \tag{A.32b}$$

$$W_s = W(\xi, \eta) = \sum_{i=1}^{4} N_i W_i - \sum_{i=1}^{4} L_i \theta_{xi} - \sum_{i=1}^{4} M_i \theta_{yi} \tag{A.32c}$$

Note that the detailed derivation of W_s is explained in:

An improved treatment of transverse shear in the mindlin-type four-node quadrilateral element

Four-node 'flat' shell element: Drilling degrees of freedom, membrane-bending coupling, warped geometry, and behaviour

So, interpolation result of displacement:

$$\begin{bmatrix} W_s \\ V_s \\ U_s \end{bmatrix} = \begin{bmatrix} W(\xi,\eta) \\ -z\theta_x(\xi,\eta) \\ z\theta_y(\xi,\eta) \end{bmatrix} = \begin{bmatrix} N_1 & -L_1 & -M_1 & \cdots & N_4 & -L_4 & -M_4 \\ 0 & -zN_1 & 0 & \cdots & 0 & -zN_4 & 0 \\ 0 & 0 & zN_1 & \cdots & 0 & 0 & zN_4 \end{bmatrix} q_s^e \tag{A.33}$$

According to geometric equation (3D):

$$\begin{bmatrix} \gamma_{xzs} \\ \gamma_{yzs} \end{bmatrix} = \begin{bmatrix} \frac{\partial}{\partial x} & 0 & \frac{\partial}{\partial z} \\ \frac{\partial}{\partial y} & \frac{\partial}{\partial z} & 0 \end{bmatrix} \begin{bmatrix} W(\xi,\eta) \\ -z\theta_x(\xi,\eta) \\ z\theta_y(\xi,\eta) \end{bmatrix} \tag{A.34}$$

The strain field can be expressed as:

$$\begin{bmatrix} \gamma_{xzs} \\ \gamma_{yzs} \end{bmatrix} = \begin{bmatrix} \frac{\partial}{\partial x} & 0 & \frac{\partial}{\partial z} \\ \frac{\partial}{\partial y} & \frac{\partial}{\partial z} & 0 \end{bmatrix} \begin{bmatrix} N_1 & -L_1 & -M_1 & \cdots & N_4 & -L_4 & -M_4 \\ 0 & -zN_1 & 0 & \cdots & 0 & -zN_4 & 0 \\ 0 & 0 & zN_1 & \cdots & 0 & 0 & zN_4 \end{bmatrix} q_s^e \tag{A.35}$$

This can be expressed as:

$$\begin{bmatrix} \gamma_{xzs} \\ \gamma_{yzs} \end{bmatrix} = \begin{bmatrix} \frac{\partial N_1}{\partial x} & -\frac{\partial L_1}{\partial x} & -\frac{\partial M_1}{\partial x} + N_1 & & & \\ \frac{\partial N_1}{\partial y} & -\frac{\partial L_1}{\partial y} - N_1 & -\frac{\partial M_1}{\partial y} & B_{s2} & B_{s3} & B_{s4} \end{bmatrix} q_s^e = \begin{bmatrix} B_{s1} & B_{s2} & B_{s3} & B_{s4} \end{bmatrix} = B_s q_s^e \tag{A.36}$$

Coordinate transformation

Since the B_m, B_b, B_s mentioned above contain terms such as $\frac{\partial N_i}{\partial x}$ and $\frac{\partial N_i}{\partial y}$ (i = 1,2,3,4,5,6,7,8). This can be calculated by Coordinate transformation.

Set:

$$x(\xi,\eta) = a_0 + a_1\xi + a_2\eta + a_3\xi\eta \tag{A.37a}$$

$$y(\xi,\eta) = b_0 + b_1\xi + b_2\eta + b_3\xi\eta \tag{A.37b}$$

As same as Equation A.19, A.20, A.21, A.22, A.23, the transformation relation between xoy and $\eta o\xi$ are expressed as Equation A.38.

$$x(\xi,\eta) = [N_1, N_2, N_3, N_4]\begin{bmatrix} x_1 & x_2 & x_3 & x_4 \end{bmatrix}^T \tag{A.38a}$$

$$y(\xi,\eta) = [N_1, N_2, N_3, N_4]\begin{bmatrix} y_1 & y_2 & y_3 & y_4 \end{bmatrix}^T \tag{A.38b}$$

According to compound function derivative rule:

$$\frac{\partial N_i}{\partial \xi} = \frac{\partial N_i}{\partial x}\frac{\partial x}{\partial \xi} + \frac{\partial N_i}{\partial y}\frac{\partial y}{\partial \xi} \tag{A.39a}$$

$$\frac{\partial N_i}{\partial \eta} = \frac{\partial N_i}{\partial x}\frac{\partial x}{\partial \eta} + \frac{\partial N_i}{\partial y}\frac{\partial y}{\partial \eta} \tag{A.39b}$$

The Equation A.39 can be expressed as:

$$\begin{bmatrix} \frac{\partial N_i}{\partial \xi} \\ \frac{\partial N_i}{\partial \eta} \end{bmatrix} = \begin{bmatrix} \frac{\partial x}{\partial \xi} & \frac{\partial y}{\partial \xi} \\ \frac{\partial x}{\partial \eta} & \frac{\partial y}{\partial \eta} \end{bmatrix} \begin{bmatrix} \frac{\partial N_i}{\partial x} \\ \frac{\partial N_i}{\partial y} \end{bmatrix} = J \begin{bmatrix} \frac{\partial N_i}{\partial x} \\ \frac{\partial N_i}{\partial y} \end{bmatrix} \tag{A.40}$$

J is called Jacobian matrix. According to Equation A.38, the Jacobian matrix is expressed as:

$$J = \begin{bmatrix} \partial \sum_{i=1}^{4} N_i x_i/\partial\xi & \partial \sum_{i=1}^{4} N_i y_i/\partial\xi \\ \partial \sum_{i=1}^{4} N_i x_i/\partial\eta & \partial \sum_{i=1}^{4} N_i y_i/\partial\eta \end{bmatrix} = \begin{bmatrix} \sum_{i=1}^{4} \partial N_i x_i/\partial\xi & \sum_{i=1}^{4} \partial N_i y_i/\partial\xi \\ \sum_{i=1}^{4} \partial N_i x_i/\partial\eta & \sum_{i=1}^{4} \partial N_i y_i/\partial\eta \end{bmatrix} \tag{A.41}$$

Therefore, the terms such as $\frac{\partial N_i}{\partial x}$ and $\frac{\partial N_i}{\partial y}$ (i = 1,2,3,4,5,6,7,8) can be calculated as:

$$\begin{bmatrix} \partial N_i/\partial x \\ \partial N_i/\partial y \end{bmatrix} = J^{-1} \begin{bmatrix} \partial N_i/\partial\xi \\ \partial N_i/\partial\eta \end{bmatrix} \quad i = 1,2,3,4,5,6,7,8 \tag{A.42}$$

According to the Equation A.1, the results of $\begin{bmatrix} \frac{\partial N_i}{\partial\xi} & \frac{\partial N_i}{\partial\eta} \end{bmatrix}^T \quad i = 1,2,3,4,5,6,7,8$ is calculated as:

$$\frac{\partial N_1}{\partial\xi} = -\frac{1}{4}(1-\eta) \quad \frac{\partial N_1}{\partial\eta} = -\frac{1}{4}(1-\xi) \tag{A.43a}$$

$$\frac{\partial N_2}{\partial\xi} = \frac{1}{4}(1-\eta) \quad \frac{\partial N_2}{\partial\eta} = -\frac{1}{4}(1+\xi) \tag{A.43b}$$

$$\frac{\partial N_3}{\partial\xi} = \frac{1}{4}(1+\eta) \quad \frac{\partial N_3}{\partial\eta} = \frac{1}{4}(1+\xi) \tag{A.43c}$$

$$\frac{\partial N_4}{\partial\xi} = -\frac{1}{4}(1+\eta) \quad \frac{\partial N_4}{\partial\eta} = \frac{1}{4}(1-\xi) \tag{A.43d}$$

$$\frac{\partial N_5}{\partial\xi} = -\frac{1}{8}\xi(1-\eta) \quad \frac{\partial N_5}{\partial\eta} = -\frac{1}{16}(1-\xi^2) \tag{A.43e}$$

$$\frac{\partial N_6}{\partial\xi} = \frac{1}{16}(1-\eta^2) \quad \frac{\partial N_6}{\partial\eta} = -\frac{1}{8}\eta(1-\xi) \tag{A.43f}$$

$$\frac{\partial N_7}{\partial\xi} = -\frac{1}{8}\xi(1+\eta) \quad \frac{\partial N_7}{\partial\eta} = \frac{1}{16}(1-\xi^2) \tag{A.43g}$$

$$\frac{\partial N_8}{\partial\xi} = -\frac{1}{16}(1-\xi^2) \quad \frac{\partial N_8}{\partial\eta} = -\frac{1}{8}\eta(1-\xi) \tag{A.43h}$$

Therefore, according to Equation A.2 and A.43, the terms includ $\begin{bmatrix} \frac{\partial L_i}{\partial\xi} & \frac{\partial L_i}{\partial\eta} \end{bmatrix}^T$ and $\begin{bmatrix} \frac{\partial M_i}{\partial\xi} & \frac{\partial M_i}{\partial\eta} \end{bmatrix}^T \quad i = 1,2,3,4$ are calculated as:

$$\begin{aligned}
\begin{bmatrix} \frac{\partial L_1}{\partial \xi} \\ \frac{\partial L_1}{\partial \eta} \end{bmatrix} &= \begin{bmatrix} (y_1 - y_4)\frac{\partial N_8}{\partial \xi} - (y_2 - y_1)\frac{\partial N_5}{\partial \xi} \\ (y_1 - y_4)\frac{\partial N_8}{\partial \eta} - (y_2 - y_1)\frac{\partial N_5}{\partial \eta} \end{bmatrix} \\
&= (y_1 - y_4) \begin{bmatrix} \frac{\partial N_8}{\partial \xi} \\ \frac{\partial N_8}{\partial \eta} \end{bmatrix} - (y_2 - y_1) \begin{bmatrix} \frac{\partial N_5}{\partial \xi} \\ \frac{\partial N_5}{\partial \eta} \end{bmatrix} \\
&= (y_1 - y_4)J^{-1} \begin{bmatrix} \frac{\partial N_8}{\partial \xi} \\ \frac{\partial N_8}{\partial \eta} \end{bmatrix} - (y_2 - y_1)J^{-1} \begin{bmatrix} \frac{\partial N_5}{\partial \xi} \\ \frac{\partial N_5}{\partial \eta} \end{bmatrix} \\
&= (y_1 - y_4)J^{-1} \begin{bmatrix} -\frac{1}{16}(1 - \xi^2) \\ -\frac{1}{8}\eta(1 - \xi) \end{bmatrix} - (y_2 - y_1)J^{-1} \begin{bmatrix} -\frac{1}{8}\xi(1 - \eta) \\ -\frac{1}{16}(1 - \xi^2) \end{bmatrix}
\end{aligned} \tag{A.44}$$

ALL the results are summarized in Equation A.45:

$$\begin{bmatrix} \frac{\partial L_2}{\partial \xi} \\ \frac{\partial L_2}{\partial \eta} \end{bmatrix} = (y_2 - y_1)J^{-1} \begin{bmatrix} -\frac{1}{8}\xi(1 - \eta) \\ -\frac{1}{16}(1 - \xi^2) \end{bmatrix} - (y_3 - y_2)J^{-1} \begin{bmatrix} \frac{1}{16}(1 - \eta^2) \\ -\frac{1}{8}\eta(1 - \xi) \end{bmatrix} \tag{A.45a}$$

$$\begin{bmatrix} \frac{\partial L_3}{\partial \xi} \\ \frac{\partial L_3}{\partial \eta} \end{bmatrix} = (y_3 - y_2)J^{-1} \begin{bmatrix} \frac{1}{16}(1 - \eta^2) \\ -\frac{1}{8}\eta(1 - \xi) \end{bmatrix} - (y_4 - y_3)J^{-1} \begin{bmatrix} -\frac{1}{8}\xi(1 + \eta) \\ \frac{1}{16}(1 - \xi^2) \end{bmatrix} \tag{A.45b}$$

$$\begin{bmatrix} \frac{\partial L_4}{\partial \xi} \\ \frac{\partial L_4}{\partial \eta} \end{bmatrix} = (y_4 - y_3)J^{-1} \begin{bmatrix} -\frac{1}{8}\xi(1 + \eta) \\ \frac{1}{16}(1 - \xi^2) \end{bmatrix} - (y_1 - y_4)J^{-1} \begin{bmatrix} -\frac{1}{16}(1 - \xi^2) \\ -\frac{1}{8}\eta(1 - \xi) \end{bmatrix} \tag{A.45c}$$

$$\begin{bmatrix} \frac{\partial M_1}{\partial \xi} \\ \frac{\partial M_1}{\partial \eta} \end{bmatrix} = (y_4 - y_1)J^{-1} \begin{bmatrix} -\frac{1}{16}(1 - \xi^2) \\ -\frac{1}{8}\eta(1 - \xi) \end{bmatrix} - (y_1 - y_2)J^{-1} \begin{bmatrix} -\frac{1}{8}\xi(1 - \eta) \\ -\frac{1}{16}(1 - \xi^2) \end{bmatrix} \tag{A.45d}$$

$$\begin{bmatrix} \frac{\partial M_2}{\partial \xi} \\ \frac{\partial M_2}{\partial \eta} \end{bmatrix} = (y_1 - y_2)J^{-1} \begin{bmatrix} -\frac{1}{8}\xi(1 - \eta) \\ -\frac{1}{16}(1 - \xi^2) \end{bmatrix} - (y_2 - y_3)J^{-1} \begin{bmatrix} \frac{1}{16}(1 - \eta^2) \\ -\frac{1}{8}\eta(1 - \xi) \end{bmatrix} \tag{A.45e}$$

$$\begin{bmatrix} \frac{\partial M_3}{\partial \xi} \\ \frac{\partial M_3}{\partial \eta} \end{bmatrix} = (y_2 - y_3)J^{-1} \begin{bmatrix} \frac{1}{16}(1 - \eta^2) \\ -\frac{1}{8}\eta(1 - \xi) \end{bmatrix} - (y_3 - y_4)J^{-1} \begin{bmatrix} -\frac{1}{8}\xi(1 + \eta) \\ \frac{1}{16}(1 - \xi^2) \end{bmatrix} \tag{A.45f}$$

$$\begin{bmatrix} \frac{\partial M_4}{\partial \xi} \\ \frac{\partial M_4}{\partial \eta} \end{bmatrix} = (y_3 - y_4)J^{-1} \begin{bmatrix} -\frac{1}{8}\xi(1+\eta) \\ \frac{1}{16}(1-\xi^2) \end{bmatrix} - (y_4 - y_1)J^{-1} \begin{bmatrix} -\frac{1}{16}(1-\xi^2) \\ -\frac{1}{8}\eta(1-\xi) \end{bmatrix} \tag{A.45g}$$

The differential relationship is expressed as follows:

$$dV^e = 2hdA^e = 2hdxdy = 2h|J|d\xi d\eta \tag{A.46}$$

A.2.3 Variational Principle

Matrix assembly

Set the nodes displacement information of iQS4 element is:

$$q^e = \begin{bmatrix} U_1 & V_1 & W_1 & \theta_{x1} & \theta_{y1} & \theta_{Z1} & \cdots & U_4 & V_4 & W_4 & \theta_{x4} & \theta_{y4} & \theta_{Z4} \end{bmatrix}^T \tag{A.47}$$

The q^e has the relationship with q_m^e, q_b^e,q_s^e as follows:

$$q^e(1,2,6,7,8,12,13,14,18,19,20,24) = q_m^e \tag{A.48a}$$

$$q^e(4,5,10,11,16,17,22,23) = q_b^e \tag{A.48b}$$

$$q^e(3,4,5,9,10,11,15,16,17,21,22,23) = q_s^e \tag{A.48c}$$

Based on these relationships, the strain field of membrane, bending, and transverse part are expressed by node displacement of iQS4 element as follows:

$$\varepsilon_m = B_m q_m^e = B_m^e q^e = \begin{bmatrix} \frac{\partial N_1}{\partial x} & 0 & 0 & 0 & 0 & \frac{\partial L_1}{\partial x} & & & \\ 0 & \frac{\partial N_1}{\partial y} & 0 & 0 & 0 & \frac{\partial M_1}{\partial y} & B_{m2}^e & B_{m3}^e & B_{m4}^e \\ \frac{\partial N_1}{\partial y} & \frac{\partial N_1}{\partial x} & 0 & 0 & 0 & \frac{\partial L_1}{\partial y} + \frac{\partial M_1}{\partial x} & & & \end{bmatrix} q^e \tag{A.49a}$$

$$\varepsilon_b = zB_b q_b^e = zB_b^e q^e = z\begin{bmatrix} 0 & 0 & 0 & 0 & \frac{\partial N_1}{\partial x} & 0 & & & \\ 0 & 0 & 0 & -\frac{\partial N_1}{\partial y} & 0 & 0 & B_{b2}^e & B_{b3}^e & B_{b4}^e \\ 0 & 0 & 0 & -\frac{\partial N_1}{\partial x} & \frac{\partial N_1}{\partial y} & 0 & & & \end{bmatrix} q^e \tag{A.49b}$$

$$\varepsilon_s = B_s q_s^e = B_s^e q^e = \begin{bmatrix} 0 & 0 & \frac{\partial N_1}{\partial x} & -\frac{\partial L_1}{\partial x} & -\frac{\partial M_1}{\partial x} + N_1 & 0 & & & \\ 0 & 0 & \frac{\partial N_1}{\partial y} & -\frac{\partial L_1}{\partial y} - N_1 & -\frac{\partial M_1}{\partial y} & 0 & B_{s2}^e & B_{s3}^e & B_{s4}^e \end{bmatrix} q^e \tag{A.49c}$$

Set:

$$\varepsilon_m = B_m^e q^e = e(q^e) \quad \varepsilon_b = zB_b^e q^e = zk(q^e) \quad \varepsilon_s = B_s^e q^e = g(q^e) \tag{A.50}$$

Therefore,

$$\begin{bmatrix} \varepsilon_x \\ \varepsilon_y \\ \gamma_{xy} \end{bmatrix} = e(q^e) + zk(q^e) \tag{A.51a}$$

$$\begin{bmatrix} \gamma_{xz} \\ \gamma_{yz} \end{bmatrix} = g(q^e) \tag{A.51b}$$

Experiment Data

The measurement data from experiment for the iQS4 element is list below:

$$e_\varepsilon = \frac{1}{2}\begin{bmatrix} \varepsilon_{xx}^+ + \varepsilon_{xx}^- \\ \varepsilon_{yy}^+ + \varepsilon_{yy}^- \\ \gamma_{xy}^+ + \gamma_{xy}^- \end{bmatrix} \tag{A.52}$$

The bending curvatures are calculated as:

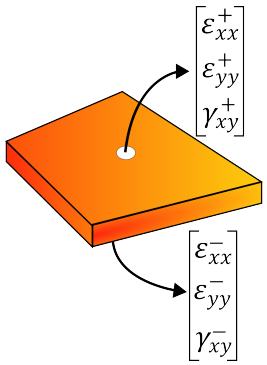


Figure A.2: The isoparametric coordinate system

$$k_{\varepsilon} = \frac{1}{2h} \begin{bmatrix} \varepsilon_{xx}^{+} - \varepsilon_{xx}^{-} \\ \varepsilon_{yy}^{+} - \varepsilon_{yy}^{-} \\ \gamma_{xy}^{+} - \gamma_{xy}^{-} \end{bmatrix} \tag{A.53}$$

The transverse strain is not able to directly calculate according to the measurements data. If want to calculate this part (g_{ε}), use Smoothing Element Analysis method. However, in the deformation of thin shell, the contributions of g_{ε} are much smaller than e_{ε} and k_{ε}. Therefore, the contributions of g_{ε} are safely omitted.

Weighted least-squares function

Define the function as follows to minimum the difference between real strain field and hypothetical strain field:

$$\Phi^{e} = \omega_{m}\|e(q^{e}) - e_{\varepsilon}\|^{2} + \omega_{k}\|k(q^{e}) - k_{\varepsilon}\|^{2} + \omega_{g}\|\mathrm{g}(q^{e})\|^{2} \tag{A.54}$$

Where ω_{m} ,ω_{k} , ω_{g} is the constant coefficient. For example, if g_{ε} is unavailable, the coefficient ω_{g} is set very small (usually $\leq 10^{-4}$) to omit the influence of transverse load (thin shell). For the situation that we can obtain e_{ε} and k_{ε}, the coefficient is set as 1. Therefore, the norms shown in Equation A.54 is expressed in Equation A.55:

$$\|e(q^e) - e_\varepsilon\|^2 = \iiint_{V^e} [e(q^e) - e_\varepsilon]^2 d_{V_e} = \frac{1}{A^e} \iint_{A^e} [e(q^e) - e_\varepsilon]^2 \, |J| d_\xi \, d_\eta \tag{A.55a}$$

$$\|k(q^e) - k_\varepsilon\|^2 = \iiint_{V^e} [k(q^e) - k_\varepsilon]^2 d_{V_e} = \frac{(2h)^2}{A^e} \iint_{A^e} [k(q^e) - k_\varepsilon]^2 \, |J| d_\xi \, d_\eta \tag{A.55b}$$

$$\|\mathrm{g}(q^e)|^2 = \iiint_{V^e} [g(q^e)]^2 d_{V_e} = \frac{1}{A^e} \iint_{A^e} [g(q^e)]^2 \, |J| d_\xi \, d_\eta \tag{A.55c}$$

Therefore, the least square functional is expressed as:

$$\begin{aligned} \Phi^e &= \frac{\omega_m}{A^e} \int_{A^e} (e(q^e) - e_e)^2 dA^e + \omega_b \frac{(2h)^2}{A^e} \int_{A^e} (k(q^e) - k_\varepsilon)^2 dA^e + \frac{\omega_s}{A^e} \int_{A^e} (g(q^e) - g_\varepsilon)^2 dA^e \\ &= \frac{1}{A^e} \int_{A^e} [\omega_m (B_m^e q^e - e_\varepsilon)^2 + \omega_b (2h)^2 (B_b^e q^e - k_\varepsilon)^2 + \omega_s (B_s^e q^e - g_\varepsilon)^2] dA^e \end{aligned} \tag{A.56}$$

In Equation A.56,

$$\begin{aligned} (B_m^e q^e - e_\varepsilon)^2 &= (B_m^e q^e - e_\varepsilon)^T (B_m^e q^e - e_\varepsilon) = [(q^e)^T (B_m^e)^T - (e_\varepsilon)^T](B_m^e q^e - e_\varepsilon) \\ &= (q^e)^T (B_m^e)^T B_m^e q^e - (q^e)^T (B_m^e)^T e_\varepsilon - (e_\varepsilon)^T B_m^e q^e + (e_\varepsilon)^T e_\varepsilon \end{aligned} \tag{A.57a}$$

$$\begin{aligned} (B_b^e q^e - k_\varepsilon)^2 &= (B_b^e q^e - k_\varepsilon)^T (B_b^e q^e - k_\varepsilon) = [(q^e)^T (B_b^e)^T - (k_\varepsilon)^T](B_b^e q^e - k_\varepsilon) \\ &= (q^e)^T (B_b^e)^T B_b^e q^e - (q^e)^T (B_b^e)^T k_\varepsilon - (k_\varepsilon)^T B_b^e q^e + (k_\varepsilon)^T k_\varepsilon \end{aligned} \tag{A.57b}$$

$$\begin{aligned} (B_s^e q^e - g_\varepsilon)^2 &= (B_s^e q^e - g_\varepsilon)^T (B_s^e q^e - g_\varepsilon) = [(q^e)^T (B_s^e)^T - (g_\varepsilon)^T](B_s^e q^e - g_\varepsilon) \\ &= (q^e)^T (B_s^e)^T B_s^e q^e - (q^e)^T (B_s^e)^T g_\varepsilon - (g_\varepsilon)^T B_s^e q^e + (g_\varepsilon)^T g_\varepsilon \end{aligned} \tag{A.57c}$$

Therefore,

$$\begin{aligned}\Phi^e = \frac{1}{A^e}\int_{A^e}\{&\omega_m[(q^e)^T(B_m^e)^T B_m^e q^e - (q^e)^T(B_m^e)^T e_\varepsilon - (e_\varepsilon)^T B_m^e q^e + (e_\varepsilon)^T e_\varepsilon] \\ &+ \omega_b(2h)^2[(q^e)^T(B_b^e)^T B_b^e q^e - (q^e)^T(B_b^e)^T k_\varepsilon - (k_\varepsilon)^T B_b^e q^e + (k_\varepsilon)^T k_\varepsilon] \\ &+ \omega_s[(q^e)^T(B_s^e)^T B_s^e q^e - (q^e)^T(B_s^e)^T g_\varepsilon - (g_\varepsilon)^T B_s^e q^e + (g_\varepsilon)^T g_\varepsilon]\}dA^e\end{aligned} \tag{A.58}$$

variation

We hope to find a displacement field that can minimum the difference between real strain field and hypothetical strain field, which means,

$$\frac{\partial \Phi^e}{\partial q^e} = 0 \tag{A.59}$$

This can be expressed as:

$$\begin{aligned}\frac{\partial \Phi^e}{\partial q^e} = \frac{2}{A^e}\int_{A^e}&\{\omega_m[(B_m^e)^T B_m^e q^e - (B_m^e)^T e_\varepsilon] + \omega_b(2h)^2[(B_b^e)^T B_b^e q^e - (B_b^e)^T k_\varepsilon] \\ &+ \omega_s[(B_s^e)^T B_s^e q^e - (B_s^e)^T g_\varepsilon]\}dA^e = 0\end{aligned} \tag{A.60}$$

which is:

$$\begin{aligned}&\int_{A^e}[\omega_m(B_m^e)^T B_m^e + \omega_b(2h)^2(B_b^e)^T B_b^e + \omega_s(B_s^e)^T B_s^e]dA^e \cdot q^e \\ &\qquad = \int_{A^e}\left[\omega_m(B_m^e)^T e_\varepsilon + \omega_b(2h)^2(B_b^e)^T k_\varepsilon + \omega_s(B_s^e)^T g_\varepsilon\right]dA^e\end{aligned} \tag{A.61}$$

So, the equation is written as:

$$K^e q^e = f^e \varepsilon^e \tag{A.62}$$

In this equation,

$$K^e = \int_{A^e} [\omega_m (B_m^e)^T B_m^e + \omega_b (2h)^2 (B_b^e)^T B_b^e + \omega_s (B_s^e)^T B_s^e] dA^e \tag{A.63a}$$

$$f^e = \left[\int_{A^e} [\omega_m (B_m^e)^T] dA^e \quad \int_{A^e} [\omega_b (2h)^2 (B_b^e)^T] dA^e \quad \int_{A^e} [\omega_s (B_s^e)^T] dA^e \right] \tag{A.63b}$$

$$\varepsilon^e = \begin{bmatrix} e_\varepsilon \\ k_\varepsilon \\ g_\varepsilon \end{bmatrix} \tag{A.63c}$$

A.2.4 Numerical integration

In order to calculate the integration in K^e and f^e, the numerical integration method is adopted.

1D situation

Method 1: Newton-cotes integration

For definite integral,

$$\int_{-1}^{1} f(\xi) d\xi \quad \xi \in [-1, 1] \tag{A.64}$$

Construct a polynomial$\Phi(\xi)$ makes that in ξ_1, ξ_2,$\cdots$,ξ_n:

$$\varphi(\xi_i) = f(\xi_i) \quad i = 1, 2, \cdots, n \tag{A.65}$$

Therefore,

$$\int_{-1}^{1} f(\xi) d\xi \approx \int_{-1}^{1} \varphi(\xi) d\xi \tag{A.66}$$

The polynomial $\Phi(\xi)$ is constructed by Lagrange interpolation:

$$\varphi(\xi) = c_0 + c_1\xi + \cdots + c_{n-1}\xi^{n-1} = \sum_{i=1}^{n} l_i(\xi) f(\xi_i) \tag{A.67a}$$

$$l_i(\xi) = \frac{(\xi-\xi_1)(\xi-\xi_2)\cdots(\xi-\xi_{i-1})(\xi-\xi_{i+1})\cdots(\xi-\xi_n)}{(\xi_i-\xi_1)(\xi_i-\xi_1)\cdots(\xi_i-\xi_{i-1})(\xi_i-\xi_{i+1})\cdots(\xi_i-\xi_n)} \quad i = 1, 2, \cdots n \tag{A.67b}$$

For $l_i(\xi)$,

$$l_i(\xi) = \begin{cases} 1 & \xi = \xi_i \\ 0 & \xi \neq \xi_i \end{cases} \quad i = 1, 2, \cdots n \tag{A.68}$$

$\Phi(\xi)$ is a polynomial with a degree of n-1. So,

$$\int_{-1}^{1} f(\xi)d\xi \approx \int_{-1}^{1} \varphi(\xi)d\xi = \int_{-1}^{1} \sum_{i=1}^{n} l_i(\xi) f(\xi_i)d\xi = \sum_{i=1}^{n} A_i f(\xi_i) \tag{A.69}$$

In this equation,

$$A_i = \int_{-1}^{1} l_i(\xi)d\xi \tag{A.70}$$

A_i is called weight. Convert the integral to a weighted sum based on known points.

Method 2: Gauss integration

Gauss integration has better resolution than former method. For the definite integral shown in Equation A.64, a polynomial $\Phi(\xi)$ is constructed to satisfy Equation A.65 and Equation A.66 as follows (in this equation, β_i is constant coefficient):

$$\varphi(\xi) = c_0 + c_1\xi + \cdots + c_{2n-1}\xi^{2n-1} = \sum_{i=1}^{n} l_i(\xi) f(\xi_i) + \sum_{i=0}^{n-1} \beta_i \xi^i P(\xi) \tag{A.71}$$

The $l_i(\xi)$ and $P(\xi)$ is expressed as follows:

$$l_i(\xi) = \frac{(\xi-\xi_1)(\xi-\xi_2)\cdots(\xi-\xi_{i-1})(\xi-\xi_{i+1})\cdots(\xi-\xi_n)}{(\xi_i-\xi_1)(\xi_i-\xi_1)\cdots(\xi_i-\xi_{i-1})(\xi_i-\xi_{i+1})\cdots(\xi_i-\xi_n)} \quad i=1,2,\cdots n \tag{A.72a}$$

$$P(\xi) = (\xi-\xi_1)(\xi-\xi_2)\cdots(\xi-\xi_n) \tag{A.72b}$$

Therefore,

$$l_i(\xi) = \begin{cases} 1 & \xi = \xi_i \\ 0 & \xi \neq \xi_i \end{cases} \quad i=1,2,\cdots n \tag{A.73}$$

$$P(\xi_i) = 0 \quad i=1,2,\cdots n \tag{A.74a}$$

$$\int_{-1}^{1} \xi^i P(\xi) d\xi = 0 \quad i=0,1,\cdots n-1 \tag{A.74b}$$

This means $P(\xi)$ andξ^i are orthogonal in [-1,1].$\Phi(\xi)$ is a polynomial with a degree of 2n-1. So,

$$\begin{aligned} \int_{-1}^{1} f(\xi)\, d\xi \approx \int_{-1}^{1} \varphi(\xi) d\xi &= \int_{-1}^{1} \left[\sum_{i=1}^{n} l_i(\xi) f(\xi_i) + \sum_{i=0}^{n-1} \beta_i \xi^i P(\xi) \right] d\xi \\ &= \sum_{i=1}^{n} A_i f(\xi_i) + \sum_{i=0}^{n-1} \int_{-1}^{1} \beta_i \xi^i P(\xi) d\xi = \sum_{i=1}^{n} A_i f(\xi_i) + 0 = \sum_{i=1}^{n} A_i f(\xi_i) \end{aligned} \tag{A.75}$$

The expression of A_i is same as Equation A.70. It converts the integral to a weighted sum based on known points.

For example, one point Gauss integration: n=1

$$\begin{aligned} \int_{-1}^{1} f(\xi) d\xi \approx \int_{-1}^{1} \varphi(\xi) d\xi &= \int_{-1}^{1} \left[l_1(\xi) f(\xi_1) + \beta_0 \xi^0 (\xi - \xi_1) \right] d\xi \\ &= 2f(\xi_1) + \beta_0 (\frac{1}{2}\xi^2 - \xi_1 \xi) \Big|_{-1}^{1} = 2f(\xi_1) - 2\beta_0 \xi_1 \end{aligned} \tag{A.76}$$

So, $\xi_1 = 0$,A_1=2, which means,

$$\int_{-1}^{1} f(\xi)d\xi \approx 2f(0) \tag{A.77}$$

Two points Gauss integration: n=2

$$\begin{aligned}
\int_{-1}^{1} f(\xi)d\xi \approx \int_{-1}^{1} \varphi(\xi)d\xi &= \int_{-1}^{1} \left[\sum_{i=1}^{2} l_i(\xi)f(\xi_i) + \sum_{i=0}^{1} \beta_i \xi^i P(\xi)\right] d\xi \\
&= \sum_{i=1}^{2} \int_{-1}^{1} l_i(\xi)d\xi f(\xi_i) + \sum_{i=0}^{1} \beta_i \int_{-1}^{1} \xi^i P(\xi)d\xi \\
&= \int_{-1}^{1} l_1(\xi)d\xi f(\xi_1) + \int_{-1}^{1} l_2(\xi)d\xi f(\xi_2) + \beta_0 \int_{-1}^{1} P(\xi)d\xi + \beta_1 \int_{-1}^{1} \xi^1 P(\xi)d\xi \\
&= \int_{-1}^{1} \frac{(\xi-\xi_2)}{(\xi_1-\xi_2)}d\xi f(\xi_1) + \int_{-1}^{1} \frac{(\xi-\xi_1)}{(\xi_2-\xi_1)}d\xi f(\xi_2) + \beta_0 \int_{-1}^{1} (\xi-\xi_1)(\xi-\xi_2)d\xi \\
&\quad + \beta_1 \int_{-1}^{1} \xi(\xi-\xi_1)(\xi-\xi_2)d\xi \\
&= f(\xi_1)\left[\frac{1}{(\xi_1-\xi_2)}(\frac{1}{2}\xi^2)\Big|_{-1}^{1} + \frac{(-\xi_2)}{(\xi_1-\xi_2)}\xi\Big|_{-1}^{1}\right] + f(\xi_2)\left[\frac{1}{(\xi_2-\xi_1)}(\frac{1}{2}\xi^2)\Big|_{-1}^{1} + \frac{(-\xi_1)}{(\xi_2-\xi_1)}\xi\Big|_{-1}^{1}\right] \\
&\quad + \beta_0\left(\frac{1}{3}\xi^3 - \frac{1}{2}(\xi_1+\xi_2)\xi^2 + \xi_1\xi_2\xi)\Big|_{-1}^{1} + \beta_1\,(\frac{1}{4}\xi^4 - \frac{1}{3}(\xi_1+\xi_2)\xi^3 + \frac{1}{2}\xi_1\xi_2\xi^2)\Big|_{-1}^{1}\right. \\
&= f(\xi_1)\Big[0 + \frac{-2\xi_2}{(\xi_1-\xi_2)}\Big] + f(\xi_2)\Big[0 + \frac{-2\xi_1}{(\xi_2-\xi_1)}\Big] + \beta_0(\frac{2}{3} - 0 + 2\xi_1\xi_2) + \beta_1(0 - \frac{2}{3}(\xi_1+\xi_2) + 0)
\end{aligned}$$

$$= \frac{-2\xi_2}{(\xi_1-\xi_2)}f(\xi_1) - \frac{2\xi_1}{(\xi_2-\xi_1)}f(\xi_2) + \beta_0(\frac{2}{3} + 2\xi_1\xi_2) + \frac{2}{3}\beta_1(\xi_1+\xi_2)$$

$$= A_1 f(\xi_1) + A_2 f(\xi_2) + \beta_0(\frac{2}{3} + 2\xi_1\xi_2) + \frac{2}{3}\beta_1(\xi_1+\xi_2) \tag{A.78}$$

Where,

$$A_1 = \frac{-2\xi_2}{(\xi_1-\xi_2)} \tag{A.79a}$$

$$A_2 = \frac{-2\xi_1}{(\xi_2 - \xi_1)} \tag{A.79b}$$

$$\frac{2}{3} + 2\xi_1\xi_2 = 0 \tag{A.79c}$$

$$\xi_2 + \xi_1 = 0 \tag{A.79d}$$

According to the equation set expressed in Equation A.79, the parameters can be obtained as follows:

$$\xi_1 = \pm\frac{1}{\sqrt{3}} \quad \xi_2 = \mp\frac{1}{\sqrt{3}} \quad A_1 = 1 \quad A_2 = 1 \tag{A.80}$$

This means:

$$\int_{-1}^{1} f(\xi)d\xi \approx \int_{-1}^{1} \varphi(\xi)d\xi = f\left(-\frac{1}{\sqrt{3}}\right) + f(\frac{1}{\sqrt{3}}) \tag{A.81}$$

2D Gauss integration

According to the results presented in Equation A.77, the results of 2D Gauss integration with n=1 is expressed as:

$$\int_{-1}^{1}\int_{-1}^{1} f(\xi,\eta)d\xi d\eta = \int_{-1}^{1} A_{\xi 1} f(\xi_1,\eta)d\eta = A_{\xi 1}A_{\eta 1} f(\xi_1,\eta_1) = 2 \times 2f(0,0) = 4f(0,0) \tag{A.82}$$

According to the results presented in Equation A.81, the results of 2D Gauss integration with n=2 is expressed as:

$$\int_{-1}^{1}\int_{-1}^{1} f(\xi,\eta)d\xi d\eta = \int_{-1}^{1}[A_{\xi 1}f(\xi_1,\eta)+A_{\xi 2}f(\xi_2,\eta)]d\eta \tag{A.83}$$

$$=A_{\xi 1}[A_{\eta 1}f(\xi_1,\eta_1)+A_{\eta 2}f(\xi_1,\eta_2)]+A_{\xi 2}[A_{\eta 1}f(\xi_2,\eta_1)+A_{\eta 2}f(\xi_2,\eta_2)]$$

Here we adopt$A_{\xi 1}=A_{\xi 2}=A_{\eta 1}=A_{\eta 2}=1$,$\xi_1=-1/\sqrt{3},\xi_2=1/\sqrt{3},\eta_1=-1/\sqrt{3},\eta_2=1/\sqrt{3}$ shown in 1D Gauss integration results (Equation A.80).Therefore, the numerical integration results are expressed as:

$$\int_{-1}^{1}\int_{-1}^{1} f(\xi,\eta)d\xi d\eta = f\left(-\frac{1}{\sqrt{3}},-\frac{1}{\sqrt{3}}\right)+f\left(-\frac{1}{\sqrt{3}},\frac{1}{\sqrt{3}}\right)+f\left(\frac{1}{\sqrt{3}},-\frac{1}{\sqrt{3}}\right)+f\left(\frac{1}{\sqrt{3}},\frac{1}{\sqrt{3}}\right) \tag{A.84}$$

Numerical integration in iFEM

Therefore, for the K^e and f^e expressed in Equation A.63 can be calculated by 2D Gauss integration when n=2. Take the first term of K^e as example:

$$\int_{\mathbf{A}^e}\omega_m(B_m^e)^T B_m^e d\mathbf{A}^e = \omega_m\int_{-1}^{1}\int_{-1}^{1}(B_m^e)^T B_m^e d\xi d\eta = \omega_m\int_{-1}^{1}\int_{-1}^{1}(B_m^e)^T d\xi d\eta\int_{-1}^{1}\int_{-1}^{1}B_m^e d\xi d\eta \tag{A.85}$$

According to Equation A.49,

$$\int_{-1}^{1}\int_{-1}^{1}B_m^e d\xi d\eta = \int_{-1}^{1}\int_{-1}^{1}\begin{bmatrix}\frac{\partial N_1}{\partial x} & 0 & 0 & 0 & 0 & \frac{\partial L_1}{\partial x} & & & \\ 0 & \frac{\partial N_1}{\partial y} & 0 & 0 & 0 & \frac{\partial M_1}{\partial y} & B_{m2}^e & B_{m3}^e & B_{m4}^e \\ \frac{\partial N_1}{\partial y} & \frac{\partial N_1}{\partial x} & 0 & 0 & 0 & \frac{\partial L_1}{\partial y}+\frac{\partial M_1}{\partial x} & & & \end{bmatrix} d\xi d\eta \tag{A.86}$$

According to results shown in Equation A.42, we can set:

$$\begin{bmatrix} f_{N_i}(\xi,\eta) \\ g_{N_i}(\xi,\eta) \end{bmatrix} = \begin{bmatrix} \frac{\partial N_i}{\partial x} \\ \frac{\partial N_i}{\partial y} \end{bmatrix} = J^{-1} \begin{bmatrix} \frac{\partial N_i}{\partial \xi} \\ \frac{\partial N_i}{\partial \eta} \end{bmatrix} \quad i = 1, 2, \cdots, 8 \tag{A.87a}$$

$$\begin{bmatrix} k_{N_i}(\xi,\eta) \\ l_{N_i}(\xi,\eta) \end{bmatrix} = \begin{bmatrix} \frac{\partial L_i}{\partial x} \\ \frac{\partial L_i}{\partial y} \end{bmatrix} \quad i = 1, 2, 3, 4 \tag{A.87b}$$

$$\begin{bmatrix} p_{N_i}(\xi,\eta) \\ q_{N_i}(\xi,\eta) \end{bmatrix} = \begin{bmatrix} \frac{\partial M_i}{\partial x} \\ \frac{\partial M_i}{\partial y} \end{bmatrix} \tag{A.87c}$$

Therefore,take the first term of the matrix in Equation A.86 as an example:

$$\begin{aligned} \int_{-1}^{1}\int_{-1}^{1} \frac{\partial N_i}{\partial x} d\xi d\eta &= \int_{-1}^{1}\int_{-1}^{1} f_{N_i}(\xi,\eta) d\xi d\eta \\ &= f_{N_i}(GP_1) + f_{N_i}(GP_2) + f_{N_i}(GP_3) + f_{N_i}(GP_4) = \sum_{i=1}^{4} f_{N_i}(GP_i) \end{aligned} \tag{A.88}$$

In Equation A.88, GP_1, GP_2, GP_3, GP_4 express Gauss Points.

$$GP_1 = \left(-\frac{1}{\sqrt{3}}, -\frac{1}{\sqrt{3}}\right), GP_2 = \left(-\frac{1}{\sqrt{3}}, \frac{1}{\sqrt{3}}\right), GP_3 = \left(\frac{1}{\sqrt{3}}, -\frac{1}{\sqrt{3}}\right), GP_4 = \left(\frac{1}{\sqrt{3}}, \frac{1}{\sqrt{3}}\right) \tag{A.89}$$

Therefore, the Equation A.86 can be expressed as:

$$\int_{-1}^{1}\int_{-1}^{1} B_m^e d\xi d\eta =$$
$$\begin{bmatrix} \sum_{i=1}^{4} f_{N_1}(GP_i) & 0 & 0 & 0 & 0 & \sum_{i=1}^{4} k_{N_1}(GP_i) & & & \\ 0 & \sum_{i=1}^{4} g_{N_1}(GP_i) & 0 & 0 & 0 & \sum_{i=1}^{4} p_{N_1}(GP_i) & \int B_{m2}^e & \int B_{m3}^e & \int B_{m4}^e \\ \sum_{i=1}^{4} g_{N_1}(GP_i) & \sum_{i=1}^{4} f_{N_1}(GP_i) & 0 & 0 & 0 & \sum_{i=1}^{4}[q_{N_1}(GP_i) + l_{N_1}(GP_i)] & & & \end{bmatrix} \tag{A.90}$$

Therefore, all definite integral list below can be calculated:

$$\begin{array}{lll} \int_{-1}^{1}\int_{-1}^{1} B_m^e d\xi d\eta & \int_{-1}^{1}\int_{-1}^{1} B_b^e d\xi d\eta & \int_{-1}^{1}\int_{-1}^{1} B_s^e d\xi d\eta \\ \int_{-1}^{1}\int_{-1}^{1} B_m^{eT} d\xi d\eta & \int_{-1}^{1}\int_{-1}^{1} B_b^{eT} d\xi d\eta & \int_{-1}^{1}\int_{-1}^{1} B_s^{eT} d\xi d\eta \end{array} \tag{A.91}$$

Therefore, the K^e and f^e can be calculated by by 2D Gauss integration when n=2.

A.2.5 Structure/global stiffness matrix

The structure has m elements, n nodes. For each element, according to Equation A.62, the expression of global structure is shown as:

$$Kq = F\varepsilon \tag{A.92}$$

The global displacement fields and experiment measurement can be expressed as:

$$q = \begin{bmatrix} U_1 & V_1 & W_1 & \theta_{x1} & \theta_{y1} & \theta_{Z1} & \cdots & U_n & V_n & W_n & \theta_{xn} & \theta_{yn} & \theta_{Zn} \end{bmatrix}^T \tag{A.93a}$$

$$\varepsilon = \begin{bmatrix} (\varepsilon^{+}_{xx1} + \varepsilon^{-}_{xx1})/2 \\ (\varepsilon^{+}_{yy1} + \varepsilon^{-}_{yy1})/2 \\ (\gamma^{+}_{xy1} + \gamma^{-}_{xy1})/2 \\ (\varepsilon^{+}_{xx1} - \varepsilon^{-}_{xx1})/2h \\ (\varepsilon^{+}_{yy1} - \varepsilon^{-}_{yy1})/2h \\ (\gamma^{+}_{xy1} - \gamma_{xy1})/2h \\ 0 \\ 0 \\ \vdots \\ (\varepsilon^{+}_{xxm} + \varepsilon^{-}_{xxm})/2 \\ (\varepsilon^{+}_{yym} + \varepsilon^{-}_{yym})/2 \\ (\gamma^{+}_{xym} + \gamma^{+}_{xym})/2 \\ (\varepsilon^{+}_{xxm} - \varepsilon^{-}_{xxm})/2h \\ (\varepsilon^{+}_{yym} - \varepsilon^{-}_{yym})/2h \\ (V^{+}_{xym} - \gamma_{xym})/2h \\ 0 \\ 0 \end{bmatrix} \tag{A.93b}$$

Note that the transverse strain is not able to directly calculate according to the measurements data. And in the deformation of thin shell, the contributions of g_ε are much smaller than k_ε and e_ε. Therefore, the contributions of g_ε are safely omitted. So, correlation components are set to 0.

The degrees of freedom (DOF) of q is $6n \times 1$. The degrees of freedom (DOF) of ε is $8m \times 1$. Therefore, the DOF of K is $6n \times 6n$. The DOF of F is $6n \times 8m$.

For example, the $i-th(i \in [1, m])$ finite element have four nodes $c_1, c_2, c_3, c_4 \quad (c_1, 2, 3, 4 \in [1, n])$. The DOF of q^e is 24×1, the DOF of ε^e is 8×1. Therefore, the displacement fields and experiment measurement of this element is expressed as:

$$q^e = \begin{bmatrix} U_{c_1} & V_{c_1} & W_{c_1} & \theta_{xc_1} & \theta_{yc_1} & \theta_{Zc_1} & \cdots & U_{c_4} & V_{c_4} & W_{c_4} & \theta_{xc_4} & \theta_{yc_4} & \theta_{Zc_4} \end{bmatrix}^T \tag{A.94a}$$

$$\varepsilon^e = \begin{bmatrix} (\varepsilon^+_{xxi} + \varepsilon^-_{xxi})/2 \\ (\varepsilon^+_{yyi} + \varepsilon^-_{yyi})/2 \\ (\gamma^+_{xyi} + \gamma^-_{xyi})/2 \\ (\varepsilon^+_{xxi} - \varepsilon^-_{xxi})/2h \\ (\varepsilon^+_{yyi} - \varepsilon^-_{yyi})/2h \\ (\gamma^+_{xyi} - \gamma_{xyi})/2h \\ 0 \\ 0 \end{bmatrix} \tag{A.94b}$$

The correspondence between q^e and q is $q(I_1) = q^e$, where the I_1 is expressed in Equation A.95.

$$I_1 = \begin{bmatrix} 6c_1 - 5 \\ 6c_1 - 4 \\ 6c_1 - 3 \\ 6c_1 - 3 \\ 6c_1 - 2 \\ 6c_1 - 1 \\ 6c_1 - 1 \\ \vdots \\ 6c_4 - 5 \\ 6c_4 - 4 \\ 6c_4 - 3 \\ 6c_4 - 2 \\ 6c_4 - 1 \\ 6c_4 - 1 \\ 6c_4 - 1 \end{bmatrix} \qquad I_2 = \begin{bmatrix} 8i - 7 \\ 8i - 6 \\ 8i - 5 \\ 8i - 4 \\ 8i - 3 \\ 8i - 2 \\ 8i - 1 \\ 8i \end{bmatrix} \tag{A.95}$$

In addition, the correspondence between ε^e and ε is $\varepsilon(I_2) = \varepsilon^e$, where the I_2 is expressed in Equation A.95.

Therefore, the assembly of K^e and f^e of the $i-th(i \in [1,m])$ finite element can be realized according to the correspondence shown in Equation A.96.

$$K(I_1^T, I_1^T) = K^e \tag{A.96a}$$

$$F(I_1^T, I_2^T) = f^e \tag{A.96b}$$

A.2.6 Solution of iFEM

When K, F, and ε is obtained and combined with displacement boundary conditions, the displacement field can be calculated according to Equation A.92.

Method 1: When the all boundary displacements are zero, set $r-th$ row and column as 0, $K_{rr} = 1$, $F\varepsilon_r = 0$ ($r = [r_1, r_2, \cdots, r_j]$ is the set of boundary nodes). As shown in Equation A.97. This operation equal to set $q_r = 0$, which is exactly the zero boundary conditions.

$$\begin{bmatrix} \cdots & 0 & \cdots \\ 0 & 1 & 0 \\ \cdots & 0 & \cdots \end{bmatrix} \begin{bmatrix} \vdots \\ q_r \\ \vdots \end{bmatrix} = \begin{bmatrix} \vdots \\ 0 \\ \vdots \end{bmatrix} \tag{A.97}$$

Method 2: When there is some nodes have a constant displacement boundary condition, which means $q_r = u$, set $r-th$ row and column as a very large number, which expressed as: $K_{rr} = \alpha K_{rr}$, $F\varepsilon_r = \alpha K_{rr} u$ ($r = [r_1, r_2, \cdots, r_j]$ is the set of boundary nodes). As shown in Equation A.98.This operation equal to set $\alpha K_{rr} u(q_r) = \alpha K_{rr} u$, which is exactly the constant boundary conditions.

$$\begin{bmatrix} \dots & \dots & \dots \\ \dots & \alpha K_{rr} & \dots \\ \dots & \dots & \dots \end{bmatrix} \begin{bmatrix} \vdots \\ \overline{q_r} \\ \vdots \end{bmatrix} = \begin{bmatrix} \vdots \\ \alpha K_{rr} \overline{u} \\ \vdots \end{bmatrix} \tag{A.98a}$$

$$\alpha \geq \max(K) \cdot 10^4 \tag{A.98b}$$

Bibliography

[1] A. AIRBUS, "A380 aircraft characteristics airport and maintenance planning," 2020.

[2] Y. Pang, G. Wu, H. Wang, D. Gao, and P. Zhang, "Bond-slip model of the cfrp-steel interface with the cfrp delamination failure," *Composite Structures*, vol. 256, p. 113015, 2021.

[3] Q. Wei, L. Zhu, J. Zhu, L. Zhuo, W. Hao, and W. Xie, "Characterization of impact fatigue damage in cfrp composites using nonlinear acoustic resonance method," *Composite Structures*, vol. 253, p. 112804, 2020.

[4] C. Wu, X.-L. Zhao, R. Al-Mahaidi, M. R. Emdad, and W. Duan, "Fatigue tests of cracked steel plates strengthened with uhm cfrp plates," *Advances in Structural Engineering*, vol. 15, no. 10, pp. 1801–1815, 2012.

[5] C. Barile, C. Casavola, P. K. Vimalathithan, M. Pugliese, and V. Maiorano, "Thermomechanical and morphological studies of cfrp tested in different environmental conditions," *Materials*, vol. 12, no. 1, p. 63, 2018.

[6] S.-Y. Cho and J.-R. Lee, "Investigation of manufacturing defects in 3d-printed cfrp using laser ultrasonic testing and x-ray micro-computed tomography," *Functional Composites and Structures*, vol. 3, no. 2, p. 025005, 2021.

[7] J. Jayaprakash, A. A. A. Samad, A. A. Abbasovich, and A. A. A. Ali, "Repair of precracked rc rectangular shear beams using cfrp strip technique," *Structural Engineering and Mechanics: An International Journal*, vol. 26, no. 4, pp. 427–439, 2007.

[8] T. Inagaki, T. Ishii, and T. Iwamoto, "On the ndt and e for the diagnosis of defects using infrared thermography," *NDT & E International*, vol. 32, no. 5, pp. 247–257, 1999.

[9] Z. Fang, W. Hu, R. Wang, and S. Chen, "Application of hyperspectral ct technology combined with machine learning in recognition of plastic components," *NDT & E International*, vol. 102, pp. 287–294, 2019.

[10] Z. Liu, J. Gao, H. Xie, and P. Wallace, "Ndt capability of digital shearography for different materials," *Optics and Lasers in Engineering*, vol. 49, no. 12, pp. 1462–1469, 2011.

[11] S. Liu, Y. Sun, M. Gu, C. Liu, L. He, and Y. Kang, "Review and analysis of three representative electromagnetic ndt methods," *Insight-Non-Destructive Testing and Condition Monitoring*, vol. 59, no. 4, pp. 176–183, 2017.

[12] G. Webb, P. J. Vardanega, and C. R. Middleton, "Categories of shm deployments: technologies and capabilities," *Journal of Bridge Engineering*, vol. 20, no. 11, p. 04014118, 2015.

[13] F. J. Carrión, J. A. Quintana, and S. E. Crespo, "Techno-economical and practical considerations for shm systems," *Journal of Civil Structural Health Monitoring*, vol. 7, no. 2, pp. 207–215, 2017.

[14] F. Ren, I. N. Giannakeas, Z. S. Khodaei, and M. F. Aliabadi, "Theoretical and experimental investigation of guided wave temperature compensation for composite structures with different thicknesses," *Mechanical Systems and Signal Processing*, vol. 200, p. 110594, 2023.

[15] S. Goossens, T. Geernaert, Z. S. Khodaei, E. Karachalios, D. Saenz-Castillo, and F. Berghmans, "Barely visible impact damage detection and location on composite materials by surface-mounted and embedded aerospace-compatible optical fibre bragg grating sensors," in *Optical Sensing and Detection VI*, vol. 11354, pp. 64–76, SPIE, 2020.

[16] E. Lizé, M. Rébillat, N. Mechbal, and C. Bolzmacher, "Optimal dual-pzt sizing and network design for baseline-free shm of complex anisotropic composite structures," *Smart Materials and Structures*, vol. 27, no. 11, p. 115018, 2018.

[17] S. Goossens, F. Berghmans, Z. S. Khodaei, F. Lambinet, E. Karachalios, D. Saenz-Castillo, and T. Geernaert, "Practicalities of bvid detection on aerospace-grade cfrp materials with optical fibre sensors," *Composite Structures*, vol. 259, p. 113243, 2021.

[18] X. Chen, S. Guo, J. Li, G. Zhang, M. Lu, and Y. Shi, "Flexible piezoelectric nanofiber composite membranes as high performance acoustic emission sensors," *Sensors and Actuators A: Physical*, vol. 199, pp. 372–378, 2013.

[19] J. Dos Reis, C. Oliveira Costa, and J. Sá da Costa, "Strain gauges debonding fault detection for structural health monitoring," *Structural Control and Health Monitoring*, vol. 25, no. 12, p. e2264, 2018.

[20] B. L. Grisso and D. J. Inman, "Temperature corrected sensor diagnostics for impedance-based shm," *Journal of Sound and Vibration*, vol. 329, no. 12, pp. 2323–2336, 2010.

[21] S. Kavitha, R. J. Daniel, and K. Sumangala, "High performance mems accelerometers for concrete shm applications and comparison with cots accelerometers," *Mechanical Systems and Signal Processing*, vol. 66, pp. 410–424, 2016.

[22] M. Gkantou, M. Muradov, G. S. Kamaris, K. Hashim, W. Atherton, and P. Kot, "Novel electromagnetic sensors embedded in reinforced concrete beams for crack detection," *Sensors*, vol. 19, no. 23, p. 5175, 2019.

[23] D. G. Bekas, Z. Sharif-Khodaei, and F. M. Aliabadi, "A smart multi-functional printed sensor for monitoring curing and damage of composite repair patch," *Smart Materials and Structures*, vol. 28, no. 8, p. 085029, 2019.

[24] C. Xu and Z. Sharif Khodaei, "A novel fabry-pérot optical sensor for guided wave signal acquisition," *Sensors*, vol. 20, no. 6, p. 1728, 2020.

[25] R. Cao, Y. Yang, M. Wang, X. Yi, J. Wu, S. Huang, and K. P. Chen, "Multiplexable intrinsic fabry–perot interferometric fiber sensors for multipoint hydrogen gas monitoring," *Optics Letters*, vol. 45, no. 11, pp. 3163–3166, 2020.

[26] S. J. Mihailov, "Fiber bragg grating sensors for harsh environments," *Sensors*, vol. 12, no. 2, pp. 1898–1918, 2012.

[27] D. Wada, H. Igawa, M. Tamayama, T. Kasai, H. Arizono, and H. Murayama, "Flight demonstration of aircraft wing monitoring using optical fiber distributed sensing system," *Smart Materials and Structures*, vol. 28, no. 5, p. 055007, 2019.

[28] P. Zhu, X. Xie, X. Sun, and M. A. Soto, "Distributed modular temperature-strain sensor based on optical fiber embedded in laminated composites," *Composites Part B: Engineering*, vol. 168, pp. 267–273, 2019.

[29] P. Mindermann, M. G. Pérez, N. Kamimura, J. Knippers, and G. T. Gresser, "Implementation of fiber-optical sensors into coreless filament-wound composite structures," *Composite Structures*, vol. 290, p. 115558, 2022.

[30] S. F. Hassan, S. Kundurthi, S. H. Vattathurvalappil, G. Cloud, and M. Haq, "A hybrid experimental and numerical technique for evaluating residual strains/stresses in bonded lap joints," *Composites Part B: Engineering*, vol. 225, p. 109216, 2021.

[31] M. Esposito, M. Gherlone, and P. Marzocca, "External loads identification and shape sensing on an aluminum wing box: An integrated approach," *Aerospace Science and Technology*, vol. 114, p. 106743, 2021.

[32] K. Speck, F. Vogdt, M. Curbach, and Y. Petryna, "Fiber optic sensors for continuous strain measurement in concrete," *BETON-UND STAHLBETONBAU*, vol. 114, no. 3, pp. 160–167, 2019.

[33] T. Jiang, L. Ren, Z.-g. Jia, D.-s. Li, and H.-n. Li, "Pipeline internal corrosion monitoring based on distributed strain measurement technique," *Structural Control and Health Monitoring*, vol. 24, no. 11, p. e2016, 2017.

[34] S. Jiang, L. Ma, X. Fan, B. Wang, and Z. He, "Real-time locating and speed measurement of fibre fuse using optical frequency-domain reflectometry," *Scientific Reports*, vol. 6, no. 1, p. 25585, 2016.

[35] F. Parent, M. Gérard, F. Monet, S. Loranger, G. Soulez, R. Kashyap, and S. Kadoury, "Intra-arterial image guidance with optical frequency domain reflectometry shape sensing," *IEEE Transactions on Medical Imaging*, vol. 38, no. 2, pp. 482–492, 2018.

[36] H. Nguyen, P. Y. Peng, D. Luss, and M. P. Harold, "Assessing intrusion by the capillary during spatially resolved mass spectrometry measurement," *Chemical Engineering Journal*, vol. 307, pp. 845–859, 2017.

[37] S. Rizzolo, E. Marin, A. Boukenter, Y. Ouerdane, M. Cannas, J. Périsse, S. Bauer, J.-R. Mace, C. Marcandella, P. Paillet, *et al.*, "Radiation hardened optical frequency domain reflectometry distributed temperature fiber-based sensors," *IEEE Transactions on Nuclear Science*, vol. 62, no. 6, pp. 2988–2994, 2015.

[38] S. Cola, L. Schenato, L. Brezzi, F. C. Tchamaleu Pangop, L. Palmieri, and A. Bisson, "Composite anchors for slope stabilisation: Monitoring of their in-situ behaviour with optical fibre," *Geosciences*, vol. 9, no. 5, p. 240, 2019.

[39] J. Sierra-Pérez, M. A. Torres-Arredondo, and A. Güemes, "Damage and nonlinearities detection in wind turbine blades based on strain field pattern recognition. fbgs, obr and strain gauges comparison," *Composite Structures*, vol. 135, pp. 156–166, 2016.

[40] C. V. Raman, "A new radiation," *Indian Journal of Physics*, vol. 2, pp. 387–398, 1928.

[41] L. Brillouin, "Diffusion de la lumière et des rayons x par un corps transparent homogène," in *Annales de Physique*, vol. 9, pp. 88–122, 1922.

[42] L. Rayleigh, "X. on the electromagnetic theory of light," *The London, Edinburgh, and Dublin Philosophical Magazine and Journal of Science*, vol. 12, no. 73, pp. 81–101, 1881.

[43] J. Cui, S. Zhao, D. Yang, and Z. Ding, "Investigation of the interpolation method to improve the distributed strain measurement accuracy in optical frequency domain reflectometry systems," *Applied Optics*, vol. 57, no. 6, pp. 1424–1431, 2018.

[44] S. Zhao, J. Cui, Z. Wu, and J. Tan, "Accuracy improvement in ofdr-based distributed sensing system by image processing," *Optics and Lasers in Engineering*, vol. 124, p. 105824, 2020.

[45] J. Zhang, P. Wei, and Q. Liu, "Monitoring a heatsink temperature field using raman-based distributed temperature sensor in a vacuum and- 173 c environment," *Sensors*, vol. 19, no. 19, p. 4186, 2019.

[46] A. Minardo, E. Catalano, A. Coscetta, G. Zeni, C. Di Maio, R. Vassallo, L. Picarelli, R. Coviello, G. Macchia, and L. Zeni, "Long-term monitoring of a tunnel in a landslide prone area by brillouin-based distributed optical fiber sensors," *Sensors*, vol. 21, no. 21, p. 7032, 2021.

[47] D. Wada, H. Igawa, M. Tamayama, T. Kasai, H. Arizono, H. Murayama, N. Isoda, and M. Katsuta, "Fiber-optic simultaneous distributed monitoring of strain and temperature for an aircraft wing during flight," *Applied Optics*, vol. 57, no. 36, pp. 10458–10465, 2018.

[48] N. Boujia, F. Schmidt, C. Chevalier, D. Siegert, and D. Pham Van Bang, "Distributed optical fiber-based approach for soil–structure interaction," *Sensors*, vol. 20, no. 1, p. 321, 2020.

[49] X. Sun, Y. Du, W. Liao, H. Ma, and J. Huang, "Measuring the heterogeneity of cement paste by truly distributed optical fiber sensors," *Construction and Building Materials*, vol. 225, pp. 765–771, 2019.

[50] N. A. A. Rahim, N. Mirabile, M. Chiani, and L. Briançon, "Millimeter-resolution distributed strain sensing of concrete structures," in *Seventh European Workshop on Optical Fibre Sensors*, vol. 11199, pp. 399–402, SPIE, 2019.

[51] Y.-S. Kwon, D.-C. Seo, B.-H. Choi, M. Y. Jeon, and I.-B. Kwon, "Strain measurement distributed on a ground anchor bearing plate by fiber optic ofdr sensor," *Applied Sciences*, vol. 8, no. 11, p. 2051, 2018.

[52] L. Gao, Y. Gong, H. Liu, B. Ji, Y. Xuan, and Y. Ma, "Experiment and numerical study on deformation measurement of cast-in-place concrete large-diameter pipe pile using optical frequency domain reflectometer technology," *Applied Sciences*, vol. 8, no. 9, p. 1450, 2018.

[53] K. Bremer, L. S. Alwis, F. Weigand, M. Kuhne, Y. Zheng, M. Krüger, R. Helbig, and B. Roth, "Evaluating the performance of functionalized carbon structures with integrated optical fiber sensors under practical conditions," *Sensors*, vol. 18, no. 11, p. 3923, 2018.

[54] S. Bersan, O. Bergamo, L. Palmieri, L. Schenato, and P. Simonini, "Distributed strain measurements in a cfa pile using high spatial resolution fibre optic sensors," *Engineering Structures*, vol. 160, pp. 554–565, 2018.

[55] A. Barrias, J. R. Casas, and S. Villalba, "Embedded distributed optical fiber sensors in reinforced concrete structures—a case study," *Sensors*, vol. 18, no. 4, p. 980, 2018.

[56] P. Lu, M. P. Buric, K. Byerly, S. R. Moon, M. Nazmunnahar, S. Simizu, A. M. Leary, R. B. Beddingfield, C. Sun, P. Zandhuis, *et al.*, "Real-time monitoring of temperature rises of energized transformer cores with distributed optical fiber sensors," *IEEE Transactions on Power Delivery*, vol. 34, no. 4, pp. 1588–1598, 2019.

[57] L. Ren, T. Jiang, Z.-g. Jia, D.-s. Li, C.-l. Yuan, and H.-n. Li, "Pipeline corrosion and leakage monitoring based on the distributed optical fiber sensing technology," *Measurement*, vol. 122, pp. 57–65, 2018.

[58] R. Chen, M. A. Zaghloul, A. Yan, S. Li, G. Lu, B. C. Ames, N. Zolfaghari, A. P. Bunger, M.-J. Li, and K. P. Chen, "High resolution monitoring of strain fields in concrete during hydraulic fracturing processes," *Optics Express*, vol. 24, no. 4, pp. 3894–3902, 2016.

[59] Z. Ding, C. Wang, K. Liu, Y. Liu, G. Xu, J. Jiang, Y. Guo, and T. Liu, "Distributed measurements of external force induced local birefringence in spun highly birefringent optical fibers using polarimetric ofdr," *Optics Express*, vol. 27, no. 2, pp. 951–964, 2019.

[60] Z. Li, P. Wei, and T. Liu, "A novel method for length of chirped fiber bragg grating sensor," in *Young Scientists Forum 2017*, vol. 10710, pp. 427–435, SPIE, 2018.

[61] Z. Ding, K. Sun, K. Liu, J. Jiang, D. Yang, Z. Yu, J. Li, and T. Liu, "Distributed refractive index sensing based on tapered fibers in optical frequency domain reflectometry," *Optics Express*, vol. 26, no. 10, pp. 13042–13054, 2018.

[62] P.-Y. Peng, M. P. Harold, and D. Luss, "Oscillations and hysteresis during hydrocarbon oxidation on a diesel oxidation catalyst: Predictive model," *Chemical Engineering Journal*, vol. 355, pp. 661–670, 2019.

[63] H. Nguyen, M. P. Harold, and D. Luss, "Spatiotemporal behavior of pt/rh/ceo2/bao catalyst during lean–rich cycling," *Chemical Engineering Journal*, vol. 262, pp. 464–477, 2015.

[64] H. Nguyen, M. P. Harold, and D. Luss, "Optical frequency domain reflectometry measurements of spatio-temporal temperature inside catalytic reactors: Applied to study wrong-way behavior," *Chemical Engineering Journal*, vol. 234, pp. 312–317, 2013.

[65] M. A. Zaghloul, A. Yan, R. Chen, M.-J. Li, R. Flammang, M. Heibel, and K. P. Chen, "High spatial resolution radiation detection using distributed fiber sensing technique," *IEEE Transactions on Nuclear Science*, vol. 64, no. 9, pp. 2569–2577, 2017.

[66] S. Rizzolo, A. Boukenter, E. Marin, T. Robin, M. Cannas, A. Morana, J. Périsse, J.-R. Macé, Y. Ouerdane, B. Nacir, *et al.*, "Evaluation of distributed ofdr-based sensing performance in mixed neutron/gamma radiation environments," *IEEE Transactions on Nuclear Science*, vol. 64, no. 1, pp. 61–67, 2016.

[67] A. Faustov, A. Gusarov, P. Mégret, M. Wuilpart, A. Zhukov, S. Novikov, V. Svetukhin, and A. Fotiadi, "Application of phosphate doped fibers for ofdr dosimetry," *Results in Physics*, vol. 6, pp. 86–87, 2016.

[68] F. Jiang, G. Zhidong, L. Zengshan, and W. Xiaodong, "A method of predicting visual detectability of low-velocity impact damage in composite structures based on logistic regression model," *Chinese Journal of Aeronautics*, vol. 34, no. 1, pp. 296–308, 2021.

[69] M. Badar, H. Kobayashi, and K. Iwashita, "Spatial resolution improvement in ofdr using four wave mixing and dsb-sc modulation," *IEEE Photonics Technology Letters*, vol. 28, no. 15, pp. 1680–1683, 2016.

[70] S. Zhao, J. Cui, and J. Tan, "Nonlinearity correction in ofdr system using a zero-crossing detection-based clock and self-reference," *Sensors*, vol. 19, no. 17, p. 3660, 2019.

[71] B. Wang, X. Fan, S. Wang, G. Yang, Q. Liu, and Z. He, "Laser phase noise compensation in long-range ofdr by using an optical fiber delay loop," *Optics Communications*, vol. 365, pp. 220–224, 2016.

[72] K. Feng, J. Cui, H. Dang, X. Sun, D. Jiang, Y. Jin, Y. Niu, and X. Zhang, "Investigation of a signal demodulation method based on wavelet transformation for ofdr to enhance its distributed sensing performance," *Sensors*, vol. 19, no. 13, p. 2850, 2019.

[73] D. Arbel and A. Eyal, "Ofdr with double interrogation for dynamic quasi-distributed sensing," *Optics Express*, vol. 22, no. 3, pp. 2299–2308, 2014.

[74] L. Shiloh and A. Eyal, "Sinusoidal frequency scan ofdr with fast processing algorithm for distributed acoustic sensing," *Optics Express*, vol. 25, no. 16, pp. 19205–19215, 2017.

[75] C. Crunelle, M. Legré, M. Wuilpart, P. Mégret, and N. Gisin, "Distributed temperature sensor interrogator based on polarization-sensitive reflectometry," *IEEE Sensors Journal*, vol. 9, no. 9, pp. 1125–1129, 2009.

[76] K. T. Wan, C. K. Leung, and N. G. Olson, "Investigation of the strain transfer for surface-attached optical fiber strain sensors," *Smart materials and structures*, vol. 17, no. 3, p. 035037, 2008.

[77] S. Zhao, J. Cui, L. Suo, Z. Wu, D.-P. Zhou, and J. Tan, "Performance investigation of ofdr sensing system with a wide strain measurement range," *Journal of Lightwave Technology*, vol. 37, no. 15, pp. 3721–3727, 2019.

[78] J. Li, J. Du, S. Wang, L. Li, L. Sun, X. Fan, Q. Liu, and Z. He, "Improving the spatial resolution of an ofdr based on recirculating frequency shifter," *IEEE Photonics Journal*, vol. 7, no. 5, pp. 1–10, 2015.

[79] L. Sun, J. Du, L. Li, and Z. He, "High order ssb modulation and its application for advanced optical comb generation based on rfs," *Optics Communications*, vol. 354, pp. 380–385, 2015.

[80] B. Wang, X. Fan, S. Wang, J. Du, and Z. He, "Millimeter-resolution long-range ofdr using ultra-linearly 100 ghz-swept optical source realized by injection-locking technique and cascaded fwm process," *Optics Express*, vol. 25, no. 4, pp. 3514–3524, 2017.

[81] X. Fan, Y. Koshikiya, and F. Ito, "Centimeter-level spatial resolution over 40 km realized by bandwidth-division phase-noise-compensated ofdr," *Optics Express*, vol. 19, no. 20, pp. 19122–19128, 2011.

[82] N. Riesen, T. T.-Y. Lam, and J. H. Chow, "Bandwidth-division in digitally enhanced optical frequency domain reflectometry," *Optics Express*, vol. 21, no. 4, pp. 4017–4026, 2013.

[83] N. Riesen, T. T. Lam, and J. H. Chow, "Resolving the range ambiguity in ofdr using digital signal processing," *Measurement Science and Technology*, vol. 25, no. 12, p. 125102, 2014.

[84] D. A. Shaddock, "Digitally enhanced heterodyne interferometry," *Optics Letters*, vol. 32, no. 22, pp. 3355–3357, 2007.

[85] Q. Liu, X. Fan, and Z. He, "Time-gated digital optical frequency domain reflectometry with 1.6-m spatial resolution over entire 110-km range," *Optics Express*, vol. 23, no. 20, pp. 25988–25995, 2015.

[86] L. Shiloh, R. Giryes, and A. Eyal, "Utilizing the sparsity of quasi-distributed sensing systems for sub-nyquist signal reconstruction," in *Seventh European Workshop on Optical Fibre Sensors*, vol. 11199, pp. 371–374, SPIE, 2019.

[87] M. Badar, P. Lu, M. Buric, and P. R. Ohodnicki Jr, "Self-correction of nonlinear sweep of tunable laser source in ofdr," in *Fiber Optic Sensors and Applications XVI*, vol. 11000, pp. 14–19, SPIE, 2019.

[88] Y. Koshikiya, X. Fan, F. Ito, Z. He, and K. Hotate, "High resolution pnc-ofdr with suppressed fading noise for dispersive media measurement," *Journal of Lightwave Technology*, vol. 31, no. 6, pp. 866–873, 2013.

[89] F. Ito, X. Fan, and Y. Koshikiya, "Long-range coherent ofdr with light source phase noise compensation," *Journal of Lightwave Technology*, vol. 30, no. 8, pp. 1015–1024, 2011.

[90] B. J. Soller, D. K. Gifford, M. S. Wolfe, and M. E. Froggatt, "High resolution optical frequency domain reflectometry for characterization of components and assemblies," *Optics Express*, vol. 13, no. 2, pp. 666–674, 2005.

[91] K. Yüksel, M. Wuilpart, and P. Mégret, "Analysis and suppression of nonlinear frequency modulation in an optical frequency-domain reflectometer," *Optics Express*, vol. 17, no. 7, pp. 5845–5851, 2009.

[92] Z. Ding, T. Liu, Z. Meng, K. Liu, Q. Chen, Y. Du, D. Li, and X. S. Yao, "Note: Improving spatial resolution of optical frequency-domain reflectometry against frequency tuning nonlinearity using non-uniform fast fourier transform," *Review of Scientific Instruments*, vol. 83, no. 6, p. 066110, 2012.

[93] K. Zhang and J. U. Kang, "Graphics processing unit accelerated non-uniform fast fourier transform for ultrahigh-speed, real-time fourier-domain oct," *Optics Express*, vol. 18, no. 22, pp. 23472–23487, 2010.

[94] S. Vergnole, D. Lévesque, and G. Lamouche, "Experimental validation of an optimized signal processing method to handle non-linearity in swept-source optical coherence tomography," *Optics Express*, vol. 18, no. 10, pp. 10446–10461, 2010.

[95] Z. Ding, X. S. Yao, T. Liu, Y. Du, K. Liu, J. Jiang, Z. Meng, and H. Chen, "Compensation of laser frequency tuning nonlinearity of a long range ofdr using deskew filter," *Optics Express*, vol. 21, no. 3, pp. 3826–3834, 2013.

[96] Y. Du, T. Liu, Z. Ding, B. Feng, X. Li, K. Liu, and J. Jiang, "Method for improving spatial resolution and amplitude by optimized deskew filter in long-range ofdr," *IEEE Photonics Journal*, vol. 6, no. 5, pp. 1–11, 2014.

[97] J. Song, W. Li, P. Lu, Y. Xu, L. Chen, and X. Bao, "Long-range high spatial resolution distributed temperature and strain sensing based on optical frequency-domain reflectometry," *IEEE Photonics Journal*, vol. 6, no. 3, pp. 1–8, 2014.

[98] J. Xing, Y. Zhang, F. Wang, K. Feng, Y. Zhang, Z. Yan, and X. Zhang, "A method based on time-scale factor for correcting the nonlinear frequency sweeping in an ofdr system," *IEEE Photonics Journal*, vol. 11, no. 3, pp. 1–8, 2019.

[99] R. M. Manuel and H. Sutherland, "Signal conditioning for compensating nonlinearity and nonrepeatability of an optical frequency scanning laser implemented in a c-ofdr system," *Applied Optics*, vol. 56, no. 3, pp. 457–461, 2017.

[100] W. Xie, Q. Zhou, F. Bretenaker, Z. Xia, H. Shi, J. Qin, Y. Dong, and W. Hu, "Fourier transform-limited optical frequency-modulated continuous-wave interferometry over several tens of laser coherence lengths," *Optics Letters*, vol. 41, no. 13, pp. 2962–2965, 2016.

[101] J. Qin, L. Zhang, W. Xie, R. Cheng, Z. Liu, W. Wei, and Y. Dong, "Ultra-long range optical frequency domain reflectometry using a coherence-enhanced highly linear frequency-swept fiber laser source," *Optics Express*, vol. 27, no. 14, pp. 19359–19368, 2019.

[102] C. Baker, Y. Lu, J. Song, and X. Bao, "Incoherent optical frequency domain reflectometry based on a kerr phase-interrogator," *Optics Express*, vol. 22, no. 13, pp. 15370–15375, 2014.

[103] D. Arbel and A. Eyal, "Dynamic optical frequency domain reflectometry," *Optics Express*, vol. 22, no. 8, pp. 8823–8830, 2014.

[104] E. Leviatan and A. Eyal, "High resolution das via sinusoidal frequency scan ofdr (sfs-ofdr)," *Optics Express*, vol. 23, no. 26, pp. 33318–33334, 2015.

[105] L. Shiloh and A. Eyal, "Fast sinusoidal frequency scan ofdr for long distance distributed acoustic sensing," in *2017 25th Optical Fiber Sensors Conference (OFS)*, pp. 1–4, IEEE, 2017.

[106] A. Y. Tkachenko, N. Smolyaninov, M. Skvortsov, I. Lobach, and S. Kablukov, "A coherent optical frequency-domain reflectometer based on a self-sweeping fiber laser for sensing applications," *Instruments and Experimental Techniques*, vol. 63, pp. 532–537, 2020.

[107] A. Y. Tkachenko, I. A. Lobach, and S. I. Kablukov, "Optical frequency domain reflectometry based on self-sweeping fiber laser," in *Seventh European Workshop on Optical Fibre Sensors*, vol. 11199, pp. 379–382, SPIE, 2019.

[108] B. Feng, K. Liu, T. Liu, J. Jiang, and Y. Du, "Improving ofdr spatial resolution by reducing external clock sampling error," *Optics Communications*, vol. 363, pp. 74–79, 2016.

[109] E. D. Moore and R. R. McLeod, "Correction of sampling errors due to laser tuning rate fluctuations in swept-wavelength interferometry," *Optics Express*, vol. 16, no. 17, pp. 13139–13149, 2008.

[110] Z. Deng, Z. Liu, B. Li, and Z. Liu, "Precision improvement in frequency-scanning interferometry based on suppressing nonlinear optical frequency sweeping," *Optical Review*, vol. 22, pp. 724–730, 2015.

[111] Z. Liu, Z. Liu, Z. Deng, and L. Tao, "Interference signal frequency tracking for extracting phase in frequency scanning interferometry using an extended kalman filter," *Applied Optics*, vol. 55, no. 11, pp. 2985–2992, 2016.

[112] X. Fan, Y. Koshikiya, and F. Ito, "Phase-noise-compensated optical frequency domain reflectometry with measurement range beyond laser coherence length realized using concatenative reference method," *Optics Letters*, vol. 32, no. 22, pp. 3227–3229, 2007.

[113] X. Fan, Y. Koshikiya, and F. Ito, "Phase-noise-compensated optical frequency-domain reflectometry," *IEEE Journal of Quantum Electronics*, vol. 45, no. 6, pp. 594–602, 2009.

[114] Y. Koshikiya, X. Fan, and F. Ito, "Influence of acoustic perturbation of fibers in phase-noise-compensated optical-frequency-domain reflectometry," *Journal of Lightwave Technology*, vol. 28, no. 22, pp. 3323–3328, 2010.

[115] X. Fan, Y. Koshikiya, N. Araki, and F. Ito, "Field trials of pnc-ofdr in different environments for detecting short beat lengths," *IEEE Photonics Technology Letters*, vol. 24, no. 15, pp. 1288–1291, 2012.

[116] Z. Ding, X. S. Yao, T. Liu, Y. Du, K. Liu, Q. Han, Z. Meng, J. Jiang, and H. Chen, "Long measurement range ofdr beyond laser coherence length," *IEEE Photonics Technology Letters*, vol. 25, no. 2, pp. 202–205, 2012.

[117] S. Ohno, D. Iida, K. Toge, and T. Manabe, "Long-range measurement of rayleigh scatter signature beyond laser coherence length based on coherent optical frequency domain reflectometry," *Optics Express*, vol. 24, no. 17, pp. 19651–19660, 2016.

[118] Z. He, T. Kazama, Y. Koshikiya, X. Fan, F. Ito, and K. Hotate, "High-reflectivity-resolution coherent optical frequency domain reflectometry using optical frequency comb source and tunable delay line," *Optics Express*, vol. 19, no. 26, pp. B764–B769, 2011.

[119] B. Wang, X. Fan, Q. Liu, and Z. He, "Compensation of optical source phase noise in long-range ofdr by using an optical fiber delay loop," in *24th International Conference on Optical Fibre Sensors*, vol. 9634, pp. 353–356, SPIE, 2015.

[120] S. Liehr, N. Nöther, and K. Krebber, "Incoherent optical frequency domain reflectometry and distributed strain detection in polymer optical fibers," *Measurement Science and Technology*, vol. 21, no. 1, p. 017001, 2009.

[121] J. Clement, G. Torregrosa, J. Hervás, D. Barrera, S. Sales, and C. R. Fernandez-Pousa, "Interrogation of a sensor array of identical weak fbgs using dispersive incoherent ofdr," *IEEE Photonics Technology Letters*, vol. 28, no. 10, pp. 1154–1156, 2016.

[122] J. Wang, Z. Li, Q. Yang, X. Fu, X. Gui, C. Wang, and H. Wang, "Interrogation of a large-capacity densely spaced fiber bragg grating array using chaos-based incoherent-

optical frequency domain reflectometry," *Optics Letters*, vol. 44, no. 21, pp. 5202–5205, 2019.

[123] K. Feng, J. Cui, H. Dang, D. Jiang, Y. Jin, X. Sun, and X. Zhang, "A ofdr signal processing method based on wavelet transform for improving its sensing performance," *IEEE Photonics Technology Letters*, vol. 31, no. 13, pp. 1108–1111, 2019.

[124] L. Suo, Z. Lei, S. Zhao, Z. Wu, and A. Takezawa, "Study on sliding-window length based on rayleigh backscattering spectrum correlation in distributed optical-fiber strain measurement," *Optical Fiber Technology*, vol. 47, pp. 126–132, 2019.

[125] D. Wada, H. Igawa, H. Murayama, and T. Kasai, "Signal processing method based on group delay calculation for distributed bragg wavelength shift in optical frequency domain reflectometry," *Optics Express*, vol. 22, no. 6, pp. 6829–6836, 2014.

[126] C. Ma, Q. Zhou, J. Qin, W. Xie, Y. Dong, and W. Hu, "Fast spectrum analysis for an ofdr using the fft and sczt combination approach," *IEEE Photonics Technology Letters*, vol. 28, no. 6, pp. 657–660, 2015.

[127] M. Zhu and H. Murayama, "Fast demodulation of ofdr based long length fbg sensing system for noisy signals," *Optics Express*, vol. 26, no. 16, pp. 19804–19814, 2018.

[128] Z. Zhang, X. Fan, M. Wu, and Z. He, "Phase-noise-compensated ofdr realized using hardware-adaptive algorithm for real-time processing," *Journal of Lightwave Technology*, vol. 37, no. 11, pp. 2634–2640, 2018.

[129] L. Shiloh, A. Eyal, and R. Giryes, "Efficient processing of distributed acoustic sensing data using a deep learning approach," *Journal of Lightwave Technology*, vol. 37, no. 18, pp. 4755–4762, 2019.

[130] S. Liehr and K. Krebber, "Application of quasi-distributed and dynamic length and power change measurement using optical frequency domain reflectometry," *IEEE Sensors Journal*, vol. 12, no. 1, pp. 237–245, 2011.

[131] S. Wang, X. Fan, Q. Liu, and Z. He, "Distributed fiber-optic vibration sensing based on phase extraction from time-gated digital ofdr," *Optics Express*, vol. 23, no. 26, pp. 33301–33309, 2015.

[132] D. Chen, Q. Liu, and Z. He, "Phase-detection distributed fiber-optic vibration sensor without fading-noise based on time-gated digital ofdr," *Optics Express*, vol. 25, no. 7, pp. 8315–8325, 2017.

[133] D. Chen, Q. Liu, and Z. He, "High-fidelity distributed fiber-optic acoustic sensor with fading noise suppressed and sub-meter spatial resolution," *Optics Express*, vol. 26, no. 13, pp. 16138–16146, 2018.

[134] L. Marcon, A. Galtarossa, and L. Palmieri, "High-frequency high-resolution distributed acoustic sensing by optical frequency domain reflectometry," *Optics Express*, vol. 27, no. 10, pp. 13923–13933, 2019.

[135] H. Li, Q. Liu, D. Chen, Y. Deng, and Z. He, "High-spatial-resolution fiber-optic distributed acoustic sensor based on ϕ-ofdr with enhanced crosstalk suppression," *Optics Letters*, vol. 45, no. 2, pp. 563–566, 2020.

[136] T. Liu, Y. Du, Z. Ding, K. Liu, Y. Zhou, and J. Jiang, "40-km ofdr-based distributed disturbance optical fiber sensor," *IEEE Photonics Technology Letters*, vol. 28, no. 7, pp. 771–774, 2015.

[137] Z. Ding, D. Yang, K. Liu, J. Jiang, Y. Du, B. Li, M. Shang, and T. Liu, "Long-range ofdr-based distributed vibration optical fiber sensor by multicharacteristics of rayleigh scattering," *IEEE Photonics Journal*, vol. 9, no. 5, pp. 1–10, 2017.

[138] C. A. Rodríguez, M. R. Ribeiro, A. Frizera, and M. J. Pontes, "Interrogation of optical fiber based on the fusion of ofdr and tra techniques," *Optical and Quantum Electronics*, vol. 48, pp. 1–6, 2016.

[139] A. Wada, S. Tanaka, and N. Takahashi, "Multipoint vibration sensing using fiber bragg gratings and current-modulated laser diodes," *Journal of Lightwave Technology*, vol. 34, no. 19, pp. 4610–4614, 2016.

[140] D. Wada, H. Igawa, and T. Kasai, "Vibration monitoring of a helicopter blade model using the optical fiber distributed strain sensing technique," *Applied Optics*, vol. 55, no. 25, pp. 6953–6959, 2016.

[141] M. Zhu, D. Leandro, M. López-Amo, and H. Murayama, "Quasi-distributed vibration sensing using ofdr and weak reflectors," *Optics Letters*, vol. 44, no. 8, pp. 1884–1887, 2019.

[142] K. Yuksel, V. Moeyaert, P. Mégret, and M. Wuilpart, "Complete analysis of multireflection and spectral-shadowing crosstalks in a quasi-distributed fiber sensor interrogated by ofdr," *IEEE Sensors Journal*, vol. 12, no. 5, pp. 988–995, 2011.

[143] T. Yoshino, "Theory and design consideration for cross-talk-free quasi-distributed sensing of fast fiber phase variation," *JOSA B*, vol. 35, no. 7, pp. 1620–1627, 2018.

[144] T. Okamoto, D. Iida, and H. Oshida, "Vibration-induced beat frequency offset compensation in distributed acoustic sensing based on optical frequency domain reflectometry," *Journal of Lightwave Technology*, vol. 37, no. 18, pp. 4896–4901, 2019.

[145] S. Liehr and K. Krebber, "A novel quasi-distributed fibre optic displacement sensor for dynamic measurement," *Measurement Science and Technology*, vol. 21, no. 7, p. 075205, 2010.

[146] E. M. Lally, M. Reaves, E. Horrell, S. Klute, and M. E. Froggatt, "Fiber optic shape sensing for monitoring of flexible structures," in *Sensors and Smart Structures Technologies for Civil, Mechanical, and Aerospace Systems 2012*, vol. 8345, pp. 831–839, SPIE, 2012.

[147] C. Shao, G. Yin, L. Lv, M. Liu, I. P. Ikechukwu, H. Han, L. Zhou, J. Zhang, W. Zhai, S. Wang, *et al.*, "Ofdr with local spectrum matching method for optical fiber shape sensing," *Applied Physics Express*, vol. 12, no. 8, p. 082010, 2019.

[148] F. Parent, S. Loranger, K. K. Mandal, V. L. Iezzi, J. Lapointe, J.-S. Boisvert, M. D. Baiad, S. Kadoury, and R. Kashyap, "Enhancement of accuracy in shape sensing of surgical needles using optical frequency domain reflectometry in optical fibers," *Biomedical Optics Express*, vol. 8, no. 4, pp. 2210–2221, 2017.

[149] P. Lorre, F. Monet, M. Gauthier, A. Poiffaut, A. Roberge, S. Kadoury, and R. Kashyap, "Extruded optical fiber triplets for 3d shape sensing for minimally invasive surgery," in *Seventh European Workshop on Optical Fibre Sensors*, vol. 11199, pp. 251–254, SPIE, 2019.

[150] T. W. Wood, B. Blake, T. E. Blue, C. M. Petrie, and D. Hawn, "Evaluation of the performance of distributed temperature measurements with single-mode fiber using rayleigh backscatter up to 1000 °c," *IEEE Sensors Journal*, vol. 14, no. 1, pp. 124–128, 2013.

[151] M. Luo, J. Liu, C. Tang, X. Wang, T. Lan, and B. Kan, "0.5 mm spatial resolution distributed fiber temperature and strain sensor with position-deviation compensation based on ofdr," *Optics Express*, vol. 27, no. 24, pp. 35823–35829, 2019.

[152] Y. Du, T. Liu, Z. Ding, Q. Han, K. Liu, J. Jiang, Q. Chen, and B. Feng, "Cryogenic temperature measurement using rayleigh backscattering spectra shift by ofdr," *IEEE Photonics Technology Letters*, vol. 26, no. 11, pp. 1150–1153, 2014.

[153] X. Lu, M. A. Soto, and L. Thévenaz, "Impact of the fiber coating on the temperature response of distributed optical fiber sensors at cryogenic ranges," *Journal of Lightwave Technology*, vol. 36, no. 4, pp. 961–967, 2017.

[154] D. Wada, H. Murayama, H. Igawa, K. Kageyama, K. Uzawa, and K. Omichi, "Simultaneous distributed measurement of strain and temperature by polarization maintaining fiber bragg grating based on optical frequency domain reflectometry," *Smart Materials and Structures*, vol. 20, no. 8, p. 085028, 2011.

[155] D. Wada, H. Igawa, and H. Murayama, "Simultaneous distributed measurement of the strain and temperature for a four-point bending test using polarization-maintaining fiber bragg grating interrogated by optical frequency domain reflectometry," *Measurement*, vol. 94, pp. 745–752, 2016.

[156] M. Zhu, H. Murayama, D. Wada, and K. Kageyama, "Dependence of measurement accuracy on the birefringence of panda fiber bragg gratings in distributed simultaneous strain and temperature sensing," *Optics Express*, vol. 25, no. 4, pp. 4000–4017, 2017.

[157] W. Li, L. Chen, and X. Bao, "Compensation of temperature and strain coefficients due to local birefringence using optical frequency domain reflectometry," *Optics Communications*, vol. 311, pp. 26–32, 2013.

[158] D.-P. Zhou, W. Li, L. Chen, and X. Bao, "Distributed temperature and strain discrimination with stimulated brillouin scattering and rayleigh backscatter in an optical fiber," *Sensors*, vol. 13, no. 2, pp. 1836–1845, 2013.

[159] Z. Ding, D. Yang, Y. Du, K. Liu, Y. Zhou, R. Zhang, Z. Xu, J. Jiang, and T. Liu, "Distributed strain and temperature discrimination using two types of fiber in ofdr," *IEEE Photonics Journal*, vol. 8, no. 5, pp. 1–8, 2016.

[160] A. Bergman, R. Davidi, A. I. Shalev, L. Ovadia, T. Langer, and M. Tur, "Increasing the measurement dynamic range of rayleigh-based ofdr interrogator using an amplifying add-on module," *IEEE Photonics Technology Letters*, vol. 28, no. 22, pp. 2621–2624, 2016.

[161] K. Feng, J. Cui, D. Jiang, H. Dang, Y. Jin, X. Sun, Y. Niu, and J. Tan, "Improvement of the strain measurable range of an ofdr based on local similar characteristics of a rayleigh scattering spectrum," *Optics Letters*, vol. 43, no. 14, pp. 3293–3296, 2018.

[162] P. R. Watekar, S. Ju, and W.-T. Han, "Bend insensitive optical fiber with ultralow bending loss in the visible wavelength band," *Optics Letters*, vol. 34, no. 24, pp. 3830–3832, 2009.

[163] M.-J. Li, P. Tandon, D. Bookbinder, S. Bickham, M. McDermott, R. Desorcie, D. Nolan, J. Johnson, K. Lewis, and J. Englebert, "Ultra-low bending loss single-mode fiber for ftth," *Journal of Lightwave Technology*, vol. 27, no. 3, pp. 376–382, 2009.

[164] P. R. Watekar, S. Ju, and W.-T. Han, "Optimized design of trenched optical fiber for ultralow bending loss at 5 mm of bending diameter," *Applied Optics*, vol. 50, no. 25, pp. E97–E101, 2011.

[165] Z. Wang, C.-L. Zhao, and S. Jin, "Design of a bending-insensitive single-mode photonic crystal fiber," *Optical Fiber Technology*, vol. 19, no. 3, pp. 213–218, 2013.

[166] K. Naeem, Y.-S. Kwon, Y. Chung, and I.-B. Kwon, "Bend-loss-free distributed sensor based on rayleigh backscattering in ge-doped-core pcf," *IEEE Sensors Journal*, vol. 18, no. 5, pp. 1903–1910, 2017.

[167] R. R. Maier, W. N. MacPherson, J. S. Barton, S. McCulloch, and B. J. Jones, "Distributed sensing using rayleigh scatter in polarization-maintaining fibres for transverse load sensing," *Measurement Science and Technology*, vol. 21, no. 9, p. 094019, 2010.

[168] D. Wada, H. Murayama, and H. Igawa, "Lateral load measurements based on a distributed sensing system of optical frequency-domain reflectometry using long-length fiber bragg gratings," *Journal of Lightwave Technology*, vol. 30, no. 14, pp. 2337–2344, 2012.

[169] D. Wada and H. Murayama, "Analytical investigation of response of birefringent fiber bragg grating sensors in distributed monitoring system based on optical frequency domain reflectometry," *Optics and Lasers in Engineering*, vol. 52, pp. 99–105, 2014.

[170] K. Yüksel and D. Pala, "Analytical investigation of a novel interrogation approach of fiber bragg grating sensors using optical frequency domain reflectometry," *Optics and Lasers in Engineering*, vol. 81, pp. 119–124, 2016.

[171] T. Feng, Y. Shang, X. Wang, S. Wu, A. Khomenko, X. Chen, and X. S. Yao, "Distributed polarization analysis with binary polarization rotators for the accurate measurement of distance-resolved birefringence along a single-mode fiber," *Optics Express*, vol. 26, no. 20, pp. 25989–26002, 2018.

[172] X. Zhang, Y. Chen, and J. Hu, "Recent advances in the development of aerospace materials," *Progress in Aerospace Sciences*, vol. 97, pp. 22–34, 2018.

[173] R. Di Sante, "Fibre optic sensors for structural health monitoring of aircraft composite structures: Recent advances and applications," *Sensors*, vol. 15, no. 8, pp. 18666–18713, 2015.

[174] Q. Xia, Z. Zhang, Y. Liu, and J. Leng, "Buckypaper and its composites for aeronautic applications," *Composites Part B: Engineering*, vol. 199, p. 108231, 2020.

[175] S.-W. Kim, M.-C. Cha, I. Lee, E.-H. Kim, I.-B. Kwon, and T.-K. Hwang, "Damage evaluation and strain monitoring of composite plates using metal-coated fbg sensors under quasi-static indentation," *Composites Part B: Engineering*, vol. 66, pp. 36–45, 2014.

[176] M. Saeedifar and D. Zarouchas, "Damage characterization of laminated composites using acoustic emission: A review," *Composites Part B: Engineering*, vol. 195, p. 108039, 2020.

[177] D. Geng, Y. Liu, Z. Shao, Z. Lu, J. Cai, X. Li, X. Jiang, and D. Zhang, "Delamination formation, evaluation and suppression during drilling of composite laminates: A review," *Composite Structures*, vol. 216, pp. 168–186, 2019.

[178] B. Hoekstra, A. Shekarian, K. Kolasangiani, D. C. Oguamanam, R. Zitoune, and H. Bougherara, "Effect of machining processes on the damage response and surface quality of open hole hybrid carbon/flax composites: An experimental study," *Composite Structures*, vol. 285, p. 115244, 2022.

[179] M. M. Ahmed, H. Dhakal, Z. Zhang, A. Barouni, and R. Zahari, "Enhancement of impact toughness and damage behaviour of natural fibre reinforced composites and their hybrids through novel improvement techniques: A critical review," *Composite Structures*, vol. 259, p. 113496, 2021.

[180] Z. Mahboob and H. Bougherara, "Fatigue of flax-epoxy and other plant fibre composites: Critical review and analysis," *Composites Part A: Applied Science and Manufacturing*, vol. 109, pp. 440–462, 2018.

[181] L. Zhang, X. Qu, Z. Zhao, H. Zhang, S. Lu, and X. Wang, "Health monitoring of composite pressure vessels through omnidirectional buckypaper sensor array," *Applied Physics A*, vol. 128, no. 3, p. 178, 2022.

[182] F. Lambinet and Z. S. Khodaei, "Measurement platform for structural health monitoring application of large scale structures," *Measurement*, vol. 190, p. 110675, 2022.

[183] F. Lambinet and Z. S. Khodaei, "Damage detection & localization on composite patch repair under different environmental effects," *Engineering Research Express*, vol. 2, no. 4, p. 045032, 2020.

[184] I. Dafydd and Z. Sharif Khodaei, "Analysis of barely visible impact damage severity with ultrasonic guided lamb waves," *Structural Health Monitoring*, vol. 19, no. 4, pp. 1104–1122, 2020.

[185] W. Staszewski, S. Mahzan, and R. Traynor, "Health monitoring of aerospace composite structures–active and passive approach," *composites Science and Technology*, vol. 69, no. 11-12, pp. 1678–1685, 2009.

[186] A. H. Seno, Z. S. Khodaei, and M. F. Aliabadi, "Passive sensing method for impact localisation in composite plates under simulated environmental and operational conditions," *Mechanical Systems and Signal Processing*, vol. 129, pp. 20–36, 2019.

[187] P. Lesiak, M. Szelag, D. Budaszewski, R. Plaga, K. Mileńko, G. Rajan, Y. Semenova, G. Farrell, A. Boczkowska, A. Domański, *et al.*, "Influence of lamination process on optical fiber sensors embedded in composite material," *Measurement*, vol. 45, no. 9, pp. 2275–2280, 2012.

[188] J. Degrieck, W. De Waele, and P. Verleysen, "Monitoring of fibre reinforced composites with embedded optical fibre bragg sensors, with application to filament wound pressure vessels," *Ndt & E International*, vol. 34, no. 4, pp. 289–296, 2001.

[189] G. Szebényi, Y. Blößl, G. Hegedüs, T. Tábi, T. Czigany, and R. Schledjewski, "Fatigue monitoring of flax fibre reinforced epoxy composites using integrated fibre-optical fbg sensors," *Composites Science and Technology*, vol. 199, p. 108317, 2020.

[190] I. N. Giannakeas, Z. S. Khodaei, and M. F. Aliabadi, "Structural health monitoring cost estimation of a piezosensorized aircraft fuselage," *Sensors*, vol. 22, no. 5, p. 1771, 2022.

[191] R. Soman, J. Wee, and K. Peters, "Optical fiber sensors for ultrasonic structural health monitoring: a review," *Sensors*, vol. 21, no. 21, p. 7345, 2021.

[192] A. Güemes, A. Fernández-López, P. F. Díaz-Maroto, A. Lozano, and J. Sierra-Perez, "Structural health monitoring in composite structures by fiber-optic sensors," *Sensors*, vol. 18, no. 4, p. 1094, 2018.

[193] J. A. Mills, A. W. Hamilton, D. I. Gillespie, I. Andonovic, C. Michie, K. Burnham, and C. Tachtatzis, "Identifying defects in aerospace composite sandwich panels using high-definition distributed optical fibre sensors," *Sensors*, vol. 20, no. 23, p. 6746, 2020.

[194] P. F. Díaz-Maroto, A. Fernández-López, J. García-Alonso, M. Iglesias, and A. Güemes, "Buckling detection of an omega-stiffened aircraft composite panel using distributed fibre optic sensors," *Thin-Walled Structures*, vol. 132, pp. 375–384, 2018.

[195] R. Soman, K. Balasubramaniam, A. Golestani, M. Karpiński, P. Malinowski, and W. Ostachowicz, "Actuator placement optimization for guided waves based structural health monitoring using fibre bragg grating sensors," *Smart Materials and Structures*, vol. 30, no. 12, p. 125011, 2021.

[196] R. Soman, "Multi-objective optimization for joint actuator and sensor placement for guided waves based structural health monitoring using fibre bragg grating sensors," *Ultrasonics*, vol. 119, p. 106605, 2022.

[197] M. Mieloszyk, K. Majewska, and W. Ostachowicz, "Application of embedded fibre bragg grating sensors for structural health monitoring of complex composite structures for marine applications," *Marine Structures*, vol. 76, p. 102903, 2021.

[198] M. Mieloszyk, M. Jurek, K. Majewska, and W. Ostachowicz, "Terahertz time domain spectroscopy and imaging application for analysis of sandwich panel with embedded fibre bragg grating sensors and piezoelectric transducers," *Optics and Lasers in Engineering*, vol. 134, p. 106226, 2020.

[199] D. Saenz-Castillo, M. Martín, S. Calvo, and A. Güemes, "Real-time monitoring of thermal history of thermoplastic automatic lamination with fbg sensors and process modelling validation," *Smart Materials and Structures*, vol. 29, no. 11, p. 115004, 2020.

[200] V. Buchinger and Z. Sharif Khodaei, "Vacuum assisted resin transfer moulding process monitoring by means of distributed fibre-optic sensors: a numerical and experimental study," *Advanced Composite Materials*, pp. 1–18, 2021.

[201] F. Lambinet and Z. Sharif Khodaei, "Development of hybrid piezoelectric-fibre optic composite patch repair solutions," *Sensors*, vol. 21, no. 15, p. 5131, 2021.

[202] C. Xu and Z. Sharif Khodaei, "Shape sensing with rayleigh backscattering fibre optic sensor," *Sensors*, vol. 20, no. 14, p. 4040, 2020.

[203] R. You, L. Ren, and G. Song, "A novel ofdr-based distributed optical fiber sensing tape: Design, optimization, calibration and application," *Smart Materials and Structures*, vol. 29, no. 10, p. 105017, 2020.

[204] A. Datta, M. Augustin, K. M. Gaddikeri, S. Viswamurthy, N. Gupta, and R. Sundaram, "Damage detection in composite aircraft wing-like test-box using distributed fiber optic sensors," *Optical Fiber Technology*, vol. 66, p. 102651, 2021.

[205] H.-P. Wang, S.-Y. Feng, X.-S. Gong, Y.-X. Guo, P. Xiang, Y. Fang, and Q.-M. Li, "Dynamic performance detection of cfrp composite pipes based on quasi-distributed optical fiber sensing techniques," *Frontiers in Materials*, vol. 8, p. 683374, 2021.

[206] M. Shamsuddoha, M. David, E. Oromiehie, and B. G. Prusty, "Distributed optical fibre sensor based monitoring of thermoplastic carbon composite cylinders under biaxial loading: experimental and numerical investigations," *Composite Structures*, vol. 261, p. 113277, 2021.

[207] O. Rufai, N. Chandarana, M. Gautam, P. Potluri, and M. Gresil, "Cure monitoring and structural health monitoring of composites using micro-braided distributed optical fibre," *Composite Structures*, vol. 254, p. 112861, 2020.

[208] M. Froggatt and J. Moore, "High-spatial-resolution distributed strain measurement in optical fiber with rayleigh scatter," *Applied Optics*, vol. 37, no. 10, pp. 1735–1740, 1998.

[209] A. Güemes, A. Fernández-López, and B. Soller, "Optical fiber distributed sensing-physical principles and applications," *Structural Health Monitoring*, vol. 9, no. 3, pp. 233–245, 2010.

[210] Y.-s. Kwon, K. Naeem, M. Y. Jeon, and I.-B. Kwon, "Enhanced sensitivity of distributed-temperature sensor with al-coated fiber based on ofdr," *Optical Fiber Technology*, vol. 48, pp. 229–234, 2019.

[211] M. Kulpa, T. Howiacki, A. Wiater, T. Siwowski, and R. Sieńko, "Strain and displacement measurement based on distributed fibre optic sensing (dfos) system integrated with frp composite sandwich panel," *Measurement*, vol. 175, p. 109099, 2021.

[212] M. Drissi-Habti, V. Raman, A. Khadour, and S. Timorian, "Fiber optic sensor embedment study for multi-parameter strain sensing," *Sensors*, vol. 17, no. 4, p. 667, 2017.

[213] M. Lai, J. Botsis, and J. Cugnoni, "Studies of hygrothermal degradation of a single fiber composite: An iterative approach with embedded optical sensors and numerical analysis," *Composites Part B: Engineering*, vol. 60, pp. 577–585, 2014.

[214] M. Arhant, N. Meek, D. Penumadu, P. Davies, and N. Garg, "Residual strains using integrated continuous fiber optic sensing in thermoplastic composites and structural health monitoring," *Experimental Mechanics*, vol. 58, no. 1, pp. 167–176, 2018.

[215] M. Shamsuddoha, M. David, E. Oromiehie, and B. G. Prusty, "Distributed optical fibre sensor based monitoring of thermoplastic carbon composite cylinders under biaxial loading: Experimental and numerical investigations," *Composite Structures*, vol. 261, p. 113277, 2021.

[216] J. H. L. Grave, M. L. Håheim, and A. T. Echtermeyer, "Measuring changing strain fields in composites with distributed fiber-optic sensing using the optical backscatter reflectometer," *Composites Part B: Engineering*, vol. 74, pp. 138–146, 2015.

[217] X. Jiang and Q. Wang, "Refractive index sensitivity enhancement of optical fiber spr sensor utilizing layer of mwcnt/ptnps composite," *Optical Fiber Technology*, vol. 51, pp. 118–124, 2019.

[218] H. Moradi, F. Hosseinibalam, and S. Hassanzadeh, "Simulation and experimental investigation about interferometric optical fiber acoustic sensor for sensitivity enhancement," *Measurement*, vol. 137, pp. 556–561, 2019.

[219] G. Woyessa, J. K. Pedersen, K. Nielsen, and O. Bang, "Enhanced pressure and thermal sensitivity of polymer optical fiber bragg grating sensors," *Optics & Laser Technology*, vol. 130, p. 106357, 2020.

[220] P. M. R. Robalinho, A. D. Gomes, and O. Frazao, "High enhancement strain sensor based on vernier effect using 2-fiber loop mirrors," *IEEE Photonics Technology Letters*, vol. 32, no. 18, pp. 1139–1142, 2020.

[221] H. Wang and J.-G. Dai, "Strain transfer analysis of fiber bragg grating sensor assembled composite structures subjected to thermal loading," *Composites Part B: Engineering*, vol. 162, pp. 303–313, 2019.

[222] J. Etches and G. Fernando, "Evaluation of embedded optical fiber sensors in composites: Efpi sensor response to fatigue loading," *Polymer Composites*, vol. 31, no. 2, pp. 284–291, 2010.

[223] V. Chean, R. M. Boumbimba, R. El Abdi, J. Sangleboeuf, P. Casari, and M. D. Habti, "Experimental characterization of interfacial adhesion of an optical fiber embedded in a composite material," *International Journal of Adhesion and Adhesives*, vol. 41, pp. 144–151, 2013.

[224] S. T. Kreger, D. K. Gifford, M. E. Froggatt, B. J. Soller, and M. S. Wolfe, "High resolution distributed strain or temperature measurements in single-and multi-mode fiber using swept-wavelength interferometry," in *Optical Fiber Sensors*, p. ThE42, Optica Publishing Group, 2006.

[225] A. Barrias, J. R. Casas, and S. Villalba, "Distributed optical fibre sensors in concrete structures: Performance of bonding adhesives and influence of spatial resolution," *Structural Control and Health Monitoring*, vol. 26, no. 3, p. e2310, 2019.

[226] F. Falcetelli, D. Cristiani, N. Yue, C. Sbarufatti, E. Troiani, R. Di Sante, and D. Zarouchas, "Qualification of distributed optical fiber sensors using probability of detection curves for delamination in composite laminates," *Structural Health Monitoring*, p. 14759217221141159, 2022.

[227] F. Clauß, M. A. Ahrens, and P. Mark, "Thermo-mechanical experiments on reinforced concrete beams: Assessing thermal, mechanical, and mixed impacts on fiber optic measurements," *Structural Concrete*, vol. 23, no. 6, pp. 3521–3537, 2022.

[228] S. Li, G. Lu, C. Lai, Y. Huang, and Y. En, "Optical-path difference on-line measurement of multiplexing fiber-optic interferometric sensors using tdm and wdm by improved optical-frequency-domain reflectometry," in *AOPC 2019: Optical Fiber Sensors and Communication*, vol. 11340, pp. 152–157, SPIE, 2019.

[229] D. G. Bekas, Z. Sharif-Khodaei, and M. F. Aliabadi, "An innovative diagnostic film for structural health monitoring of metallic and composite structures," *Sensors*, vol. 18, no. 7, p. 2084, 2018.

[230] M. Gupta, J. Gao, C. C. Aggarwal, and J. Han, "Outlier detection for temporal data: A survey," *IEEE Transactions on Knowledge and Data Engineering*, vol. 26, no. 9, pp. 2250–2267, 2013.

[231] H. Shen, X. Li, Q. Cheng, C. Zeng, G. Yang, H. Li, and L. Zhang, "Missing information reconstruction of remote sensing data: A technical review," *IEEE Geoscience and Remote Sensing Magazine*, vol. 3, no. 3, pp. 61–85, 2015.

[232] S. A. Bagherzadeh and M. Sabzehparvar, "A local and online sifting process for the empirical mode decomposition and its application in aircraft damage detection," *Mechanical Systems and Signal Processing*, vol. 54, pp. 68–83, 2015.

[233] D. Stankovic, L. A. Bisby, and G. P. Terrasi, "Influence of temperature on the mechanical performance of unidirectional carbon fiber reinforced polymer straps," *Materials*, vol. 14, no. 8, p. 1903, 2021.

[234] C. Hong, Q. Yang, X. Sun, W. Chen, and K. Han, "A theoretical strain transfer model between optical fiber sensors and monitored substrates," *Geotextiles and Geomembranes*, vol. 49, no. 6, pp. 1539–1549, 2021.

[235] A. Claridge-Chang and P. N. Assam, "Estimation statistics should replace significance testing," *Nature Methods*, vol. 13, no. 2, pp. 108–109, 2016.

[236] Y. Fu, J. Zhu, S. Wang, and Z. Xi, "Reduced complexity snr estimation via kolmogorov-smirnov test," *IEEE Communications Letters*, vol. 19, no. 9, pp. 1568–1571, 2015.

[237] J. J. Vaske, J. Beaman, and C. C. Sponarski, "Rethinking internal consistency in cronbach's alpha," *Leisure Sciences*, vol. 39, no. 2, pp. 163–173, 2017.

[238] G. R. Hancock and J. An, "A closed-form alternative for estimating ω reliability under unidimensionality," *Measurement: Interdisciplinary Research and Perspectives*, vol. 18, no. 1, pp. 1–14, 2020.

[239] B. L. Thompson, S. B. Green, and Y. Yang, "Assessment of the maximal split-half coefficient to estimate reliability," *Educational and Psychological Measurement*, vol. 70, no. 2, pp. 232–251, 2010.

[240] G. Spiliotopoulou, "Reliability reconsidered: Cronbach's alpha and paediatric assessment in occupational therapy," *Australian Occupational Therapy Journal*, vol. 56, no. 3, pp. 150–155, 2009.

[241] J. M. Cortina, "What is coefficient alpha? an examination of theory and applications.," *Journal of Applied Psychology*, vol. 78, no. 1, p. 98, 1993.

[242] I. Iso and B. OIML, "Guide to the expression of uncertainty in measurement," *Geneva, Switzerland*, vol. 122, pp. 16–17, 1995.

[243] F. Yu and Y. Okabe, "Linear damage localization in cfrp laminates using one single fiber-optic bragg grating acoustic emission sensor," *Composite Structures*, vol. 238, p. 111992, 2020.

[244] A. Elshafey, H. Marzouk, X. Gu, M. Haddara, and R. Morsy, "Use of fiber bragg grating array and random decrement for damage detection in steel beam," *Engineering Structures*, vol. 106, pp. 348–354, 2016.

[245] M. Yeager, M. Todd, W. Gregory, and C. Key, "Assessment of embedded fiber bragg gratings for structural health monitoring of composites," *Structural Health Monitoring*, vol. 16, no. 3, pp. 262–275, 2017.

[246] B.-H. Choi and I.-B. Kwon, "Strain pattern detection of composite cylinders using optical fibers after low velocity impacts," *Composites Science and Technology*, vol. 154, pp. 64–75, 2018.

[247] A. Stewart, G. Carman, and L. Richards, "Health monitoring technique for composite materials utilizing embedded thermal fiber optic sensors," *Journal of Composite Materials*, vol. 39, no. 3, pp. 199–213, 2005.

[248] X. Cheng and Z. Sharif Khodaei, "Temperature calibration for guided wave hybrid system with fbg-based fabry-perot sensor," *Journal of Intelligent Material Systems and Structures*, p. 1045389X221109251, 2022.

[249] R. De Oliveira, O. Frazão, J. Santos, and A. Marques, "Optic fibre sensor for real-time damage detection in smart composite," *Computers & Structures*, vol. 82, no. 17-19, pp. 1315–1321, 2004.

[250] F. Li, H. Murayama, K. Kageyama, and I. Ohsawa, "Multiple damage assessment in composite laminates using a doppler-effect-based fiber-optic sensor," *Measurement Science and Technology*, vol. 20, no. 11, p. 115109, 2009.

[251] L. Rippert, M. Wevers, and S. Van Huffel, "Optical and acoustic damage detection in laminated cfrp composite materials," *Composites Science and Technology*, vol. 60, no. 14, pp. 2713–2724, 2000.

[252] N. Takeda, Y. Okabe, J. Kuwahara, S. Kojima, and T. Ogisu, "Development of smart composite structures with small-diameter fiber bragg grating sensors for damage detection: Quantitative evaluation of delamination length in cfrp laminates using lamb wave sensing," *Composites Science and Technology*, vol. 65, no. 15-16, pp. 2575–2587, 2005.

[253] H. Tsuda and J.-R. Lee, "Strain and damage monitoring of cfrp in impact loading using a fiber bragg grating sensor system," *Composites Science and Technology*, vol. 67, no. 7-8, pp. 1353–1361, 2007.

[254] H. Tsuda, N. Toyama, K. Urabe, and J. Takatsubo, "Impact damage detection in cfrp using fiber bragg gratings," *Smart Materials and Structures*, vol. 13, no. 4, p. 719, 2004.

[255] F.-m. Yu, Y. Okabe, Q. Wu, and N. Shigeta, "A novel method of identifying damage types in carbon fiber-reinforced plastic cross-ply laminates based on acoustic emission detection using a fiber-optic sensor," *Composites Science and Technology*, vol. 135, pp. 116–122, 2016.

[256] H. Zhang, Q. Wu, W. Xu, and K. Xiong, "Damage evaluation of complex composite structures using acousto-ultrasonic detection combined with phase-shifted fiber bragg grating and dual-frequency based data processing," *Composite Structures*, vol. 281, p. 115000, 2022.

[257] F. Lambinet and Z. Sharif Khodaei, "Development of hybrid piezoelectric-fibre optic composite patch repair solutions," *Sensors*, vol. 21, no. 15, p. 5131, 2021.

[258] K. Shivakumar and L. Emmanwori, "Mechanics of failure of composite laminates with an embedded fiber optic sensor," *Journal of composite materials*, vol. 38, no. 8, pp. 669–680, 2004.

[259] W. Zhou, Z. Wu, and L. Mevel, "Vibration-based damage detection to the composite tank filled with fluid," *Structural Health Monitoring*, vol. 9, no. 5, pp. 433–445, 2010.

[260] M. Cuadrado, J. Pernas-Sanchez, J. A. Artero-Guerrero, and D. Varas, "Detection of barely visible multi-impact damage on carbon/epoxy composite plates using frequency response function correlation analysis," *Measurement*, vol. 196, p. 111194, 2022.

[261] L. Cheng, A. Cigada, *et al.*, "Experimental strain modal analysis for beam-like structure by using distributed fiber optics and its damage detection," *Measurement Science and Technology*, vol. 28, no. 7, p. 074001, 2017.

[262] P. Capoluongo, C. Ambrosino, S. Campopiano, A. Cutolo, M. Giordano, I. Bovio, L. Lecce, and A. Cusano, "Modal analysis and damage detection by fiber bragg grating sensors," *Sensors and Actuators A: Physical*, vol. 133, no. 2, pp. 415–424, 2007.

[263] Y. Xu, D.-M. Chen, and W. Zhu, "Damage identification of beam structures using free response shapes obtained by use of a continuously scanning laser doppler vibrometer system," *Mechanical Systems and Signal Processing*, vol. 92, pp. 226–247, 2017.

[264] Y. Wang, M. Liang, and J. Xiang, "Damage detection method for wind turbine blades based on dynamics analysis and mode shape difference curvature information," *Mechanical Systems and Signal Processing*, vol. 48, no. 1-2, pp. 351–367, 2014.

[265] Z. Tian, S. Howden, Z. Ma, W. Xiao, and L. Yu, "Pulsed laser-scanning laser doppler vibrometer (pl-sldv) phased arrays for damage detection in aluminum plates," *Mechanical systems and signal processing*, vol. 121, pp. 158–170, 2019.

[266] O. Rifaie-Graham, E. A. Apebende, L. K. Bast, and N. Bruns, "Self-reporting fiber-reinforced composites that mimic the ability of biological materials to sense and report damage," *Advanced Materials*, vol. 30, no. 19, p. 1705483, 2018.

[267] S. Goossens, B. De Pauw, T. Geernaert, M. S. Salmanpour, Z. S. Khodaei, E. Karachalios, D. Saenz-Castillo, H. Thienpont, and F. Berghmans, "Aerospace-grade surface mounted optical fibre strain sensor for structural health monitoring on composite structures evaluated against in-flight conditions," *Smart Materials and Structures*, vol. 28, no. 6, p. 065008, 2019.

[268] C. Soutis and P. Curtis, "Prediction of the post-impact compressive strength of cfrp laminated composites," *Composites Science and Technology*, vol. 56, no. 6, pp. 677–684, 1996.

[269] J. Zhang, C. Soutis, and J. Fan, "Strain energy release rate associated with local delamination in cracked composite laminates," *Composites*, vol. 25, no. 9, pp. 851–862, 1994.

[270] C. Garnier, M.-L. Pastor, B. Lorrain, and O. Pantalé, "Fatigue behavior of impacted composite structures," *Composite Structures*, vol. 100, pp. 443–450, 2013.

[271] S. I. Thorsson, S. P. Sringeri, A. M. Waas, B. P. Justusson, and M. Rassaian, "Experimental investigation of composite laminates subject to low-velocity edge-on impact and compression after impact," *Composite Structures*, vol. 186, pp. 335–346, 2018.

[272] H. Li, Z. S. Khodaei, and M. F. Aliabadi, "Multiscale modelling of material degradation and failure in plain woven composites: A novel approach for reliable predictions enabled by meta-models," *Composites Science and Technology*, p. 109910, 2023.

[273] M. Zhuang, L. Morse, Z. S. Khodaei, and M. Aliabadi, "Statistical inference of the equivalent initial flaw size distribution for an anisotropic material with the dual boundary element method," *International Journal of Fatigue*, vol. 158, p. 106702, 2022.

[274] J. T. Siivola, S. Minakuchi, T. Mizutani, and N. Takeda, "Evaluation of damage detectability in practical sandwich structure application conditions using distributed fiber optic sensor," *Structural Health Monitoring*, vol. 15, no. 1, pp. 3–20, 2016.

[275] N. Alexopoulos, C. Bartholome, P. Poulin, and Z. Marioli-Riga, "Damage detection of glass fiber reinforced composites using embedded pva–carbon nanotube (cnt) fibers," *Composites Science and Technology*, vol. 70, no. 12, pp. 1733–1741, 2010.

[276] S. Rivallant, C. Bouvet, E. Abi Abdallah, B. Broll, and J.-J. Barrau, "Experimental analysis of cfrp laminates subjected to compression after impact: The role of impact-induced cracks in failure," *Composite Structures*, vol. 111, pp. 147–157, 2014.

[277] M. N. Saleh, H. M. El-Dessouky, M. Saeedifar, S. T. De Freitas, R. J. Scaife, and D. Zarouchas, "Compression after multiple low velocity impacts of ncf, 2d and 3d woven composites," *Composites Part A: Applied Science and Manufacturing*, vol. 125, p. 105576, 2019.

[278] X. Sun and S. Hallett, "Failure mechanisms and damage evolution of laminated composites under compression after impact (cai): Experimental and numerical study," *Composites Part A: Applied Science and Manufacturing*, vol. 104, pp. 41–59, 2018.

[279] D. Munzke, D. Kraus, R. Eisermann, S. Kübler, M. Schukar, L. Nagel, S. Hickmann, and V. Trappe, "Distributed fiber-optic strain sensing with millimeter spatial resolution for the structural health monitoring of multiaxial loaded gfrp tube specimens," *Polymer Testing*, vol. 80, p. 106085, 2019.

[280] Y. Feng, Y. He, X. Tan, T. An, and J. Zheng, "Experimental investigation on different positional impact damages and shear-after-impact (sai) behaviors of stiffened composite panels," *Composite Structures*, vol. 178, pp. 232–245, 2017.

[281] S. Minakuchi, H. Tsukamoto, H. Banshoya, and N. Takeda, "Hierarchical fiber-optic-based sensing system: impact damage monitoring of large-scale cfrp structures," *Smart Materials and Structures*, vol. 20, no. 8, p. 085029, 2011.

[282] N. Chandarana, D. M. Sanchez, C. Soutis, and M. Gresil, "Early damage detection in composites during fabrication and mechanical testing," *Materials*, vol. 10, no. 7, p. 685, 2017.

[283] H.-P. Wang, Y.-Q. Ni, J.-G. Dai, and M.-D. Yuan, "Interfacial debonding detection of strengthened steel structures by using smart cfrp-fbg composites," *Smart Materials and Structures*, vol. 28, no. 11, p. 115001, 2019.

[284] K. I. Tserpes, V. Karachalios, I. Giannopoulos, V. Prentzias, and R. Ruzek, "Strain and damage monitoring in cfrp fuselage panels using fiber bragg grating sensors. part i: Design, manufacturing and impact testing," *Composite Structures*, vol. 107, pp. 726–736, 2014.

[285] R. Ruzek, P. Kudrna, M. Kadlec, V. Karachalios, and K. Tserpes, "Strain and damage monitoring in cfrp fuselage panels using fiber bragg grating sensors. part ii: Mechanical testing and validation," *Composite Structures*, vol. 107, pp. 737–744, 2014.

[286] H. Rocha, U. Lafont, and J. P. Nunes, "Optimisation of through-thickness embedding location of fibre bragg grating sensor in cfrp for impact damage detection," *Polymers*, vol. 13, no. 18, p. 3078, 2021.

[287] T. Okabe and S. Yashiro, "Damage detection in holed composite laminates using an embedded fbg sensor," *Composites Part A: Applied Science and Manufacturing*, vol. 43, no. 3, pp. 388–397, 2012.

[288] X. Zhang, R. Chen, A. Wang, Y. Xu, Y. Jiang, H. Ming, and W. Zhao, "Monitoring the failure forms of a composite laminate system by using panda polarization maintaining fiber bragg gratings," *Optics Express*, vol. 27, no. 13, pp. 17571–17580, 2019.

[289] Y. Okabe, T. Mizutani, S. Yashiro, and N. Takeda, "Detection of microscopic damages in composite laminates," *Composites Science and Technology*, vol. 62, no. 7-8, pp. 951–958, 2002.

[290] M. Petrovic, P. Mihailovic, L. Brajovic, S. J. Petricevic, I. Zivkovic, A. Kojovic, and V. Radojevic, "Intensity fiber-optic sensor for structural health monitoring calibrated by impact tester," *IEEE Sensors Journal*, vol. 16, no. 9, pp. 3047–3053, 2016.

[291] E. Bocherens, S. Bourasseau, V. Dewynter-Marty, S. Py, M. Dupont, P. Ferdinand, and H. Berenger, "Damage detection in a radome sandwich material with embedded fiber optic sensors," *Smart Materials and Structures*, vol. 9, no. 3, p. 310, 2000.

[292] A. Rajabzadeh, R. Heusdens, R. C. Hendriks, and R. M. Groves, "Characterisation of transverse matrix cracks in composite materials using fibre bragg grating sensors," *Journal of Lightwave Technology*, vol. 37, no. 18, pp. 4720–4727, 2019.

[293] J. Sierra-Pérez, A. Güemes, L. E. Mujica, and M. Ruiz, "Damage detection in composite materials structures under variable loads conditions by using fiber bragg gratings and principal component analysis, involving new unfolding and scaling methods," *Journal of Intelligent Material Systems and Structures*, vol. 26, no. 11, pp. 1346–1359, 2015.

[294] J. Sierra-Perez, A. Güemes, and L. E. Mujica, "Damage detection by using fbgs and strain field pattern recognition techniques," *Smart Materials and Structures*, vol. 22, no. 2, p. 025011, 2012.

[295] J. Alvarez-Montoya, A. Carvajal-Castrillón, and J. Sierra-Pérez, "In-flight and wireless damage detection in a uav composite wing using fiber optic sensors and strain field pattern recognition," *Mechanical Systems and Signal Processing*, vol. 136, p. 106526, 2020.

[296] A. Panopoulou, T. Loutas, D. Roulias, S. Fransen, and V. Kostopoulos, "Dynamic fiber bragg gratings based health monitoring system of composite aerospace structures," *Acta Astronautica*, vol. 69, no. 7-8, pp. 445–457, 2011.

[297] C. Y. Park, B.-W. Jang, J. H. Kim, C.-G. Kim, and S.-M. Jun, "Bird strike event monitoring in a composite uav wing using high speed optical fiber sensing system," *Composites Science and Technology*, vol. 72, no. 4, pp. 498–505, 2012.

[298] T. Bergmayr, S. Höll, C. Kralovec, and M. Schagerl, "Local residual random forest classifier for strain-based damage detection and localization in aerospace sandwich structures," *Composite Structures*, vol. 304, p. 116331, 2023.

[299] D. Cristiani, F. Falcetelli, N. Yue, C. Sbarufatti, R. Di Sante, D. Zarouchas, and M. Giglio, "Strain-based delamination prediction in fatigue loaded cfrp coupon specimens by deep learning and static loading data," *Composites Part B: Engineering*, vol. 241, p. 110020, 2022.

[300] S. Goossens, F. Berghmans, K. Muñoz, M. Jiménez, E. Karachalios, D. Saenz-Castillo, and T. Geernaert, "A global assessment of barely visible impact damage for cfrp subcomponents with fbg-based sensors," *Composite Structures*, vol. 272, p. 114025, 2021.

[301] B.-H. Choi and I.-B. Kwon, "Damage mapping using strain distribution of an optical fiber embedded in a composite cylinder after low-velocity impacts," *Composites Part B: Engineering*, vol. 173, p. 107009, 2019.

[302] M. Ciminello, "Distributed fiber optic for structural health monitoring system based on auto-correlation of the first-order derivative of strain," *IEEE Sensors Journal*, vol. 19, no. 14, pp. 5818–5824, 2019.

[303] J.-P. Berrut and L. N. Trefethen, "Barycentric lagrange interpolation," *SIAM review*, vol. 46, no. 3, pp. 501–517, 2004.

[304] S. McKinley and M. Levine, "Cubic spline interpolation," *College of the Redwoods*, vol. 45, no. 1, pp. 1049–1060, 1998.

[305] K. Xu, "The chebyshev points of the first kind," *Applied Numerical Mathematics*, vol. 102, pp. 17–30, 2016.

[306] C. B. Barber, D. P. Dobkin, and H. Huhdanpaa, "The quickhull algorithm for convex hulls," *ACM Transactions on Mathematical Software (TOMS)*, vol. 22, no. 4, pp. 469–483, 1996.

[307] D. P. Huttenlocher, G. A. Klanderman, and W. J. Rucklidge, "Comparing images using the hausdorff distance," *IEEE Transactions on pattern analysis and machine intelligence*, vol. 15, no. 9, pp. 850–863, 1993.

[308] J. Zhang, J. Liu, S. Hirdaris, M. Zhang, and W. Tian, "An interpretable knowledge-based decision support method for ship collision avoidance using ais data," *Reliability Engineering & System Safety*, vol. 230, p. 108919, 2023.

[309] S. Lee, J. Lim, and I. H. Suh, "Progressive feature matching: Incremental graph construction and optimization," *IEEE transactions on Image Processing*, vol. 29, pp. 6992–7005, 2020.

[310] F. Bellavia, "Sift matching by context exposed," *IEEE transactions on pattern analysis and machine intelligence*, vol. 45, no. 2, pp. 2445–2457, 2022.

[311] J.-C. Lee and M. Shirzaei, "Novel algorithms for pair and pixel selection and atmospheric error correction in multitemporal insar," *Remote Sensing of Environment*, vol. 286, p. 113447, 2023.

[312] J. Khodadoust, M. A. Medina-Pérez, O. Loyola-González, R. Monroy, and A. M. Khodadoust, "A secure and robust indexing algorithm for distorted fingerprints and latent palmprints," *Expert Systems with Applications*, vol. 206, p. 117806, 2022.

[313] W. Dai, Y. Zhang, P. Li, Z. Fang, and S. Scherer, "Rgb-d slam in dynamic environments using point correlations," *IEEE Transactions on Pattern Analysis and Machine Intelligence*, vol. 44, no. 1, pp. 373–389, 2020.

[314] A. L. Moura, J. R. Camacho, S. C. Guimaraes Jr, and C. H. Salerno, "A functional language to implement the divide-and-conquer delaunay triangulation algorithm," *Applied Mathematics and Computation*, vol. 168, no. 1, pp. 178–191, 2005.

[315] P. Shivanasab and R. A. Abbaspour, "An incremental algorithm for simultaneous construction of 2d voronoi diagram and delaunay triangulation based on a face-based data structure," *Advances in Engineering Software*, vol. 169, p. 103129, 2022.

[316] D. Karimi and S. E. Salcudean, "Reducing the hausdorff distance in medical image segmentation with convolutional neural networks," *IEEE Transactions on Medical Imaging*, vol. 39, no. 2, pp. 499–513, 2019.

[317] Y. Gao, M. Wang, R. Ji, X. Wu, and Q. Dai, "3-d object retrieval with hausdorff distance learning," *IEEE Transactions on Industrial Electronics*, vol. 61, no. 4, pp. 2088–2098, 2013.

[318] J. Zhang, J. Pang, J. Yu, and P. Wang, "An efficient assembly retrieval method based on hausdorff distance," *Robotics and Computer-Integrated Manufacturing*, vol. 51, pp. 103–111, 2018.

[319] A. Fischer, C. Y. Suen, V. Frinken, K. Riesen, and H. Bunke, "Approximation of graph edit distance based on hausdorff matching," *Pattern Recognition*, vol. 48, no. 2, pp. 331–343, 2015.

[320] O. Schutze, X. Esquivel, A. Lara, and C. A. C. Coello, "Using the averaged hausdorff distance as a performance measure in evolutionary multiobjective optimization," *IEEE Transactions on Evolutionary Computation*, vol. 16, no. 4, pp. 504–522, 2012.

[321] S. Rebay, "Efficient unstructured mesh generation by means of delaunay triangulation and bowyer-watson algorithm," *Journal of Computational Physics*, vol. 106, no. 1, pp. 125–138, 1993.

[322] K. Buchin and W. Mulzer, "Delaunay triangulations in o (sort (n)) time and more," *Journal of the ACM (JACM)*, vol. 58, no. 2, pp. 1–27, 2011.

[323] S. Lo, "3d delaunay triangulation of 1 billion points on a pc," *Finite Elements in Analysis and Design*, vol. 102, pp. 65–73, 2015.

[324] Z. Wu, L. Zhang, Z. Ying, J. Ke, and X. Hu, "Low-velocity impact performance of hybrid 3d carbon/glass woven orthogonal composite: Experiment and simulation," *Composites Part B: Engineering*, vol. 196, p. 108098, 2020.

[325] M. Richardson and M. Wisheart, "Review of low-velocity impact properties of composite materials," *Composites Part A: Applied Science and Manufacturing*, vol. 27, no. 12, pp. 1123–1131, 1996.

[326] S. Shah, S. Karuppanan, P. Megat-Yusoff, and Z. Sajid, "Impact resistance and damage tolerance of fiber reinforced composites: A review," *Composite Structures*, vol. 217, pp. 100–121, 2019.

[327] W. L. Ko, W. L. Richards, and V. T. Tran, "Displacement theories for in-flight deformed shape predictions of aerospace structures," *NASA/TP-2007-214612*, pp. 1–74, 2007.

[328] L.-H. Kang, D.-K. Kim, and J.-H. Han, "Estimation of dynamic structural displacements using fiber bragg grating strain sensors," *Journal of Sound and Vibration*, vol. 305, no. 3, pp. 534–542, 2007.

[329] A. Kefal, E. Oterkus, A. Tessler, and J. L. Spangler, "A quadrilateral inverse-shell element with drilling degrees of freedom for shape sensing and structural health monitoring," *Engineering Science and Technology-an International Journal-Jestech*, vol. 19, no. 3, pp. 1299–1313, 2016.

[330] C. De Mooij, M. Martinez, and R. Benedictus, "ifem benchmark problems for solid elements," *Smart Materials and Structures*, vol. 28, no. 6, p. 065003, 2019.

[331] M. Gherlone, P. Cerracchio, and M. Mattone, "Shape sensing methods: Review and experimental comparison on a wing-shaped plate," *Progress in Aerospace Sciences*, vol. 99, pp. 14–26, 2018.

[332] M. Esposito and M. Gherlone, "Material and strain sensing uncertainties quantification for the shape sensing of a composite wing box," *Mechanical Systems and Signal Processing*, vol. 160, p. 107875, 2021.

[333] M. Esposito and M. Gherlone, "Composite wing box deformed-shape reconstruction based on measured strains: Optimization and comparison of existing approaches," *Aerospace Science and Technology*, vol. 99, p. 105758, 2020.

[334] A. Tessler and J. L. Spangler, "A least-squares variational method for full-field reconstruction of elastic deformations in shear-deformable plates and shells," *Computer Methods in Applied Mechanics and Engineering*, vol. 194, no. 2-5, pp. 327–339, 2005.

[335] U. Papa, S. Russo, A. Lamboglia, G. Del Core, and G. Iannuzzo, "Health structure monitoring for the design of an innovative uas fixed wing through inverse finite element method (ifem)," *Aerospace Science and Technology*, vol. 69, pp. 439–448, 2017.

[336] A. Tessler and J. L. Spangler, "Inverse fem for full-field reconstruction of elastic deformations in shear deformable plates and shells," in *2nd European Workshop on Structural Health Monitoring*, pp. 1–9, 2004.

[337] A. Kefal and E. Oterkus, "Displacement and stress monitoring of a panamax containership using inverse finite element method," *Ocean Engineering*, vol. 119, pp. 16–29, 2016.

[338] A. Kefal, "An efficient curved inverse-shell element for shape sensing and structural health monitoring of cylindrical marine structures," *Ocean Engineering*, vol. 188, p. 106262, 2019.

[339] A. Kefal and E. Oterkus, "Displacement and stress monitoring of a chemical tanker based on inverse finite element method," *Ocean Engineering*, vol. 112, pp. 33–46, 2016.

[340] A. Kefal, J. B. Mayang, E. Oterkus, and M. Yildiz, "Three dimensional shape and stress monitoring of bulk carriers based on ifem methodology," *Ocean Engineering*, vol. 147, pp. 256–267, 2018.

[341] M. Li, A. Kefal, E. Oterkus, and S. Oterkus, "Structural health monitoring of an offshore wind turbine tower using ifem methodology," *Ocean Engineering*, vol. 204, p. 107291, 2020.

[342] M. Y. Liu, F. Zhou, H. Song, X. L. Yang, and J. Wang, "Deformation reconstruction for a heavy-duty machine column through the inverse finite element method," *IEEE Sensors Journal*, vol. 20, no. 16, pp. 9218–9225, 2020.

[343] D. Versino, M. Gherlone, M. Mattone, M. Di Sciuva, and A. Tessler, "C0 triangular elements based on the refined zigzag theory for multilayer composite and sandwich plates," *Composites Part B: Engineering*, vol. 44, no. 1, pp. 218–230, 2013.

[344] P. Cerracchio, M. Gherlone, M. Di Sciuva, and A. Tessler, "A novel approach for displacement and stress monitoring of sandwich structures based on the inverse finite element method," *Composite Structures*, vol. 127, pp. 69–76, 2015.

[345] A. Kefal, A. Tessler, and E. Oterkus, "An enhanced inverse finite element method for displacement and stress monitoring of multilayered composite and sandwich structures," *Composite Structures*, vol. 179, pp. 514–540, 2017.

[346] A. Kefal, I. Tabrizi, M. Tansan, E. Kisa, and M. Yildiz, "An experimental implementation of inverse finite element method for real-time shape and strain sensing of composite and sandwich structures," *Composite Structures*, vol. 258, p. 113431, 2021.

[347] M. Gherlone, P. Cerracchio, M. Mattone, M. Di Sciuva, and A. Tessler, "An inverse finite element method for beam shape sensing: theoretical framework and experimental validation," *Smart Materials and Structures*, vol. 23, no. 4, p. 045027, 2014.

[348] F. Zhao, L. Xu, H. Bao, and J. Du, "Shape sensing of variable cross-section beam using the inverse finite element method and isogeometric analysis," *Measurement*, vol. 158, p. 107656, 2020.

[349] K. Chen, K. Cao, G. Gao, and H. Bao, "Shape sensing of timoshenko beam subjected to complex multi-node loads using isogeometric analysis," *Measurement*, vol. 184, p. 109958, 2021.

[350] F. Zhao and H. Bao, "An improved inverse finite element method for shape sensing using isogeometric analysis," *Measurement*, vol. 167, p. 108282, 2021.

[351] K. Chen, D. He, Y. Zhao, H. Bao, and J. Du, "A unified full-field deformation measurement method for beam-like structure," *IEEE Transactions on Instrumentation and Measurement*, vol. 71, pp. 1–10, 2022.

[352] R. Roy, M. Gherlone, and C. Surace, "A shape sensing methodology for beams with generic cross-sections: Application to airfoil beams," *Aerospace Science and Technology*, vol. 110, p. 106484, 2021.

[353] J. Wang, L. Ren, R. You, T. Jiang, Z. Jia, and G.-x. Wang, "Experimental study of pipeline deformation monitoring using the inverse finite element method based on the ibeam3 element," *Measurement*, vol. 184, p. 109881, 2021.

[354] R. You and L. Ren, "An enhanced inverse beam element for shape estimation of beam-like structures," *Measurement*, vol. 181, p. 109575, 2021.

[355] F. Zhao, H. Bao, J. Liu, and K. Li, "Shape sensing of multilayered composite and sandwich beams based on refined zigzag theory and inverse finite element method," *Composite Structures*, vol. 261, p. 113321, 2021.

[356] P. Savino and F. Tondolo, "A new approach for displacement and stress monitoring of tunnel based on ifem methodology," *Smart Materials and Structures*, vol. 31, no. 1, p. 015013, 2021.

[357] H. Zhu, Z. Du, and Y. Tang, "Automatic free span assessment for subsea pipelines using static strain data," *Ocean Engineering*, vol. 263, p. 112413, 2022.

[358] H. Zhu, Z. Du, and Y. Tang, "Numerical study on the displacement reconstruction of subsea pipelines using the improved inverse finite element method," *Ocean Engineering*, vol. 248, p. 110763, 2022.

[359] L. Ren, R. You, J. Liu, and H. Li, "Development of a novel inclinometer by inverse finite element method for soil deformation monitoring," *Smart Materials and Structures*, vol. 30, no. 8, p. 085037, 2021.

[360] L. Colombo, C. Sbarufatti, and M. Giglio, "Definition of a load adaptive baseline by inverse finite element method for structural damage identification," *Mechanical Systems and Signal Processing*, vol. 120, pp. 584–607, 2019.

[361] M. Li, A. Kefal, B. C. Cerik, and E. Oterkus, "Dent damage identification in stiffened cylindrical structures using inverse finite element method," *Ocean Engineering*, vol. 198, p. 106944, 2020.

[362] L. Colombo, D. Oboe, C. Sbarufatti, F. Cadini, S. Russo, and M. Giglio, "Shape sensing and damage identification with ifem on a composite structure subjected to impact damage and non-trivial boundary conditions," *Mechanical Systems and Signal Processing*, vol. 148, p. 107163, 2021.

[363] M. Li, Z. Wu, H. Yang, and H. Huang, "Direct damage index based on inverse finite element method for structural damage identification," *Ocean Engineering*, vol. 221, p. 108545, 2021.

[364] A. Kefal, C. Diyaroglu, M. Yildiz, and E. Oterkus, "Coupling of peridynamics and inverse finite element method for shape sensing and crack propagation monitoring of plate structures," *Computer Methods in Applied Mechanics and Engineering*, vol. 391, p. 114520, 2022.

[365] M. Li, D. Jia, Z. Wu, S. Qiu, and W. He, "Structural damage identification using strain mode differences by the ifem based on the convolutional neural network (cnn)," *Mechanical Systems and Signal Processing*, vol. 165, p. 108289, 2022.

[366] S. Niu, Y. Zhao, and H. Bao, "Shape sensing of plate structures through coupling inverse finite element method and scaled boundary element analysis," *Measurement*, vol. 190, p. 110676, 2022.

[367] S. Niu, Y. Guo, H. Bao, and G. Leng, "A unified measurement method for shape sensing of plate structure," *IEEE Transactions on Instrumentation and Measurement*, vol. 72, pp. 1–13, 2022.

[368] C. Shang, K. Chen, S. Niu, H. Bao, and J. Du, "An effective deformation measurement method for distorted elements in mindlin plates," *IEEE Transactions on Instrumentation and Measurement*, vol. 71, pp. 1–12, 2022.

[369] Z. Li, K. Chen, Z. Wang, G. Leng, and H. Bao, "An effective calibration method based on fuzzy network for enhancing the accuracy of inverse finite element method," *Measurement*, vol. 202, p. 111708, 2022.

[370] F. Zhao, H. Bao, and J. Du, "A real-time deformation displacement measurement method for timoshenko beams with multiple singularities," *IEEE Transactions on Instrumentation and Measurement*, vol. 70, pp. 1–10, 2021.

[371] D. Oboe, L. Colombo, C. Sbarufatti, and M. Giglio, "Comparison of strain pre-extrapolation techniques for shape and strain sensing by ifem of a composite plate subjected to compression buckling," *Composite Structures*, vol. 262, p. 113587, 2021.

[372] A. Kefal, I. E. Tabrizi, M. Yildiz, and A. Tessler, "A smoothed ifem approach for efficient shape-sensing applications: Numerical and experimental validation on composite structures," *Mechanical Systems and Signal Processing*, vol. 152, p. 107486, 2021.

[373] R. Roy, A. Tessler, C. Surace, and M. Gherlone, "Efficient shape sensing of plate structures using the inverse finite element method aided by strain pre-extrapolation," *Thin-Walled Structures*, vol. 180, p. 109798, 2022.

[374] A. Tessler, H. Riggs, and S. Macy, "A variational method for finite element stress recovery and error estimation," *Computer Methods in Applied Mechanics and Engineering*, vol. 111, no. 3-4, pp. 369–382, 1994.

[375] S. Niu, Y. Guo, and H. Bao, "A triangular inverse element coupling mixed interpolation of tensorial components technique for shape sensing of plate structure," *Measurement*, vol. 202, p. 111688, 2022.

[376] D. Poloni, D. Oboe, C. Sbarufatti, and M. Giglio, "Towards a stochastic inverse finite element method: A gaussian process strain extrapolation," *Mechanical Systems and Signal Processing*, vol. 189, p. 110056, 2023.

[377] B. Wang, X. Ke, K. Du, X. Bi, P. Hao, and C. Zhou, "A novel strain field reconstruction method for test monitoring," *International Journal of Mechanical Sciences*, vol. 243, p. 108038, 2023.

[378] M. Abdollahzadeh, H. Ali, M. Yildiz, and A. Kefal, "Experimental and numerical investigation on large deformation reconstruction of thin laminated composite structures using inverse finite element method," *Thin-Walled Structures*, vol. 178, p. 109485, 2022.

[379] M. Abdollahzadeh, I. E. Tabrizi, A. Kefal, and M. Yildiz, "A combined experimental/numerical study on deformation sensing of sandwich structures through inverse analysis of pre-extrapolated strain measurements," *Measurement*, vol. 185, p. 110031, 2021.

[380] D. Oboe, C. Sbarufatti, and M. Giglio, "Physics-based strain pre-extrapolation technique for inverse finite element method," *Mechanical Systems and Signal Processing*, vol. 177, p. 109167, 2022.

[381] H. Chen, X. He, L. Qing, Y. Wu, C. Ren, R. E. Sheriff, and C. Zhu, "Real-world single image super-resolution: A brief review," *Information Fusion*, vol. 79, pp. 124–145, 2022.

[382] A. Tessler and T. J. Hughes, "An improved treatment of transverse shear in the mindlin-type four-node quadrilateral element," *Computer Methods in Applied Mechanics and Engineering*, vol. 39, no. 3, pp. 311–335, 1983.

[383] R. Cook, "Four-node 'flat'shell element: drilling degrees of freedom, membrane-bending coupling, warped geometry, and behavior," *Computers & Structures*, vol. 50, no. 4, pp. 549–555, 1994.

[384] R. Roy, A. Tessler, C. Surace, and M. Gherlone, "Shape sensing of plate structures using the inverse finite element method: Investigation of efficient strain–sensor patterns," *Sensors*, vol. 20, no. 24, p. 7049, 2020.

[385] C. Xu, "Condition monitoring of composite structure with fibre optic sensors," 2022.

[386] Y. Zhang, Q. Fan, F. Bao, Y. Liu, and C. Zhang, "Single-image super-resolution based on rational fractal interpolation," *IEEE Transactions on Image Processing*, vol. 27, no. 8, pp. 3782–3797, 2018.

[387] J. Yang, J. Wright, T. S. Huang, and Y. Ma, "Image super-resolution via sparse representation," *IEEE Transactions on Image Processing*, vol. 19, no. 11, pp. 2861–2873, 2010.

[388] H. Chang, D.-Y. Yeung, and Y. Xiong, "Super-resolution through neighbor embedding," in *Proceedings of the 2004 IEEE Computer Society Conference on Computer Vision and Pattern Recognition, 2004. CVPR 2004.*, vol. 1, pp. I–I, IEEE, 2004.

[389] R. Timofte, V. De Smet, and L. Van Gool, "Anchored neighborhood regression for fast example-based super-resolution," in *Proceedings of the IEEE international conference on computer vision*, pp. 1920–1927, 2013.

[390] R. Timofte, V. De Smet, and L. Van Gool, "A+: Adjusted anchored neighborhood regression for fast super-resolution," in *Computer Vision–ACCV 2014: 12th Asian Conference on Computer Vision, Singapore, Singapore, November 1-5, 2014, Revised Selected Papers, Part IV 12*, pp. 111–126, Springer, 2015.

[391] C. Dong, C. C. Loy, K. He, and X. Tang, "Image super-resolution using deep convolutional networks," *IEEE Transactions on Pattern analysis and Machine Intelligence*, vol. 38, no. 2, pp. 295–307, 2015.

[392] Y. Li and Z. Sharif-Khodaei, "Accuracy of distributed strain sensing with single-mode fibre in composite laminates under thermal and vibration loads," *Structural Control and Health Monitoring*, vol. 2023, 2023.